Modeling and numerical analysis of damage behavior of concrete

Ajmal Hasan Monnamitheen Abdul Gafoor

Institut für Statik
Technische Universität Braunschweig

Bericht Nr. 2019-123

Modeling and numerical analysis of damage behavior of concrete

Von der
Fakultät Architektur, Bauingenieurwesen und Umweltwissenschaften
der Technischen Universität Carolo-Wilhelmina
zu Braunschweig

zur Erlangung des Grades eines
Doktor-Ingenieurs (Dr.-Ing.)
genehmigte

Dissertation

von
Ajmal Hasan, Monnamitheen Abdul Gafoor
geboren am 28. März 1987
aus Tirunelveli, Indien

Eingereicht am: 25. Juni 2018
Disputation am: 12. Oktober 2018

Berichterstatter/in: Prof. Dr.-Ing. Dieter Dinkler
Prof. Dr.-Ing. Laura De Lorenzis

2019

Von der Fakultät Architektur, Bauingenieurwesen und Umweltwissenschaften
der Technischen Universität Carolo-Wilhelmina zu Braunschweig
zur Erlangung des Grades
eines Doktor-Ingenieurs (Dr.-Ing.)

genehmigte Dissertation

Eingereicht am: 25. Juni 2018
Disputation am: 12. Oktober 2018
Berichterstatter/in: Prof. Dr.-Ing. Dieter Dinkler
Prof. Dr.-Ing. Laura De Lorenzis

ISBN 978-3-926031-24-2

Gedruckt bzw. veröffentlicht mit Unterstützung
des Deutschen Akademischen Austauschdienstes.

Herausgeber: Prof. Dr.-Ing. Dieter Dinkler

Kurzfassung

Bauwerke sind während ihrer Lebensdauer unterschiedlichen Einwirkungen und Umwelteinflüssen ausgesetzt, die das Bauwerk schädigen können. Die Akkumulation und Ausbreitung der Schäden können im schlimmsten Fall zum Einsturz eines Bauwerks führen. Auch lokal begrenzte Schäden können zum Versagen von Bauteilen oder Strukturkomponenten oder zum Verlust der Gebrauchstauglichkeit führen. Dabei versagt die Struktur in der Regel aufgrund einer vorangegangenen Schädigung des verwendeten Baustoffs. Deshalb sollten die Bemessungsvorschriften für die Dimensionierung von Bauwerken das nichtlineare Verformungsverhalten der Baustoffe sowie deren Schadensentwicklung berücksichtigen.

Eine Alternative zu aufwändigen experimentellen Untersuchungen der Baustoffe sind Ansätze auf Grundlage der Kontinuumsmechanik. Dabei werden fallabhängig phänomenologische Modelle zur Beschreibung der Schädigung der Baustoffe eingesetzt. In der vorliegenden Arbeit wird das Verformungsverhalten von Beton mit makroskopisch phänomenologischen Modellen beschrieben. Bei komplexen Belastungen wie beispielsweise Erdbeben sind zyklische und dynamische Effekte zu berücksichtigen, die mit einer Geschichtsvariablen erfasst werden können. Zu diesem Zweck werden die Modellgleichungen mit einer Vergleichsdehnung, die von den Invarianten des Spannungstensors abhängt, formuliert. Das Versagen von Beton unter Zug und Druck ist im Nachbruchbereich als Entfestigung beschrieben. Bei zyklischer Belastung werden Geschichtsvariablen verwendet, um die Rissöffnung und das Rissschließen effektiv beschreiben zu können. Die implizite Gradientenmethode wird für die Beschreibung der Bruchprozesszone gewählt. Die nichtlokale Vergleichsdehnung und die Geschichtsvariablen werden mit einem Schadenskriterium verknüpft. Die Beschreibung der inelastischen Dehnungen erfolgt mit einer Bruchfläche analog zur Fließregel der Plastizitätstheorie. Die gewählten Modelle mit und ohne Berücksichtigung von inelastischen Dehnungen stimmen qualitativ und quantitativ sehr gut mit experimentellen Ergebnissen aus der Literatur überein. Verschiedene Anwendungen verdeutlichen die Qualität des Modells für die Vorhersage von Bruchphänomenen sowie Rissinitiierung und Rissausbreitung.

Abstract

Any structure in the fields of engineering is prone to various kinds of loading conditions and unfavorable environmental impact during its lifespan. Consequently, damages are introduced to the structure. Further accumulation and propagation of the damage may eventually lead to complete failure. Thus, unpredictable failures of structures or structural components lead to serious economic consequences. Any structural failure is caused by the failure of materials used in construction. Therefore, the design rules of structures must incorporate the nonlinear deformation behavior of materials such as initiation of damage/crack and its propagation. In the presence of expensive experimental approaches, modeling approaches based on continuum damage mechanics have been serving as alternative and efficient computational tools to describe the failure mechanisms of diverse materials. Several damage models have been developed to simulate the monotonic deformation behavior of concrete. If complex loadings such as earthquakes or impacts are considered, cyclic and dynamic aspects of loading must be additionally taken into account. For this purpose, a 3D continuum damage model is formulated using a unified equivalent strain, which depends on invariants of elastically predicted stresses. The failure of concrete in tension and compression is characterized by softening behavior. Two history deformation variables are introduced to describe the unilateral behavior (i.e., crack opening and closure) effectively. The implicit-gradient method is also incorporated for regularizing the boundary value problem. The nonlocal equivalent strain and the history parameter are combined by a single damage loading function. To capture the irreversible permanent strains, a failure surface is included and also enabled for crack opening/closure. The proposed models with and without the incorporation of inelastic strains show qualitatively and quantitatively very good agreement with experimental results from the literature. Applications of the model are finally presented to demonstrate the ability and effectiveness of the model in predicting fracture phenomena such as crack initiation and propagation.

Contents

Nomenclature

Indices

0	Initial
+	Tension
-	Compression
t	Tension
c	Compression or characteristic
e	Element
g	Global level
m	Material or local level
n	Neumann boundary
p	Prescribed or predicted value
w	Weighted quantity
bc	Biaxial compression
ie	Internal energy
ke	Kinetic energy
ee	Energy equivalence
se	Strain equivalence
el	Elastic part
in	Inelastic part
epd	Elasto-plastic damage
max	Maximum
min	Minimum
sym	Symmetric
nod	Node
dim	Spatial dimensions
$n, n+1$	Time steps
$k, k+1$	Iterative steps

Matrices

$\boldsymbol{I}_{\mathrm{d}}$	Deviatoric projection matrix
$\boldsymbol{I}_{\mathrm{h}}$	Volumetric/hydrostatic projection matrix
$\boldsymbol{K}$	Structural stiffness matrix

Scalars

α_{p}	Dilatancy constant
α_{L}	Model parameter
β_{L}	Model parameter
κ	History deformation parameter

κ_{c}	History deformation parameter in compression
κ_{t}	History deformation parameter in tension
λ	Inelastic multiplier
λ_{c}	Inelastic multiplier in compression
λ_{t}	Inelastic multiplier in tension
ρ	Density of material
σ_{max}	Maximum principal stress $\boldsymbol{\sigma}^{\mathrm{p}}$
σ_{m}	Mean stress
ε_{c}	Maximum compressive strain corresponding to f_{c}
ε_{i}	Principal strain in i^{th} direction, i=1, 2, 3
E_{ie}	Internal energy
E_{ke}	Kinetic energy
I_1	First invariant of stress tensor $\boldsymbol{\sigma}^{\mathrm{p}}$
I_2	Second invariant of stress tensor $\boldsymbol{\sigma}^{\mathrm{p}}$
J_2	Second invariant of deviatoric stress tensor $\boldsymbol{\sigma}^{\mathrm{p}}$
n_{e}	Number of finite elements
n_{nod}	Number of nodes in an element
Q	Heat supply
r_{q}	Rate of generation of heat per unit mass
T	Temperature
t	Time
w, r	Triaxial weight factor
Y	Damage energy release rate
ψ	Helmholtz free internal energy per unit volume
E	Young's modulus of the material
ν	Poisson's ratio
P_{ext}	External power of surface traction $\boldsymbol{t}$ and body forces $\boldsymbol{b}$
W_{ext}	Rate of external mechanical work done by surface traction $\boldsymbol{t}$ and body forces $\boldsymbol{b}$
η	Specific entropy
s	Entropy per unit mass
ζ	Local deformation measure
$\hat{\zeta}$	Nonlocal quantity of local variable ζ
$\hat{\epsilon}$	Nonlocal equivalent strain
ϵ	Local equivalent strain
D	Local damage variable
$\hat{D}$	Nonlocal damage variable
f_{t}	Uniaxial tensile strength of concrete
f_{c}	Uniaxial compressive strength of concrete

$f_{\mathrm{t}0}$	Initial tensile yield strength of concrete
$f_{\mathrm{c}0}$	Initial compressive yield strength of concrete
f_{bc}	Biaxial compressive strength of concrete
H_{t}	Hardening modulus of concrete in tension
H_{c}	Hardening modulus of concrete in compression
h^{+}	Isotropic hardening variable in tension
h^{-}	Isotropic hardening variable in compression
l_{c}	Characteristic length scale
c	Gradient parameter of length squared
ϵ_{g} or ϵ_{m}	Tolerance at global or material level

Second-order Tensors

$\boldsymbol{\sigma}$	Stress tensor
$\boldsymbol{\sigma}^{\mathrm{p}}$	Elastically predicted stress tensor
$\boldsymbol{\sigma}_{\mathrm{d}}$	Deviatoric stress tensor
$\boldsymbol{\sigma}_{\mathrm{h}}$	Volumetric/hydrostatic stress tensor
$\boldsymbol{\varepsilon}$	Total strain tensor
$\boldsymbol{\varepsilon}^{\mathrm{el}}$	Elastic strain tensor
$\boldsymbol{\varepsilon}^{\mathrm{in}}$	Inelastic strain tensor
$\boldsymbol{\varepsilon}_{\mathrm{d}}$	Deviatoric strain tensor
$\boldsymbol{\varepsilon}_{\mathrm{h}}$	Volumetric/hydrostatic strain tensor

Fourth-order Tensors

$\mathbb{F}$	Flexibility tensor
$\mathbb{H}$	Elasticity tensor
$\mathbb{I}$	Symmetric identity tenssor
$\mathbb{M}$	Damage effect tenssor
$\mathbb{S}$	Elastic compliance tensor

Vectors

$\boldsymbol{\xi}$	Distance from the point $\boldsymbol{x}$ to a point in its vicinity
$\boldsymbol{b}$	Body force
$\boldsymbol{d}$	Nodal displacement vector
$\boldsymbol{m}$	Vector used for getting $\boldsymbol{I}_{\mathrm{h}}$
$\boldsymbol{n}$	Unit normal vector
$\boldsymbol{q}$	Heat flux from the surface
$\boldsymbol{r}$ or $\boldsymbol{x}$	Position vector of a material point
$\boldsymbol{t}$	Surface traction
$\boldsymbol{u}$	Displacement field
$\boldsymbol{v}$	Velocity field
$\ddot{\boldsymbol{u}}$	Acceleration field

Other Symbols

$\{x, y, z\}$	Cartesian coordinates
$\{\xi, \eta, \zeta'\}$	Natural or reference coordinates
Γ	Boundary
V	Volume domain under consideration
S	Surface domain under consideration
$\int_V$	Integration over volume V
$\int_S$	Integration over area S
Δ	Incremental change/difference
∇^2	Laplacian operator
$\nabla^{(i)}$	i^{th} order of gradient operator
∇^{sym}	Symmetric gradient
$\delta(\cdot)$	Virtual quantity
$\partial(\cdot)$	Partial differentiation
$d(\cdot)$	Total differentiation
$\dot{(\cdot)}$ or $\frac{d(\cdot)}{dt}$	Time derivative
$H(\cdot)$	Heaviside function
$\hat{\cdot}$	Nonlocal quantity
$\tilde{\cdot}$	Effective quantity
$\Big\lvert \cdot \Big\rvert$	Determinant
$[\cdot]^T$	Transpose of matrix
$(\cdot)$	Scalar product
$\times$	Cross product

1 Introduction

All the structures, which are in the fields of Civil, Mechanical and Aerospace engineering, are subjected to various kinds of loading conditions, unfavorable conditions of surrounding environments and natural calamities such as earthquakes, tsunamis, cyclones and floods, etc., during their service life. As a result, damages are introduced into the structures, which in turn gradually reduce the strength, stability and serviceability of the structures. Moreover, these damages are accumulated and distributed in the vicinity over a certain period up to which the loads are acting on the structures and may eventually lead to failure. In the present day, unpredictable failures of structures or structural components occurring in the industries/fields lead to serious economic consequences. Any structural failure is caused by failure of the materials used in construction. Hence, each and every individual structural component of the structures must be designed in such a way that it can resist the induced forces due to the application of external loading during its service. In order to ensure the safety in the applications and to prevent the worst consequences, nonlinear deformation behavior of the materials such as the initiation of damages or cracks and the propagation of cracks have to be properly investigated and incorporated in the existing design philosophies.

1.1 Motivation

In the case of civil engineering structures that are strongly exposed to earthquake excitation, a large amount of kinetic energy is transferred into the structures, which could lead to high amplitude oscillations and related stress states. If elastic behavior of the material is assumed, the proof of safety against material failure generally leads to an unrealistic and very inefficient design. In order to reduce the material effort, the design has to take into account the ductility of the material and/or structures, which is able to dissipate the encountered kinetic energy. The ductile behavior of steel leads to a proper earthquake resistance of the structures if the limit load philosophy is taken into account. Nonetheless, steel may be too expensive in many cases. On the other hand, the most important and common material used in the field of civil engineering structures is reinforced concrete. But it needs a different design philosophy to achieve earthquake resistance [9]. Since concrete is a brittle material, the failure and the post-failure behavior depend strongly on the rotation capacity of failure regions, which leads to additional design limits. Experimental approaches based on expensive testing of the real models in laboratories are mainly applied to investigate the failure of reinforced concrete structures. Hence, the developed design rules, which are used to predict the useful life or failure of materials, mostly deal with empirical estimations of the ductility and limit load capacity [37].

By contrast, continuous research developments in the understanding of continuum solid mechanics and their gaining acceptance lead to the introduction of Continuum Damage Mechanics (CDM), which has been employed in an extensive range of materials to describe the mechanism of progressive internal damages (evolution of the internal damages) experienced by the mechanical properties of materials, causing the initiation of macro-cracks/failures. The fast growing techniques in the field has made the use of computational mechanical tools to carry out life/failure prediction a realistic alternative, which can be successfully adopted in many designs and damage assessment situations.

Although the past few decades of various research have contributed towards the development of continuum damage models to understand the behavior and fracture mechanisms of different materials, the numerical investigations of reinforced concrete structures under earthquake excitation lead to very sophisticated approaches, if highly nonlinear behavior and damage to the material are taken into account. In the case of complex loads such as earthquakes and impacts, cyclic and dynamic aspects must be additionally taken into account in the modeling of concrete.

1.2 Structure of the thesis

This section presents how the thesis chapters are organized. In order to provide enough fundamentals and basic concepts to the reader, the chapters discuss a brief review of literature, concepts of material and local/nonlocal damage modeling in addition to the continuum damage models developed in this research work and their implementation into in-house finite element codes called codeBlue. The thesis consists of twelve chapters as follows:

Chapter 2 provides a detailed review of the presently available literature proposing various continuum damage models developed for concrete material and provides a strong basis for the present research work. Models based on linear and nonlinear fracture mechanics, models based on local and nonlocal damage theories, and models based on discrete element methods are discussed. The regularized models are also included. At the end, the objectives of the present work are defined.

Chapter 3 gives a brief introduction to material modeling and basic equations of continuum mechanics. A concise description of kinematic relations and thermodynamic conservation laws are also added.

Chapter 4 describes the local approach of damage modeling in detail. The physical meaning of the damage variable to evolution of the damage variable are discussed. Frequently used damage evolution laws for concrete and their description are also described. How the damage variables are adopted in literature in view of describing the distinct behavior of concrete are also explained with respective equations.

Chapter 5 investigates the influence of various history deformation parameters used in literature for modeling the softening behavior of concrete using selected damage evolution laws. Based on the obtained results, a suitable damage evolution law is also proposed.

Chapter 6 deals with the fundamental issues of localization of deformation related to finite element implementation and the significance of nonlocal phenomena by incorporating an internal length. It also discusses how regularization methods can be used to enhance local damage models. Additionally, a brief comparison of gradient-enhanced damage models and phase-field models has also been provided.

Chapter 7 elaborates an elastic-damage model proposed in this work for deformation behavior of concrete material. It also discusses how this model is enabled for describing the unilateral behavior of concrete using a single loading surface and single damage variable.

Chapter 8 deals with the incorporation of inelastic deformation behavior into the previously developed unilateral isotropic damage model in order to capture the irreversible or permanent strains in the concrete. The coupling strategy and numerical integration scheme of the coupled model are described.

Chapter 9 discusses the numerical implementation of damage models into the finite element codes. The governing equations of an initial-boundary value problem are briefly given and finite element discretization is provided. This is followed by weak formulations, development of finite element model, assembly of finite elements, and linearization. Finally, a solving procedure is also outlined.

Chapter 10 illustrates the validations of the isotropic damage models. The results obtained from numerical analyses are compared with that of experimental results available from literature under various types of loading.

Chapter 11 demonstrates the capabilities of the proposed damage models in describing the fracture processes with the help of simulating selected concrete fracture problems available in the literature by means of numerical analyses.

Chapter 12 summarizes the developments and important features of damage models along with concluding remarks. Possible future research directions are also outlined at the end.

2 Literature Review

In the framework of continuum mechanics, non-linear models for the description of elastic structures are state of art. In the past several decades, a number of models have been developed in the framework of continuous media to understand the deformation behavior of concrete. Although the plastic behavior of concrete is not fully understood, research has been performed and models developed that used plasticity theory to simulate concrete behavior [8,23,117,148]. However, a negative stiffness degradation in the case of strain-softening of the material in the post-peak regime is not well described by these plasticity models. In this chapter, several models within the framework of continuum mechanics available from the literature are reviewed to understand their abilities and the limitations of their applications. It will provide a strong basis for the research work being carried out and helps to identify problems or difficulties and come up with interesting ideas and discussions for the advancement of the existing models.

2.1 Linear and non-linear fracture mechanics

There are some numerical approaches based on fracture mechanics such as: the stress intensity factor approach based on the stresses near crack tip exceeding yield stress, the energy balance approach based on the concept of strain energy released exceeding the absorbed energy, the Dugdale model (Strip-yield model) and the Barenblatt model (Cohesive force model). The stress intensity factor approach requires a very fine Finite Element (FE) mesh close to the crack tip to explain crack propagation, whereas the energy balance approach requires coarser mesh for the same. Dugdale's model, which is based on a plastic zone near the crack tip within which a stress equal to the yield strength acting across the crack, is developed for modeling cracks of ductile materials [7,57,65]. On the other hand, a Barenblatt model similar to Dugadale's model based on the forces (cohesive forces) of interaction between the opposite sides of the crack surfaces is developed for modeling of purely brittle materials by imposing the stress variation with the deformation [10,11]. Nonetheless, these models could not be applied without initial crack. Moreover, the conventional linear-elastic fracture mechanics (LEFM) based on the prediction of infinite stresses and strains at a crack tip always yields to unrealistic conclusions.

Earlier in most cases, concrete was considered as a homogeneous material while dealing with fractures on the macro level. But, in reality, concrete is a heterogeneous material and hence, the linear elastic fracture mechanics (LEFM) is not sufficient to describe the fracture processes of normal concrete structures [7,85] for the following reasons.

- LEFM is only valid for homogeneous material like steel or any non-linear material whose deformation confined to a small region surrounding the crack tip in ductile fracture.
- The failure of concrete due to its heterogeneity, because of the large size of aggregates occurs by the distributed cracking or damage in a progressively fractured process zone, and thus the damage zone becomes larger than that of elastic materials or metals. That is

why the material exhibits a complex non-linear mechanical behavior.

- The aforementioned models of LEFM are not able to describe the formation of cracks when implemented in Finite Element Analyses.

Therefore, an alternative model is required to capture the fracture process zone of concrete and can be easily implemented in Finite Element Analyses without having further difficulties.

In order to overcome these issues, Non-linear fracture mechanics is introduced for studying the fracture of concrete structures at the macro level by considering concrete as an equivalent homogeneous continuum. The need of a feasible method using FEM became the base for the development of a model as the Fictitious crack model or the Cohesive crack model. This is the first model proposed by Hillerborg in 1976 to analyze the fracture of concrete, as a non-linear fracture mechanics representation based on two parameters namely the strength and fracture energy. This model characterizes the line of damage or a crack by a stress-displacement $(\sigma - w)$ rather than stress-strain $(\sigma - \varepsilon)$ relation, since the shape of the $(\sigma - w)$-curve (for the same fracture energy) might greatly influence the fracture behavior [74, 77]. The model is applied to micro-cracking, non-yielding materials (such as concrete) with an approximation of linear stress-strain relation up to peak stress. The model has also been successfully applied to some types of fiber-reinforced concrete and plastics as well as to wood. It could be applied to all types of tensile fracture if only the material properties were known and adequate tools were available for the numerical analyses [75, 76].

2.2 Local and nonlocal continuum models

The first continuum damage model in which a scalar internal variable was defined by the effective stress concept was introduced by Kachanov [81, 83] to characterize the creep failure of metals under uniaxial loads. Later, a considerable amount of research has been devoted to the formulation of constitutive models to describe internal degradation of solids with the framework of continuum mechanics. It includes the continuum damage theories to model fatigue, creep, creep-fatigue interaction and ductile plastic damage [51].

Nevertheless, concrete as a heterogeneous material neither yields nor fails when maximum stress is reached, instead showing decrease in stress with increasing deformation (strain). This behavior is called Strain-softening. This softening response is accompanied by a reduction of the unloading stiffness of concrete, and irreversible (permanent) deformations, which are localized in narrow zones often called cracks or shear bands. It is understood that, as soon as strain-softening begins, any elastic or elastic-plastic material loses stability when the matrix of its tangent moduli ceases to be positive definite. On the strain-softening (declining) branch, the tangent Young's modulus is negative, which means that the matrix of tangent moduli is not positive-definite anymore. Thus, the characterization of strain-softening in terms of stress, strain, state variables of continuum medium causes instability. This could be avoided by describing the strain-softening by a stress-displacement $(\sigma - w)$ rather than stress-strain $(\sigma - \varepsilon)$ as in the case of the Hillerborg model. In spite of that, the strain-softening damage tends to localize within a zone or vanishing volume (a line or short segment or surface). Therefore, the strain localization, which is a mode of instability due to strain softening, eventually causes the strong spurious mesh sensitivity in FE solutions [12]. In addition, the line crack models like the Fictitious crack model have disadvantages such as: the possibility of destruction of the stiffness matrix leading to complications in programming due to the split of a node into two nodes and renumbering of nodes and direction of propagation as unknown. These drawbacks facilitated for the advancement of the line crack model to a smeared crack model or Crack Band model characterized by three parameters namely the tensile strength, the fracture energy and the cracking front width. In this model, the gradual strain-softening, which is a gradual decrease of stress to zero with increasing strain, is characterized by imposing a lower limit on the element size and by adopting the energy dissipation (fracture energy) due to localized cracking per unit length of fracture as a material property (mesh independent). Thereby, the strain localization to a vanishing volume and the associated sensitivity of mesh, and the effect of micro-cracking in the crack band are avoided. The crack is modeled by changing the isotropic elastic moduli matrix to an orthotropic one, reducing the material stiffness in the direction normal to the cracks in the band. A mode I crack following a curved path or propagating in an arbitrary direction with respect to the mesh lines is modeled as a zigzag crack band whose overall direction in the mesh approximates the actual crack direction. This model is treated as local continuum with a minimum size of localization region [19].

The works of Bažant [13–15] address the issues related with the theory of strain-softening behavior in classical (local) and nonlocal continuum. The distributed cracking in brittle and heterogeneous materials like concrete could be macroscopically described as strain-softening. Strain-softening in a local continuum can be mathematically correct but not exactly representing the strain-softening behavior of materials like concrete or geomaterials. Because experimental investigations show that those materials consume finite energy and exhibit finite size of the deformation localization during the strain-softening process. Hence, the micro-cracking pattern that occurs during the strain-softening of concrete is first studied using a classical nonlocal continuum theory, which is inspired by the introduction of a nonlocal continuum approach during the 1960s. It is found that the width of the strain localization region and the energy consumed by strain-softening failure converged to zero as the element size is decreased to zero, and the response exhibited extreme noise due to the instability of the continuum. Then, an imbricate nonlocal continuum is developed by adding a characteristic length scale as an integral form to prevent the vanishing mesh size. It means that a finite element system containing a mesh of imbricated (regularly overlapping) elements of fixed characteristic length is used. The numerical studies of imbricate nonlocal continuum confirmed that it is feasible in FEM and renders convergence in solutions because the mesh dependency as well as stability issues are avoided unlike in local continuum [17].

In spite of the fact that the imbricate nonlocal continuum insured the proper convergence and eliminated spurious mesh sensitivity, it is later identified that unnecessary computational complications are raised due to the consideration of all response (strains and stresses obtained from strains) as nonlocal and zero-energy spurious modes of instability are encountered. As a result, non local damage theory is updated by treating only the variables controlling strain softening as nonlocal and the elastic part of the strain as local to prevent such localization [126]. And it is shown that the key attribute of nonlocal formulation of strain softening is to define the elastic behavior of strain (kinematic variable) including unloading and reloading as local, which leads to better convergence of nonlocal damage solutions, since the minimum size of the localization region acts as a localization limiter. Furthermore, this nonlocal approach based on the introduction of characteristic length scale captures strain and damage localization for a model, since the width of the localization band is proportional to the internal length introduced in the constitutive description through the weight function. This approach requires no imbrication of elements and no overlay with the local continuum as in [15, 20]. In the nonlocal continuum formulations, the characteristic length of a heterogeneous material such as concrete represented as a material property governs the minimum possible width of strain-softening zone. The measurement of this length as a ratio of the fracture energy (energy dissipated per unit area) to the energy dissipated per unit volume is experimentally determined roughly as 2.7 times the maximum size of aggregate [21]. The nonlocal model discussed so far is based on the single variable, the damage controlling the strain-softening such that the damage energy release rate is averaged over the representative volume of the material and also based on the constitutive relations derived within the framework of thermodynamics irreversible processes. It is also shown that the spatial averaging alternatively worked well.

By contrast, another model has been developed using effective stress concepts by incorporating a damage parameter in the constitutive equations, postulating a damage criterion describing large difference between tension and compression strength, and supplying a power law as a kinetic damage evolution law (hardening/softening) for softening of brittle materials. An equivalent damage strain is proposed in terms of principal stresses instead of principal strains in a similar way without any omission of parameters responsible for the distinction between tension and compression. The elaboration of the work is performed with FEM [28]. In a similar fashion, a unified local approach has also been developed by establishing the stress-strain relation and the damage evolution (power law) with a criterion for damage growth, which makes the distinction between brittle damage (variable damage surface under given loading) and fatigue damage (invariable damage surface). Mesh sensitivity is reduced by using the concept of elementary cell as a characteristic scale in the mesh [118].

However, the solutions of local continuum approaches suffer with severe lack of mesh objectivity, whereas the nonlocal solutions converge after mesh refinement [52]. Furthermore, the aforementioned models are developed based on the consideration of isotropic damage for sake of simplicity in most cases.

In spite of the success of various fracture based models or continuum based models in solving many engineering problems, their usage is limited due to the specific applications only under particular load cases. However, the lack of equilibrium at the crack tip if more cracks are formed, and the problem of localization into a vanishing volume and mesh-sensitive solutions are solved by several other nonlocal/gradient dependent models. Nonetheless, the difficulties in modeling due to opening and closure of micro-cracks (unilateral effects) under cyclic/reverse loading and the combined effect of cracking and plasticity at the damaged points still remain challenging. It is well-known that concrete or geomaterials actually show strain-softening, leading to complete loss of strength. Specifically speaking, this kind of strain-softening occurs not only in tension but also in compression. As the qualitative behavior of concrete is considered as cohesive soils (frictional materials with cohesion), the loss of strength can be assumed as vanishing of cohesion. This is understood that any model (plasticity) should be considered with yield criterion, the flow rule, and the hardening rule accounting for hardening as well as softening with evolution of internal variables in the yield function. Therefore, Lubliner *et. al* [98] at first developed such a constitutive model based on an internal variable-formulation of plasticity theory for non-linear analysis of concrete by using a modified version of Mohr-Columb criterion to fit the experimental data.

When dealing with cyclic loading, which is a particular case of earthquakes, the cracking behavior of concrete under tension or crushing under compression is essential. The reversal of external loading also causes changes in stiffness, thus ensuring its non-linearity. In order to cope with this kind of unilateral effects, most of the coupled plastic-damage or elastic-damage models introduce two independent internal damage variables to represent the distinct behavior of concrete in tension as well as in compression. The evolution of these two damage variables is related to a damage loading surface [104] or sometimes total damage could be a weighted sum of these damages in tension and compression related to two different loading surfaces, expressed in terms of positive and negative damage energy release rates respectively [107]. Occasionally, the total damage could also be estimated from two damage variables using a multiplicative relation [42, 94] to consider elastic stiffness recovery during loading/unloading processes. Besides the use of the additive and multiplicative relations, the spectral decomposition is also sometimes used to obtain the positive (tension) and negative (compression) parts of effective stresses that are linked to these damage variables [35, 149]. An effective damage could also be considered as a function of two independent history deformation variables associated with two different loading surfaces [105, 106]. These history variables are related to damage equivalent strains in tension and compression respectively.

A thermodynamically consistent constitutive model, which is a generalization of classical plasticity theory and isotropic damage theory of Kachanov, is proposed [99]. Coupling between plasticity and damage is achieved through a simultaneous solution of the plastic and the damage problem. The Euler Backward method of numerical scheme is adopted for the integration of the resulting constitutive equations to solve plane stress non-linear problems using FEM.

In similar fashion, another constitutive damage model [62] is formulated based on an effective stress tensor by introducing two scalar damage variables as internal variables, as well as a plastic-strain tensor, for massive concrete, merely for the seismic analysis of gravity and arch dams. Afterwards, the model is also extended to account for concrete strain-rate dependency, suitable for seismic analysis of large scale structures, by introducing independent viscous regularization (with the addition of fluidity parameters and flow functions as in a classic Perzyna regularization) into the respective rate-independent evolution laws of damage. Quite refined approaches defined from damage mechanics are presently available and some approaches have also been developed by considering tensorial damage variables and conditions of material orthotropy or anisotropy. Nonetheless, for the sake of simplicity and to account for easily manageable design purposes, and to minimize the number of parameters involved to describe for concrete material, the plastic viscous-damage model [62] is upgraded to a model [63] where the contributions from plastic deformations and viscous effects due to strain-rate dependency were discarded. In spite of its final intuitive format, the dissimilar behavior under tension and compression, the stiffness recovery upon load reversal, the strength enhancement under two-dimensional (2D) or three-dimensional (3D) compression could be easily predicted by the model. These features are accomplished by performing a split over the stress tensor obtained elastically, which includes the model in the so-called strain-driven category, since the elastic stress tensor is computed explicitly on the basis of the strain tensor. Concerning the reinforcement, rebars were reproduced with a FE mesh constituted by 2-nodded truss elements. The non-linear performance of each rebar is reproduced with the Giuffrè-Menegotto Pinto cyclic model, which is also explicit in terms of the rebar strains. The reinforcement FE mesh overlaps the one for concrete counterpart, and perfect bond between both materials is assumed. The efficiency of the global model is illustrated with two applications, namely a 3D-plain concrete arch dam, and a six-floor 2D-reinforced concrete wall tested on a large-scale shaking table.

On the other hand, the inelastic behavior of concrete could also be modeled using a thermodynamically well-founded elastic-plastic damage model [149] constructed by combination of the general formulation of free energy potential with a tensile-compressive double hardening plasticity theory and two-parameter damage expression, for inelastic behavior of concrete. Herein, the concept of effective plastic energy storage rates is proposed, which are conjugate forces of hardening variables in an undamaged configuration. The proposed free energy potential could serve as a thermodynamic link between plastic and damage evolution. An analogy between the evolution of hardening variables and that of a plastic strain is used to postulate the formulation of plastic free energy. This approach is validated by a series of tests in plane stress condition.

In the case of heterogeneous materials or quasi-brittle materials such as concrete, which is generally a mixture of coarse aggregate, sand, and hydrated cement paste, the transition zone in between the coarse aggregate particles or the interface between the stiff grains and the cement matrix is weaker than the rest of the cement matrix/paste, because of the physical boundary between the different materials. Therefore, it exhibits a micro-cracking pattern that occurs at the weaker zone, being different in tensile and in compressive loading, i.e., orthogonal to the loading direction in tension and parallel to it in compression. Consequently, the nucleation, growth and coalescence of these micro-cracks under progressive loading result in macroscopic crack patterns, which leads to loss of overall stiffness. Thus, the internal change of a material depending on the direction of applied loading is essentially an anisotropic phenomenon. In such cases, each load causes micro-cracks to grow in one preferential direction, affecting the material response to subsequent loads in different directions. And a scalar damage variable as in the case of isotropic damage has limitation in describing the actual state of damage and hence, this kind of induced anisotropy responsible for the large dis-symmetry in tension/compression of concrete behavior must be incorporated in constitutive modeling. Therefore, damage in concrete should be considered as anisotropic for a more reliable representation of damage. This results in the development of various models describing the distributed state of the anisotropic damage in terms of the damage variables as vectors or higher rank tensors [3, 31, 34] and using micro-plane theories [16, 88, 89] in spite of their complications. Nevertheless, the second order symmetric tensors are commonly considered as the effective way of representing the state of anisotropic elastic damage as they could be mathematically simpler in computations than the higher rank tensors and are more convenient for practical applications, which is clear from the references [34, 53, 54, 112] and therein.

In addition to the description of anisotropic damage, the Cauchy stress tensor (nominal or effective) is sometimes split-up into tensile and compressive components using the spectral decomposition [24, 51] in order to clearly distinguish stress contributions due to tension or to compression. Consequently, independent non-linear mechanisms of concrete degradation can be produced. By means of which, all the shear components are vanishing, except normal components of the stress tensor. The concept of split-up of Cauchy or effective stress tensors into tensile and compressive components has been also performed with the description of isotropic damage [30, 62, 149].

To model the anisotropic damage behavior of elastic-brittle materials under multi-axial state of stress, by employing a second rank symmetric damage tensor, an irreversible thermodynamic theory of the constitutive and the damage evolution equations is developed. The Helmholtz free energy is expressed as a function of simultaneous invariants of the elastic strain tensor and the damage tensor by taking account of the unilateral behavior [104] of the material. The developed constitutive equations were applied to describe the anisotropic elastic damage behavior of high-strength concrete under various loading histories [112].

Simple one-dimensional localization problems were analyzed nonlocal (integral) constitutive models used in simulations of damage and fracture processes of quasi-brittle materials. It is shown that certain nonlocal approaches are incapable of reproducing the entire material degradation process up to complete failure(leading to residual stresses) and the formulations are not capable of modeling a complete macroscopic crack. Moreover, the load-displacement diagrams obtained with the nonlocal model using the linear local softening law were not realistic, whereas nonlocal models with exponential local softening law showed a more reasonable response [79]. On the other hand, a cohesive finite element method is developed based on incorporating segments of cohesive surfaces into continuum finite elements that is applicable when crack growth is discontinuous. The crack is modeled as a collection of overlapping cohesive segments, which are added as displacement jumps by using the partition-of-unity property of finite element shape functions, instead of considering the single entity of a crack and that propagating. A combination of overlapping crack segments could behave as a continuous crack. In addition, the method allowed for complex crack patterns including the simulation of crack nucleation at multiple locations, growth, coalescence and branching, since crack segments were added at arbitrary positions and with arbitrary orientations, where attention is restricted to a small deformation formulation [131].

Indeed, discrete or smeared crack approaches have their domain of applications. Discrete crack models are appropriate for modeling one or more dominant cracks, whereas smeared crack models could simulate the diffuse cracking patterns arising due to heterogeneity (of concrete and presence of reinforcement). Even the smeared crack model could not properly capture the crack initiation, growth, coalescence and branching. By means of cohesive segments as a bridge between the traditional discrete and smeared crack models through exploitation of the partition-of-unity property of finite element shape functions, the simulation of the initiation and growth of a dominant crack is enabled even without predefinition [47, 48].

A nonlocal model in which nonlocal displacements, obtained as the nonlocal Average of local displacements, were considered to derive the evolution of damage and the resulting model exhibited a satisfactory behavior and is attractive from the computational point of view, especially regarding the computation of the consistent tangent matrix [132]. Nevertheless, the linearization of nonlocal integral equations is still not straightforward [122].

2.3 Gradient dependent models

On the other hand, by utilizing methods developed in the theory of fluid interfaces, the behavior of localization of deformation for the case of hyper-elastic materials is examined by incorporating the gradient dependent term in the expression for strain energy density in order to avoid the loss of ellipticity of the governing equilibrium equations [143]. The approach overcame one of the major shortcomings in constitutive equations for solids admitting localization of deformation at finite strains, i.e., their inability to provide physically acceptable solutions to boundary value problems in the post-localization range due to loss of ellipticity of the governing equations. Thus, the modified strain energy function leading to equilibrium equations, which always remain elliptic, suggested not only the direction but also the width of the deformation bands providing for the first time a predictive unifying method for the study of pre- and post-localization behavior.

A nonlocal constitutive equation based on the limit/yield stress as a function of strain and strain gradient is introduced for simulating softening phenomena with a proper localization in one-dimensional problems [134, 135]. A second-order gradient dependent plasticity theory in the finite element context [45] in which the yield strength or yield function not only depends on an equivalent strain measure but also a Laplacian operator is developed. Moreover, a plastic multiplier is also discretized in order to properly solve the resulting non-linear differential equations. But the dependency imposed higher-order (C^1) continuity requirements on the discretization of plastic multiplier, while the discretization of the displacement field requires C^0-continuous interpolation functions. A gradient-enhanced damage is also formulated in which the Laplacian of the internal variable, which memorizes the damage, enters the damage loading function in addition to the conventional dependence on this internal variable itself. And the damage is embedded into thermodynamics by defining a nonlocal damage variable as a function of the nonlocal history variable and also by considering the existence of a linear relation between the damage variable and history parameter that measures the maximum damage experienced by the material [44].

It is shown that the cracking and the fracture of quasi-brittle materials like concrete could be modeled realistically even with a relatively simple, isotropic model when the deformation measure of the model governs the growth of damage and the objectivity with respect to mesh orientation could only be assessed in two- or three-dimensional setting with the gradient enhancement by incorporating higher order deformation gradients [120, 121]. Viscous, thermal or other non-mechanical effects were not taken into account, and further small strains and rotations were assumed. This approach is validated by examining the problems having Mode-I fracture mechanism and friction/aggregate interlock not playing a role (no anisotropy), and the failure dominated by tensional stresses (no unilateral effect) [123]. It is also found that the enhanced models allow for the propagation of waves having dispersive nature in the softening zone under quasi-static loading conditions. The gradient damage model seems to be both conceptually and computationally simpler than the gradient plasticity model, since C^0-continuity of the interpolation suffices for implicit models rendering stable and efficient numerical solution algorithm, thereby leading to more localized deformation than the nonlocal model [122, 124].

From the review of constitutive models, namely gradient-enhanced isotropic damage and gradient-enhanced plasticity models, it seems that the algorithm for the damage model is simpler than that for the gradient plasticity model. This is related to the issue of the additional boundary conditions that emerge in such higher-order continuum theories for the purpose of modeling localization phenomena in quasi-brittle and frictional materials as large-scale finite element simulations [46].

The development of phenomenological nonlocal approaches based on implicit gradient-enhanced damage necessitates to identify the models, which are capable to describe the damage process in quasi-brittle materials. Hence, five mutually different implementations of implicit gradient-enhanced damage constitutive models were examined with respect to their ability to describe crack initiation and crack propagation. The results of one-dimensional crack analysis showed that models based on a nonlocal equivalent strain with a constant length parameter and a power-law damage evolution lead to well-defined crack opening, but models with a decreasing length parameter upon increasing damage, a nonlocal damage variable or a model of nonlocal history parameter yield zero crack opening. If the exponential damage evolution laws are used, then the nonlocal equivalent strain model and the nonlocal history parameter model, both with a constant length scale lead to an infinite crack opening. But, regardless of the evolution law, such large crack openings could be obtained by a nonlocal equivalent strain model with a length parameter increasing with strain. Also, during crack propagation analysis revealed the inability of the damage models with a decreasing length parameter upon increasing damage to describe the real processes due to a mesh dependency. On the other hand, the nonlocal equivalent strain model and the nonlocal history parameter model with a constant length scale, and the nonlocal equivalent strain model with a length parameter increasing with strain are well capable of describing the crack propagation phenomena [69].

Having different approaches in practice, it is also found that the nonlocal and implicit gradient formulations are largely equivalent and the responses of both models in wave propagation, localization and at cracks are remarkably and qualitatively good in agreement, when compared to explicit gradient formulations. When well-defined spatial interactions exist in a material, the nonlocal approach may be preferred because it could model the nonlocality in a more transparent way. However, the interactions near notches and cracks are questionable. This issue is not present for the gradient approach, where the treatment of boundaries is much better defined from a mathematical view-point. Since the nonlocality is introduced on a phenomenological basis in most practical cases and the nonlocal gradient equations can be efficiently linearized by introducing an additional equation containing gradient terms conveniently in weak form [22,116,123], the implicit gradient formulation is preferred rather than the integral model [125]. Therefore, implicit gradient formulations have been successfully implemented for intended results under various loading environments such as high-temperature loading [116] or chemical loading [42] and earthquake loading [86, 145].

On the contrary, anisotropic continuum damage models were developed by incorporating the higher-order strain gradients to simulate the localized mode I as well as mixed mode failures of quasi-brittle materials up to the complete loss of load carrying capacity. The governing equations remained local in a finite element sense and could be solved by introducing an additional field for the gradient term. Consequently, the loss of well-posedness of the boundary value problem is avoided. The anisotropic description adopted here is based on micro-plane theory [88, 89].

As discussed, since the direct introduction of gradient of the damage variable leads to the requirements of C^1 interpolation of the displacements, another method [55] is proposed for the regularization of continuum damage models based on gradient enhancement of the free energy functional in which a new nonlocal variable field is introduced while preserving C^0 interpolation and an isotropic scalar damage is considered. The strategy is formulated as a pure minimization problem and examined with numerical examples of infinitely long pre-cracked or circular holed bricks subjected to tension. This method efficiently removed pathological mesh dependence together with the numerical difficulties connected with the calculation in the softening range of the materials.

Additionally, a coupled damage-plasticity model based on gradient enhancement of the free-energy (Helmholtz) function is developed by restricting attention to a small strain quasi-static case and considering isotropic scalar damage [56]. The regularization, which is achieved by accounting for nonlocal interaction through an interaction potential, is performed on both the damage parameter and internal plastic variable, since both inelastic mechanisms include softening. The behavior of the coupled model is demonstrated by the test problem of an infinitely long brick with a circular hole subjected tension and it is showed that this method efficiently removes the pathological mesh dependence together with the numerical difficulties in softening range.

2.4 Phase-field models

Another class of models based on continuum mechanics has been developed for modeling the brittle fracture of materials. A review on phase-field models given by [6] provides an overview of existing quasi-static and dynamic phase-field formulations developed among the scientific community of physics and mechanics. Generally, a phase-field approach incorporates a continuous field variable (the field order parameter) having a smooth transition between multiple physical phases within a system. Yet, within the context of fracture mechanics, the order parameters describe the smooth transition between the states (phases) of undamaged and fully damaged materials. Thus, the field used to approximate the sharp crack discontinuity by a smeared surface is referred to as the crack field. By defining a proper evolution of such field variables, this approach can be used to model the fracture processes of various materials. Moreover, phase-field modeling of fracture has recently been considered as an elegant way of simulating complicated fracture processes, because of its ability to simulate such processes including crack, initiation, propagation, merging, and branching in all situations and applied to model brittle/ductile fracture of solids and shells [5, 6].

The development of phase-field models in the field of fracture mechanics has originated from the pioneering work on the variational formulation of brittle fracture by using a minimization of the energy functional to overcome the Griffth theory of brittle fracture [64] and later this minimization problem was regularized in order to improve its efficiency in numerical calculations by introducing the crack field parameter and an internal length scale to control the width of the transition zone [27]. Subsequently, the thermodynamically consistent phase-field models [108, 109] for brittle fracture have also been developed based on the description of continuum damage mechanics.

At this point, it is noteworthy to mention that the so-called crack field parameter and the internal length adopted in the phase-field models are similar to the nonlocal variable (gradient enhanced local variable) and the characteristic internal length scale commonly adopted in the nonlocal damage models [18, 52, 126] or the gradient damage models [22, 44, 67, 115, 119]. Thus, the averaging equation of phase-field variables can be conceived as a special case of the nonlocal averaging equation of damage variable in the gradient-enhanced damage models. In order to have a better understanding of these approaches, a brief summary on the comparison of both gradient damage models and phase-field models based on the work [50] is therefore provided in Section 6.2.3.

2.5 Peridynamic models

The classical continuum mechanics theories are generally based on partial differential equations. A separate law has to be introduced to simulate crack or damage evolution, since the partial derivatives do not exist on crack surfaces and other discontinuities. A continuum model does not distinguish between points in a body where a discontinuity in displacement or any of its spatial derivatives are located. The essential feature of the peridynamic models is the use of integration, rather than that of differentiation, for computing the force on a material particle. Since the spatial derivatives are not used, the equations remain equally valid at points or surfaces of discontinuity. Therefore, the method of peridynamics falls into the category of nonlocal models because particles separated by a finite distance (called material horizon) could interact with each other [136]. This approach permits the solution of fracture problems in which the location of a crack is not known in advance using the same equations either on or off the crack surface or crack tip. This model assumes that Newton's second law is valid on every infinitesimally small particle within the domain of analysis. A specified force density function, called the pairwise force function, (with units of force per unit volume) between each pair of infinitesimally small particles is postulated to act as if the particles are closer together than the material horizon. The pairwise force function may be assumed to be a function of the relative position and the relative displacement between the two particles. A detailed survey on important analytical and numerical results and applications of the peridynamic theory can be found in [59]. Thus, the major elasticity and damage aspects of concrete behavior could be modeled correctly in a qualitative sense by the peridynamic model, even using the very basic zeroth order peridynamic damage model described. However, the quantitative agreement between the peridynamic model and the observed material behavior in the compressive regime is poor. But a first-order micro elastic damage model (with modification to account for enhanced micro elastic strength in the compressive strain regime) could be a promising one for modeling concrete in compression. Also, one-dimensional models of discrete reinforcing bars could be easily added to two-dimensional plain concrete models, hence enabling the modeling of reinforced concrete structures [70]. Since the peridynamic model described being a central-force model, is limited to modeling materials with a Poisson's ratio of 1/4, a generalized peridynamic model is developed by adding pairwise peridynamic moments, in addition to pairwise forces, to simulate linear elastic materials with varying Poisson's ratios. The new model is called the 'micro-polar peridynamic model'. The micro-polar peridynamic model could be implemented within a finite element context to enable efficacious application of boundary conditions and efficient computational solutions using an implicit, rather than an explicit solution algorithm, which is suitable for quasi-static simulation of damage and cracking in concrete structures. With this model, very simple tensile damage mechanisms at the micro structural (peridynamic) level, micro-cracking (damage) and fracture mechanics were observed in concrete structures [71]. This peridynamic FE model is much more efficient than discrete-based peridynamic models [70] as the number degrees of freedom could be reduced significantly from the discrete particle approach. This peridynamic model is sufficiently general to model any isotropic linear elastic continuum.

2.6 Smooth Particle Hydrodynamic (SPH) models

A mesh-less particle method known as the SPH method [146] has been investigated as a nonlocal regularization without any additional regularization measures for the solutions of instability due to strain-softening. A series of numerical experiments, using both SPH and FE solvers, demonstrated to show that the width of the strain-softening region is controlled by the smoothing length in SPH but in FE controlled by the element size. The smoothing length represents the damage-related length controlling the damage/strain softening localization. Thus, it is independent of spatial discretization density, which ensured the inherent nonlocal properties of SPH method. Moreover, it is found that stress wave propagation continues in the presence of strain-softening and the waves continue to propagate within the localization zone. Neither the strain localization into a single element nor the spurious mesh sensitivity is observed.

3 Fundamentals of Material Modeling

In the modeling of structures, several assumptions are made regarding geometry, kinematics and behavior of material. Such assumptions regarding the material behavior are usually based on experimental investigations. The modeling of material is called as Constitutive modeling. Hence, the constitutive modeling needs a proper understanding of its physical behavior including motion or deformation. Further, the theory of continuum mechanics postulates conservation laws those have to be satisfied at every material point of a continuum under mechanical or thermodynamic system. This chapter deals with basic concepts, equations of continuum mechanics and related laws of conservation. The following contents are widely available in literature [51, 114, 140, 151].

3.1 Constitutive relations

3.1.1 Displacements

Let us consider a body subjected to body forces and surface tractions. In order to study deformation of the body, the displacement is generally defined throughout the volume of the body. It is defined by a displacement vector field $\boldsymbol{u}$ of any material point belonging to the body. As the displacement of any point is a function of its initial coordinates, the displacement field describes how the body displaces or deforms. For a three-dimensional problem, the displacement field $\boldsymbol{u}$ in Cartesian coordinates $(x,\, y,\, z)$ is given by

$$\boldsymbol{u}(x,y,z) = \left\{ \begin{array}{c} u(x,y,z) \\ v(x,y,z) \\ w(x,y,z) \end{array} \right\} . \tag{3.1}$$

3.1.2 Stress and strain tensors

Under the action of such external forces, the internally induced forces acting on any internal surfaces keep each material point in equilibrium. Thus, the internal forces are mathematically described as stresses. The state of stress at that point can be completely characterized by Cauchy stress tensor $\boldsymbol{\sigma}$. Since the stress and its conjugate strain tensors are symmetric, it is convenient to represent the stress tensor $\boldsymbol{\sigma}$ and the strain tensor $\boldsymbol{\varepsilon}$ in column matrices form as

$$\boldsymbol{\sigma} = \left\{ \sigma_{\mathrm{x}} \quad \sigma_{\mathrm{y}} \quad \sigma_{\mathrm{z}} \quad \sigma_{\mathrm{yz}} \quad \sigma_{\mathrm{xz}} \quad \sigma_{\mathrm{xy}} \right\}^{T} , \tag{3.2}$$

$$\boldsymbol{\varepsilon} = \left\{ \varepsilon_{\mathrm{x}} \quad \varepsilon_{\mathrm{y}} \quad \varepsilon_{\mathrm{z}} \quad \gamma_{\mathrm{yz}} \quad \gamma_{\mathrm{xz}} \quad \gamma_{\mathrm{xy}} \right\}^{T} , \tag{3.3}$$

where $\{\cdot\}^{T}$ denotes transpose of the vector.

3.1.3 Split of stress and strain tensor

When the considered infinitesimal cubic element deforms, the changes may occur due to expansion or contraction of the element and due to distortion. Thus, these mechanisms of deformation lead to decomposition of strains in order to measure the respective deformation separately. Consequently, the hydrostatic strain tensor $\boldsymbol{\varepsilon}_\mathrm{h}$ measures the volumetric changes either expansion or contraction and the deviatoric strain tensor $\boldsymbol{\varepsilon}_\mathrm{d}$ measures the distortion. Both the decomposed tensors are mathematically expressed as linearly dependent on $\boldsymbol{\varepsilon}$ as follows (in matrix form):

$$\boldsymbol{\varepsilon}_\mathrm{h} = \boldsymbol{I}_\mathrm{h}\, \boldsymbol{\varepsilon}, \tag{3.4}$$

$$\boldsymbol{\varepsilon}_\mathrm{d} = \boldsymbol{I}_\mathrm{d}\, \boldsymbol{\varepsilon} = \boldsymbol{\varepsilon} - \boldsymbol{\varepsilon}_\mathrm{h}, \tag{3.5}$$

where $\boldsymbol{I}_\mathrm{h}$, $\boldsymbol{I}_\mathrm{d}$ are hydrostatic and deviatoric projection matrices.

$$\boldsymbol{I}_\mathrm{h} = \frac{1}{3}\boldsymbol{m}\boldsymbol{m}^T, \tag{3.6}$$

$$\boldsymbol{I}_\mathrm{d} = \boldsymbol{I} - \boldsymbol{I}_\mathrm{h}, \tag{3.7}$$

where $\boldsymbol{I}$ is identity matrix and $\boldsymbol{m} = \begin{Bmatrix} 1 & 1 & 1 & 0 & 0 & 0 \end{Bmatrix}^T$. The mean strain ε_m is defined by

$$\sigma_\mathrm{m} = \frac{1}{3}\left(\varepsilon_\mathrm{x} + \varepsilon_\mathrm{y} + \varepsilon_\mathrm{z}\right) = \frac{1}{3}\boldsymbol{m}^T\, \boldsymbol{\varepsilon}. \tag{3.8}$$

Similarly, the stress tensor $\boldsymbol{\sigma}$ can also be split into its mean (hydrostatic) and deviatoric parts. They are expressed as

$$\boldsymbol{\sigma}_\mathrm{h} = \boldsymbol{I}_\mathrm{h}\, \boldsymbol{\sigma}, \tag{3.9}$$

$$\boldsymbol{\sigma}_\mathrm{d} = \boldsymbol{I}_\mathrm{d}\, \boldsymbol{\sigma} = \boldsymbol{\sigma} - \boldsymbol{\sigma}_\mathrm{h}. \tag{3.10}$$

The mean stress σ_m is defined by

$$\sigma_\mathrm{m} = \frac{1}{3}\left(\sigma_\mathrm{x} + \sigma_\mathrm{y} + \sigma_\mathrm{z}\right) = \frac{1}{3}\boldsymbol{m}^T\, \boldsymbol{\sigma}. \tag{3.11}$$

3.1.4 Stress-strain relations

Under the assumption of linear elastic deformation behavior of materials, the constitutive equation, which relates the stresses and strains, is most generally expressed as (in tensor form)

$$\boldsymbol{\sigma} = \mathbb{H} : \boldsymbol{\varepsilon}, \qquad \text{or} \qquad \boldsymbol{\varepsilon} = \mathbb{S} : \boldsymbol{\sigma}, \tag{3.12}$$

where $\mathbb{H}$ is the fourth-order elasticity tensor and $\mathbb{S}$ is the elastic compliance tensor. Thus, equation (3.12) describing the mechanical behavior of the given material is called as generalized Hooke's law or constitutive law.

3.2 Kinematic relations

Let us consider that the system under body forces and traction undergoes infinitesimally small deformation. Consequently, the displacement gradient becomes sufficiently small. Hence, the higher order terms of the displacement gradient involved in the finite deformation theory are neglected.

Thus, the infinitesimal strain tensor to measure strains under small deformations is approximated as linear functional of displacement field $\boldsymbol{u}$, which is given by

$$\boldsymbol{\varepsilon} = \triangledown^{\mathrm{sym}}\,\boldsymbol{u} = \frac{1}{2}\left[\nabla\,\boldsymbol{u} + (\nabla\,\boldsymbol{u})^T\right], \tag{3.13}$$

where ∇ is the differential operator, $\triangledown^{\mathrm{sym}}\,\boldsymbol{u}$ is the symmetric gradient of the displacement field. For the three-dimensional problem, the strain-displacement relations are given in matrix representation as follows:

$$\boldsymbol{\varepsilon} = \left\{\begin{matrix} \varepsilon_{\mathrm{x}} \\ \varepsilon_{\mathrm{y}} \\ \varepsilon_{\mathrm{z}} \\ \gamma_{\mathrm{yz}} \\ \gamma_{\mathrm{xz}} \\ \gamma_{\mathrm{xy}} \end{matrix}\right\} = \begin{bmatrix} \frac{\partial}{\partial x} & 0 & 0 \\ 0 & \frac{\partial}{\partial y} & 0 \\ 0 & 0 & \frac{\partial}{\partial z} \\ 0 & \frac{\partial}{\partial z} & \frac{\partial}{\partial y} \\ \frac{\partial}{\partial z} & 0 & \frac{\partial}{\partial x} \\ \frac{\partial}{\partial y} & \frac{\partial}{\partial x} & 0 \end{bmatrix} \left\{\begin{matrix} u \\ v \\ w \end{matrix}\right\}. \tag{3.14}$$

3.3 Basic laws of mechanics

The forces acting on the body cause motion and deformation. In the case of deformable bodies, the system of forces should obey basic conservation laws at every point under the consideration of small deformation. Thus, the forces on the body are governed by following balance laws:

1. Balance of mass
2. Balance of linear momentum (Impulse)
3. Balance of angular momentum

3.3.1 Balance of mass

Let us consider the control volume V fixed in space. The density of the material of the body at a spatial point P is denoted by ρ and $\boldsymbol{n}$ is the normal vector. Then, the mass balance states that

$$\int_S \rho \boldsymbol{v} \cdot \boldsymbol{n} \, dS + \int_V \dot{\rho} \, dV = 0. \tag{3.15}$$

Using Gauss divergence theorem and rearrangement of terms, equation (3.15) is obtained as

$$\int_V \left\{ \nabla \cdot (\rho \boldsymbol{v}) + \dot{\rho} \right\} dV = 0. \tag{3.16}$$

That means that the balance law of mass at every point of continuum reads as

$$\nabla \cdot (\rho \boldsymbol{v}) + \dot{\rho} = 0. \tag{3.17}$$

For constant density, $\dot{\rho} = 0$, equation (3.17) further reduces to

$$\rho \nabla \cdot \boldsymbol{v} = 0. \tag{3.18}$$

3.3.2 Balance of linear momentum (Impulse)

If the body is subjected to body force $\boldsymbol{b}(\boldsymbol{x},t)$ and surface traction $\boldsymbol{t}(\boldsymbol{x},t)$ acting on the boundary along the normal $\boldsymbol{n}$ to the surface, then the total forces acting on the body is balanced by the rate of change of linear momentum in the fixed frame. Thus, the balance law reads as

$$\int_V \boldsymbol{b} \, dV + \int_S \boldsymbol{t} \, dS = \int_V \rho \ddot{\boldsymbol{u}} \, dV. \tag{3.19}$$

Using Gauss divergence theorem and Cauchy's formula $\boldsymbol{t} = \boldsymbol{\sigma} \cdot \boldsymbol{n}$, equation (3.19) is rearranged as follows:

$$\int_V \left\{ \boldsymbol{b} + \nabla \cdot \boldsymbol{\sigma} - \rho \ddot{\boldsymbol{u}} \right\} dV = 0. \tag{3.20}$$

Thus, equation (3.20) reduces in local form as

$$\nabla \cdot \boldsymbol{\sigma} + \boldsymbol{b} - \rho \ddot{\boldsymbol{u}} = 0. \tag{3.21}$$

This equation is called as *Cauchy's equation of motion*, which describes the motion of any continuum. Sometimes it is also known as the *strong, local or point-wise equation of equilibrium.*

Additionally, appropriate boundary conditions may be used such as Dirichlet boundary and Neumann boundary condition on the boundary S to solve the partial differential equations (3.21).

3.3.3 Balance of angular momentum

If ρ is the density of a material at a point P of an infinitesimal volume V and its velocity $\boldsymbol{v}$, the sum of moments of all forces about any point P' is balanced by the angular momentum. Thus, the balance law is stated as

$$\int_V \boldsymbol{r} \times \boldsymbol{b}\, dV + \int_S \boldsymbol{r} \times \boldsymbol{t}\, dS = \int_V \boldsymbol{r} \times \rho \ddot{\boldsymbol{u}}\, dV, \tag{3.22}$$

where $\boldsymbol{r}$ is the position vector of point P with respect to point P'. After transformation and rearrangement of terms, the balance law is obtained as

$$\int_V \boldsymbol{r} \times \Big\{ \nabla \cdot \boldsymbol{\sigma} + \boldsymbol{b} - \rho \ddot{\boldsymbol{u}} \Big\}\, dV + \int e_{\mathrm{i}} \times \boldsymbol{\sigma}^T e_{\mathrm{i}}\, dV = 0. \tag{3.23}$$

This leads to symmetry condition of the stress tensor, i.e $\boldsymbol{\sigma} = \boldsymbol{\sigma}^T$.

3.4 Basic laws of thermodynamics

If a body is subjected to body forces and surface traction undergoing deformation, the changes in the state is called *thermodynamic process*, which may be *reversible or irreversible* and such system is called as *a thermodynamic system*. A certain set of specified quantities completely characterizes the state of changes (say, deformation) in the system. Such quantities specified in the current state of a system are called as *thermodynamic state variables*. The state variables may be external (observable) or internal (hidden), whether it can be observable from outside or not. When the thermodynamic state of a system does not change with time, the system is in *thermodynamically equilibrium*. These state variables are generally governed by thermodynamic laws, namely,

1. First law of thermodynamics
2. Second law of thermodynamics

Nevertheless, the thermodynamic state of a continuum in general is a non-uniform and non-equilibrium state, and also the thermodynamic process is irreversible, since the strain or temperature may differ from a location to another in the continuum and may also vary with time [111].

3.4.1 First law of thermodynamics

The first law of thermodynamics states that the rate of internal energy plus that of kinetic energy of a thermodynamic system is equal to the rate of external mechanical work plus the rate of heat transferred to the system due to heat flux and heat source during the loading. It is also known as *law of energy conservation*.

The kinetic energy E_{ke} and internal energy E_{ie} are given by

$$E_{\text{ke}} = \int_V \frac{1}{2}\rho\, \boldsymbol{v} \cdot \boldsymbol{v}\, dV, \tag{3.24}$$

$$E_{\text{ie}} = \int_V \psi\, dV, \tag{3.25}$$

where ψ is the internal energy per unit volume and $\boldsymbol{v}$ is the velocity of the material point. Hence, the change in kinetic energy and that of internal energy of the continuum during time t_1 to t_2 is given by

$$E_{\text{ke}}^{1-2} = \int_{t_1}^{t_2} \int_V \frac{1}{2}\rho\, \frac{d\boldsymbol{v}}{dt} \cdot \boldsymbol{v}\, dV\, dt, \tag{3.26}$$

$$E_{\text{ie}}^{1-2} = \int_{t_1}^{t_2} \int_V \dot{\psi}\, dV\, dt. \tag{3.27}$$

If r_{q} is the rate of generation of heat per unit mass and $\boldsymbol{q}$ is the heat flux from the surface, then the heat supplied to the system is obtained by

$$Q^{1-2} = \int_{t_1}^{t_2} \int_V (\rho\, r_{\text{q}} - \nabla \cdot \boldsymbol{q})\, dV\, dt. \tag{3.28}$$

The external power of surface traction and body forces can be written as

$$P_{\text{ext}} = \int_S \boldsymbol{t} \cdot \boldsymbol{v}\, dS + \int_V \boldsymbol{b} \cdot \boldsymbol{v}\, dV. \tag{3.29}$$

Then, the mechanical power done, i.e., the rate of external mechanical work, by surface traction and body forces during time t_1 to t_2 is given by

$$W_{\text{ext}}^{1-2} = \int_{t_1}^{t_2} P_{\text{ext}}\, dt. \tag{3.30}$$

Since the forces do not change their points of application during the interval of time, equation (3.30) reduces to

$$W_{\text{ext}}^{1-2} = \int_S \int_{\boldsymbol{u}} \boldsymbol{t}\, d\boldsymbol{u}\, dS + \int_V \int_{\boldsymbol{u}} \boldsymbol{b}\, d\boldsymbol{u}\, dV. \tag{3.31}$$

Thus, the first law requires that

$$W_{\text{ext}}^{1-2} + Q^{1-2} = E_{\text{ke}}^{1-2} + E_{\text{ie}}^{1-2}. \tag{3.32}$$

After substituting Cauchy's formula and using Gauss divergence theorem, then rearrangement of terms, equation (3.32) may lead to

$$\frac{d\psi}{dt} = \boldsymbol{\sigma} : \dot{\varepsilon} + (\rho\, r_{\text{q}} - \nabla \cdot \boldsymbol{q}). \tag{3.33}$$

This equation (3.33) is valid under small strain assumptions. Further, under quasi-static loading condition, i.e., $E_{\text{ke}} = 0$, the first law of thermodynamics gives the definition of *strain energy density function* ψ per unit volume as follows:

$$\psi = \frac{1}{2}\boldsymbol{\varepsilon} : \mathbb{H} : \boldsymbol{\varepsilon}, \tag{3.34}$$

when the following relations are valid,

$$\boldsymbol{\sigma} = \frac{\partial \psi}{\partial \boldsymbol{\varepsilon}}; \qquad d\psi = \boldsymbol{\sigma} : d\boldsymbol{\varepsilon}. \tag{3.35}$$

3.4.2 Second law of thermodynamics

The non-equilibrium thermodynamics of a continuum is described by the second law of thermodynamics. It states that the rate of increase in the entropy of a system is never less than the rate of increase in the entropy due to the heat source and the heat flux. It is also known as *entropy inequality*.

If a system is considered under an absolute temperature T and an entropy per unit mass s due to the heat transfer Q, the change in the entropy from state a to state b for the irreversible process is defined as

$$\Delta s = \int_a^b \frac{dQ}{T}. \tag{3.36}$$

If the specific rate of the entropy increase is given by $d\eta/dt$, the change in the entropy of the system can also be expressed as

$$\Delta s = \int_V \int_t \rho \frac{d\eta}{dt}\, dt\, dV. \tag{3.37}$$

According to the second law,

$$\int_V \int_t \rho \frac{d\eta}{dt}\, dt\, dV \geq \int_a^b \frac{dQ}{T}. \tag{3.38}$$

Substituting Q and using Gauss divergence theorem, equation (3.38) is obtained as

$$\rho \frac{d\eta}{dt} - \frac{\rho\, r_{\text{q}}}{T} + \frac{\boldsymbol{q}}{T} \geq 0. \tag{3.39}$$

This equation (3.39) is known as *Clausius-Duhem inequality* and must be satisfied for every possible process. Substitution of the first law of thermodynamics (3.33) into (3.39) leads to

$$\rho T \frac{d\eta}{dt} + \boldsymbol{\sigma} : \dot{\varepsilon} - \frac{d\psi}{dt} + \boldsymbol{q} \cdot \frac{\nabla T}{T} \geq 0. \tag{3.40}$$

Thus, this inequality imposes restrictions on the constitutive relations and provides the background of the thermodynamic constitutive theory for the dissipative process of a continuum.

4 Local Modeling of Damage

This chapter discusses local approaches of continuum damage models. The damage equivalence principles in view of effective stress concepts are briefly described. The state of damage is characterized by introducing inner damage variables as scalar or tensor to discriminate isotropic and anisotropic behavior of damage respectively. Furthermore, damage criteria and various damage evolution laws that are specifically used for modeling damage of concrete are also explained.

4.1 Damage variable

Within the context of continuum damage mechanics, an internal damage variable is generally introduced to measure the deformation characteristics of a damaged material from elastic state to fracture. Such variables of different mathematical nature (scalars, vector or tensor quantities) have different physical meaning. CDM theories separate conveniently into micro mechanical and phenomenological models. In the former, the internal damage variable represents some average of the microscopic defects that characterize the state of internal deterioration (reduction of load bearing area or distribution of micro-cracks). In the latter, the damage variables are defined based on the influence of an internal degradation exerted on the macroscopic properties such as stiffness modulus, yield stress, and density of material [51].

4.2 Damage equivalence principles

It is assumed that the material properties of any damaged deformable body are in the undamaged state and the effective stress will be used to measure the change occurred due to the introduction of damage. The effective stress concept is particularly convenient and simple in view of the computational point [138]. Moreover, the damaged body is in the conventional or real stress state, and its material properties are determined by the effective material properties [100]. There are two hypotheses commonly available for the estimation of the effective properties of the material.

4.2.1 Principle of strain equivalence

According to this hypothesis [138], the strain associated with a damaged state of a material under the applied stress $\boldsymbol{\sigma}$, as shown in Figure 4.1b, is equivalent to the strain associated with an undamaged state of the material under the effective stress $\tilde{\boldsymbol{\sigma}}$, as shown in Figure 4.1a. In the sense of an effective stress or a net stress introduced by Kachanov [82], damage is defined as a macroscopic state variable that affects the macro-mechanical properties of the material. If the isotropic damage is described by a scalar variable D and the anisotropic damage is characterized

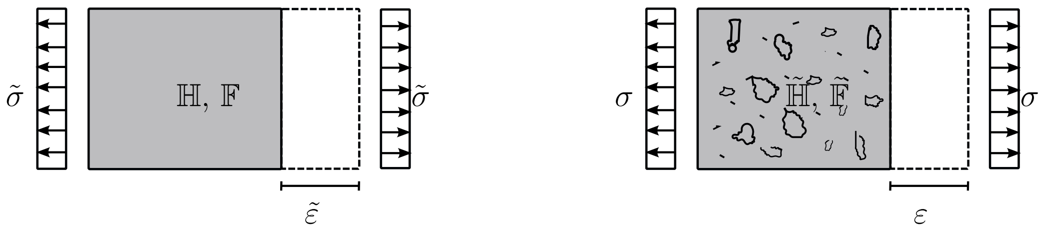

(a) Undamaged material ($\mathbb{H}$, $\mathbb{F}$)   **(b)** Damaged material ($\tilde{\mathbb{H}}$, $\tilde{\mathbb{F}}$)

Figure 4.1: Strain equivalence

by a fourth-rank damage effect tensor $\mathbb{M} = \mathbb{M}(\boldsymbol{D})$, then the effective variables for anisotropic damage are defined as follows:

$$\tilde{\varepsilon}(\tilde{\boldsymbol{\sigma}},0) = \boldsymbol{\varepsilon}(\boldsymbol{\sigma},D); \qquad \tilde{\boldsymbol{\sigma}} = \mathbb{M} : \boldsymbol{\sigma}. \tag{4.1}$$

For an isotropic damage, $\mathbb{M}(\boldsymbol{D})$ reduces to $(1-D)^{-1}\boldsymbol{I}$ and the effective variables are subsequently defined as follows:

$$\tilde{\varepsilon}(\tilde{\boldsymbol{\sigma}},0) = \boldsymbol{\varepsilon}(\boldsymbol{\sigma},D); \qquad \tilde{\boldsymbol{\sigma}} = \frac{\boldsymbol{\sigma}}{1-D}. \tag{4.2}$$

Though the principle of strain equivalence is clear and simple to be applied, the resulting compliance tensor from $\mathbb{M}(\boldsymbol{D})$ has inconvenience of its asymmetry [111]. A method of symmetrization must be employed additionally to obviate this problem.

4.2.2 Principle of energy equivalence

The existence of a strain energy function and/or a complementary strain energy function necessitates the symmetry of the elastic modulus and the compliance tensors. Hence, the hypothesis of the energy equivalence, which satisfies the symmetry requirement for the elastic tensors, as its intrinsic consequence was proposed [111]. It states that the total complementary elastic strain energy $\Phi^{\mathrm{el}}(\boldsymbol{\sigma},D)$ of a damaged state with the conventional stress $\boldsymbol{\sigma}$, as shown in Figure 4.2b, is equivalent to the total complementary elastic strain energy $\tilde{\Phi}_0^{\mathrm{el}}(\tilde{\boldsymbol{\sigma}},0)$ of the conventional (undamaged, $D = 0$) state with the effective stress $\tilde{\boldsymbol{\sigma}}$, as shown in Figure 4.2a. Accordingly, the valid equations are given by

$$\tilde{\Phi}_0^{\mathrm{el}}(\tilde{\boldsymbol{\sigma}},0) = \Phi^{\mathrm{el}}(\boldsymbol{\sigma},D), \tag{4.3}$$

$$\tilde{\Phi}_0^{\mathrm{el}}(\tilde{\boldsymbol{\sigma}},0) = \frac{1}{2}\boldsymbol{\sigma}^T : \mathbb{F} : \boldsymbol{\sigma}, \tag{4.4}$$

$$\Phi^{\mathrm{el}}(\boldsymbol{\sigma},D) = \Phi^{\mathrm{el}}(\tilde{\boldsymbol{\sigma}},0) = \frac{1}{2}\tilde{\boldsymbol{\sigma}}^T : \mathbb{F} : \tilde{\boldsymbol{\sigma}} = \frac{1}{2}\boldsymbol{\sigma}^T : \tilde{\mathbb{F}} : \boldsymbol{\sigma}, \tag{4.5}$$

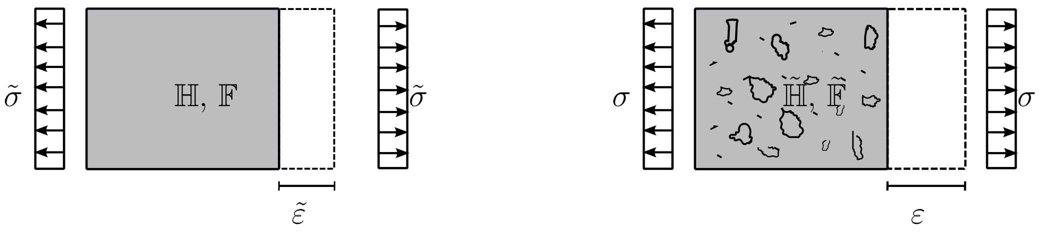

(a) Undamaged material ($\mathbb{H}$, $\mathbb{F}$) **(b)** Damaged material ($\tilde{\mathbb{H}}$, $\tilde{\mathbb{F}}$)

Figure 4.2: Complementary strain energy equivalence

where $\mathbb{F}(= \mathbb{H}^{-1})$ refers to the fourth-order flexibility tensor of the undamaged material and the effective flexibility tensor $\tilde{\mathbb{F}}$ is obtained as $\tilde{\mathbb{F}} = \mathbb{M}^T : \mathbb{F} : \mathbb{M}$. Consequently, for an anisotropic damage, the effective variables are defined as follows [39]:

$$\tilde{\boldsymbol{\sigma}} = \mathbb{M} : \boldsymbol{\sigma}; \qquad \tilde{\boldsymbol{\varepsilon}} = \mathbb{M}^{-T} : \boldsymbol{\varepsilon}, \tag{4.6}$$

and for an isotropic damage,

$$\tilde{\boldsymbol{\sigma}} = \frac{\boldsymbol{\sigma}}{1 - D}; \qquad \tilde{\boldsymbol{\varepsilon}} = (1 - D)\boldsymbol{\varepsilon}. \tag{4.7}$$

Since the growth of micro-cracking of a material usually influences both the stress and strain distribution, the energy based damage equivalence is more realistic than the other equivalence principle in which the local stiffness drop results in a local stress decrease exclusively. Even though the strain equivalence works reasonably well for isotropic damage materials, it yields asymmetric stiffness matrices for anisotropic materials as the damage variable is defined as a tensor. Due to this non-symmetry of the resultant effective stress tensor in the case of anisotropic damage, the principle of total energy equivalence is applied in place of the strain equivalence concept [4, 100, 150]. Nevertheless, it is limited as it does not allow for the physically adequate description of phenomena other than damage coupled elasticity [141].

4.3 Isotropic damage

Material damage induced by micro-voids in isotropic distributions or by micro-cracks of random distributions is generally characterized by an isotropic damage, if their size and density are sufficiently small. According to the classical continuum damage mechanics approach, the stress-strain relationships can be written based on linear elastic behavior of the damaged material using the effective stress concepts as follows:

1. *Principle of strain equivalence* [51, 82, 96, 119, 138, 139]

$$\boldsymbol{\sigma}_{\text{se}} = (1 - D)\mathbb{H} : \boldsymbol{\varepsilon}. \tag{4.8}$$

2. *Principle of energy equivalence* [22, 36, 39, 42, 43, 80]

$$\boldsymbol{\sigma}_{\text{ee}} = (1-D)^2 \mathbb{H} : \boldsymbol{\varepsilon}, \tag{4.9}$$

$$\mathbb{H} = \frac{\nu E}{(1+\nu)(1-2\nu)} \left(\boldsymbol{I} \boldsymbol{I} + \frac{1-2\nu}{\nu} \mathbb{I} \right), \tag{4.10}$$

where $\boldsymbol{\sigma}$ represents the Cauchy stress tensor, $\boldsymbol{\varepsilon}$ the linear strain tensor, $\mathbb{H}$ the fourth-order elastic stiffness tensor, E the Young's Modulus, ν the Poisson's ratio, $\boldsymbol{I}$ and $\mathbb{I}$ the symmetric identity tensors of rank two and four respectively. The subscripts se or ee correspond to the strain or the energy equivalence principles. The scalar internal damage variable D denotes an isotropic damage that usually satisfies the condition $(0 \leq D \leq 1)$. The damage variable D is a monotonically increasing quantity expressing the level of material degradation. D values zero for the initial or undamaged material and increases up to 1 for the completely damaged material showing full loss of stiffness and coherence at which the material is no longer able to transfer the stresses. Furthermore, it is assumed that there is no effect of damage on the Poisson's ratio ν, but only the stiffness of the material or the elastic stiffness matrix is affected by damage.

4.3.1 Thermodynamic consistency

In the framework of thermodynamics, the elastic free energy $\boldsymbol{\Psi}_0$ of the undamaged material for the linear elastic behavior is written as

$$\boldsymbol{\Psi}_0(\boldsymbol{\varepsilon}) = \frac{1}{2} \boldsymbol{\varepsilon} : \mathbb{H} : \boldsymbol{\varepsilon}. \tag{4.11}$$

If the material degradation is considered as an irreversible process of thermodynamics as a history dependent behavior, the so-called internal hidden variable D will contribute to the Helmholtz free energy (per unit volume) $\boldsymbol{\Psi}(\boldsymbol{\varepsilon}, D)$. Then, equation (4.8) or (4.9) can also be written as [28, 103]

$$\boldsymbol{\sigma} = \boldsymbol{\sigma}(\boldsymbol{\varepsilon}, D) = \frac{\partial \boldsymbol{\Psi}}{\partial \boldsymbol{\varepsilon}}. \tag{4.12}$$

In the case of strain equivalence (4.8), the expression for $\boldsymbol{\Psi}$ reads as

$$\boldsymbol{\Psi}_{\text{se}} = (1-D) \boldsymbol{\Psi}_0(\boldsymbol{\varepsilon}). \tag{4.13}$$

But, in the case of energy equivalence (4.9), the expression for $\boldsymbol{\Psi}$ reads as

$$\boldsymbol{\Psi}_{\text{ee}} = (1-D)^2 \boldsymbol{\Psi}_0(\boldsymbol{\varepsilon}). \tag{4.14}$$

The growth of damage leads to the dissipation of energy, as the damage comprises the creation and propagation of cracks and voids. Taking time derivative of the Helmholtz free energy

$\mathbf{\Psi}(\varepsilon, D)$ yields the energy dissipation rate of the damage process φ as follows:

$$\varphi = -\frac{d\mathbf{\Psi}}{dt} = -\frac{\partial \mathbf{\Psi}}{\partial D}\frac{dD}{dt} = Y\dot{D}. \tag{4.15}$$

Herein, the scalar quantity Y implies the release rate of the elastic strain energy caused by the development of damage D. Since the damage-associated variable Y plays a similar role of the strain energy release rate in fracture mechanics, it is called damage energy release rate or strain energy density release rate [111]. In the case of strain equivalence (4.8), Y is defined as

$$Y_{\mathrm{se}} = -\frac{d\mathbf{\Psi}_{\mathrm{se}}}{dD} = -\mathbf{\Psi}_0, \tag{4.16}$$

and in the case of energy equivalence (4.9), Y is defined as

$$Y_{\mathrm{ee}} = -\frac{d\mathbf{\Psi}_{\mathrm{ee}}}{dD} = 2(1-D)\mathbf{\Psi}_0. \tag{4.17}$$

4.3.2 Spectral decomposition of the stress tensor

Since concrete has distinct behaviors in tension and compression, the Cauchy stress tensor (nominal and effective) is decomposed into two parts (+ve and -ve) using the spectral decomposition technique as in [35, 87, 138, 139, 149], in order to adequately characterize the damage in concrete. Hereafter, the superscripts '+' and '-' refer to tensile and compressive parts respectively. Therefore, the decomposed tensors are written as follows:

$$\boldsymbol{\sigma} = \boldsymbol{\sigma}^{+} + \boldsymbol{\sigma}^{-}, \qquad \tilde{\boldsymbol{\sigma}} = \tilde{\boldsymbol{\sigma}}^{+} + \tilde{\boldsymbol{\sigma}}^{-}, \tag{4.18}$$

where $\boldsymbol{\sigma}^{+}$ and $\boldsymbol{\sigma}^{-}$ are the tensile and compressive parts of the stress state respectively. These can be related with the principal unit vectors of $\boldsymbol{\sigma}(\vec{n}_1, \vec{n}_2, \vec{n}_3)$:

$$\boldsymbol{\sigma} = \sum_{i=1}^{3} \sigma_{\mathrm{i}} \vec{n}_{\mathrm{i}} \otimes \vec{n}_{\mathrm{i}}, \tag{4.19}$$

$$\boldsymbol{\sigma}^{+} = \sum_{\mathrm{i}=1}^{3} H(\sigma_{\mathrm{i}}) \sigma_{\mathrm{i}} \vec{n}_{\mathrm{i}} \otimes \vec{n}_{\mathrm{i}}, \qquad \boldsymbol{\sigma}^{-} = \sum_{i=1}^{3} H(-\sigma_{\mathrm{i}}) \sigma_{\mathrm{i}} \vec{n}_{\mathrm{i}} \otimes \vec{n}_{\mathrm{i}}, \tag{4.20}$$

where $H(\cdot)$ is a Heaviside step function.

4.3.3 Damage criterion function

The damage growth/evolution is governed by the deformation history parameter κ that is a scalar variable representing the most severe deformation the material experienced. κ gets a threshold value below which the damage development is considered as zero. Thus, the damage evolution is fully described by a scalar function as follows:

$$D = D(\kappa). \tag{4.21}$$

In the concept of local continuum damage mechanics, a damage criterion can be completely described by the history parameter κ at time t. If the vector $\vec{x}$ characterizes the present position of a point of consideration, and $\vec{\xi}$ the relative positions of the material points in a surrounding volume V, then it can be written at time t as

$$D(\vec{x},t) = D(\kappa(\vec{x},t)), \tag{4.22}$$

$$\kappa(\vec{x},t) = \text{Sup}[\kappa_0, \zeta(\vec{x},\tau|\tau \leq t)], \tag{4.23}$$

where κ_0 is an initial threshold value set for κ. The value of the actual history parameter κ can be determined by the evolution of certain local measure of deformation state ζ. Thus, the increase of damage is only possible when the state variable ζ grows and equals an evolving threshold value $\kappa \geq 0$. If ζ is less than κ and if ζ does not increase, there is no growth of damage, but the material has a constant damage. Thus, the evolution of damage at a point of continuum could be described by the scalar function $D(\kappa)$ on the basis of a limiting function or a damage loading function f by

$$f = f(\zeta,\kappa) = \zeta - \kappa(\zeta). \tag{4.24}$$

Thus, the elasticity domain is defined by the criterion function f. For $f < 0$, there is no damage growth and the response remains linear elastic. Moreover, the evolution of history parameter κ can also be expressed mathematically by the Kuhn-Tucker loading and unloading relations [28, 52, 67, 69, 125]

$$\dot{\kappa} \geq 0, \qquad f \leq 0, \qquad f\dot{\kappa} = 0, \tag{4.25}$$

such that always $f \leq 0$. The initial elastic domain is set by an initial threshold value of κ as κ_0. It is assumed that the damage growth is possible when $f = 0$ and this is the only dissipative mechanism in the brittle failure of concrete if inelastic strains are not taken into account. During this damage process, the consistency condition $\dot{f} = 0$ must be satisfied on the boundary of the element considered. Thus, this condition exemplifies that the rate of change of the history parameter depends on the rate of change of the local deformation state variable considered, which reads as

$$\dot{\kappa} = \left\langle \dot{\zeta} \right\rangle, \tag{4.26}$$

where $\langle \cdot \rangle$ is the McCauley bracket defined as

$$\left\langle x \right\rangle = \begin{cases} x & \text{if } x \geq 0, \\ 0 & \text{if } x < 0. \end{cases} \tag{4.27}$$

Herein, it can also be observed from equations (4.26, 4.27) that the history parameter κ can only increase monotonically during loading/unloading processes.

4.3.4 Damage evolution laws - Single damage variable

In order to obtain a realistic shape of the stress-strain diagram with a proper strain-softening behavior of materials, various material damage models define damage evolution laws using different functions by specifying the mechanical dissipation potential. The damage evolution equation for the failure process can usually be written as follows [118, 119, 126]:

$$\dot{D} = \begin{cases} g(D,\kappa)\dot{\kappa} & \text{if} \quad \zeta = \kappa, \\ 0 & \text{if} \quad \zeta < \kappa. \end{cases} \tag{4.28}$$

It is usual practice that the damage evolution law, which is often defined by $D(\kappa)$, can be obtained from equation (4.28) by integration and using the consistency relation $\dot{f} = 0$. But the evolution function $g(D,\kappa)$ is obtained by differentiation of D with respect to κ. Among various definitions of the damage evolution law $D(\kappa)$, few of them suitably applicable for materials showing quasi-brittle fracture are discussed here.

In order to obtain a realistic shape of the stress-strain relation, Pijaudier-Cabot and Bažant [126] defined the damage evolution as follows:

$$D(\kappa) = 1 - \left[\frac{1}{1 + b(\kappa - \kappa_0)^n}\right], \tag{4.29}$$

where b, n and κ_0 represent the material damage parameters in order to obtain the realistic curve, as shown in Figure 4.3.

Linear softening laws

Nevertheless, for theoretical developments, the damage evolution, which is often defined as a

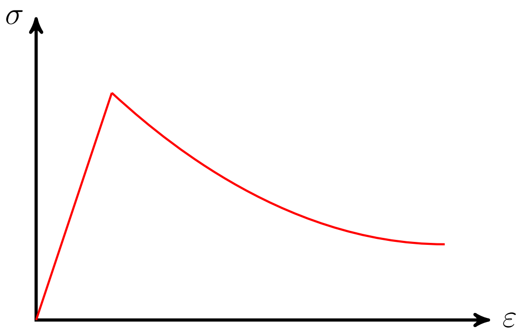

Figure 4.3: Stress-strain relation [126]

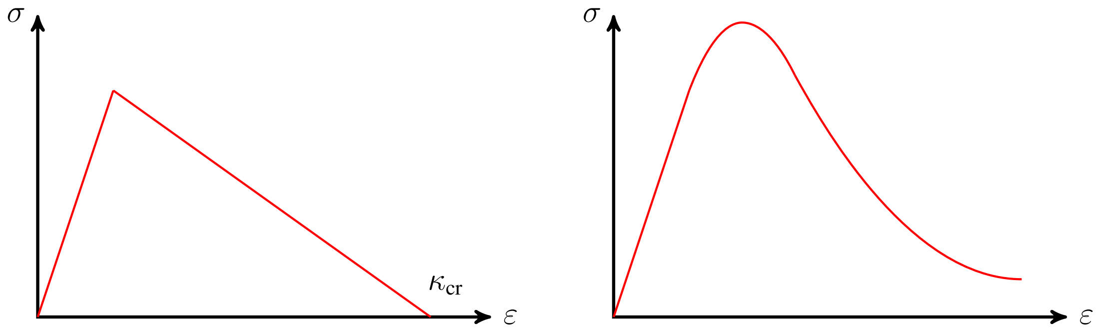

(a) Linear softening [46]

(b) Power softening [118]

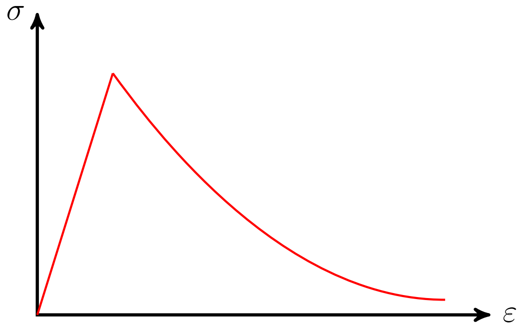

(c) Exponential softening [123]

Figure 4.4: Typical stress-strain relations for various softening laws

linear approximation law, is expressed as [46, 119, 120, 125]

$$D(\kappa) = \begin{cases} \frac{\kappa_{\mathrm{cr}}}{\kappa}\frac{\kappa-\kappa_0}{\kappa_{\mathrm{cr}}-\kappa_0} & \text{if} \quad \kappa_0 \leq \kappa \leq \kappa_{\mathrm{cr}}, \\ 1 & \text{if} \quad \kappa \geq \kappa_{\mathrm{cr}}, \end{cases} \tag{4.30}$$

or sometimes as [60]

$$D(\kappa) = \begin{cases} \frac{\kappa}{\kappa_{\mathrm{cr}}} & \text{if} \quad \kappa_0 \leq \kappa \leq \kappa_{\mathrm{cr}}, \\ 1 & \text{if} \quad \kappa \geq \kappa_{\mathrm{cr}}. \end{cases} \tag{4.31}$$

Herein, equation (4.30) or (4.31) results in a linear softening stress-strain relation followed by the complete fracture of the material that occurs when κ becomes equal to κ_{cr}, as depicted in Figure 4.4a.

Power softening laws

However, the softening behavior of real materials is usually non-linear in which the stress decreases gradually for increasing strain after reaching the fracture strength. Therefore, in order to capture the nonlinear post-peak behavior of the material, the damage evolution law, which is sometimes assumed by adopting material dependent parameters such as γ and α' as exponents [28, 118], is expressed by

$$D(\kappa) = 1 - (1 - D_0)\left[\frac{\kappa_{\text{cr}}^{\gamma} - \kappa^{\gamma}}{\kappa_{\text{cr}}^{\gamma} - \kappa_0^{\gamma}}\right]^{\frac{1}{\alpha'}}, \tag{4.32}$$

where $D_0 = D(\kappa = \kappa_0) \geq 0$ corresponding to the initial state of damage, with a critical threshold κ_{cr} at complete rupture ($D = 1$).
Besides the power softening law (4.32), the power law [66, 69] can also be assumed as a generalization of the linear law (4.30) as follows:

$$D(\kappa) = 1 - \frac{\kappa_0}{\kappa}\left[\frac{\kappa_{\text{cr}} - \kappa}{\kappa_{\text{cr}} - \kappa_0}\right]^{\alpha'}. \tag{4.33}$$

The exponent α' is the decay parameter mainly influencing the slope of the stress decrease, i.e., it determines the final softening stage close to complete fracture.
By introducing an additional exponent β' into (4.33), a modified expression of power law [66, 68, 119] is sometimes adopted as

$$D(\kappa) = 1 - \left[\frac{\kappa_0}{\kappa}\right]^{\beta'}\left[\frac{\kappa_{\text{cr}} - \kappa}{\kappa_{\text{cr}} - \kappa_0}\right]^{\alpha'}, \tag{4.34}$$

where β' influences mainly the initial rate of the damage growth to have more flexible form. Such power softening laws yield stress-strain curves as similar to the curve shown in Figure 4.4b.

Exponential softening laws

On the other hand, an exponential form of softening preferred by several authors [29, 67, 123] can be expressed as

$$D(\kappa) = 1 - \frac{\kappa_0}{\kappa}(1 - \alpha) - \alpha\frac{\kappa_0}{\kappa}e^{-\beta(\kappa-\kappa_0)}. \tag{4.35}$$

This law is a slightly modified version of law (4.40). The parameter α ensures the long tail in the stress-strain softening curve with residual stresses even if the damage variable approaches unity but never reaches the limit value $D = 1$. The parameter β determines the rate at which the damage grows. The higher value implies the faster growth of damage and results in a more brittle response [123]. Another simplified form of exponential law [69] can be obtained from equation (4.35) by setting $\alpha = 1$. Such a typical exponential softening law provides stress-softening behavior, as depicted in Figure 4.4c.

In a similar fashion, a more flexible form of the exponential law, which is characterized by the parameters n_1, n_2, and β, can be expressed as follows [66]:

$$D(\kappa) = 1 - \left(1 - \frac{\kappa_0}{\kappa}\right)\left(0.01\frac{\kappa_0}{\kappa}\right)^{n_1} - \left(0.01\frac{\kappa_0}{\kappa}\right)^{n_2} e^{-\beta(\kappa-\kappa_0)}, \tag{4.36}$$

Further, an another form of the exponential softening, which is based on the Weibull law of failure probability of microscopic defects [78, 97], is provided by

$$D(\kappa) = \begin{cases} 0 & \text{if } \kappa < \kappa_0, \\ 1 - e^{-\left[\frac{\kappa-\kappa_0}{\kappa_\mathrm{d}}\right]^{g_\mathrm{d}}} & \text{if } \kappa \geq \kappa_0, \end{cases} \tag{4.37}$$

where κ_d rules how fast D approaches 1 and $g_\mathrm{d} = 2$ is a shape parameter [78]. The exponential damage law [60], which sometimes uses a single parameter β influencing the post-peak region or the growth of damage, reads as simple as

$$D(\kappa) = 1 - e^{-\beta\kappa}. \tag{4.38}$$

4.3.5 Damage evolution laws - Two damage variables

Under the cyclic loading, as the strain increases, the mechanism of the stiffness degradation becomes complicated due to the opening and closing of micro-cracks (Unilateral effect). In order to describe the distinct behavior of concrete in tension and compression and also to account for the non-linearity in strain-softening, the damage models have to be developed with the coupling of two independent scalar damage variables, D^+ (tensile effect) and D^- (compressive effect).
Nonetheless, a single scalar damage variable D can be defined as the weighted sum of D^+ and D^- by the kinematics of the damage and a damage evolution law is first proposed in the exponential form based on the experimental results obtained [103]. The single damage variable $D(\kappa)$ reads as

$$D(\kappa) = \alpha^+ D^+ + \alpha^- D^-, \tag{4.39}$$

$$D^\pm(\kappa) = 1 - \frac{\kappa_0}{\kappa}(1 - A^\pm) - A^\pm e^{-B^\pm(\kappa-\kappa_0)}, \tag{4.40}$$

where $\alpha^\pm$, $A^\pm$ and $B^\pm$ are characteristic parameters of the material, $+$ represents tension or traction, and $-$ represents compression.
Instead of the average set in equation (4.39), the damage due to tension from the damage due to compression can also be distinguished depending on the sign of stress (in the case of cyclic loading or stress reversal). Thus, two independent scalar damage variables such as D^+ for positive stresses and D^- for negative stresses along with the use of split-up of the effective stress tensors could be used [104, 107].

$$D(\kappa) = D^+(\kappa^+), \tag{4.41}$$

$$D(\kappa) = D^-(\kappa^-), \tag{4.42}$$

where $D(\kappa)$ follows the same law as given in equation (4.40), and gets form of equation (4.41) if crack opens and gets form of equation (4.42) if crack closes. If the loads are complex, the damage may be a combination of D^+ and D^-. But each damage variable results in two different loading surfaces respectively.

On the other hand, the damage variable D can also be defined to describe the responses due to tension and compression (4.43) [42, 43, 93, 94]. Thus, it is modified to incorporate the crack opening/closing behavior, which is modeled as the elastic stiffness recovery during unloading, by means of a multiplicative parameter ($0 < s < 1$) on D^+ .

$$D(\kappa) = 1 - (1 - D^+)(1 - D^-), \tag{4.43}$$

$$D(\kappa) = 1 - (1 - s(\bar{\boldsymbol{\sigma}})D^+)(1 - D^-), \tag{4.44}$$

where $s = s(r(\hat{\bar{\boldsymbol{\sigma}}}))$ represents the stiffness recovery and r being a weight function of effective stress, which ranges from 0 in pure compressive loading to 1 in pure tensile loading.

A similar approach, which is inspired from the criteria presented in [103], is adopted to take the unilateral effect of concrete into account for the damage evolution [30, 62, 63, 149]. These evolution equations read as

$$D^+(\kappa^+) = 1 - \frac{\kappa_0^+}{\kappa^+} e^{-A^+\left[1 - \frac{\kappa^+}{\kappa_0^+}\right]}, \qquad \text{if} \qquad \kappa^+ \geq \kappa_0^+ \tag{4.45}$$

$$D^-(\kappa^-) = 1 - \frac{\kappa_0^-}{\kappa^-}(1 - A^-) - A^- e^{-B^-\left[1 - \frac{\kappa^-}{\kappa_0^-}\right]}, \qquad \text{if} \qquad \kappa^- \geq \kappa_0^- \tag{4.46}$$

where A^+, A^- and B^- are material parameters as in [30, 62].

On the contrary, an effective damage variable D can be directly correlated with the thermodynamic history parameters κ^+ and κ^- through the driving variable κ [106].

$$\kappa = r\kappa^+ + (1 - r)\kappa^-, \tag{4.47}$$

$$r = \frac{\sum \left\langle \tilde{\sigma}_{\mathrm{i}} \right\rangle}{\sum |\tilde{\sigma}_{\mathrm{i}}|}, \tag{4.48}$$

$$D(\kappa) = 1 - \frac{\kappa_0}{\kappa}(1 - A) - Ae^{-B(\kappa - \kappa_0)}, \tag{4.49}$$

where r is triaxial factor and $\tilde{\sigma}_{\mathrm{i}}$ is ith effective principal stress. A and B are the variables determining the shape of the damage evolution laws and subsequently behavioral laws.

4.3.6 Proposed damage evolution law

Having various definitions for the evolution of damage, it is essential to adopt a suitable law for the damage evolution while various history parameters are available in literature to be considered as a driving force for deformation. In the meantime, it is also important whether the principle of strain equivalence or the principle of energy equivalence is assumed, since this assumption becomes a vital role in the strain-softening behavior of material. It is found that the existing literature intensively discusses the damage behavior of concrete using the principle of strain equivalence, whereas the damage models based on the principle of energy equivalence have not been widely discussed so far. Nevertheless, the assumption of energy equivalence has advantages over strain equivalence in the case of anisotropic damage description as discussed in Section 4.2.2.

Therefore, a suitable damage evolution law is proposed here to account for the principle of energy equivalence exclusively based on the analyses performed in this work, which are discussed in Chapter 5. Such a simplified law similar to Weibull's failure distribution, which exhibits an exponential softening, takes the form as follows:

$$D(\kappa) = 1 - \left[\frac{\kappa_0}{\kappa}\right]^{\beta_1} e^{-\beta_2 \left[\frac{\kappa - \kappa_0}{\kappa_0}\right]}, \tag{4.50}$$

where β_1 and β_2 are model parameters defining the shape of damage evolution or post-peak softening. β_1 influences the initial rate of damage growth. The higher values of β_1 shows more brittle response. The exponent β_2 is the decay parameter determining the slope of stress decrease, in other words ensuring the long tail in the softening curve with residual stresses. The lower values of β_2 are slower down the damage growth and keep the damage variable approaching unity, but the limit value $D = 1$ never reached.
It can be noticed from various definitions that the damage variable shows asymptotic behavior approaching $D = 1$ (in the cases of exponential laws), which means that there will never be the possibility of complete fracture or failure. But, in the case of linear law or aforesaid power laws, the complete fracture ($D = 1$) is resulted when κ becomes equal to κ_{cr}.

4.3.7 Influence of model parameters

In order to study the influence of model parameters on the softening behavior of the material, tensile loading under 1D-situation is considered to cause homogeneous deformation. In such case, $\kappa = \epsilon = \varepsilon$. The damage evolution and the corresponding stress-strain curves are obtained for varying the values of model parameters β_1 and β_2.

Figures 4.5 and 4.6 show the damage evolution and stress-strain responses respectively for the increasing values of β_1, whereas β_2 is kept constant as 0.18. It is observed that a higher value of β_1 makes the initial damage growth faster, as shown in Figure 4.5 and thus leads to more brittle response of stress-strain curve, as depicted in Figure 4.6. Moreover, it is worth to mention here that the same evolution law (7.2) can be used to model the hardening behavior of concrete as well, as Figure 4.6 shows hardening behavior for $\beta_1 = 0.20$, which is the case of material behavior under compression.

On the other hand, Figure 4.7 and 4.8 show the damage evolution and stress-strain responses

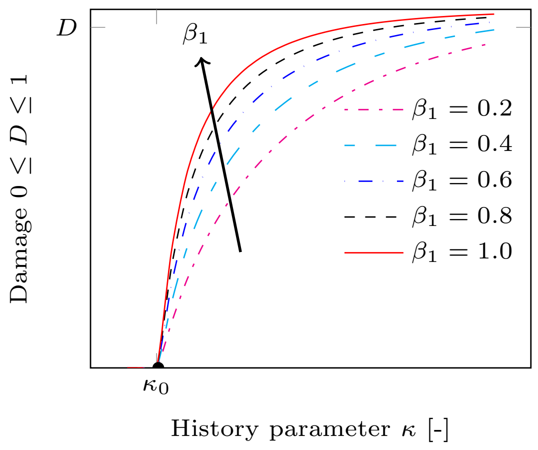

Figure 4.5: Damage evolution for $\beta_2 = 0.18$

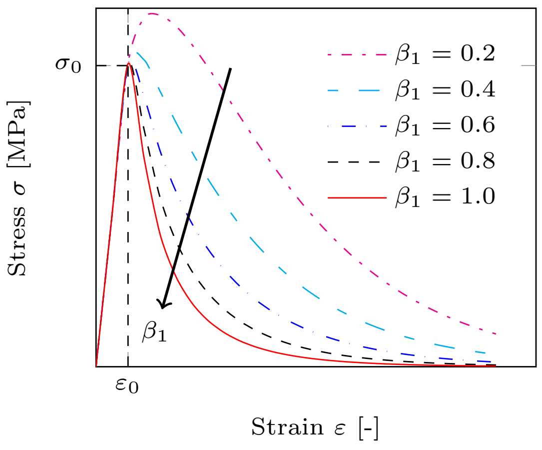

Figure 4.6: Stress-strain responses for $\beta_2 = 0.18$

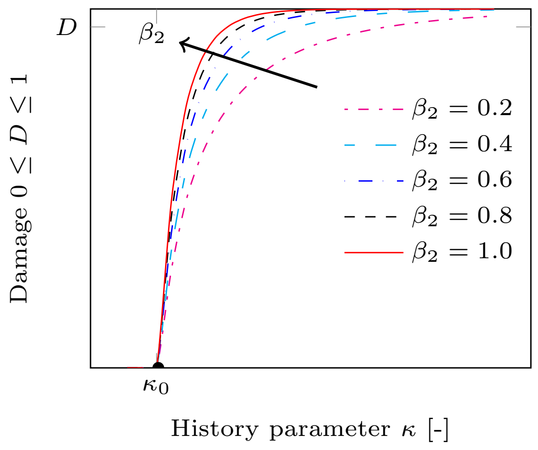

Figure 4.7: Damage evolution for $\beta_1 = 0.75$

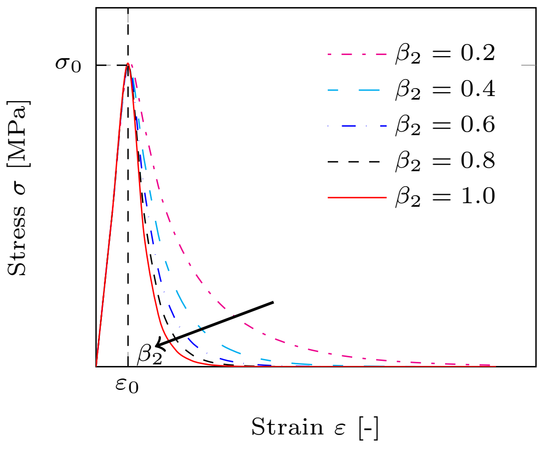

Figure 4.8: Stress-strain responses for $\beta_1 = 0.75$

respectively for the increasing values of β_2, whereas β_1 is kept constant as 0.75. It is noticed that a higher value of β_2 makes the later damage growth faster, as seen in Figure 4.7 and thus results in zero residual stresses in the post-peak regime of the curve, as observed in Figure 4.8.

4.4 Anisotropic damage

Since scalar damage variables as in the case of isotropic damage have limitations in describing the actual state of damage due to micro cracking, the damage induced anisotropy is generally incorporated in constitutive modeling with the use of the damage variables as vectors or higher rank tensors [3, 31, 34] and using micro-plane theories [16, 88, 89] in spite of their complications. Thus, the use of damage effect tensors $\mathbb{M}(\boldsymbol{D})$ of fourth-order in the case of anisotropic damage is recommended for a more reliable representation of damage of concrete. If the damaged material is modeled using constitutive laws of the effective undamaged material based on strain equivalence, then effective stress and resulting effective stiffness tensors are respectively expressed as

$$\tilde{\boldsymbol{\sigma}} = \mathbb{M} : \boldsymbol{\sigma} \tag{4.51}$$

$$\tilde{\mathbb{H}} = \mathbb{M}^{-1} : \mathbb{H}. \tag{4.52}$$

As seen in Section 4.2, the adoption of strain equivalence thus leads itself to asymmetric compliance or stiffness tensors and loss of integrability. The matrix representation of $\mathbb{M}$ of the symmetric fourth-order tensor is not symmetric in any reference system except the principal one [34]. Therefore, the incorporation of damage induced anisotropy along with the strain equivalence necessitates the symmetrizing techniques. On the other hand, the use of the energy equivalence itself overcomes this issue of symmetry and integrability [39, 111]. According to the anisotropic damage based on the principle of energy equivalence, the effective stress and strain tensors are given by,

$$\tilde{\boldsymbol{\sigma}} = \mathbb{M} : \boldsymbol{\sigma}; \qquad \tilde{\boldsymbol{\varepsilon}} = \mathbb{M}^{-T}\boldsymbol{\varepsilon}. \tag{4.53}$$

Hence, the symmetric effective stiffness tensor is consequently obtained as follows:

$$\tilde{\mathbb{H}} = \mathbb{M}^{-1} : \mathbb{H} : \mathbb{M}^{-T}. \tag{4.54}$$

The tensor $\mathbb{M}$ is generally in a diagonal matrix form. There are various definitions available for this tensor [111, 147] and the references therein. For example, the damage effect tensor $\mathbb{M}(\boldsymbol{D})$, which is in terms of damage tensor $\boldsymbol{D}$, can be mathematically represented as (in matrix notation)

$$\mathbb{M}(\boldsymbol{D}) = \begin{bmatrix} \frac{1}{1-D_1} & 0 & 0 & 0 & 0 & 0 \\ 0 & \frac{1}{1-D_2} & 0 & 0 & 0 & 0 \\ 0 & 0 & \frac{1}{1-D_3} & 0 & 0 & 0 \\ 0 & 0 & 0 & \frac{1}{1-\frac{D_2+D_3}{2}} & 0 & 0 \\ 0 & 0 & 0 & 0 & \frac{1}{1-\frac{D_3+D_1}{2}} & 0 \\ 0 & 0 & 0 & 0 & 0 & \frac{1}{1-\frac{D_1+D_2}{2}} \end{bmatrix}. \tag{4.55}$$

The tensor components are concerned with the orthonormal basis in the principal directions $\vec{n}_\mathrm{i}$ of the damage tensor $\boldsymbol{D}$. It is assumed such that the principal directions of $\boldsymbol{D}$ coincide with the principal directions of stress field at the specified material element and their corresponding three principal damages are D_1,D_2,D_3 [33]. Thus, the symmetric second-order damage tensor $\boldsymbol{D}$ is written in principal coordinate system as follows:

$$\boldsymbol{D} = \begin{bmatrix} D_1 & 0 & 0 \\ 0 & D_2 & 0 \\ 0 & 0 & D_3 \end{bmatrix} \tag{4.56}$$

Furthermore, the damage tensor $\boldsymbol{D}$ and the damage effect tensor $\mathbb{M}(\boldsymbol{D})$ of principal coordinate system (4.55) can still be transformed into any arbitrary coordinate system based on the coordinate transformation law [34]. Consequently, the damage tensor can be written in terms of generalized coordinate system as

$$\boldsymbol{D}' = \begin{bmatrix} D_1 & D_6 & D_5 \\ & D_2 & D_4 \\ \text{sym} & & D_3 \end{bmatrix} \tag{4.57}$$

The damage tensor $\boldsymbol{D}'$ (4.57) can also be written conveniently in Voigt notation like second-order symmetric stress and strain tensors as

$$\boldsymbol{D}' = \begin{Bmatrix} D_1 & D_2 & D_3 & 2D_{23} & 2D_{13} & 2D_{12} \end{Bmatrix}^T . \tag{4.58}$$

Similarly, the damage effect tensor of arbitrary system $\mathbb{M}'(\boldsymbol{D}')$ can be easily obtained [34]. However, the evolution of principal damages can be described as discussed in Section 4.3. In this fashion, the evolution of damage D_i along i$^\mathrm{th}$ principal direction is driven by the history deformation parameter κ_i along its corresponding direction. It is thus expressed as

$$D_\mathrm{i} = D_\mathrm{i}(\kappa_\mathrm{i}). \tag{4.59}$$

5 Choice of State Variables

The past decades of research show that the local deformation state variable ζ has been recognized as the damage energy release rate Y or the states of strain with growth of damage (equivalent strain ϵ) or the effective stress $\tilde{\sigma}$ or the equivalent stress $\tilde{\sigma}_{\text{eq}}$. It represents the local measure of deformation of the material at a point of continuum under consideration. Thus, it is later related to the damage history deformation parameter κ. Subsequently, it necessitates the analysts to ensure a parameter, which is more relevant and appropriate to be assumed as the local measure of deformation driving the degradation of the material. Hence, this chapter is devoted for the analysis of the elasticity based damage model in which an isotropic damage is driven by different state variables as history parameters to understand the material behavior at a point under uniaxial setting and also to recommend a more suitable history parameter for the better description of the strain-softening behavior realistically.

5.1 Available history parameters

There are four approaches widely adopted in the literature for the assumption of the history parameter. For the actual expression of local measures, reader may refer to the quoted references.

Approach 1 $\zeta = Y$, as the damage energy release rate

κ is related to the scalar measure of the damage energy release rate Y, which follows equation (4.16) [103, 107, 126, 138, 149]. According to the second law of thermodynamics or the Clausius-Duhem inequality, $\varphi \geq 0$, the rate of damage, $\dot{D} \geq 0$ is always satisfied, since Y is a positive-definite function of $\boldsymbol{\varepsilon}$. Then, the damage loading function f is written as

$$f = f(Y, \kappa) = Y - \kappa(Y). \tag{5.1}$$

In one-dimensional cases, Y is defined as

$$Y_{\text{se}} = \frac{1}{2} E \varepsilon^2, \tag{5.2}$$

$$Y_{\text{ee}} = (1 - D) E \varepsilon^2, \tag{5.3}$$

using strain equivalence (4.8) and energy equivalence (4.9) respectively.

Approach 2 $\zeta = \epsilon$, as the damage equivalent strain

To represent the equivalence between the uniaxial and multiaxial states of strain and to consider their effect on the development of damage, and if the damage criterion defines the strain states with the potential increase of damage, the scalar measure of local deformation called damage equivalent strain or local equivalent strain denoted by ϵ is considered as κ [28, 67, 107, 123].

Then, the damage loading function f takes a form as

$$f = f(\epsilon, \kappa) = \epsilon - \kappa(\epsilon). \tag{5.4}$$

In one-dimensional cases, ϵ will be taken equal to the total applied strain ε, i.e., $\epsilon = \varepsilon$.

Approach 3 $\zeta = \tilde{\sigma}^{\mathrm{i}}$, as the effective stress

The damage growth is sometimes related to the effective stress as the damage causes the decrease in the Cauchy stress. If the split-up of the effective stress is considered to account for the unilateral behavior of damaged concrete, κ can be related to the effective stress $\tilde{\sigma}^{\mathrm{i}}$ [104]. Then, the damage loading function f is given by

$$f^+ = f(\tilde{\sigma}^+, \kappa) = \tilde{\sigma}^+ - \kappa^+(\tilde{\sigma}^+); \qquad f^- = f(\tilde{\sigma}^-, \kappa) = \tilde{\sigma}^- - \kappa^-(\tilde{\sigma}^-). \tag{5.5}$$

In one-dimensional cases, $\tilde{\sigma}^{\mathrm{i}} = \frac{\sigma^{\mathrm{i}}}{1-D}$, where i$= +/-$ represents tension/compression.

Approach 4 $\zeta = \tilde{\sigma}^{\mathrm{i}}_{\mathrm{eq}}$, as the equivalent stress

In order to clearly define the concepts of loading, unloading or reloading, the scalar positive quantity termed as the equivalent stress is introduced as a consequence of the stress split-up. Thus, κ can also be related to the scalar measure of the equivalent stress $\tilde{\sigma}^{\mathrm{i}}_{\mathrm{eq}}$ [62, 63]. Then, the damage loading function f is expressed by,

$$f^+ = f(\tilde{\sigma}^+_{\mathrm{eq}}, \kappa) = \tilde{\sigma}^+_{\mathrm{eq}} - \kappa^+(\tilde{\sigma}^+_{\mathrm{eq}}); \qquad f^- = f(\tilde{\sigma}^-_{\mathrm{eq}}, \kappa) = \tilde{\sigma}^-_{\mathrm{eq}} - \kappa^-(\tilde{\sigma}^-_{\mathrm{eq}}). \tag{5.6}$$

In one-dimensional cases, $\tilde{\sigma}^{\mathrm{i}}_{\mathrm{eq}} = \frac{\sigma^{\mathrm{i}}}{(1-D)\sqrt{E}}$, where i$= +/-$ represents tension/compression.
A comparison of suitability analysis using a 1D material damage model based on these aforementioned approaches with selected damage evolution laws under the assumption of both the equivalence principles is discussed in the following section.

5.2 Analysis of 1D isotropic damage model

In order to study the influence of the history parameters on the softening behavior of the material, a pure tensile loading under 1D-setting is considered to cause the homogeneous deformation. Accordingly, the stress-strain relations (4.8, 4.9) for the linear elasticity within the context of continuum damage theory based on the strain and energy equivalence principles reduce respectively to

$$\sigma_{\mathrm{se}} = (1 - D)E\varepsilon, \tag{5.7}$$

$$\sigma_{\mathrm{ee}} = (1 - D)^2 E\varepsilon. \tag{5.8}$$

The axial total strain ε is monotonically increasing. The deformation history parameter κ of those models is adopted as equal to the various state variables ζ with the damage evolution laws such as the linear softening law (4.30), the exponential law (4.35), the modified power law (4.34), and the proposed softening law (4.50) using the principle of strain equivalence, which is inconsistent, as well as the principle of energy equivalence. The damage evolution and the corresponding simulated stress-strain curves obtained from the numerical analyses are compared with the experimental stress-strain curve [84], as shown in Figures 5.1-5.8. The material properties $E = 31.7$ [GPa] and $\nu = 0.2$ are taken from the experimental data [84]. The set of selected material dependent parameters such as α, β, α', β', β_1, β_2, and the initial damage threshold κ_0, the critical damage threshold κ_{cr}, and the final threshold κ_{f} are given in Table 5.1.

Table 5.1: Material parameters for different state history variables

History Parameter	Linear softening law (4.30)	Exponential law (4.35)	Mod. power law (4.34)	Proposed law (4.50)
$\kappa = \epsilon$ $[-]$	- - $\kappa_0 = 1.15 \times 10^{-4}$ $\kappa_{\mathrm{cr}} = 3 \times 10^{-4}$ $\kappa_{\mathrm{f}} = 6 \times 10^{-4}$	$\alpha = 0.96$ $\beta = 11000$ $\kappa_0 = 1.15 \times 10^{-4}$ $\kappa_{\mathrm{cr}} = \mathrm{Nil}$ $\kappa_{\mathrm{f}} = 6 \times 10^{-4}$	$\alpha' = 5$ $\beta' = 0.9$ $\kappa_0 = 1.15 \times 10^{-4}$ $\kappa_{\mathrm{cr}} = 5.8 \times 10^{-4}$ $\kappa_{\mathrm{f}} = 6 \times 10^{-4}$	$\beta_1 = 1.1$ $\beta_2 = 0.18$ $\kappa_0 = 1.15 \times 10^{-4}$ $\kappa_{\mathrm{cr}} = \mathrm{Nil}$ $\kappa_{\mathrm{f}} = 6 \times 10^{-4}$
$\kappa = Y$ [MPa]	- - $\kappa_0 = 4 \times 10^{-4}$ $\kappa_{\mathrm{cr}} = 110 \times 10^{-4}$ $\kappa_{\mathrm{f}} = 114 \times 10^{-4}$	$\alpha = 0.96$ $\beta = 11000$ $\kappa_0 = 4 \times 10^{-4}$ $\kappa_{\mathrm{cr}} = \mathrm{Nil}$ $\kappa_{\mathrm{f}} = 114 \times 10^{-4}$	$\alpha' = 5$ $\beta' = 0.9$ $\kappa_0 = 4 \times 10^{-4}$ $\kappa_{\mathrm{cr}} = 110 \times 10^{-4}$ $\kappa_{\mathrm{f}} = 114 \times 10^{-4}$	$\beta_1 = 1.1$ $\beta_2 = 0.18$ $\kappa_0 = 4 \times 10^{-4}$ $\kappa_{\mathrm{cr}} = \mathrm{Nil}$ $\kappa_{\mathrm{f}} = 114 \times 10^{-4}$
$\kappa = \tilde{\sigma}$ [MPa]	- - $\kappa_0 = 3.5$ $\kappa_{\mathrm{cr}} = 18$ $\kappa_{\mathrm{f}} = 38$	$\alpha = 0.96$ $\beta = 11000$ $\kappa_0 = 3.5$ $\kappa_{\mathrm{cr}} = \mathrm{Nil}$ $\kappa_{\mathrm{f}} = 38$	$\alpha' = 5$ $\beta' = 0.9$ $\kappa_0 = 3.5$ $\kappa_{\mathrm{cr}} = 18$ $\kappa_{\mathrm{f}} = 38$	$\beta_1 = 1.1$ $\beta_2 = 0.18$ $\kappa_0 = 3.5$ $\kappa_{\mathrm{cr}} = \mathrm{Nil}$ $\kappa_{\mathrm{f}} = 38$
$\kappa = \tilde{\sigma}_{eq}$ $[\frac{\mathrm{MPa}}{\sqrt{\mathrm{MPa}}}]$	- - $\kappa_0 = 0.02$ $\kappa_{\mathrm{cr}} = 0.1$ $\kappa_{\mathrm{f}} = 0.25$	$\alpha = 0.96$ $\beta = 11000$ $\kappa_0 = 0.02$ $\kappa_{\mathrm{cr}} = \mathrm{Nil}$ $\kappa_{\mathrm{f}} = 0.25$	$\alpha' = 5$ $\beta' = 0.9$ $\kappa_0 = 0.02$ $\kappa_{\mathrm{cr}} = 0.1$ $\kappa_{\mathrm{f}} = 0.25$	$\beta_1 = 1.1$ $\beta_2 = 0.18$ $\kappa_0 = 0.02$ $\kappa_{\mathrm{cr}} = \mathrm{Nil}$ $\kappa_{\mathrm{f}} = 0.25$

5.3 Results and discussions

Remark 1 The results shown in Figures 5.1 and 5.2 correspond to the assumption that the deformation of the material is driven by the damage equivalent strain ϵ equal to the applied total strain ε based on the strain and energy equivalence respectively. It is observed from Figure 5.1a that the damage evolutions are more or less similar even though damage variables take three different definitions such as linear softening (4.30), exponential softening (4.35) and modified power law (4.34). The strain-softening behaviors of the model based on the principle of strain equivalence (5.7) using the respective damage evolution are compared with the experimental stress-strain curve [84] in Figure 5.1b. It is clear that strain-softening models based on (4.30) and (4.34) result in zero stress after certain strain as the complete fracture is assumed to occur when the threshold reaches critical value. On the other hand, the model based on the exponential softening (4.35), which leads to certain residual stresses in the final regime as the damage is assumed to approach unity asymptotically, may seem to be realistic. Based on the results of existing damage models and the reproduced results, as illustrated in Figure 5.1, the strain equivalence provides good results for the chosen material properties and chosen material dependent parameters.

Nevertheless, consideration of the energy equivalence (5.8) leads to a more realistic behavior than the strain equivalence principle, as both the stress and strain distributions are influenced. In order to illustrate that the stress-softening behavior of the model based on such damage evolution using the energy equivalence is studied and the results are shown in Figure 5.2b. It indicates that the energy equivalence provides better identical stress-strain behavior of the material than the strain equivalence, but such predicted curves reveal that the damage development is much faster than the experimental damage development for the same set of material properties and parameters, and registering zero residual stresses soon after reaching critical thresholds. Thus, the results based on the damage evolution laws (4.30), (4.35) and (4.34) provide earlier prediction of damage leading to collapse when the energy equivalence is used, which is contrast to the case of strain equivalence.

Hence, the introduction of the new softening law (4.50), which is exclusively meant for the energy equivalence, is proposed. The predicted stress-strain curves of the material model based

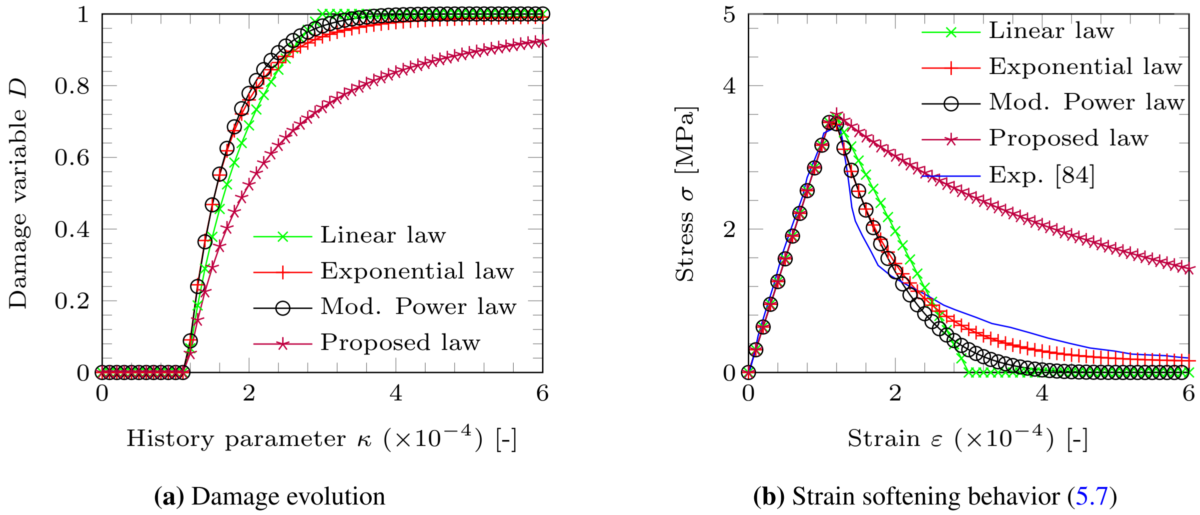

(a) Damage evolution

(b) Strain softening behavior (5.7)

Figure 5.1: Principle of strain equivalence ($\kappa = \epsilon$)

on (4.50) using both the equivalence principles are depicted in Figures 5.1b and 5.2b respectively in which the simulated softening behavior predicted by the proposed law (4.50) using the energy equivalence agrees well with experimental curve.

Remark 2 If the material deformation is driven by the damage energy release rate Y based on the strain equivalence (5.7), it is clear from equation (4.16) that Y is totally dependent on the applied total strain ε. The material properties and material dependent parameters used are kept unchanged here. For the selected and proposed damage evolution laws, the damage evolution and the corresponding simulated stress-strain curves are obtained, as shown in Figures 5.3 and 5.4. It is observed from Figure 5.3b that the softening regime in the present case using the linear softening law (4.30) is no more linear as predicted in *Approach 1* using the strain equivalence, but it could be used, since it moderately shows nonlinear behavior and also almost agrees with experimental results. At the same time, the modified power law (4.34) predicts the softening behavior as resulted in the *Approach 1* using the strain equivalence. In a similar way, the proposed law (4.50) predicts the softening as modified power law (4.34). Nonetheless, both the laws result in zero residual stresses at the final region thus leading to complete fracture. By contrast, the exponential law (4.35) with $\kappa = Y$ results in faster growth of damage showing very brittle response and also causes minimum residual stresses.

Remark 3 and 4 When the material deformation is driven either by the effective stress $\tilde{\sigma}$ or by the effective equivalent stress $\tilde{\sigma}_{\text{eq}}$ based on both the equivalence principles (5.7), Figures 5.5-5.8 exemplify that the damage evolution and the softening behaviors are almost identical. But various softening responses are obviously observed with respect to the damage evolution laws. The modified power law (4.34) predicts the softening closely but resulting in vanishing stresses in the final regime. In the case of exponential law (4.35), the stress drops suddenly to a minimum without showing any gradual decrease soon after the initiation of the damage, and there-

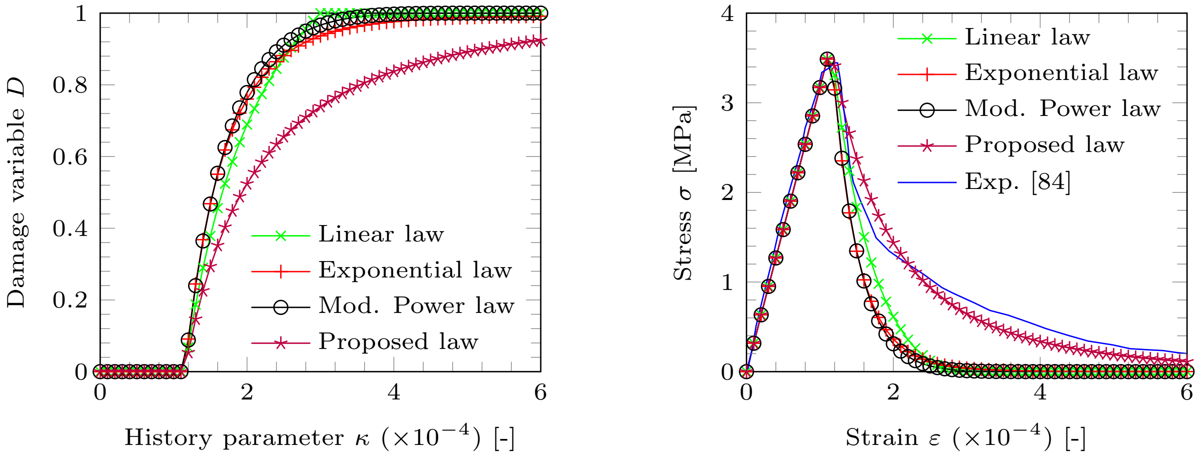

(a) Damage evolution **(b)** Strain softening behavior (5.8)

Figure 5.2: Principle of energy equivalence ($\kappa = \epsilon$)

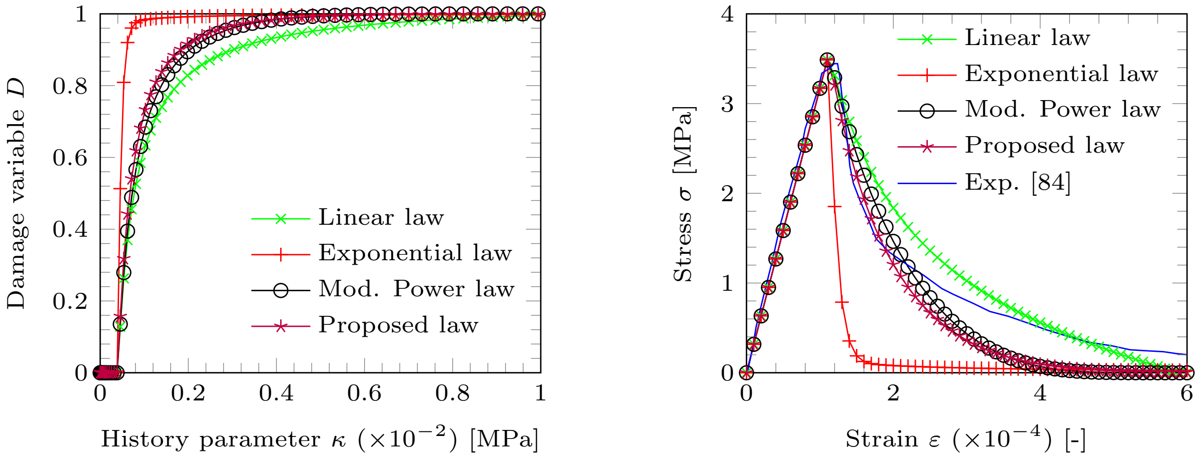

(a) Damage evolution **(b)** Strain softening behavior (5.7)

Figure 5.3: Principle of strain equivalence ($\kappa = Y$)

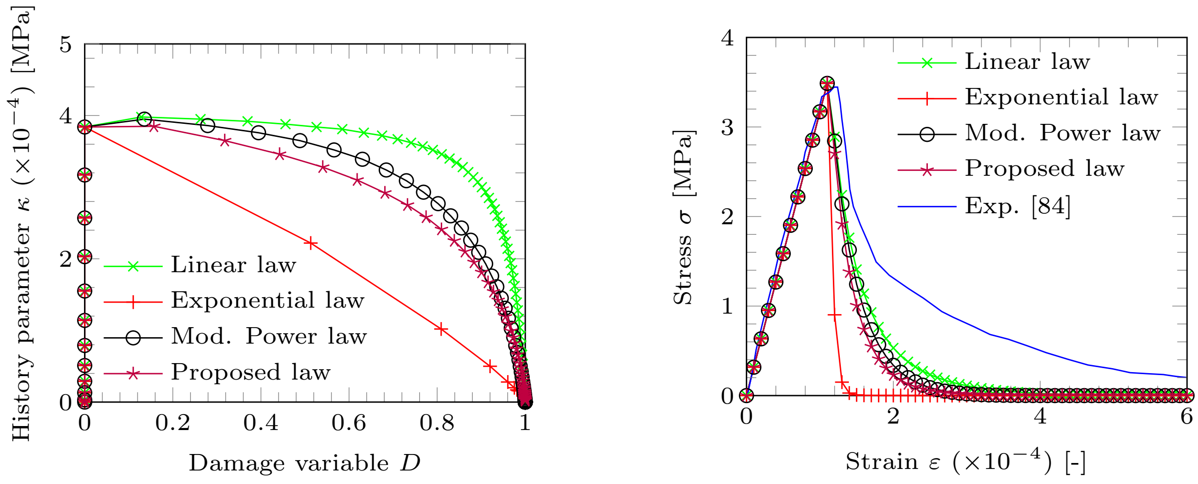

(a) Damage evolution **(b)** Strain softening behavior (5.8)

Figure 5.4: Principle of energy equivalence ($\kappa = Y$)

after residual stresses are observed. Further, the linear softening law (4.30) and the proposed law (4.50) show softening responses, which are not consistent in both approaches.

It is really interesting to notice that the softening responses under the assumption of strain equivalence in the case of modified power law (4.34) are identical irrespective of the selection of history parameters even though it results in vanishing stresses or complete fracture. But it is not the case under the assumption of energy equivalence.

Furthermore, when the energy equivalence is assumed, the models based on the history parameters such as Y, $\tilde{\sigma}$, and $\tilde{\sigma}_{\text{eq}}$ provide unintended softening responses, which are highly spurious. These imply that all the adopted damage evolution laws are not appropriate to simulate the exact material behavior with the chosen model parameters under the assumption of energy

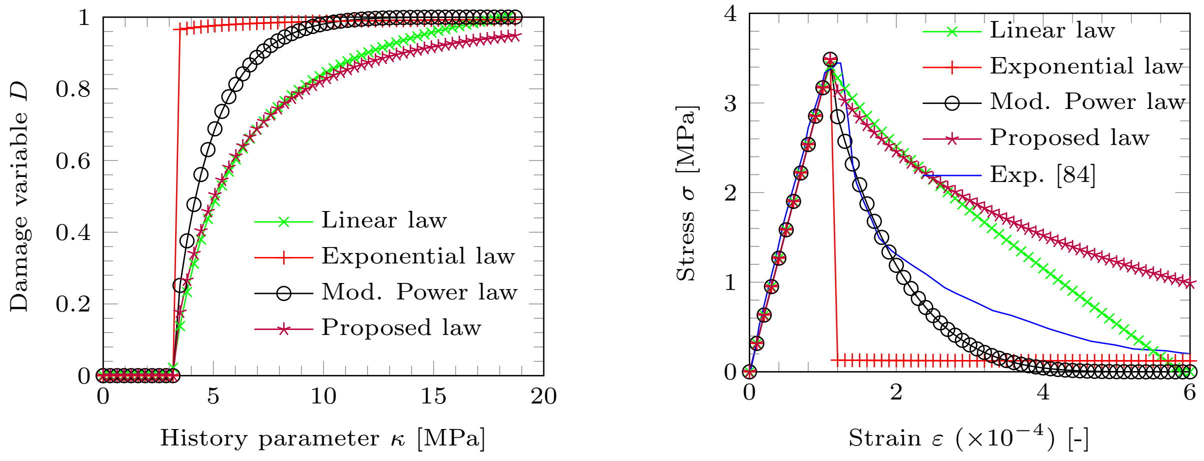

(a) Damage evolution

(b) Strain softening behavior (5.7)

Figure 5.5: Principle of strain equivalence ($\kappa = \tilde{\sigma}$)

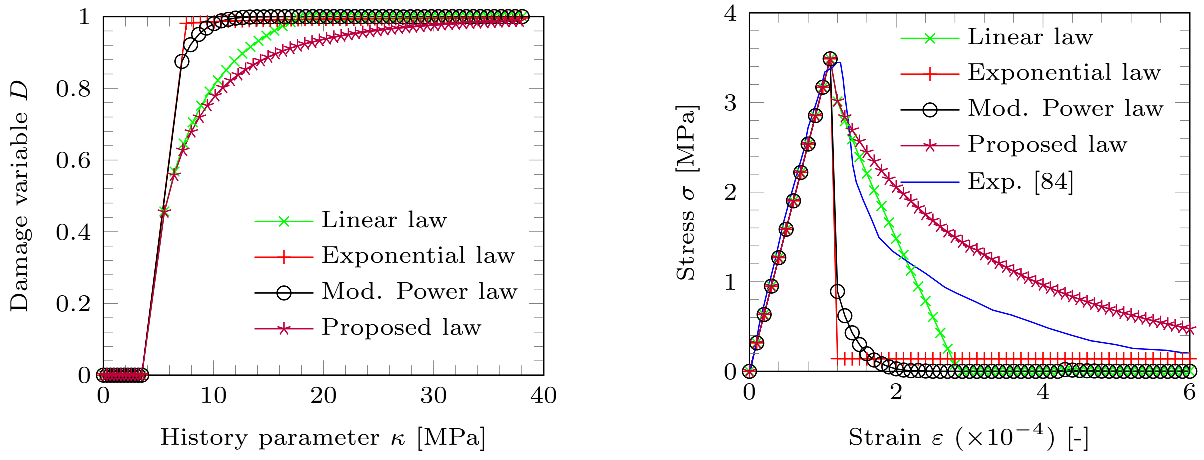

(a) Damage evolution

(b) Strain softening behavior (5.8)

Figure 5.6: Principle of energy equivalence ($\kappa = \tilde{\sigma}$)

equivalence even though these laws have been adopted in various models under the assumption of strain equivalence.

The mechanism of micro-cracking of concrete reveals that the large strains mainly occur due to the initiation of micro-cracks. Subsequently, the failure of material specimen occurs due to a micro-crack traversing across the entire cross-section and separating the specimen into two parts leading to opening the crack up. Consequently, the material stiffness decreases with the increase in strain thus leading to the changes in stress-strain relationships [61].

Moreover, it is understood that the displacement or deformation is primarily considered as a fundamental measure and can be measured directly without any other physical quantity, since both are defined as the total or relative movement of any material point in a body. As the

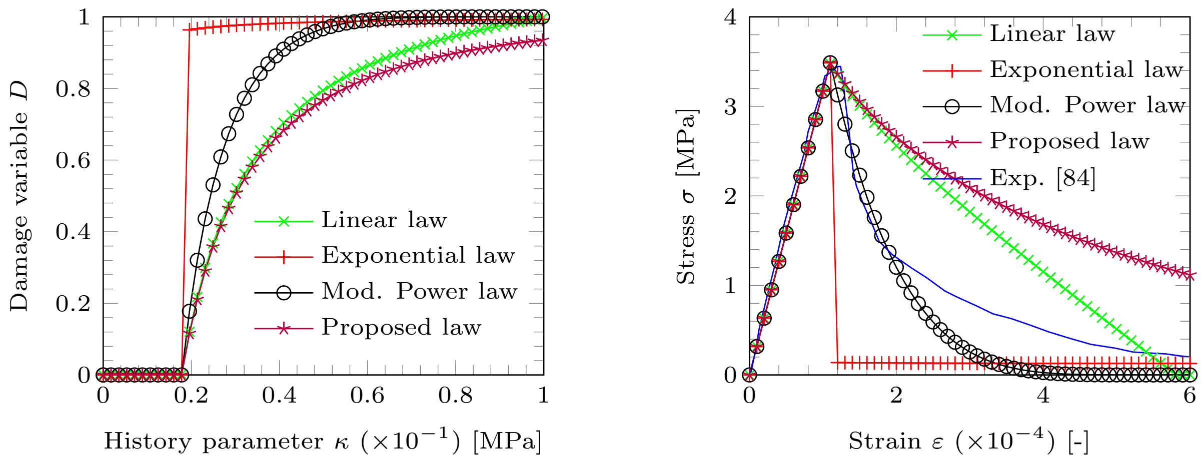

(a) Damage evolution **(b)** Strain softening behavior (5.7)

Figure 5.7: Principle of strain equivalence ($\kappa = \tilde{\sigma}_{\text{eq}}$)

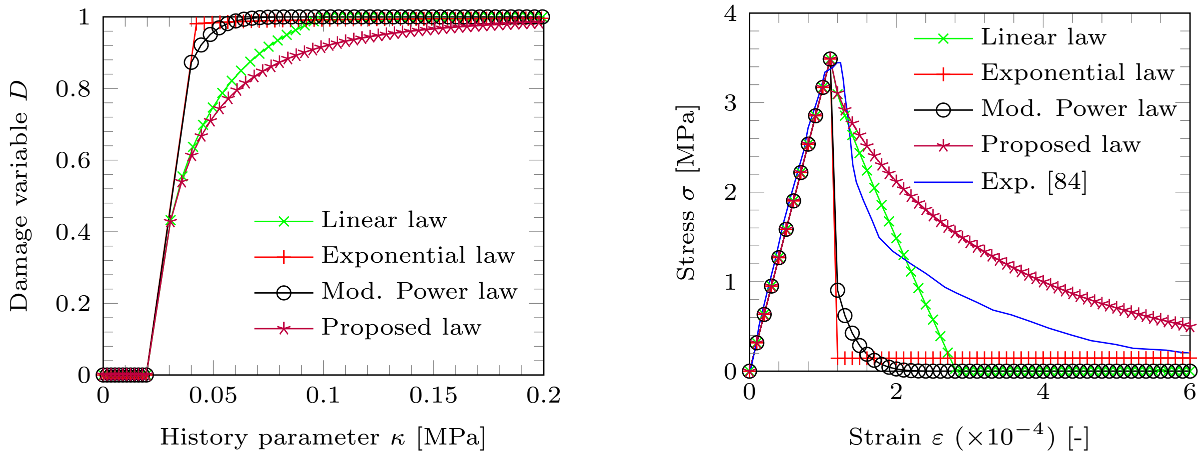

(a) Damage evolution **(b)** Strain softening behavior (5.8)

Figure 5.8: Principle of energy equivalence ($\kappa = \tilde{\sigma}_{\text{eq}}$)

damage equivalent strain ϵ and the damage energy release rate Y are positively based on the development of strain or deformation, these could directly be related to the damage and its growth. Nonetheless, the definition of the energy release rate Y could lead to the non-physical response, since it gives a slight development of damage at the notch [123].

Therefore, the damage equivalent strain ϵ would be more appropriate to be assumed as a history deformation parameter than the derived quantities such as the damage energy release rate Y, the effective stress $\tilde{\sigma}$ or the equivalent effective stress $\tilde{\sigma}_{\text{eq}}$ in order to describe the behavior of micro-cracking and opening-up of cracks in concrete effectively, since it can obviously be estimated from the strain, which is an independent measure.

6 Extension to Nonlocal Modeling of Damage

Most of the brittle heterogeneous materials like concrete, rocks exhibit a progressive damage failure due to distributed cracking and thus result in negative stiffness after reaching the peak stress. This typical behavior is generally termed as strain softening in the structural analyses. Continuum damage mechanics has recently become a popular and promising approach to model this kind of material behavior. Subsequently, the implementation of such local continuum damage models in FEM programs causes numerical difficulties such as ill-posedness of boundary value problems and damage localization to a vanishing volume (line or surface), consequently leading to vanishing dissipation of energy and mesh dependency due to negative stiffness. Hence, this chapter is devoted to discuss the fundamental issues of the localization of deformation related to the finite element implementation and the significance of nonlocal phenomena by incorporating an internal length. Afterwards, few regularization methods have been discussed. Additionally, a brief comparison of gradient-enhanced damage models and phase-field models has also been provided.

6.1 Significance of nonlocal phenomena

In this section, the issues why classical continuum models suffer from the extensive mesh dependency, the localization of deformation, and the other numerical difficulties [49, 111] are discussed in a mathematical point of view. In addition, a few numerical results are also discussed demonstrating how the incorporation of a characteristic internal length in the continuum models enriches the ability of the models to allow the localization of deformation without losing well-posedness of the rate boundary value problem.

6.1.1 Material instability

According to the stability criterion [49, 73, 111] in the mechanical point of view, the inner product of the stress rate $\dot{\boldsymbol{\sigma}}$ and the strain rate $\dot{\boldsymbol{\varepsilon}}$ is always positive

$$\dot{\boldsymbol{\varepsilon}}^T \, \dot{\boldsymbol{\sigma}} > 0. \tag{6.1}$$

When the strain softening occurs, this inner product (6.1) becomes negative. Thus, the driving force causing the localization phenomena is a material instability due to the violation of the stability criterion by the constitutive relationship. Moreover, the predominant load-carrying mechanism of material (multi-axial) due to the frictional effects in pre-cracked concrete may result in a non-symmetric constitutive relation. Thus, the loss of symmetry between the stress rate and strain rate tensors can also lead to the material instability.

Mathematically, the stability condition according to Hill [73] for a stable material having a material tangential tensor $\mathbb{H}(D)$, which in general could be non-symmetric, and an isotropic damage D can be written as

$$\dot{\boldsymbol{\varepsilon}}^T\,\mathbb{H}(D)\,\dot{\boldsymbol{\varepsilon}} > 0. \tag{6.2}$$

Consequently, the condition for the onset of the material instability can be given by

$$\dot{\boldsymbol{\varepsilon}}^T\,\mathbb{H}(D)\,\dot{\boldsymbol{\varepsilon}} = 0. \tag{6.3}$$

In other words, the existence of a non-trivial solution of equation (6.3), leads to loss of positive-definiteness of the material as

$$\left|\mathbb{H}(D) + \mathbb{H}(D)^T\right| = 0. \tag{6.4}$$

6.1.2 Structural instability

Structural instability can be a consequence of the material instability. Hill's stability criterion for a structure occupying a volume V can be written as

$$\int_V \dot{\boldsymbol{\varepsilon}}^T\,\dot{\boldsymbol{\sigma}}\,dV > 0, \tag{6.5}$$

for all kinematically admissible strain rate tensors $\dot{\boldsymbol{\varepsilon}}$ [49]. Supplying the stress-strain relation in the above integral (6.5), the condition, which guarantees the structural stability, becomes

$$\int_V \dot{\boldsymbol{\varepsilon}}^T\,\mathbb{H}(D)\,\dot{\boldsymbol{\varepsilon}}\,dV > 0. \tag{6.6}$$

Besides the equality of the above condition (6.6), the onset of the structural instability is provided by

$$\int_V \dot{\boldsymbol{\varepsilon}}^T\,\mathbb{H}(D)\,\dot{\boldsymbol{\varepsilon}}\,dV = 0. \tag{6.7}$$

Subsequent application of the finite element discretization of (6.7) leads to

$$\dot{\boldsymbol{d}}^T\,\boldsymbol{K}\,\dot{\boldsymbol{d}} = 0, \tag{6.8}$$

where $\boldsymbol{K}$ is the structural stiffness matrix and $\boldsymbol{d}$ is the vector of nodal displacements. If there is a possibility of a non-trivial solution of the above equation (6.8), $\boldsymbol{K}$ will become singular. As a result, the loss of positive-definiteness of $\boldsymbol{K}$ associated with the structural instability can be given by

$$\left|\boldsymbol{K} + \boldsymbol{K}^T\right| = 0. \tag{6.9}$$

Thus, it is evident that the structural stiffness matrix $\boldsymbol{K}$ may cease to be positive-definite due to the local loss of positive-definiteness of the material tangent matrix $\mathbb{H}(D)$.

6.1.3 Loss of uniqueness

In the case of post-failure computations, it is most important to ensure that uniqueness of the solution is not violated while following the post-peak equilibrium path. That means that, at the same level, there do not exist other equilibrium states at a lower energy level [49]. Any stress state of a structure must satisfy an equilibrium condition, which is written in rate form as

$$\nabla \cdot \dot{\boldsymbol{\sigma}} + \rho\, \dot{\boldsymbol{b}} = 0. \tag{6.10}$$

Suppose the uniqueness is violated, there must be two different stress rates $\dot{\boldsymbol{\sigma}}_A$ and $\dot{\boldsymbol{\sigma}}_B$ satisfying the above condition (6.10). Subsequently, one can obtain

$$\nabla \cdot \dot{\boldsymbol{\sigma}}_A + \rho\, \dot{\boldsymbol{b}} - \left(\nabla \cdot \dot{\boldsymbol{\sigma}}_B + \rho\, \dot{\boldsymbol{b}}\right) = 0, \tag{6.11}$$

$$\nabla \cdot \dot{\boldsymbol{\sigma}}_A - \nabla \cdot \dot{\boldsymbol{\sigma}}_B = \nabla \cdot \Delta\dot{\boldsymbol{\sigma}} = 0, \tag{6.12}$$

where Δ refers to the difference between the two stress states. Thereupon, the weak form of equation (6.12) using the rate form of the stress-strain relation and also using a weight function $\delta\dot{\varepsilon}$ can be expressed as follows:

$$\int_V \delta\dot{\boldsymbol{\varepsilon}}^T\, \mathbb{H}(D)\, \Delta\dot{\varepsilon}\, dV = 0. \tag{6.13}$$

Performing the finite element discretization of equation (6.13) leads to the system of equations

$$\delta\boldsymbol{d}^T\, \boldsymbol{K}\, \Delta\dot{\boldsymbol{d}} = 0, \tag{6.14}$$

where $\boldsymbol{K}$ is structural stiffness matrix and $\Delta\dot{\boldsymbol{d}}$ is the vector of increments of nodal displacement rates for any virtual displacement field $\delta\boldsymbol{d}$. Thus, multiple solutions exist if and only if the condition (6.14) is satisfied. In addition, a possible non-trivial solution of the condition (6.14) can be given as

$$\left|\boldsymbol{K}\right| = 0. \tag{6.15}$$

The condition (6.15) is valid for a symmetric material tangent tensor $\mathbb{H}(D)$ as the notions of the loss of stability and the loss of uniqueness coincide. In the case of a non-symmetric tensor operator, the loss of stability (6.9) precedes the loss of uniqueness (6.15) [49].

On the other hand, unique solutions are possible at a material point under consideration as long as the stress increases monotonically with increasing strain. In such a way, a condition for the local uniqueness becomes valid, which can be written in rate form as

$$\dot{\boldsymbol{\sigma}} = \mathbb{H}(D)\, \dot{\varepsilon} > 0. \tag{6.16}$$

Thus, the uniqueness of deformation is guaranteed as far as the condition (6.16) is satisfied. On the other hand, if $\dot{\boldsymbol{\sigma}} = 0$, then a non-trivial solution is possible only when the material tangent tensor $\mathbb{H}(D)$ becomes singular [49]. Accordingly, the loss of uniqueness can be mathematically expressed as

$$\Big|\mathbb{H}(D)\Big| = 0. \tag{6.17}$$

6.1.4 Loss of ellipticity

The crucial consequence of the material instability or the loss of positive-definiteness of the material tangent matrix $\mathbb{H}(D)$ may lead to not only structural instability but also a loss of ellipticity of the equilibrium rate equations. To achieve the well-posedness of the rate equilibrium equations, ellipticity for static loadings or hyperbolicity for dynamic loadings is a necessary condition [49, 95]. For a well-posed problem, the ellipticity condition can be mathematically written in matrix form as

$$\boldsymbol{n}^T\,\mathbb{H}(D)\,\boldsymbol{n} > 0, \tag{6.18}$$

if there exists a normal vector $\boldsymbol{n}$ of discontinuity of the material a having tangential symmetric matrix $\mathbb{H}(D)$. Due to the loss of positive-definiteness of the tangent matrix $\mathbb{H}(D)$, the local continuum damage models cause the loss of ellipticity, which means that equation (6.18) becomes

$$\Big|\boldsymbol{n}^T\,\mathbb{H}(D)\,\boldsymbol{n}\Big| = 0. \tag{6.19}$$

If small deformations and strains are assumed, then the loss of material stability expressed by (6.4) is valid and becomes a necessary condition for the loss of ellipticity [49]. In order to prove that, if strain rate field $\dot{\boldsymbol{\varepsilon}}$ with an arbitrary vector $\boldsymbol{m}$ is given by

$$\dot{\boldsymbol{\varepsilon}} = \frac{1}{2}\,(n_{\mathrm{i}}m_{\mathrm{j}} + n_{\mathrm{j}}m_{\mathrm{i}}), \tag{6.20}$$

then loss of material stability (6.3) leads to $m_{\mathrm{i}}\,n_{\mathrm{j}}\,H_{\mathrm{ijkl}}\,m_{\mathrm{k}}\,n_{\mathrm{l}} = 0$. Thus, this condition is valid for any arbitrary $\boldsymbol{m}$ if and only if

$$\Big|\tfrac{1}{2}\boldsymbol{n}^T\,(\mathbb{H}^T + \mathbb{H})\,\boldsymbol{n}\Big| = 0. \tag{6.21}$$

The condition (6.21) is satisfied, if the material instability exists. It means that the loss of ellipticity can only occur if the loss of material stability occurs.

6.1.5 Mesh sensitivity analysis

The strain softening is usually modeled as a negative slope in the stress-strain diagram within the context of classical continuum damage theory and in turn the matrix of tangential moduli ceases to be positive-definite. As a result, the local modeling of strain softening damage subsequently tends to localize in a zone of vanishing volume and the failure at zero energy dissipation upon mesh refinement. This is physically unacceptable, since the energy dissipation per unit volume is always finite. Thereupon, the localization due to the strain softening leads to the finite element solutions exhibiting spurious mesh sensitivity [17, 20, 52, 126].

Figure 6.1 depicts the numerical load-displacement responses of the local and nonlocal damage models (nonlocal integral method) of an elastic bar of length L consisting of n constant sized linear elements subjected to compression [126]. The response curves of sufficiently small elements exhibit snap-back, and apparently the mesh refinement gives very different results, as shown in Figure 6.1a. Thus, the local damage theory suffers from spurious mesh sensitivity. Figure 6.1b shows distinctly that the values of dissipated energy due to the local modeling of damage declines as the mesh refines, and approximately converges to zero as n tends to infinity. This is practically unacceptable. On the other hand, a nonlocal regularization of the local model leads to mesh-insensitive results, as observed in Figure 6.1a and a finite energy dissipation, as shown in Figure 6.1b.

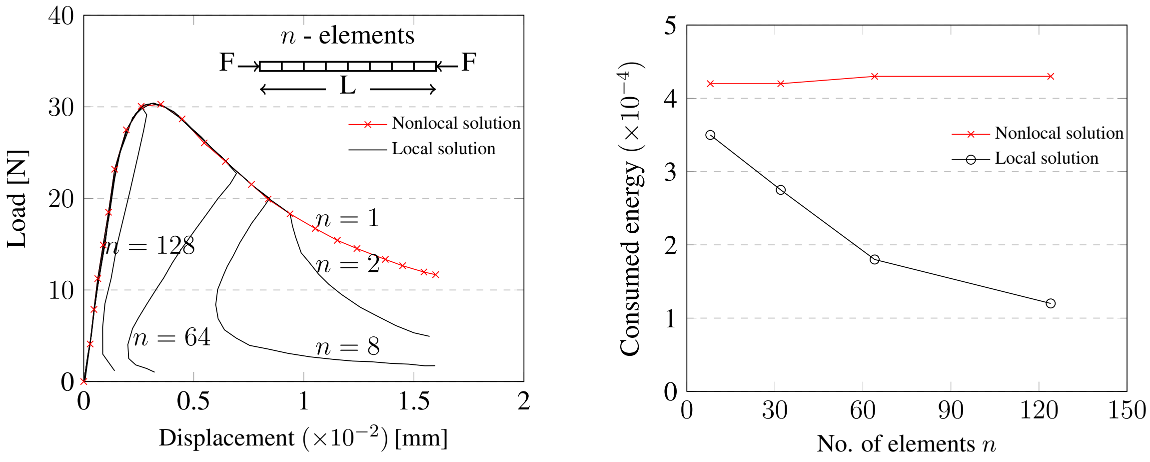

(a) Deformation curves **(b)** Dissipated energy

Figure 6.1: Local and nonlocal computations using bar elements (1D) [126]

On the other hand, a square plate with a central circular hole was examined using local and nonlocal averaging methods [52]. The plate was supported at one side and loaded with a prescribed displacement at the opposite side. But only the upper right quarter plate of various meshes has been considered in the analysis due to its symmetry. Figure 6.2 shows the total tensile forces plotted against the prescribed displacement of the upper edge of the quarter plate corresponding to the local and nonlocal modeling of the plate under a plane stress configuration. The mesh refinement obviously leads to mesh-dependent softening curves, as shown in Figure 6.2a. Additionally, damage distributions obtained in two different meshes from the local modeling are also depicted in Figure 6.3. As a consequence, vanishing energy dissipation due to damage causes apparently damage localization in an area with decreasing volume. By contrast, Figure 6.2b displays the numerical responses that are converged upon the mesh-refinement by the nonlocal

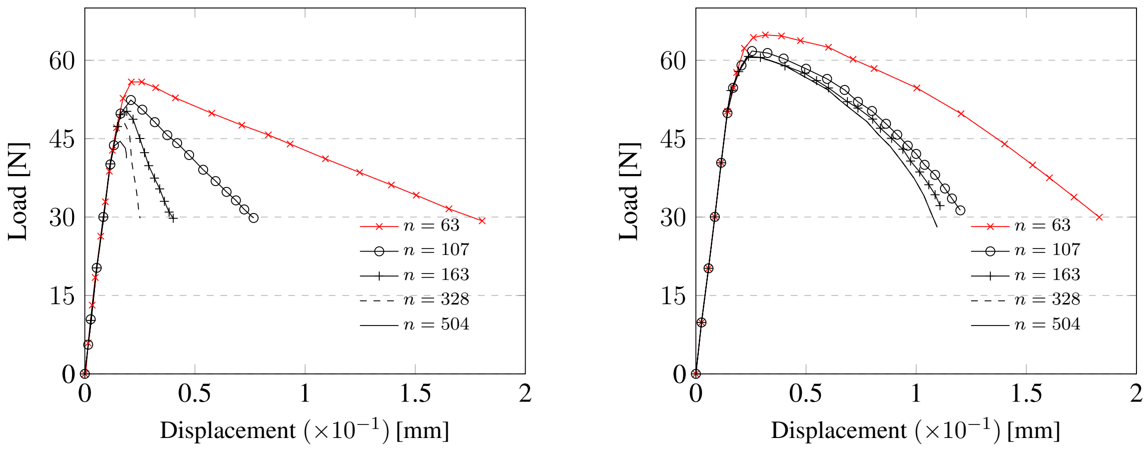

(a) Deformation curves **(b)** Deformation curves

Figure 6.2: Local and nonlocal computations using plane elements (2D) [52]

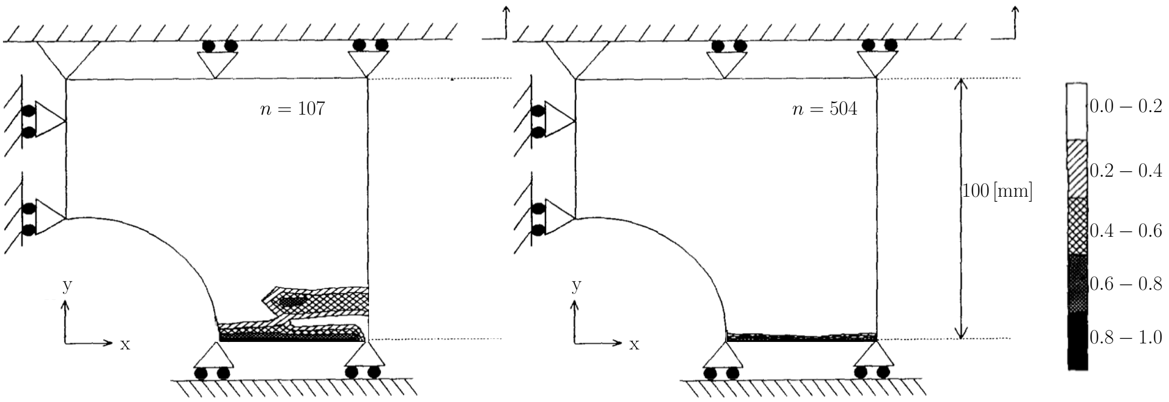

Figure 6.3: Local modeling of plate - damage distribution in two different meshes [52]

regularization of averaging strains.

As discussed, the above numerical examples of the bar and plane elements prove that the local softening damage models are incapable of describing the behavior of the localization phenomena of the chosen material realistically. Therefore, the nonlocal regularization of any local model must be done in order to describe the material behavior correctly. However, for a detailed analysis of failure mechanisms, the damage models must be, of course, in three-dimensional to have a better understanding of deformation behavior. Meanwhile, in the case of the localization problem, three-dimensional local damage models are not exceptional because they also lead to physically inconsistent results.

In order to visualize the localization of deformation into a volume equivalent to the mesh size, a one-dimensional bar of size 50 [mm] × 1 [mm] × 1 [mm] is analyzed under a pure tensile loading. The bar is discretized along the loading direction with n number of constant sized brick elements (Hex8). In order to trigger the damage localization, the initial damage threshold value κ_0 is only set to the center element of the bar, whereas the other elements in the rest of the

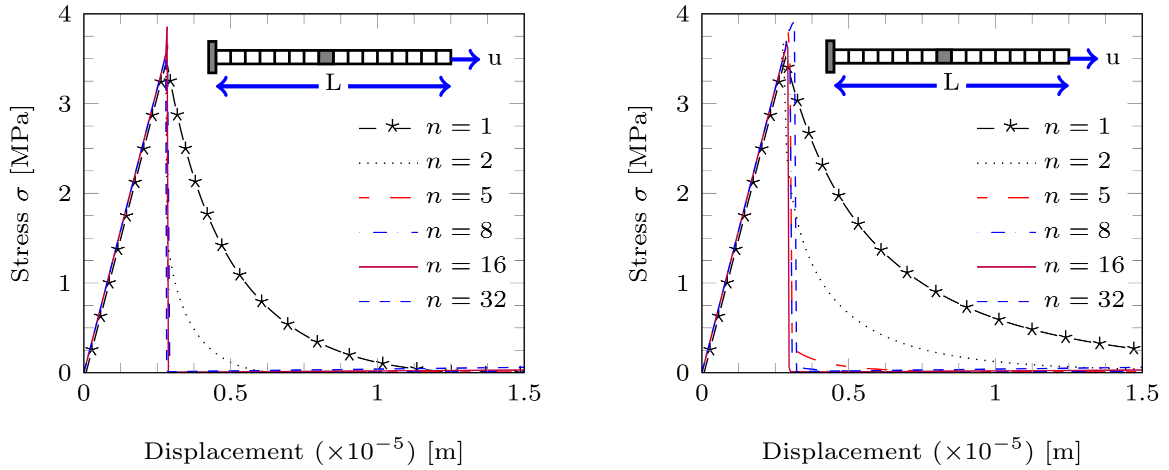

(a) Deformation curves for linear law **(b)** Deformation curves for proposed law

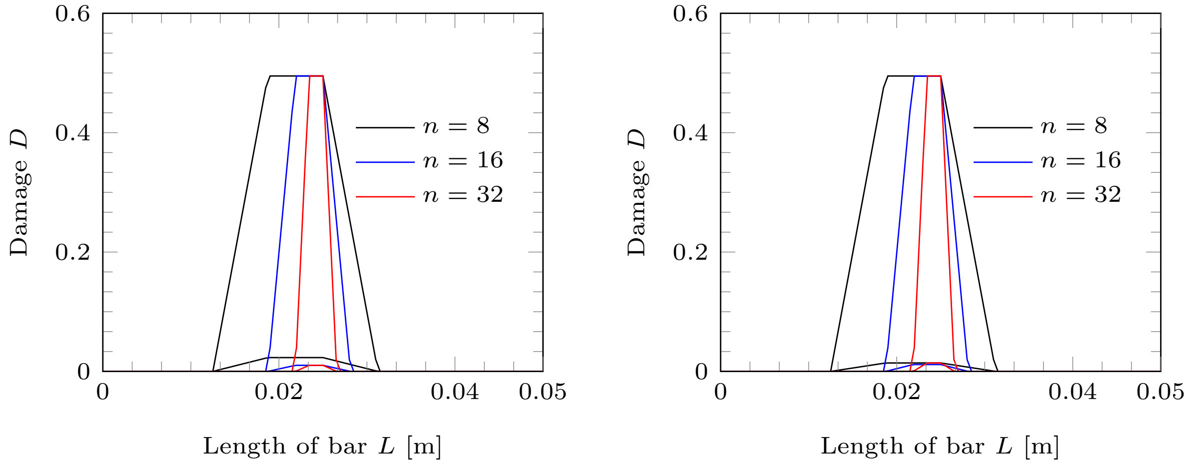

(c) Damage distribution for linear law **(d)** Damage distribution for proposed law

Figure 6.4: Local computations obtained using solid brick elements for linear law (4.30) and proposed law (4.50). (a,b) Stress-deformation curves and (c,d) Damage distributions at two different load steps

bar are allowed to behave elastically. The local modeling of material behavior is adopted using two different damage softening laws (4.30, 4.50) to display similar trending curves with salient features of the isotropic damage model discussed in Chapter 7. Adopted material parameters (Data 2) and model parameters are provided in Table 10.1.

The numerical stress-displacement curves for various meshes are depicted in Figure 6.4. The resulting curves corresponding to the use of the linear softening law and the proposed softening law are shown in Figures 6.4a and 6.4b respectively. It is undeniably observed in Figures 6.4a and 6.4b that the softening curves of every mesh are not converging and thus the non-unique responses are physically unacceptable any more. Moreover, the sudden drop of stresses to minimum residual stresses observed are due to the assumption of energy equivalence. Mesh-dependent solutions are obviously due to the fact that the localization of deformation occurs with the width equal to the mesh size, which can be undoubtedly viewed from Figures 6.4c and 6.4d. Thus, it displays typical differences of damage distributions obtained along the bar at two different load steps. It is indeed clear that the width of localization differs upon the mesh refinement and turns into the size of element in the respective mesh. As a consequence, it leads to unlimited small dissipation of energy for the damage growth in the material. Thus, the energy dissipation related to its deformation bandwidth is governed by the size of the element. Hence, regularization of the local damage models are very essential to avoid such material instabilities and other consequences in the numerical calculations.

6.2 Methods of regularization

In order to avoid such spurious results due to the mesh-dependency and the material instabilities in numerical investigations of the local continuum theories and to preserve the well-posedness of the boundary-value problems, the scheme of procedure used to introduce an internal length scale is called regularization [49, 111]. As discussed in Section 2.2, the regularization can be done in several ways such as:

- by limiting the size of finite element meshes (the Crack Band model [19] or the cell model [25]),
- by introducing the mesh-dependent softening modulus [111],
- by incorporating the couple stress and microplane-gradient tensors besides the stress and strain tensors to retain the ellipticity even after the onset of the material instability (Cosserat continuum [22, 49, 111]),
- by adding rate-dependent terms into the constitutive relations (artificial viscosity [49, 111]) in the problems of transient loadings, and
- by employing nonlocal damage theories [18, 52, 126] using an integral form with a nonlocal weight function or gradient dependent theories for the problems of transient analysis [92], plasticity theories [45, 49, 110], and damage theories [36, 44, 119].

Nevertheless, this section presents a summary of few successfully implemented popular techniques among the scientific community based on the research developments [18, 49, 111, 119].

6.2.1 Nonlocal integral method

Any nonlocal variable $\hat{\zeta}$ at any material point $\boldsymbol{x}$ can be written as the weighted average of its local counterpart ζ over its surrounding volume domain V [18, 89, 119, 126]:

$$\hat{\zeta}(\boldsymbol{x}) = \frac{1}{V}\int_V g(\boldsymbol{\xi})\zeta(\boldsymbol{x}+\boldsymbol{\xi})\, dV, \tag{6.22}$$

where the vectorial variable $\boldsymbol{\xi}$ represents the distance from the point $\boldsymbol{x}$ to a point in its vicinity over an infinitesimal volume dV and $g(\boldsymbol{\xi})$ is a certain weight function decaying smoothly with distance. This weight function can be assumed as, for example, any polynomial function or sometimes as Green function

$$g(\boldsymbol{\xi}) = \frac{1}{2\,l}\,\exp\left(-\frac{\boldsymbol{\xi}}{l}\right), \tag{6.23}$$

or popularly as Gaussian distribution function

$$g(\boldsymbol{\xi}) = \frac{1}{\left(l\,\sqrt{2\,\pi}\right)^{N_{\text{dim}}}}\,\exp\left(-\frac{\boldsymbol{\xi}^2}{2l^2}\right), \tag{6.24}$$

where N_{dim} is the number of spatial dimensions and the length parameter l governs the volume domain in which significant nonlocal interactions in the vicinity exist. It must therefore be interpreted as an internal length scale of the microstructure of the material. Furthermore, it is also often necessary that the weight function $g(\boldsymbol{\xi})$ must satisfy the normalizing condition

$$\frac{1}{V}\int_V g(\boldsymbol{\xi})\,dV = 1, \tag{6.25}$$

to ensure that the nonlocal operator does not alter a uniform field. Thus, the local continuum is resumed when $l \to 0$ as $\hat{\zeta}$ equals ζ for homogeneous strain states.

Thus, the application of the nonlocal integral method works well to provide mesh-insensitive results, as shown Figure 6.1a and also leads to the finite dissipation of energy, as observed in Figure 6.1b. The weakest portion of the material or the maximum damage can be easily identified by the maximum value of nonlocal variable field. Nonetheless, the implementation of the nonlocal integral models in FEM programs may be computationally ineffective because there is a need of global averaging and the linearization of such equations are not easily straightforward [122]. An appropriate way to such nonlocal integral models was later proposed by using the gradient terms [92, 110] and the application of gradient terms in the local damage models have also been formulated [119, 123], which will be discussed in the next section.

6.2.2 Gradient methods

6.2.2.1 Explicit gradient method

According to [89, 92, 110, 119], the nonlocal integral equation (6.22) can be approximated by a partial differential equation. Therefore, the corresponding local variable ζ of (6.22) is expanded using its Taylor series and is given by

$$\zeta(\boldsymbol{x},\boldsymbol{\xi}) = \zeta(\boldsymbol{x}) + \nabla^{(1)}\,\zeta(\boldsymbol{x})\,\cdot\,\boldsymbol{\xi}^{(1)} + \frac{1}{2!}\,\nabla^{(2)}\,\zeta(\boldsymbol{x})\,\cdot^{(2)}\,\boldsymbol{\xi}^{(2)} + \frac{1}{3!}\,\nabla^{(3)}\,\zeta(\boldsymbol{x})\,\cdot^{(3)}\,\boldsymbol{\xi}^{(3)}$$

$$+\frac{1}{4!}\nabla^{(4)}\zeta(\boldsymbol{x})\;\cdot^{(4)}\;\boldsymbol{\xi}^{(4)}+\dots, \tag{6.26}$$

where $\nabla^{(i)}$ and $\cdot^{(i)}$ represent the i^{th} order gradient operator and the i^{th} order inner product respectively; $\boldsymbol{\xi}^{(i)}$ refers to the i factor dyadic product $\boldsymbol{\xi}\boldsymbol{\xi}\dots\boldsymbol{\xi}$. Subsequent substitution of (6.26) in (6.22) yields the following form of nonlocal variable:

$$\begin{aligned}\hat{\zeta}(\boldsymbol{x}) &= \frac{1}{V}\int_V g(\boldsymbol{\xi})\zeta(\boldsymbol{x})\,dV+\frac{1}{V}\int_V g(\boldsymbol{\xi})\nabla\zeta(\boldsymbol{x})\;\cdot\;\boldsymbol{\xi}\,dV\\ &\quad+\frac{1}{2!V}\int_V g(\boldsymbol{\xi})\nabla^{(2)}\zeta(\boldsymbol{x})\;\cdot^{(2)}\;\boldsymbol{\xi}^{(2)}\,dV\\ &\quad+\frac{1}{3!V}\int_V g(\boldsymbol{\xi})\nabla^{(3)}\zeta(\boldsymbol{x})\;\cdot^{(3)}\;\boldsymbol{\xi}^{(3)}\,dV+\dots\end{aligned} \tag{6.27}$$

Assuming an isotropic influence of the averaging equation, the integrals of the odd terms in (6.27) vanish and further truncation of the higher order terms of Taylor series after quadratic term gives

$$\hat{\zeta}(\boldsymbol{x}) = \frac{1}{V}\int_V g(\boldsymbol{\xi})\zeta(\boldsymbol{x})\,dV+\frac{1}{2!V}\int_V g(\boldsymbol{\xi})\nabla^{(2)}\zeta(\boldsymbol{x})\;\cdot^{(2)}\;\boldsymbol{\xi}^{(2)}\,dV, \tag{6.28}$$

and subsequent transformation into the partial differential equation yields

$$\hat{\zeta}(\boldsymbol{x}) = \zeta(\boldsymbol{x})+c\,\nabla^2\,\zeta(\boldsymbol{x}), \tag{6.29}$$

where ∇^2 denotes the Laplacian operator and c is a coefficient, which can be determined by the weight function $g(\boldsymbol{\xi})$ and the averaging volume V. The above gradient equation (6.29) will be simply given in the form as follows:

$$\hat{\zeta} = \zeta+c\,\nabla^2\,\zeta, \tag{6.30}$$

where c can be defined as a gradient parameter of a length squared such that an internal length is incorporated in the gradient formulation. As the nonlocal variable $\hat{\zeta}(\boldsymbol{x})$ is explicitly depending on the Laplacian of the local variable in (6.30), this method is called as Explicit gradient method. However, the consequence of explicit dependence on the Laplacian of the local variable leads to complications in embedding (6.30) in the finite element analysis as it leads to the C^1 continuity requirements of displacement fields. Hence, such continuity requirements of equation (6.29) can be avoided by an implicit method [60, 121].

6.2.2.2 Implicit gradient method

According to [60, 121], equation (6.29) is differentiated twice and subsequently reordered as

$$\nabla^2\,\zeta(\boldsymbol{x}) = \nabla^2\,\hat{\zeta}(\boldsymbol{x})-c\,\nabla^4\,\zeta(\boldsymbol{x}), \tag{6.31}$$

and subsequently substituting (6.31) into (6.29) yields

$$\hat{\zeta}(\boldsymbol{x}) = \zeta(\boldsymbol{x}) + c\,\nabla^2\,\hat{\zeta}(\boldsymbol{x}) - c^2\,\nabla^4\,\zeta(\boldsymbol{x}). \tag{6.32}$$

Further simplification of (6.32) gives the gradient equation of second-order accuracy as similar to (6.30) as follows:

$$\hat{\zeta} - c\,\nabla^2\,\hat{\zeta} = \zeta, \tag{6.33}$$

where c denotes again the gradient parameter of the length squared as in the previous case. This parameter can also be considered as a dependent parameter on the local strain or damage level [67]. Though the above equation (6.33) treats the nonlocal variable $\hat{\zeta}$ as an independent variable implicitly, it enables a straightforward C^0-continuous finite element approximation. However, an additional boundary condition concerning the nonlocal variable $\hat{\zeta}$ becomes necessary to solve the averaging partial differential equation (6.33). From a mathematical point of view, the boundary can be specified in form of either a Neumann type or a Dirichlet type

$$\nabla\,\hat{\zeta}\cdot\boldsymbol{n} = \hat{\zeta}^{\mathrm{p}}_{\mathrm{n}} \quad \text{or} \quad \hat{\zeta} = \hat{\zeta}^{\mathrm{p}} \quad \text{on the boundary}\,\Gamma_{\mathrm{b}}, \tag{6.34}$$

where $\boldsymbol{n}$ denotes the external normal unit vector at every point in the boundary of consideration. Nevertheless, the physical interpretation of the additional boundary conditions is still unresolved. Therefore, according to [92, 110, 119], a simple natural boundary condition can be adopted as

$$\nabla\,\hat{\zeta}\cdot\boldsymbol{n} = 0, \tag{6.35}$$

at every point of the boundary. Thus, the assumption of the boundary condition (6.35) ensures that the average of the nonlocal variable $\hat{\zeta}$ over the entire domain equals that of its local counterpart ζ as the gradient vanishes [121, 123].

6.2.3 Phase-field method: A special case of gradient method

From the past two decades, the phase-field modeling of fracture has also become popular among the scientific community. Phase-field models and gradient-enhanced damage models seem to be dissimilar approaches to fracture problems [50]. However, both the approaches are the kinds of regularizing the fracture models.

According to the phase-field approaches in view of fracture mechanics concept, the basic idea is to approximate the sharp crack discontinuity Γ by a smeared surface Γ_{l} using a phase-field (crack field) variable $\hat{d}$, which describes the phase field within the range $0 \leq \hat{d} \leq 1$. Following the notations used in the nonlocal integral or gradient damage models discussed previously, the *hat* $(\hat{\cdot})$ here indicates the regularized/spatially averaged variable considered. Hence, $\hat{d} = 0$ represents the undamaged or intact state of the material, whereas $\hat{d} = 1$ denotes the fully damaged or broken material as similar to the definitions of commonly adopted damage variable in continuum damage mechanics. In a multi-dimensional setting, the discontinuity Γ is approximated by the functional Γ_{l}

$$\Gamma_{\mathrm{l}} = \int_V \gamma_{\mathrm{l}}\, dV = \int_V \frac{1}{4l}\big(\hat{d}^2 + 4l^2 \nabla\hat{d} \cdot \nabla\hat{d}\big)\, dV, \tag{6.36}$$

where γ_{l} is the crack surface density function and l the length scale parameter.

According to [50,64], if a volume V having an internal discontinuity boundary Γ_{d} is considered, then the potential energy Ψ_{pot} for the case of a discrete description of brittle fracture based on the Griffth's theory is given by

$$\Psi_{\mathrm{pot}} = \int_V \psi^{\mathrm{e}}(\boldsymbol{\varepsilon})\, dV + \int_{\Gamma_{\mathrm{d}}} \mathcal{G}_{\mathrm{c}}\, dA, \tag{6.37}$$

where $\psi^{\mathrm{e}}(\boldsymbol{\varepsilon})$ is the elastic energy density function of the infinitesimal strain tensor $\boldsymbol{\varepsilon}$; $\mathcal{G}_{\mathrm{c}}$ represents the fracture energy, which is the amount of energy dissipated during the fracture process upon the creation of a unit of fracture surface. In order to regularize crack topology, the work required to create a unit crack surface area is expressed by

$$\int_{\Gamma_{\mathrm{d}}} \mathcal{G}_{\mathrm{c}}\, dA \approx \int_V \mathcal{G}_{\mathrm{c}}\, \gamma_{\mathrm{l}}(\hat{d},\nabla\hat{d})\, dV, \tag{6.38}$$

as a volume integral in terms of the phase-field variable $\hat{d}$ and the fracture energy $\mathcal{G}_{\mathrm{c}}$. Now, as similar to damage mechanics, the evolution of phase-field variable has been related to the growth of crack so as to model the loss of stiffness after the peak stress. Hence, a degradation function $h(\hat{d})$ is introduced like the damage evolution laws adopted in the damage models. In addition, $h(\hat{d})$ must satisfy certain conditions [108] to ensure damage propagation and limit the value of $\hat{d}$ by an upper bound (equal to 1). In most models, $h(\hat{d})$ is adopted as a quadratic polynomial [50] as follows:

$$h(\hat{d}) = (1 - \hat{d})^2. \tag{6.39}$$

This function now will enter into the elastic energy density function to represent the damaged state [27], which is given by

$$\psi^{\mathrm{e}}(\boldsymbol{\varepsilon},\hat{d}) = h(\hat{d})\, \psi_0(\boldsymbol{\varepsilon}) \tag{6.40}$$

This formulation is further refined to consider the additive decomposition of elastic energy of the undamaged state $\psi_0(\boldsymbol{\varepsilon})$ into a damaged part and an intact part [109], i.e $\psi_0(\boldsymbol{\varepsilon}) = \psi_0^{\mathrm{d}}(\boldsymbol{\varepsilon}) + \psi_0^{\mathrm{i}}(\boldsymbol{\varepsilon})$, in such a way that the influence of degradation is only on the damaged part:

$$\psi^{\mathrm{e}}(\boldsymbol{\varepsilon},\hat{d}) = h(\hat{d})\, \psi_0^{\mathrm{d}}(\boldsymbol{\varepsilon}) + \psi_0^{\mathrm{i}}(\boldsymbol{\varepsilon}) \tag{6.41}$$

Substituting equations (6.38) and (6.41) into equation (6.37) gives the total potential energy of the smeared formulation for brittle fracture Ψ_{pot} and subsequently minimizing the resulting total energy Ψ_{pot} [108] lead to the equilibrium equations:

$$\nabla \cdot \boldsymbol{\sigma} = \mathbf{0}, \tag{6.42}$$

$$h'(\hat{d})\mathcal{H} + \frac{\mathcal{G}_{\text{c}}}{2l}\left(\hat{d} - 4l^2\nabla^2\hat{d}\right) = 0, \tag{6.43}$$

along with boundary conditions $\boldsymbol{n}\cdot\boldsymbol{\sigma} = \bar{\boldsymbol{t}}, \boldsymbol{u} = \bar{\boldsymbol{u}}, \boldsymbol{n}\cdot\nabla\hat{d} = 0$. Herein, $\bar{\boldsymbol{t}}$ and $\bar{\boldsymbol{u}}$ are the prescribed boundary traction and displacements receptively [50]; $\mathcal{H}$ denotes the history variable similar to κ used in the damage models. Thus, for comparison, $\mathcal{H}$ can be replaced by κ. Moreover, according to thermodynamics, the Cauchy stress $\boldsymbol{\sigma}$ and the thermodynamically associated damage energy release rate $Y_{\hat{d}}$ of phase-field models can be obtained by differentiating equation (6.41) w.r.t $\boldsymbol{\varepsilon}$ and $\hat{d}$ respectively as follows:

$$\boldsymbol{\sigma} = \frac{\partial\psi^{\text{e}}}{\partial\boldsymbol{\varepsilon}} = h(\hat{d})\,\frac{\partial\psi_0^{\text{d}}}{\partial\boldsymbol{\varepsilon}} + \frac{\partial\psi^{\text{i}}}{\partial\boldsymbol{\varepsilon}}, \tag{6.44}$$

$$Y_{\hat{d}} = -\frac{\partial\psi^{\text{e}}}{\partial\hat{d}} = -h'(\hat{d})\,\psi_0^{\text{d}}(\boldsymbol{\varepsilon}) = -h'(\hat{d})\,\kappa. \tag{6.45}$$

Therefore, the history field κ reads

$$\kappa = \mathcal{H} = \max\psi_0^{\text{d}}(\boldsymbol{\varepsilon}). \tag{6.46}$$

6.2.3.1 Similar diffusion (averaging) equation

The diffusion (averaging) equation (6.43) of the phase-field models with the history field (6.46) is rearranged as follows:

$$\hat{d} - 4l^2\nabla^2\hat{d} = d, \tag{6.47}$$

where $d = -\frac{2lh'(\hat{d})\kappa}{\mathcal{G}_{\text{c}}}$ represents the local damage/crack field and $c = (2l)^2$ is equivalent to the gradient parameter on comparing the above diffusion equation (6.47) of phase-field approach with the gradient equation (6.33) of gradient damage models. Thus, equation (6.47) implies that it is the implicit form of the gradient damage equation (6.33), if d has been considered as a local damage variable for nonlocal enrichment using gradient method, i.e., $\hat{\zeta} = \hat{d}$.

6.2.3.2 Differences in broadening zone

If the damage models consider the principle of strain equivalence for describing the constitutive behavior of the material, the degradation function typically will look like

$$h(\hat{d}) = 1 - \hat{d}. \tag{6.48}$$

Subsequent substitution of equation (6.48) into (6.44) yields

$$Y_{\hat{d}} = \kappa. \tag{6.49}$$

As a result, $Y_{\hat{d}}$ does not vanish even when $\hat{d} = 1$ at complete loss of integrity. It means that the broadening of damage zone is continued. On the other hand, if the phase-field models consider the degradation function (6.39), then substitution of the same equation into (6.44) results in

$$Y_{\hat{d}} = 2(1 - \hat{d})\,\kappa. \tag{6.50}$$

Here, the complete loss of integrity when $\hat{d} = 1$ makes the damage energy release rate (6.50) equal to zero and thus, it ensures a constant bandwidth in the wake of the crack tip. Nonetheless, the broadening of the damage zone can be avoided by adopting the strategy of vanishing function as the internal length scale in the gradient-damage modeling [67], which resembles the constant bandwidth of the phase-field approach discussed above.

6.2.3.3 Similar broadening zone

Nevertheless, if the principle of energy equivalence is adopted to describe the constitutive behavior of materials, as will be adopted in the present work, then the degradation function matches the degradation polynomial function (6.39) of phase-field models. Therefore, in this case, the resulting damage energy release rate $Y_{\hat{d}}$ becomes

$$Y_{\hat{d}} = 2(1 - \hat{d})\,\kappa, \tag{6.51}$$

as similar to equation (6.50). Thus, the gradient-damage models based on the principle of energy equivalence lead to a constant bandwidth during the complete loss of integrity as it is the case of phase-field models with quadratic polynomial degradation.

Consequently, the difference between the gradient-enhanced damage models and the phase-field models to brittle fracture is only in their interpretation, but both are almost identical in the mathematical sense. It can be observed that the right-hand side term of the diffusion equation (6.47) is interpreted as the local damage field of the gradient damage equation (6.33). On the other hand, phase-field models naturally incorporates an internal length scale into the local damage field [50] and hence, they are only meaningful with the incorporation of the internal length scale as it can not be taken as zero.

Thus, both the phase-field models and the gradient-damage models are mathematically identical in view of application but having different formulations as the phase-field models intrinsically offer a crucial regularization through its gradient averaging or diffusion equation.

However, the present work considers the extension of the local continuum damage models by incorporating the implicit gradient method, as this method has been successfully implemented for intended results under various loading environments [22, 42, 86, 116, 145].

7 Isotropic Damage Model

This chapter deals with an isotropic damage coupled with the elastic deformation behavior of the material, which is initially developed in the research project. As for concrete, several continuum damage models based on isotropic and anisotropic damage are available in literature. Most of the coupled plastic damage or elastic damage models consider two damage variables for tension and compression, since concrete exhibits ductile behavior in compression and brittle behavior in tension. In such cases, the effective stresses are decomposed into positive (tension) and negative (compression) stresses using the spectral decomposition [51]. On the other hand, some other models developed using two different loading surfaces each for tension and compression to characterize the distinct behavior of concrete [106]. Instead of two different damage variables or two damage loading surfaces, the model uses single damage variable and single loading surface for characterizing the different behavior of concrete in tension and compression. The evolution of isotropic damage D is driven by a history deformation parameter κ. Thereupon κ is related to a damage equivalent strain ϵ, which is due to Lubliner failure criterion [98]. The damage evolution law exhibits exponential softening behavior based on modified exponential softening (7.6).

7.1 Constitutive modeling of damage

The stress-strain relation for the elastic-damage material behavior can be written using the principle of energy equivalence as follows:

$$\boldsymbol{\sigma} = (1 - D)^2 \mathbb{H} : \boldsymbol{\varepsilon}, \tag{7.1}$$

where $\boldsymbol{\sigma}$ and $\boldsymbol{\varepsilon}$ are the second-order Cauchy stress tensor and the strain tensor respectively; $\mathbb{H}$ is the fourth-order elasticity tensor of the undamaged material. The damage variable D is a scalar measure of effective isotropic damage. Inelastic strain evolution is not considered. Thus, the strain-softening behavior of concrete is described by the constitutive law (7.1).

7.1.1 Damage evolution law

The damage variable D is generally considered to be driven by a history deformation parameter κ, which is described as a maximum deformation of a material occurred during tension or compression loading path. Therefore, κ is a monotonically increasing parameter during loading/unloading processes and the accumulation of damage. Hence, as proposed in Section 4.3.6, the damage evolution law (4.50) exhibiting an exponential softening is explicitly expressed as a function of κ as follows (which is given here once again for clarity):

$$D(\kappa) = 1 - \left[\frac{\kappa_0}{\kappa}\right]^{\beta_1} e^{-\beta_2 \left[\frac{\kappa - \kappa_0}{\kappa_0}\right]}, \tag{7.2}$$

where κ_0 is an initial threshold to set the initial elastic domain below which there is no damage. β_1 and β_2 are model parameters characterizing the softening behavior of the material after the peak stress. β_1 controls the initial growth of damage and β_2 ensures the later damage growth and its large extent. Thus, D is limited to the range $0 \leq D \leq 1$ at any case.

7.1.2 Damage equivalent strain

In the framework of continuum damage mechanics, it is obvious that κ is often related to a scalar measure of deformation state, a damage equivalent strain ϵ at a point of continuum considered locally. There are several alternatives for determining the local measure ϵ. In this work, ϵ is defined as a unified damage equivalent strain for describing tensile cracking as well as crushing failure and is expressed by,

$$\epsilon = \frac{1}{(1-\alpha_\mathrm{L})E}\Big(\alpha_\mathrm{L} I_1 + \sqrt{3J_2} + \beta_\mathrm{L} H \sigma_\mathrm{max}\Big), \tag{7.3}$$

where I_1 and J_2 are the first invariant of the elastically predicted stress tensor $\boldsymbol{\sigma}^\mathrm{p}$ and the second invariant of the deviatoric part of $\boldsymbol{\sigma}^\mathrm{p}$ respectively; σ_max is the maximum principal stress of $\boldsymbol{\sigma}^\mathrm{p}$ and H is a Heaviside function, where $H = 1$ if $\sigma_\mathrm{max} > 0$, else $H = 0$. The parameters α_L and β_L depend on the uniaxial tensile and compressive strengths of concrete as defined in [98].

The expression (7.3) is inspired from the failure criterion of Lubliner [94, 98, 149] and slightly transformed in order to express the damage criterion in strain space, which will be discussed in the following section.

7.1.3 Damage surface criterion

As similar to yield or failure surfaces of materials, a function is generalized here to limit the initial elastic domain and also to allow the growth of the effective damage. The damage criterion f is conveniently used to relate κ to the unified damage equivalent strain ϵ. Therefore, the associated single damage loading surface is written as

$$f = \epsilon - \kappa, \tag{7.4}$$

with κ as a maximum threshold value reached during tensile/compression loading path. Thus, it is defined by

$$\kappa = \mathrm{Sup}\Big[\kappa_0, \max \quad \epsilon\Big], \tag{7.5}$$

where the initial threshold value κ_0, which is determined from the thresholds of tension $\kappa_{0\mathrm{t}}$ and compression $\kappa_{0\mathrm{c}}$ by $\kappa_0 = \kappa_{0\mathrm{t}} H + \kappa_{0\mathrm{c}}(1-H)$ to limit the initial elastic domain. In addition, the above expression (7.5) can also be expressed as in (7.6) in order to account for the unilateral behavior of concrete by introducing two independent history variables κ_t and κ_c for κ:

$$\kappa_\mathrm{t} = \mathbf{Sup}\Big[\kappa_{0\mathrm{t}}, \max \quad \epsilon\Big] \;\; ; \;\; \kappa_\mathrm{c} = \mathbf{Sup}\Big[\kappa_{0\mathrm{c}}, \max \quad \epsilon\Big], \tag{7.6}$$

$$\kappa = \kappa_\mathrm{t} H + \kappa_\mathrm{c}(1 - H). \tag{7.7}$$

Remarks

The expression (7.7) along with the prescribed initial damage threshold value κ_0 is more than sufficient to capture the initial elasticity domain as well as the failure surface under pure tension and pure compression. But it overestimates the elastic domain in the case of complex load conditions, especially in the compression predominant regions. Therefore, an additional parameter δ_r is introduced to deactivate tensile domination where the compression is predominant. Thus, the expression (7.7) and corresponding initial threshold are modified as

$$\kappa = \kappa_\mathrm{t} H(1 - \delta_\mathrm{r}) + \kappa_\mathrm{c}(1 - H + \delta_\mathrm{r}), \tag{7.8}$$

$$\kappa_0 = \kappa_{0\mathrm{t}} H(1 - \delta_\mathrm{r}) + \kappa_{0\mathrm{c}}(1 - H + \delta_\mathrm{r}), \tag{7.9}$$

where δ_r is an activation parameter and it is defined as

$$\delta_\mathrm{r} = \begin{cases} 1, & \text{if } \; 0.10 \geq r > 0 \\ 0, & \text{else.} \end{cases} \tag{7.10}$$

$$r = \frac{\sum_{\mathrm{i}=1}^{3} \langle \sigma_\mathrm{i} \rangle}{\sum_{\mathrm{i}=1}^{3} |\sigma_\mathrm{i}|}, \tag{7.11}$$

where r is the triaxial weight factor adopted [94] and its range lies $0 \leq r \leq 1$. For pure tension, $r = 1$ and for compression, $r = 0$.

Similarly, the model parameters used in (7.2) are written for various load paths as follows:

$$\beta_\mathrm{j} = \beta_\mathrm{jt} H(1 - \delta_\mathrm{r}) + \beta_\mathrm{jc}(1 - H + \delta_\mathrm{r}), \;\; \text{for j} = 1{,}2. \tag{7.12}$$

The evolution of history parameter κ can mathematically be expressed by the Kuhn-Tucker loading/unloading relations [28, 52]:

$$f \leq 0, \qquad \dot{\kappa} \geq 0, \qquad f\dot{\kappa} = 0, \tag{7.13}$$

where $\dot{(\;)}$ represents the derivative of any variable with respect to time t. The function $f < 0$ means that the material response remains linear elastic, as there is no damage development. The damage initiates when $f = 0$, since this is the merely dissipative mechanism considered in the present model for the brittle failure of concrete. During the damage evolution, the consistency condition $\dot{f} = 0$ must always be valid. Moreover, the damage remains constant if $\dot{\kappa} = 0$.

7.1.4 Consistency of thermodynamics

In general, the process of undergoing deformation of any material is a thermodynamic irreversible one [111]. Therefore, any constitutive modeling of a material behavior must be consistent with the principles of thermodynamics. Thus, the thermodynamic consistency of the proposed model is discussed in this section.

According to the thermodynamic laws, a generalized form of the Clausius-Duhem inequality for any allowable dissipation process is expressed as similar to (3.40) as

$$\boldsymbol{\sigma} : \dot{\boldsymbol{\varepsilon}} - \dot{\psi} + \rho \dot{\eta} T - \boldsymbol{q} \frac{\nabla T}{T} \geq 0, \tag{7.14}$$

where ρ, η and T refer to the material density, the entropy density per unit mass and the absolute temperature respectively. $\boldsymbol{q}$ is the heat flux. Within this context, the Helmholtz free energy ψ (per unit volume) can be written in terms of internal state variables characterizing the nonlinear deformation behavior of concrete both in tension and compression based on the principle of energy equivalence as follows:

$$\psi(\boldsymbol{\varepsilon}, D(\kappa)) = \frac{1}{2}(1 - D)^2 \boldsymbol{\varepsilon} : \mathbb{H} : \boldsymbol{\varepsilon}. \tag{7.15}$$

Taking time derivative of equation (7.15), the rate of change of free energy can be expressed as

$$\dot{\psi} = \frac{\partial \psi}{\partial \boldsymbol{\varepsilon}} \dot{\boldsymbol{\varepsilon}} + \frac{\partial \psi}{\partial D} \frac{\partial D}{\partial \kappa} \dot{\kappa}. \tag{7.16}$$

For any isothermal and adiabatic mechanical dissipation process ($\dot{T} = 0$ and $\boldsymbol{q} = 0$), the Clausius-Duhem inequality (7.14) reduces to

$$\boldsymbol{\sigma} : \dot{\boldsymbol{\varepsilon}} - \dot{\psi} \geq 0. \tag{7.17}$$

Substitution of equation (7.16) into equation (7.17) and then simplification gives

$$\left(\boldsymbol{\sigma} - \frac{\partial \psi}{\partial \boldsymbol{\varepsilon}}\right) : \dot{\boldsymbol{\varepsilon}} - \frac{\partial \psi}{\partial D} \frac{\partial D}{\partial \kappa} \dot{\kappa} \geq 0, \tag{7.18}$$

where $-\frac{\partial \psi}{\partial D}$ is the damage energy release rate, which remains always positive during the damage growth. It is denoted by Y and defined as

$$Y = -\frac{\partial \psi}{\partial D} = (1 - D) \boldsymbol{\varepsilon} : \mathbb{H} : \boldsymbol{\varepsilon}. \tag{7.19}$$

For any admissible process of energy dissipation by following equation (7.18), the following relations can be easily obtained as

$$\boldsymbol{\sigma} - \frac{\partial \psi}{\partial \boldsymbol{\varepsilon}} = 0, \tag{7.20}$$

$$Y \dot{D} \geq 0, \tag{7.21}$$

$$Y \frac{\partial D}{\partial \kappa} \dot{\kappa} \geq 0 \quad \text{or} \quad Y \left(\frac{\partial D}{\partial \kappa_{\mathrm{t}}} \dot{\kappa}_{\mathrm{t}} + \frac{\partial D}{\partial \kappa_{\mathrm{c}}} \dot{\kappa}_{\mathrm{c}} \right) \geq 0. \tag{7.22}$$

Thus, the non-negativity of equations (7.21) and (7.22) prove that the damage process respects the Clausius-Duhem inequality.

7.1.5 Numerical algorithm

In this section, the scheme of a numerically updating algorithm of the constitutive equations of the model is presented in order to enable for the possible implementation into the finite element (FE) codes. It is important that the history of strains is assumed to be given as input from the FE codes. The numerical scheme is provided in Algorithm 1.

Algorithm 1 (Algorithm of the isotropic damage model)

Input: Number of steps n, time t, history variables $\kappa_{0\mathrm{c}}$, $\kappa_{0\mathrm{t}}$ and material parameters (cf. table 10.1)

Output: D_{n+1} and σ_{n+1} at current time step t_{n+1}

```
[1.1]  At $t_{n=0}$, damage is $D_{n=0} = 0$
[1.2]  Strain update at Gauss points at $t_{n+1}$
[1.3]      $\boldsymbol{\varepsilon}_{n+1} = \boldsymbol{\varepsilon}_n + \Delta\boldsymbol{\varepsilon}$
[1.4]  Evaluate elastic predictor
[1.5]      Elastic stress $\boldsymbol{\sigma}^{\mathrm{p}}_{n+1} = \mathbb{H} : \boldsymbol{\varepsilon}_{n+1}$ at $t_{n+1}$
[1.6]      Compute $I_1$, $J_2$ and $\sigma_{\max}$ of $\boldsymbol{\sigma}^{\mathrm{p}}_{n+1}$
[1.7]      $\epsilon_{n+1}$ and threshold parameters at $t_{n+1}$ are obtained from (7.3), (7.6)-(7.9) respectively.
[1.8]  Check for damage admissibility
[1.9]      if $f_{n+1} = \epsilon_{n+1} - \kappa_{n+1} \leq 0$
[1.10]     then
[1.11]         $\boldsymbol{\sigma}_{n+1} = \boldsymbol{\sigma}^{\mathrm{p}}_{n+1}$
[1.12]         $D_{n+1} = D_n = 0$
[1.13]         exit
[1.14]     else if $f_{n+1} = 0$ and $\kappa_{n+1} - \kappa_n \geq 0$
[1.15]     then compute damage corrector
[1.16]         Compute $D_{n+1}$ (7.2) and update $\sigma_{n+1}$ (7.1)
[1.17]     exit
```

During the process of damage, it is verified that every current state of continuum respects the Kuhn-Tucker loading/unloading conditions (7.13).

7.1.6 Consistent tangent modulus

The consistent tangent stiffness is required for the successful implementation of the present damage model into the finite element codes. Therefore, the tangent stiffness modulus, which is consistent with the integration algorithm, is developed by linearizing the update equation (7.1).

If the current state of stress $\boldsymbol{\sigma}_{n+1}$ at t_{n+1} lies inside the elastic domain (i.e $f < 0$), then the corresponding elastic-damage tangent modulus $\mathbb{H}_{\mathrm{ed}}$ or the effective tangent modulus $\tilde{\mathbb{H}}$ is simply provided by

$$\mathbb{H}_{\mathrm{ed}} = \tilde{\mathbb{H}} = (1 - D_{n+1})^2\, \mathbb{H}. \tag{7.23}$$

The above tangent modulus (7.23) is valid when the current state is on the damage loading surface and the elastic unloading occurs. During the process of damage evolution, $\boldsymbol{\sigma}_{n+1}$ is the solution of the nonlinear equation, since the strain-softening occurs due to the damage growth. Therefore, the system of nonlinear equations is linearized to estimate the corresponding elastic-damage tangent modulus $\mathbb{H}_{\mathrm{ed}}$ or the effective tangent modulus $\tilde{\mathbb{H}}$ and it is obtained as

$$\mathbb{H}_{\mathrm{ed}} = \tilde{\mathbb{H}} = \left.\frac{\partial \boldsymbol{\sigma}}{\partial \boldsymbol{\varepsilon}}\right|_{n+1} = (1 - D_{n+1})^2\, \mathbb{H} - 2(1 - D_{n+1})\, \mathbb{H}\, \boldsymbol{\varepsilon}_{n+1} \left.\frac{\partial D}{\partial \boldsymbol{\varepsilon}}\right|_{n+1}, \tag{7.24}$$

where

$$\left.\frac{\partial D}{\partial \boldsymbol{\varepsilon}}\right|_{n+1} = \left.\frac{\partial D}{\partial \kappa}\right|_{n+1} \left.\frac{\partial \kappa}{\partial \boldsymbol{\varepsilon}}\right|_{n+1}. \tag{7.25}$$

7.2 Gradient enhancement of damage

In this section, how the gradient enhancement of the local continuum model from a general concept of nonlocal continua is achieved is presented. As the presence of damage variable helps in modeling the strain-softening behavior of the material, this quantity is first considered for the nonlocal enrichment. Thus, the nonlocal quantity $\hat{D}$ based on the definition (6.22) is defined as

$$\hat{D} = \frac{1}{V} \int_V g(\boldsymbol{\xi}) D(\boldsymbol{x} + \boldsymbol{\xi}) dV. \tag{7.26}$$

As discussed in Section 6.2.2.2, the above integral (7.26) is approximated by a partial differential equation according to [110, 121] and is given by

$$\hat{D} - l_{\mathrm{c}}^2 \nabla^2 \hat{D} = D, \tag{7.27}$$

where l_{c} is the characteristic length scale, which is used to regularize the localization of damage and ∇^2 is the Laplacian operator. An appropriate boundary condition (either the Dirichlet boundary or the Neumann boundary) must be used to solve the partial differential equation (7.27). Nevertheless, the present work adopts a natural boundary condition at every point of the boundary as provided below:

$$\nabla \hat{D} \cdot \boldsymbol{n} = 0. \tag{7.28}$$

The boundary condition (7.28) ensures that the average of damage $\hat{D}$ over the entire domain equals that of local damage D [123, 144]. As a consequence, the nonlocal damage variable $\hat{D}$ enters into the constitutive law (7.1) and therefore, the stress-strain relation can be rewritten as follows:

$$\boldsymbol{\sigma} = (1 - \hat{D})^2 \mathbb{H} : \boldsymbol{\varepsilon}. \tag{7.29}$$

As a result, the local damage variable D reflected in equations (7.14), (7.19) and (7.23) is replaced by $\hat{D}$. The Kuhn-Tucker loading/unloading relations (7.13) still remain valid. The thermodynamic consistency is respected as well, which is discussed in the following section.

7.2.1 Thermodynamic consistency

As a result of gradient enhancement of damage variable D and also due to the consequent introduction of $\hat{D}$ in the constitutive law, the rate of change of free energy expressed in (7.16) becomes

$$\dot{\psi} = \frac{\partial \psi}{\partial \boldsymbol{\varepsilon}} \dot{\boldsymbol{\varepsilon}} + \frac{\partial \psi}{\partial \hat{D}} \dot{\hat{D}}. \tag{7.30}$$

Under the assumption of the isothermal and adiabatic processes, substituting (7.30) into (7.17) and subsequent simplification yields

$$\left(\boldsymbol{\sigma} - \frac{\partial \psi}{\partial \boldsymbol{\varepsilon}} \right) : \dot{\boldsymbol{\varepsilon}} + Y \dot{\hat{D}} \geq 0, \tag{7.31}$$

where the damage energy release rate Y gets

$$Y = -\frac{\partial \psi}{\partial \hat{D}} = (1 - \hat{D}) \boldsymbol{\varepsilon} : \mathbb{H} : \boldsymbol{\varepsilon}. \tag{7.32}$$

Consequently, the non-negativity of equations (7.21) and (7.22) combines and results in

$$Y \dot{\hat{D}} \geq 0, \tag{7.33}$$

such that the damage process respects the Clausius-Duhem inequality.

7.3 Gradient enhancement of equivalent strain

As the averaging of damage variable leads to spurious residual stresses and expansion of the softening zone across the bar [18] and also the damage growth in the present model is driven by the equivalent strain ϵ, the averaging procedure is therefore applied to ϵ. Consequently, the nonlocal quantity $\hat{\epsilon}$ is defined as

$$\hat{\epsilon} = \frac{1}{V}\int_V g(\boldsymbol{\xi})\epsilon(\boldsymbol{x}+\boldsymbol{\xi})dV. \tag{7.34}$$

The above integral (7.34) is approximated by a partial differential equation according to [110, 121] and is given by

$$\hat{\epsilon} - l_{\mathrm{c}}^2\nabla^2\hat{\epsilon} = \epsilon, \tag{7.35}$$

where l_{c} and ∇^2 are defined as in the previous Section 7.2. In the present case, a natural boundary condition at every point of the boundary adopted is given below:

$$\nabla\hat{\epsilon}\cdot\boldsymbol{n} = 0. \tag{7.36}$$

The boundary condition ensures that the average of nonlocal equivalent strain $\hat{\epsilon}$ over the entire domain equals that of the local equivalent strain ϵ [123].

Hence, κ is related to the distributed damage strain, i.e., the nonlocal equivalent strain $\hat{\epsilon}$ in the gradient enhanced damage model. Subsequently, the damage criterion (7.4) is rewritten as follows:

$$f = \hat{\epsilon} - \kappa. \tag{7.37}$$

The Kuhn-Tucker loading/unloading relations (7.13) and the equations related to the thermodynamic consistency discussed in Section 7.1.4 even so remain valid. Assuming the length scale $l_{\mathrm{c}} = 0$, the local continuum model is resumed, as $\hat{\epsilon} = \epsilon$.

8 Coupled Inelastic-isotropic Damage Model

As will be discussed in Chapter 10, the simplified isotropic damage model based on purely elastic deformation behavior has limitations in capturing the permanent strains (inelastic strains) during unloading conditions. Thus, the unloading of the model leaves zero residual strains, thereby only causing the stiffness degradation in tension or compression. On the other hand, it is witnessed from the experimental studies on concrete [72, 84, 104, 113] that concrete exhibits inelastic/permanent deformation to some extent under direct cyclic loading or reverse cyclic loading even though this inelastic deformation is not as large as that observed in ductile materials like steel. Thence, the incorporation of inelastic deformation behavior is unavoidable to model the deformation behavior of concrete correctly. Therefore, this chapter describes coupling of inelastic deformation through Lubliner-Lee failure criterion [93, 94] with the isotropic damage behavior of concrete through a damage loading surface discussed in the previous Chapter 7.

8.1 Constitutive relations

Although the physical significance of inelastic or irreversible deformations in concrete is not well-described so far, several failure theories postulate inelastic strain evolution for concrete. These include single failure surfaces such as Rankine criterion, Modified-Rankine criterion, Drucker-Prager criterion, Willam-Warnke criterion [148], Ehlers surface criterion [58], Lubliner criterion [98], Lubliner-Lee failure criterion [93, 94] and multi-surface failure theories [22, 41, 115]. But the yield criterion of Lubliner *et al.* [98], which was later extended by Lee and Fenves [93, 94], found to be successful in modeling concrete behavior under both monotonic and cyclic loading conditions. This model uses one loading surface that couples plasticity and isotropic damage by effective plastic strain. The isotropic damage variable is described by means of two damage variables in multiplicative manner in order to take the crack opening/closing effects into account.

However, this section describes the model of Lee and Fenves [93,94] considered for the inelastic evolution of strains that is coupled with the unilateral description of isotropic damage. Isotropic linear hardening is considered in tension as well as compression [149].

8.1.1 Inelastic deformation

In the theory of inelasticity under small deformations, the total strain tensor ε is decomposed into the elastic part of strain $\varepsilon^{\mathrm{el}}$ and the inelastic part of strain $\varepsilon^{\mathrm{in}}$ such that:

$$\varepsilon = \varepsilon^{\mathrm{el}} + \varepsilon^{\mathrm{in}}. \tag{8.1}$$

Subsequently, by taking time derivative of equation (8.4), the total strain rate $\dot{\varepsilon}$ can be written as

$$\dot{\varepsilon} = \dot{\varepsilon}^{\text{el}} + \dot{\varepsilon}^{\text{in}}, \tag{8.2}$$

where $\dot{\varepsilon}^{\text{el}}$ and $\dot{\varepsilon}^{\text{in}}$ refer to the rates of the elastic and inelastic strain tensors respectively.

8.1.2 Constitutive law

After coupling of the inelastic strains into the isotropic damage model based on the energy equivalence, the generalized Hook's law (7.1) becomes as

$$\boldsymbol{\sigma} = \mathbb{M}^{-1} : \mathbb{H} : \mathbb{M}^{-T} : \boldsymbol{\varepsilon}^{\text{el}} = \mathbb{M}^{-1} : \mathbb{H} : \mathbb{M}^{-T} : (\boldsymbol{\varepsilon} - \boldsymbol{\varepsilon}^{\text{in}}), \tag{8.3}$$

where $\mathbb{H}$ is the fourth-order undamaged elastic stiffness tensor, $\mathbb{M}$ is the fourth-order damage effect tensor, $\mathbb{M} = (1 - D)^{-1}\,\mathbb{I}$, and D is the effective-isotropic damage. Thereafter, the elastic strain $\boldsymbol{\varepsilon}^{\text{el}}$ can be expressed as

$$\boldsymbol{\varepsilon}^{\text{el}} = \mathbb{M}^{T} : \mathbb{H}^{-1} : \mathbb{M} : \boldsymbol{\sigma}. \tag{8.4}$$

Accordingly, the effective stress and strain tensors can be expressed respectively as

$$\tilde{\boldsymbol{\sigma}} = \mathbb{M} : \boldsymbol{\sigma} = \frac{\boldsymbol{\sigma}}{(1 - D)}, \qquad \tilde{\boldsymbol{\varepsilon}} = \mathbb{M}^{-T} : \boldsymbol{\varepsilon} = (1 - D)\,\mathbb{I} : \boldsymbol{\varepsilon}. \tag{8.5}$$

Remarks

The damage variable D is determined using the damage law (7.2) in the case of elastic-damage model both in tension and in compression. Although the law (7.2) models the proper softening behavior of concrete under tension, it yields an underestimated hardening-softening behavior under compression. It means that a lower peak-stress value from which the softening begins is predicted due to the incorporation of inelastic deformation. Thus, the damage evolution law (7.2) with the existing model parameters is not sufficient to model the behavior of concrete material perfectly. As a result, it entails a slight modification in the damage evolution so as to capture an appropriate behavior in compression as well. Thus, the softening law (7.2) is further modified with an additional model parameter β_3 as follows:

$$D(\kappa) = 1 - \left[\frac{\kappa_0}{\kappa}\right]^{\beta_1} e^{-\beta_2\left[\frac{\kappa-\kappa_0}{\kappa_0}\right]} - (1 - \beta_3)\frac{\kappa_0}{\kappa}. \tag{8.6}$$

It is also noteworthy to mention that the nonlinear hardening behavior under compression is primarily controlled by damage as the linear isotropic hardening is considered in the following section (Section 8.1.3).

8.1.3 Inelastic failure surface

It is familiar that concrete exhibits distinct behavior in tension and compression. The failure criterion initially developed by Lubliner *et al.* [98] and later extended by Lee and Fenves [94] is adopted here. This criterion is expressed here in the effective stress space in which a slight modification is embodied in this work by including a reduction factor $(1 - D_{\mathrm{eq}})$ to the limiting strength as follows:

$$F(\tilde{\sigma},h^{\pm}) = \left(\alpha\,\tilde{I}_1 + \sqrt{3\tilde{J}_2} + \beta^{\pm}(h^{\pm})\,H\,\tilde{\sigma}_{\max}\right) - (1-\alpha)\,\bar{f}_{\mathrm{c}}(h^{-})\,(1 - D_{\mathrm{eq}}), \tag{8.7}$$

where $\tilde{I}_1$ and $\tilde{J}_2$ are the first-invariant of the effective stress $\tilde{\boldsymbol{\sigma}}$ and the second-invariant of the deviatoric part of the effective stress $\tilde{\boldsymbol{\sigma}}$ respectively, H is the Heaviside step function ($H = 1$ for $\tilde{\sigma}_{\max} > 0$ and $H = 0$ for $\tilde{\sigma}_{\max} < 0$), $\tilde{\sigma}_{\max}$ is the maximum principal stress, and $D_{\mathrm{eq}}(= D)$ is an equivalent damage. The dimensionless constants α and β are defined as follows [98]:

$$\alpha = \frac{f_{\mathrm{bc}}/f_{\mathrm{c0}} - 1}{2f_{\mathrm{bc}}/f_{\mathrm{c0}} - 1}, \qquad \beta^{\pm}(h^{\pm}) = (1-\alpha)\frac{\bar{f}_{\mathrm{c}}(h^{-})}{\bar{f}_{\mathrm{t}}(h^{+})} - (1+\alpha), \tag{8.8}$$

where f_{bc} and f_{c0} are the initial flow stresses in equibiaxial and uniaxial compression respectively. The experiments confirm the ratio $f_{\mathrm{bc}}/f_{\mathrm{c0}}$ ranging from 1.10 to 1.16.

Remarks

Tension or compression dominant regions are defined by the Heaviside function H depending on the maximum principal stresses. This function always does not work well, for example, in the case of multi-axial loading situations. Therefore, the following definition is proposed for H in this work in order to describe the material behavior appropriately.

$$H = \begin{cases} 0, & \text{if } \tilde{I}_1 \leq 0 \\ 1, & \text{if } \left|\tilde{I}_1\right| \leq 0.64 f_{\mathrm{c}} \text{ and } w > 0 \\ 1. & \text{otherwise} \end{cases} \tag{8.9}$$

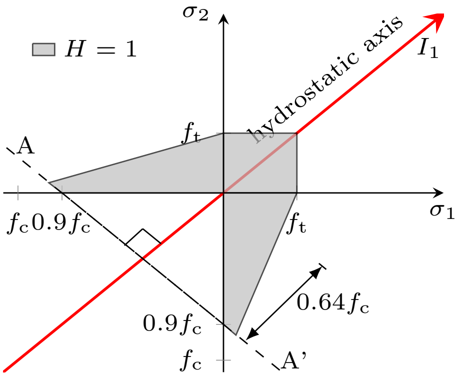

Figure 8.1: Tensile dominant regions (shaded regions)

The proposed definition (8.9) is described using a two-dimensional geometric representation, as shown in Figure 8.1 that highlights the regions wherever tension is dominant. The dashed line AA' is normal to the hydrostatic axis. The Heaviside function (8.9) is considered during the damage process as well. This assumption can be a better alternative to the introduction of activation parameter discussed in Section 7.1.3.

In order to consider the isotropic hardening, the hardening functions are adopted in tension as well as compression by assuming linear functions as below:

$$\bar{f}_\mathrm{t} = f_\mathrm{t0} + H_\mathrm{t}\, h^+, \qquad \bar{f}_\mathrm{c} = f_\mathrm{c0} + H_\mathrm{c}\, h^-, \tag{8.10}$$

such that the evolution functions of the tensile and compressive hardening can be defined as

$$\dot{\bar{f}}_\mathrm{t} = H_\mathrm{t}\, \dot{h}^+, \qquad \dot{\bar{f}}_\mathrm{c} = H_\mathrm{c}\, \dot{h}^-, \tag{8.11}$$

where H_t and H_c are the hardening modulus in tension and compression respectively and f_t0 is the initial flow stress in uniaxial tension. The hardening variables h^+ in tension and h^- in compression are defined in rate form [94, 98] as follows:

$$\dot{h}^+ = w\, \dot{\varepsilon}^\mathrm{in}_\mathrm{max}, \qquad \dot{h}^- = -(1-w)\, \dot{\varepsilon}^\mathrm{in}_\mathrm{min}, \tag{8.12}$$

where w is the triaxial weight factor obtained from the effective stress $\tilde{\boldsymbol{\sigma}}$ using the definition (7.11).

8.1.4 Non-associative flow rule

In order to obtain the volumetric expansion or dilatancy of frictional materials like concrete properly under given loading, the definition of a non-associative flow rule is important. As soon as the failure surface criterion F is satisfied, the material starts to flow in-elastically upon further increase of the loading. The inelastic deformation is measured by the evolution of inelastic strains $\boldsymbol{\varepsilon}^\mathrm{in}$, which is evaluated by the flow rule as follows:

$$\dot{\boldsymbol{\varepsilon}}^\mathrm{in} = \dot{\lambda}\, \frac{\partial Q}{\partial \boldsymbol{\sigma}}, \tag{8.13}$$

where $\dot{\lambda}$ is a non-negative inelastic multiplier as a consistency parameter that can be obtained from the inelasticity consistency condition $\dot{f} = 0$ in such a way that the following loading/unloading conditions during the inelastic deformation process must be satisfied.

$$F \le 0, \qquad \dot{\lambda} \ge 0, \qquad F\,\dot{\lambda} = 0, \qquad \lambda\,\dot{F} = 0, \tag{8.14}$$

The scalar inelastic potential function Q in (8.13) is usually assumed as a function different from the failure surface function F to consider non-associated flow rule, and thereby the direction of inelastic flow $\frac{\partial Q}{\partial \boldsymbol{\sigma}}$ is not normal to the failure function F. This can be easily fulfilled by adopting the Drucker-Prager function as Q expressed in the effective stress space such that:

$$Q(\tilde{\boldsymbol{\sigma}}) = \alpha_{\text{p}}\, \tilde{I}_1 + \sqrt{3\tilde{J}_2}, \tag{8.15}$$

where α_{p} is the dilation constant. Thus, the flow rule (8.13) relates the failure loading surface and the constitutive law (8.3).

Remarks

According to the experimental investigations [113], the inelastic strains progressively vanish and the material recovers its initial stiffness during the first compression loading phase. During the crack closure, the evolution of inelastic strains is partially explained by the friction developed by the discontinuity lips. Thus, the inelastic model is enabled to predict such behaviors of stiffness recovery and vanishing inelastic strains by means of allowing a stress-shift σ_{shift} about $2.5\,[\text{MPa}]$ in the compression region. Thus, the damaged stiffness remains constant until the actual stress nullifies this stress-shift. As soon as the stress-shift is nullified, the initial stiffness is recovered at the corresponding state of strain. In addition, the inelastic multiplier appearing in the flow rule (8.13) is introduced with two separate inelastic multipliers for tension and compression as follows:

$$\dot{\lambda} = \dot{\lambda}_{\text{t}}\, H + \dot{\lambda}_{\text{c}}\, (1 - H), \tag{8.16}$$

as similar to the definition of history deformation parameter (7.7) so as to deactivate the effect of inelastic strains developed due to tensile loading on compression phase. Hence, the evolution of inelastic strains due to tension does not have any influence on the compressive behavior and *vice versa*. Meanwhile, the loading/unloading conditions (8.14) are still valid, but $\dot{\lambda}_{\text{t}}$ or $\dot{\lambda}_{\text{c}}$ is itself a monotonically increasing multiplier.

8.2 Numerical algorithm

The model equations that describe the stress-strain relationships, become nonlinear owing to the incorporation of the damage and inelastic deformations. Furthermore, closed-form solutions are not possible for the above nonlinear equations that formulate an initial value problem. Therefore, the closed-form solutions of such equations can be explicitly obtained by performing a two-step algorithm, i.e., an elastic-inelastic operator split of the constitutive equations [1, 51, 137].

In this section, the numerical integration procedure for updating the constitutive relations is presented. The implicit-Euler backward method is used for the time discretization. At the beginning of the step at t_{n+1}, knowing the given strain increment $\Delta\varepsilon_{n+1}$, the values of stress and other internal variables from the previous step t_n, the updated values at the end of the current step t_{n+1} are computed.

There are two sequential processes, corresponding to the damage evolution and the inelastic evolution involved in the coupled model, involved in the numerical integration scheme. During the damage process, the damage variable D_{n+1} is evaluated by knowing the history deformation parameters κ_{n+1}. The stress at t_{n+1} at the end of the step is obtained from equation (8.3) instead of equation (7.1). During the inelastic process, the stress obtained at t_{n+1} at the end of the damage process enters as the trial stress at the elastic predictor step with the given strain increment $\Delta\boldsymbol{\varepsilon}_{n+1}$ and the value of inelastic strain $\boldsymbol{\varepsilon}_n^{\text{in}}$ from the previous step. The inelastic strain $\boldsymbol{\varepsilon}_{n+1}^{\text{in}}$ and the nominal and effective stresses ($\boldsymbol{\sigma}_{n+1}$ and $\tilde{\boldsymbol{\sigma}}_{n+1}$) at the end of the step are computed by using the implicit-return mapping algorithm [1,22,51,152] discussed in Section 8.2.1.

8.2.1 Implicit return-mapping

The inelastic corrector step restores the consistency condition by *returning* the trial stress to the yield or failure surface through the closest point projection. Thus, this method of corrector step is usually performed using an incremental function (implicit function) is called as *implicit return-mapping*.

As discussed earlier, the return mapping procedure is executed only if the elastic trial state violates inelastic admissibility. Thus, the material residual equations associated with the coupled inelastic-damage problem, which are the residual strains and the failure surface criterion, can be written equivalently at the current step t_{n+1} as

$$\mathbf{r}_{\boldsymbol{\sigma},n+1} := \boldsymbol{\varepsilon}_{n+1} - \boldsymbol{\varepsilon}_{n+1}^{\text{el}} - \boldsymbol{\varepsilon}_{n+1}^{\text{in}} = \mathbf{0}, \tag{8.17}$$

$$\mathbf{r}_{\lambda,n+1} := F_{n+1} = 0. \tag{8.18}$$

Consequently, the vector of material residual equations $\mathbf{r}_{\text{m}}$ at the current step t_{n+1} is combined as follows:

$$\mathbf{r}_{\text{m}} = \begin{bmatrix} \mathbf{r}_{\boldsymbol{\sigma}} \\ \mathbf{r}_{\lambda} \end{bmatrix}. \tag{8.19}$$

The above algebraic system of equations (8.19) can be solved by the Newton-Raphson method. Any solution to the system (8.19) must be obtained subject to the constraint $\dot{\lambda} > 0$ such that it must satisfy the condition $F_{n+1} \leq 0$. Therefore, the Newton-Raphson iteration scheme for better approximated solutions are obtained by linearizing the residual equations (8.19). The linearized system of equations involving the iterative differences $\Delta\boldsymbol{\sigma}$ and $\Delta\lambda$ as unknowns within the current step at Gauss points reads

$$\begin{bmatrix} \frac{\partial \mathbf{r}_{\boldsymbol{\sigma}}}{\partial \boldsymbol{\sigma}} & \frac{\partial \mathbf{r}_{\boldsymbol{\sigma}}}{\partial \lambda} \\ \frac{\partial \mathbf{r}_{\lambda}}{\partial \boldsymbol{\sigma}} & \frac{\partial \mathbf{r}_{\lambda}}{\partial \lambda} \end{bmatrix}_k \begin{bmatrix} \Delta\boldsymbol{\sigma} \\ \Delta\lambda \end{bmatrix}_{k+1} = \begin{bmatrix} -\mathbf{r}_{\boldsymbol{\sigma}} \\ -\mathbf{r}_{\lambda} \end{bmatrix}_k, \tag{8.20}$$

where $\Delta\boldsymbol{\sigma}_{k+1}$ and $\Delta\lambda_{k+1}$ are the approximated solutions at the end of iteration $k+1$. $\Delta(\cdot)$

Algorithm 2 (Algorithm of the coupled inelastic-damage model)

Input: Number of steps n, time t, given strain increment $\Delta\boldsymbol{\varepsilon}_{n+1}$
material parameters (cf. table 10.1) and model parameters (cf. table 10.2)

Output: σ_{n+1}, λ_{n+1} and $\boldsymbol{\varepsilon}^{\text{in}}_{n+1}$ at current time step t_{n+1}

```
[2.1]  At $t_{n=0}$, $\lambda_{n=0} = 0$ and $\boldsymbol{\varepsilon}^{\text{in}}_{n=0} = \mathbf{0}$
[2.2]  Damage process
[2.3]      Go to Algorithm 1
[2.4]          Obtain $D_{n+1}$
[2.5]  Inelastic process
[2.6]      Evaluate elastic predictor
[2.7]          Trial stress $\boldsymbol{\sigma}_{n+1}$ from (8.3)
[2.8]              $\boldsymbol{\sigma}_{n+1} = \mathbb{M}^{-1}_{n+1} : \mathbb{H} : \mathbb{M}^{-T}_{n+1} : (\boldsymbol{\varepsilon}_{n+1} - \boldsymbol{\varepsilon}^{\text{in}}_{n})$
[2.9]          Compute effective stress $\tilde{\boldsymbol{\sigma}}_{n+1}$ from (8.5)
[2.10]         Compute invariants $\tilde{I}_1$, $\tilde{J}_2$ and principal stress $\tilde{\sigma}_{\max}$ of $\tilde{\boldsymbol{\sigma}}_{n+1}$
[2.11]     Check for inelastic admissibility
[2.12]     if $F_{n+1} \leq 0$
[2.13]     then
[2.14]         $\boldsymbol{\sigma}_{n+1} = \boldsymbol{\sigma}_{n+1}$
[2.15]         $\tilde{\boldsymbol{\sigma}}_{n+1} = \tilde{\boldsymbol{\sigma}}_{n+1}$
[2.16]         $\lambda_{n+1} = \lambda_n$ and
[2.17]         $\boldsymbol{\varepsilon}^{\text{in}}_{n+1} = \boldsymbol{\varepsilon}^{\text{in}}_{n}$
[2.18]         exit
[2.19]     else if $F_{n+1} > 0$
[2.20]     then Compute inelastic corrector
[2.21]         Solve the system of algebraic equations
[2.22]             Using Implicit return-mapping
[2.23]             Go to Algorithm 3
[2.24]             Update the values
[2.25]             $\boldsymbol{\sigma}_{n+1}$
[2.26]             $\lambda_{n+1}$ and $\boldsymbol{\varepsilon}^{\text{in}}_{n+1}$
[2.27]     exit
[2.28] Exit
```

means the iterative differences between the iterations $k+1$ and k. If the predefined tolerance level ϵ_{m} is achieved, then the iterative procedure is stopped and the stress values and inelastic multiplier are updated at the end of the step. The complete numerical integration scheme for the coupled model is summarized in Algorithms 2 and 3.

Algorithm 3 (The Newton-Raphson algorithm for the return-mapping)

Input: Within the current time step t_{n+1}, initialize iteration counter, $k := 0$,
initial guess $\Delta\boldsymbol{\sigma} := \mathbf{0}$, $\Delta\lambda := 0$, $\lambda_{n+1,k=0} := \lambda_n$, $\boldsymbol{\varepsilon}^{\text{in}}_{n+1,k=0} = \boldsymbol{\varepsilon}^{\text{in}}_n$

Output: Material tolerance ϵ_{m}

```
[3.1]  Obtain material residuals $\mathbf{r}_{\text{m}}$ at $t_{n+1}$
[3.2]      $\mathbf{r}_{\boldsymbol{\sigma},n+1} := \boldsymbol{\varepsilon}_{n+1} - \boldsymbol{\varepsilon}^{\text{el}}_{n+1} - \boldsymbol{\varepsilon}^{\text{in}}_{n+1}$
[3.3]      $\mathbf{r}_{\lambda,n+1} := F_{n+1}$ from (8.7)
[3.4]  Start Newton-Raphson iterations for $\Delta\boldsymbol{\sigma}$ and $\Delta\lambda$
[3.5]      Solve the system of equations (8.20) at $t_{n+1}$
[3.6]          $\begin{bmatrix} \frac{\partial \mathbf{r}_{\boldsymbol{\sigma}}}{\partial \boldsymbol{\sigma}} & \frac{\partial \mathbf{r}_{\boldsymbol{\sigma}}}{\partial \lambda} \\ \frac{\partial \mathbf{r}_{\lambda}}{\partial \boldsymbol{\sigma}} & \frac{\partial \mathbf{r}_{\lambda}}{\partial \lambda} \end{bmatrix}_k \begin{bmatrix} \Delta\boldsymbol{\sigma} \\ \Delta\lambda \end{bmatrix}_{k+1} = \begin{bmatrix} -\mathbf{r}_{\boldsymbol{\sigma}} \\ -\mathbf{r}_{\lambda} \end{bmatrix}_k$
[3.7]          Approximate the unknowns (iterative differences) $\Delta\boldsymbol{\sigma}_{k+1}$ and $\Delta\lambda_{k+1}$
[3.8]      Check for convergence
[3.9]      if $|\mathbf{r}_{\text{m}}| \leq \epsilon_{\text{m}}$
[3.10]     then
[3.11]         Stop iterative scheme and update the values
[3.12]             $\boldsymbol{\sigma}_{k+1} = \boldsymbol{\sigma}_k + \Delta\boldsymbol{\sigma}_{k+1}$
[3.13]             $\lambda_{k+1} = \lambda_k + \Delta\lambda_{k+1}$
[3.14]         Return to Algorithm 2
[3.15]     else
[3.16]         Go to Step 3.4
```

8.3 Consistent tangent modulus

For the complete implementation of the coupled damage model into the finite element codes, the associated consistent tangent stiffness modulus, which is consistent with integration algorithm discussed in Section 8.2, is developed by linearizing the residual equations $\mathbf{r}_{\text{m}}$ (8.19).

If the current state of stress $\boldsymbol{\sigma}_{n+1}$ at t_{n+1} lies inside the elastic domain (i.e $F < 0$), then the corresponding coupled inelastic-damage tangent modulus $\mathbb{H}_{\text{epd}}$ or the effective tangent modulus $\tilde{\mathbb{H}}$ is simply provided by

$$\mathbb{H}_{\text{epd}} = \tilde{\mathbb{H}} = \mathbb{M}^{-1} : \mathbb{H} : \mathbb{M}^{-T}. \tag{8.21}$$

The tangent modulus (8.21) is valid when the current state is on the inelastic loading surface and the elastic unloading occurs. During the damage and inelastic processes, $\boldsymbol{\sigma}_{n+1}$ is the updated value at the end of inelastic-predictor step. Upon convergence of the return-mapping equations, the differentiation of the residual equations $\mathbf{r}_{\mathrm{m}}$ (8.19) with respect to $\boldsymbol{\varepsilon}_{n+1}$ yields

$$\begin{bmatrix} \frac{\partial \mathbf{r}_{\boldsymbol{\sigma}}}{\partial \boldsymbol{\sigma}} & \frac{\partial \mathbf{r}_{\boldsymbol{\sigma}}}{\partial \lambda} \\ \frac{\partial \mathbf{r}_{\lambda}}{\partial \boldsymbol{\sigma}} & \frac{\partial \mathbf{r}_{\lambda}}{\partial \lambda} \end{bmatrix} \begin{bmatrix} \frac{\partial \boldsymbol{\sigma}}{\partial \boldsymbol{\varepsilon}} \\ \frac{\partial \lambda}{\partial \boldsymbol{\varepsilon}} \end{bmatrix} = - \begin{bmatrix} \mathbb{I} \\ \mathbf{0} \end{bmatrix} . \tag{8.22}$$

By inverting the linearized system (8.22), the resulting tangent relations can be explicitly written as

$$\begin{bmatrix} \frac{\partial \boldsymbol{\sigma}}{\partial \boldsymbol{\varepsilon}} \\ \frac{\partial \lambda}{\partial \boldsymbol{\varepsilon}} \end{bmatrix} = \begin{bmatrix} \frac{\partial \mathbf{r}_{\boldsymbol{\sigma}}}{\partial \boldsymbol{\sigma}} & \frac{\partial \mathbf{r}_{\boldsymbol{\sigma}}}{\partial \lambda} \\ \frac{\partial \mathbf{r}_{\lambda}}{\partial \boldsymbol{\sigma}} & \frac{\partial \mathbf{r}_{\lambda}}{\partial \lambda} \end{bmatrix}^{-1} \begin{bmatrix} \mathbb{I} \\ \mathbf{0} \end{bmatrix} . \tag{8.23}$$

Subsequently, the consistent tangent stiffness modulus $\mathbb{H}_{\text{epd}}$ is precisely written as

$$\mathbb{H}_{\text{epd}} = \left. \frac{\partial \boldsymbol{\sigma}}{\partial \boldsymbol{\varepsilon}} \right|_{n+1} , \tag{8.24}$$

that is the derivative of the algorithmic constitutive function $\boldsymbol{\sigma}_{n+1}$ with respect to the strain tensor $\boldsymbol{\varepsilon}_{n+1}$.

At this point, it is worth mentioning that the consistent tangent modulus (8.24) of the fourth-order tensor is non-symmetric, as the coupled damage model employs the non-associative flow rule (8.13). If an associative flow rule is employed, then the modulus (8.24) would become symmetric.

9 Numerical Implementation

As discussed in Chapter 3, the fundamental equations of material (constitutive) modeling such as the kinematic equation, constitutive law, equilibrium equation and implicit-gradient equation along with specified boundary conditions define an initial-boundary value problem. This problem usually represents a non-linear problem, as it may contain geometric and/or material nonlinearities. Such problems often can not be solved analytically. It is therefore necessary to employ some kind of numerical method to obtain approximate solutions. Finite Difference Method (FDM) and Finite Element Method (FEM) are the most widely used methods in engineering applications. The present work employs FEM to solve the formulated initial-boundary value problem.

The detailed description of the finite element formulation is readily available in the text books [2, 38, 51, 129, 130] for further reference. However, the following sections address the basic steps necessary to build a finite element model including linearization and solving procedures.

9.1 Governing equations of the problem

Considering a physical system under body forces and traction undergoing infinitesimally small deformation, then the physical problem of deformation process is governed by the following mathematical relations.

The kinematic relation of the system (3.13) can be, in simple form, given by

$$\boldsymbol{\varepsilon} = \nabla^{\text{sym}} \boldsymbol{u}. \tag{9.1}$$

Thus, the internal resistance developed in the system is measured by the stress tensor $\boldsymbol{\sigma}$ through the constitutive law that is given by

$$\boldsymbol{\sigma} = \boldsymbol{\sigma}(\boldsymbol{\varepsilon}, D), \tag{9.2}$$

as a function of the observed variable $\boldsymbol{\varepsilon}$ and internal variables such as D and $\boldsymbol{\varepsilon}^{\text{in}}$. Further, if the inertial effect is ignored, the partial differential equation of equilibrium (3.21) can be reduced to

$$\nabla \cdot \boldsymbol{\sigma} + \boldsymbol{b} = 0. \tag{9.3}$$

The above equation is always subjected to the following Dirichlet and Neumann boundary conditions specified on the boundary S

$$\boldsymbol{u} = \boldsymbol{u}^{\text{p}}, \qquad \text{on } S_{\boldsymbol{u}^{\text{p}}}, \tag{9.4}$$

$$\boldsymbol{t} = \boldsymbol{\sigma} \cdot \boldsymbol{n} = \boldsymbol{t}^{\text{p}}, \quad \text{on } S_{\boldsymbol{t}^{\text{p}}}, \tag{9.5}$$

where $\boldsymbol{u}^{\mathrm{p}}$ and $\boldsymbol{t}^{\mathrm{p}}$ are the prescribed boundary values on the boundary S for the displacement field and traction field respectively.

As discussed in Section 6.2.2.2, an additional equation, which has to be solved along with the equilibrium equation (9.3) to avoid ill-posedness of the problem, is the implicit gradient equation (6.33) and is rewritten as

$$\hat{\zeta} - l_{\mathrm{c}}^{2}\,\nabla^{2}\,\hat{\zeta} - \zeta = 0, \tag{9.6}$$

where l_{c} is the characteristic internal length, along with the prescribed Neumann boundary condition on the boundary S as

$$\nabla\,\hat{\zeta}\cdot\boldsymbol{n} = \hat{\zeta}_{\mathrm{n}}^{\mathrm{p}}. \tag{9.7}$$

9.2 Weak formulations

In order to solve the partial differential equations of strong form involved in continuum mechanics using FEM, these equations (9.3, 9.6) have to be first transformed into integral equations of weak form equivalently. This transformation can easily be achieved by using the principle of virtual work.

9.2.1 Weak form of equilibrium equation

With the help of principle of virtual work, the weak form of the equilibrium equation (9.3) is obtained as

$$\int_{V} \delta\boldsymbol{u}\,(\nabla\cdot\boldsymbol{\sigma} + \boldsymbol{b})\,dV = 0. \tag{9.8}$$

Subsequently, the application of partial integration and the Guass divergence theorem leads to the weak form as follows

$$\int_{V} \boldsymbol{\sigma} : \delta\boldsymbol{\varepsilon}\,dV = \int_{V} \boldsymbol{b}\cdot\delta\boldsymbol{u}\,dV + \int_{S} \boldsymbol{t}^{\mathrm{p}}\cdot\delta\boldsymbol{u}\,dS, \tag{9.9}$$

after substituting the kinematic equations (3.13) and along with the boundary condition (9.5). $\delta\boldsymbol{u}$ and $\delta\boldsymbol{\varepsilon}$ are the virtual displacement field and resulting virtual strain respectively. Moreover, the physical meaning of equation (9.9) states that the external work $\delta W_{\mathrm{ext}}^{u}$ by virtual displacements $\delta\boldsymbol{u}$ is balanced by the internal work $\delta W_{\mathrm{int}}^{u}$ developed due to the application of virtual displacements $\delta\boldsymbol{u}$. Thus, the virtual works are given by

$$\delta W_{\mathrm{int}}^{u} = \int_{V} \boldsymbol{\sigma} : \delta\boldsymbol{\varepsilon}\,dV, \tag{9.10}$$

$$\delta W_{\text{ext}}^{u} = \int_V \boldsymbol{b} \cdot \delta\boldsymbol{u}\, dV + \int_S \boldsymbol{t}^{\text{p}} \cdot \delta\boldsymbol{u}\, dS. \tag{9.11}$$

9.2.2 Weak form of gradient equation

In a similar fashion, the weak form of the gradient equation (9.6) can also be written as

$$\int_V \delta\hat{\zeta}_{\text{w}} \, (\hat{\zeta} - l_{\text{c}}^2 \, \nabla^2 \, \hat{\zeta} - \zeta) \, dV = 0, \tag{9.12}$$

using the virtual quantity $\delta\hat{\zeta}_{\text{w}}$, which is the conjugated variable of nonlocal variable under consideration. By employing partial integration and subsequently using the Guass divergence theorem into (9.12), the weak form of gradient equation becomes

$$\int_V \delta\hat{\zeta}_{\text{w}} \, \hat{\zeta} \, dV - \int_V \delta\hat{\zeta}_{\text{w}} \, \zeta \, dV + \int_V l_{\text{c}}^2 \, \nabla \, (\delta\hat{\zeta}_{\text{w}}) \cdot \nabla \, \hat{\zeta} \, dV = \int_S l_{\text{c}}^2 \, \delta\hat{\zeta}_{\text{w}} \, \hat{\zeta}_{\text{n}}^{\text{p}} \, dS, \tag{9.13}$$

along with the natural boundary (9.7). From this equation (9.13), it can be equivalently interpreted as internal and external virtual works due to

$$\delta W_{\text{int}}^{\hat{\zeta}} = \int_V \delta\hat{\zeta}_{\text{w}} \, \hat{\zeta} \, dV - \int_V \delta\hat{\zeta}_{\text{w}} \, \zeta \, dV + \int_V l_{\text{c}}^2 \, \nabla \, (\delta\hat{\zeta}_{\text{w}}) \cdot \nabla \, \hat{\zeta} \, dV, \tag{9.14}$$

$$\delta W_{\text{ext}}^{\hat{\zeta}} = \int_S l_{\text{c}}^2 \, \delta\hat{\zeta}_{\text{w}} \, \hat{\zeta}_{\text{n}}^{\text{p}} \, dS. \tag{9.15}$$

It is assumed that the natural boundary becomes homogeneous by considering the vanishing gradient setting $\hat{\zeta}_{\text{n}}^{\text{p}} = 0$ in equation (9.13) during the numerical analysis. Furthermore, the conjugated virtual quantity would be taken as an equivalent stress $\hat{\sigma}_{\text{eq}}$ while considering the equivalent strain $\hat{\epsilon}$ as a nonlocal variable, whereas the conjugated virtual quantity would be taken as the damage energy release rate $\hat{Y}$ while considering the damage variable $\hat{D}$ as nonlocal variable.

9.3 Finite element discretization

The continuous domain V is subdivided into n_{e} sub-domains V_{e}, i.e., finite elements such that the approximated geometry becomes

$$V = \bigcup_{e=1}^{n_{\text{e}}} V_{\text{e}}. \tag{9.16}$$

Therefore, the solution of every unknown field variable must be approximated by a continuous function within the element such that the function satisfies prescribed conditions (nodal values) at a finite number of points (nodes). Thus, the finite element approximation can be achieved by choosing appropriate interpolation polynomial functions. In this problem, the unknown field variables are the displacement field $\boldsymbol{u}$ as a primary variable and the nonlocal variable $\hat{\zeta}$ as a secondary variable in an element. Hence, within the isoparametric formulations, the same shape functions are generally used to interpolate both the coordinates and displacements of a point within the element from the coordinates and displacements of nodes. Accordingly, the coordinates $\mathbf{x}\,(=\{x\,y\,z\}^T)$, displacement field $\boldsymbol{u}\,(=\{u\,v\,w\}^T)$ and $\hat{\zeta}$ of a point are interpolated over an element by using respective shape functions $N_{ui}(\boldsymbol{\xi})$ and $N_{\hat{\zeta}_i}(\boldsymbol{\xi})$ as

$$\mathbf{x}(\boldsymbol{\xi}) = \sum_{i=1}^{n_{\text{nod}}} N_{ui}(\boldsymbol{\xi})\,\hat{\mathbf{x}}_i, \tag{9.17}$$

$$\boldsymbol{u}(\boldsymbol{\xi}) = \sum_{i=1}^{n_{\text{nod}}} N_{ui}(\boldsymbol{\xi})\,\boldsymbol{d}_{ui} = \boldsymbol{N}_u\,\mathbf{d}_u, \tag{9.18}$$

$$\hat{\zeta}(\boldsymbol{\xi}) = \sum_{i=1}^{n_{\text{nod}}} N_{\hat{\zeta}_i}(\boldsymbol{\xi})\,d_{\hat{\zeta}_i} = \boldsymbol{N}_{\hat{\zeta}}\,\mathbf{d}_{\hat{\zeta}}, \tag{9.19}$$

where $\boldsymbol{\xi}$ is a system of local or natural or reference coordinates within an element V_{e} to define the shape functions, $\hat{\mathbf{x}}_i$ the vector of global coordinates of any node of the element, $\boldsymbol{d}_{ui}\,(=\{u_i\,v_i\,w_i\}^T)$ the vector of three mutual displacements and $d_{\hat{\zeta}_i}$ the nonlocal d.o.f. at the i^{th} node respectively, $\mathbf{d}_u$ the vector of nodal displacement d.o.f. and $\mathbf{d}_{\hat{\zeta}}$ the vector of nodal nonlocal d.o.f of the element respectively, and n_{nod} is the number of nodes in the element. equation (9.17) provides the relation between local and global coordinates system.

Subsequently, the virtual displacement field $\delta\boldsymbol{u}$ as well as the virtual nonlocal field $\delta\hat{\zeta}$ can also be written as

$$\delta\boldsymbol{u}(\boldsymbol{\xi}) = \sum_{i=1}^{n_{\text{nod}}} N_{ui}(\boldsymbol{\xi})\,\delta\boldsymbol{d}_{ui} = \boldsymbol{N}_u\,\delta\mathbf{d}_u, \tag{9.20}$$

$$\delta\hat{\zeta}_{\text{w}}(\boldsymbol{\xi}) = \sum_{i=1}^{n_{\text{nod}}} N_{\hat{\zeta}_i}(\boldsymbol{\xi})\,\delta d_{\hat{\zeta}_i} = \boldsymbol{N}_{\hat{\zeta}}\,\delta\mathbf{d}_{\hat{\zeta}}. \tag{9.21}$$

With the help of equations (9.18, 9.20) and the kinematic relation (9.1), the strain $\boldsymbol{\varepsilon}$ can be easily obtained as

$$\boldsymbol{\varepsilon} = \nabla^{\text{sym}} \sum_{i=1}^{n_{\text{nod}}} N_{ui}(\boldsymbol{\xi})\,\boldsymbol{d}_{ui} = \sum_{i=1}^{n_{\text{nod}}} \nabla^{\text{sym}}\,N_{ui}(\boldsymbol{\xi})\,\boldsymbol{d}_{ui} = \sum_{i=1}^{n_{\text{nod}}} \boldsymbol{B}_{ui}\,\boldsymbol{d}_{ui} = \boldsymbol{B}_u\,\mathbf{d}_u, \tag{9.22}$$

where $\boldsymbol{B}_{ui} = \nabla^{\text{sym}}\,N_{ui}$ represents the strain-displacement matrix in Voigt notation. Subsequently, the virtual displacement $\delta\boldsymbol{u}$ yields the virtual strain $\delta\boldsymbol{\varepsilon}$ as

$$\delta\boldsymbol{\varepsilon} = \sum_{i=1}^{n_{\text{nod}}} \boldsymbol{B}_{ui}\,\delta\boldsymbol{d}_{ui} = \boldsymbol{B}_u\,\delta\mathbf{d}_u. \tag{9.23}$$

In a similar fashion as the gradients of actual and virtual displacements, the gradients of actual and virtual quantities of nonlocal field variable such as $\nabla\,\hat{\zeta}$ and $\nabla\,\delta\hat{\zeta}$ can be expressed by

$$\nabla\,\hat{\zeta} = \sum_{i=1}^{n_{\mathrm{nod}}} \nabla\, N_{\hat{\zeta}_i}\, d_{\hat{\zeta}_i} = \sum_{i=1}^{n_{\mathrm{nod}}} \boldsymbol{B}_{\hat{\zeta}_i}\, d_{\hat{\zeta}_i} = \boldsymbol{B}_{\hat{\zeta}}\, \mathbf{d}_{\hat{\zeta}}, \tag{9.24}$$

$$\nabla\,\delta\hat{\zeta}_{\mathrm{w}} = \sum_{i=1}^{n_{\mathrm{nod}}} \nabla\, N_{\hat{\zeta}_i}\, \delta d_{\hat{\zeta}_i} = \sum_{i=1}^{n_{\mathrm{nod}}} \boldsymbol{B}_{\hat{\zeta}_i}\, \delta d_{\hat{\zeta}_i} = \boldsymbol{B}_{\hat{\zeta}}\, \delta\mathbf{d}_{\hat{\zeta}}. \tag{9.25}$$

The strain-displacement matrix $\boldsymbol{B}$ can be not written directly, as it involves the gradients and the derivatives with respect to the global coordinates (x, y, z), which are not available directly. Therefore, there is a need of a transformation matrix, which can be simply obtained by the inverse of Jacobian matrix $\boldsymbol{J}$. Thus, the vector of partial derivatives with respect to the global coordinates can be written in terms of the derivatives of the local coordinates (ξ, η, ζ') as

$$\nabla_{\boldsymbol{x}} = \begin{bmatrix} \frac{\partial}{\partial x} \\ \frac{\partial}{\partial y} \\ \frac{\partial}{\partial z} \end{bmatrix} = \boldsymbol{J}^{-1} \begin{bmatrix} \frac{\partial}{\partial \xi} \\ \frac{\partial}{\partial \eta} \\ \frac{\partial}{\partial \zeta'} \end{bmatrix} = \boldsymbol{J}^{-1}\,\nabla_{\boldsymbol{\xi}}, \tag{9.26}$$

where the Jacobian matrix $\boldsymbol{J}$ is defined as

$$\boldsymbol{J} = \begin{bmatrix} \frac{\partial x}{\partial \xi} & \frac{\partial y}{\partial \xi} & \frac{\partial z}{\partial \xi} \\ \frac{\partial x}{\partial \eta} & \frac{\partial y}{\partial \eta} & \frac{\partial z}{\partial \eta} \\ \frac{\partial x}{\partial \zeta'} & \frac{\partial y}{\partial \zeta'} & \frac{\partial z}{\partial \zeta'} \end{bmatrix}. \tag{9.27}$$

Moreover, the determinant of the Jacobian matrix $\boldsymbol{J}$ is often referred to the Jacobian J, i.e., $J = |\boldsymbol{J}|$. It is regarded as a scale factor not equal to zero. The present work adopts linear shape functions for the nonlocal field variable, whereas linear or quadratic shape functions for the displacement field.

9.4 Finite element model

Substituting the resulting finite element approximations from Section 9.3 into the weak forms of equilibrium equation (9.9) and gradient equation (9.13) yields the respective virtual works δU_u^{e} and $\delta U_{\hat{\zeta}}^{\mathrm{e}}$ over the element as follows (in matrix notation):

$$\delta U_u^{\mathrm{e}} = \delta\mathbf{d}_u \left(\int_{V_{\mathrm{e}}} \boldsymbol{B}_u^T\, \boldsymbol{\sigma}\, dV_{\mathrm{e}} - \int_{V_{\mathrm{e}}} \boldsymbol{N}_u^T\, \boldsymbol{b}\, dV_{\mathrm{e}} - \int_{S_{\mathrm{e}}} \boldsymbol{N}_u^T\, \boldsymbol{t}^{\mathrm{p}}\, dS_{\mathrm{e}} \right), \tag{9.28}$$

$$\delta U_{\hat{\zeta}}^{\mathrm{e}} = \delta\mathbf{d}_{\hat{\zeta}} \left(\int_{V_{\mathrm{e}}} \boldsymbol{N}_{\hat{\zeta}}^T\, (\hat{\zeta} - \zeta)\, dV_{\mathrm{e}} + l_c^2 \int_{V_{\mathrm{e}}} \boldsymbol{B}_{\hat{\zeta}}^T\, \nabla\,\hat{\zeta}\, dV_{\mathrm{e}} - l_{\mathrm{c}}^2 \int_{S_{\mathrm{e}}} \boldsymbol{N}_{\hat{\zeta}}^T\, \hat{\zeta}_{\mathrm{n}}^{\mathrm{p}}\, dS_{\mathrm{e}} \right). \tag{9.29}$$

As the virtual work of the element is zero for the arbitrary values of virtual quantities such as $\delta\mathbf{d}_u$ and $\delta\mathbf{d}_{\hat{\zeta}}$, equations (9.28) and (9.29) turn into residuals of equilibrium and gradient equations as follows:

$$\mathbf{r}^{\mathrm{e}}_u = \int_{V_{\mathrm{e}}} \boldsymbol{B}_u^T \boldsymbol{\sigma}\, dV_{\mathrm{e}} - \int_{V_{\mathrm{e}}} \boldsymbol{N}_u^T \boldsymbol{b}\, dV_{\mathrm{e}} - \int_{S_{\mathrm{e}}} \boldsymbol{N}_u^T \boldsymbol{t}^{\mathrm{p}}\, dS_{\mathrm{e}} = \mathbf{0}, \tag{9.30}$$

$$\mathbf{r}^{\mathrm{e}}_{\hat{\zeta}} = \int_{V_{\mathrm{e}}} \boldsymbol{N}_{\hat{\zeta}}^T (\hat{\zeta} - \zeta)\, dV_{\mathrm{e}} + l_c^2 \int_{V_{\mathrm{e}}} \boldsymbol{B}_{\hat{\zeta}}^T \nabla \hat{\zeta}\, dV_{\mathrm{e}} - l_{\mathrm{c}}^2 \int_{S_{\mathrm{e}}} \boldsymbol{N}_{\hat{\zeta}}^T \hat{\zeta}^{\mathrm{p}}_{\mathrm{n}}\, dS_{\mathrm{e}} = \mathbf{0}. \tag{9.31}$$

Thus, the element vectors of internal and external nodal forces can be devised as follows:

$$\mathbf{f}^{\mathrm{e}}_{u,int} = \int_{V_{\mathrm{e}}} \boldsymbol{B}_u^T \boldsymbol{\sigma}\, dV_{\mathrm{e}}, \tag{9.32}$$

$$\mathbf{f}^{\mathrm{e}}_{u,ext} = \int_{V_{\mathrm{e}}} N_u^T \boldsymbol{b}\, dV_{\mathrm{e}} + \int_{S_{\mathrm{e}}} N_u^T \boldsymbol{t}^{\mathrm{p}}\, dS_{\mathrm{e}}, \tag{9.33}$$

$$\mathbf{f}^{\mathrm{e}}_{\hat{\zeta},int} = \int_{V_{\mathrm{e}}} \boldsymbol{N}_{\hat{\zeta}}^T (\hat{\zeta} - \zeta)\, dV_{\mathrm{e}} + l_c^2 \int_{V_{\mathrm{e}}} \boldsymbol{B}_{\hat{\zeta}}^T \nabla \hat{\zeta}\, dV_{\mathrm{e}}, \tag{9.34}$$

$$\mathbf{f}^{\mathrm{e}}_{\hat{\zeta},ext} = l_{\mathrm{c}}^2 \int_{S_{\mathrm{e}}} \boldsymbol{N}_{\hat{\zeta}}^T \hat{\zeta}^{\mathrm{p}}_{\mathrm{n}}\, dS_{\mathrm{e}}. \tag{9.35}$$

Thereby, equations (9.30) and (9.31) representing the finite element equations can be expressed by the following compact form

$$\mathbf{r}^{\mathrm{e}} = \begin{bmatrix} \mathbf{r}^{\mathrm{e}}_u \\ \mathbf{r}^{\mathrm{e}}_{\hat{\zeta}} \end{bmatrix} = \begin{bmatrix} \mathbf{f}^{\mathrm{e}}_{u,int} - \mathbf{f}^{\mathrm{e}}_{u,ext} \\ \mathbf{f}^{\mathrm{e}}_{\hat{\zeta},int} - \mathbf{f}^{\mathrm{e}}_{\hat{\zeta},ext} \end{bmatrix} = \begin{bmatrix} 0 \\ 0 \end{bmatrix}. \tag{9.36}$$

This completes the development of a finite element model.

9.5 Assembly of finite elements

In order to obtain the system of equations to represent the global system, the virtual works of all the elements resulting from equations (9.28) and (9.29) are thereafter summed up respectively as follows:

$$\delta U_u = \sum_{e=1}^{n_{\mathrm{e}}} \delta U^{\mathrm{e}}_u, \qquad \delta U_{\hat{\zeta}} = \sum_{e=1}^{n_{\mathrm{e}}} \delta U^{\mathrm{e}}_{\hat{\zeta}}. \tag{9.37}$$

Correspondingly, the residuals of equilibrium equation and gradient equation of the global system read as

$$\mathbf{r}_u = \bigcup_{e=1}^{n_\mathrm{e}} \mathbf{r}_u^\mathrm{e}, \qquad\qquad \mathbf{r}_{\hat{\zeta}} = \bigcup_{e=1}^{n_\mathrm{e}} \mathbf{r}_{\hat{\zeta}}^\mathrm{e}. \tag{9.38}$$

As a result, after assembling all the element residual vectors $\mathbf{r}^\mathrm{e}$, the residual vector $\mathbf{R}$ of the global system becomes

$$\mathbf{R} = \bigcup_{e=1}^{n_\mathrm{e}} \mathbf{r}^\mathrm{e} = \begin{bmatrix} \mathbf{r}_u \\ \mathbf{r}_{\hat{\zeta}} \end{bmatrix} = \bigcup_{e=1}^{n_\mathrm{e}} \begin{bmatrix} \mathbf{f}^\mathrm{e}_{u,int} - \mathbf{f}^\mathrm{e}_{u,ext} \\ \mathbf{f}^\mathrm{e}_{\hat{\zeta},int} - \mathbf{f}^\mathrm{e}_{\hat{\zeta},ext} \end{bmatrix} = \begin{bmatrix} \mathbf{0} \\ \mathbf{0} \end{bmatrix}. \tag{9.39}$$

The residual equations (9.39) resulting from the weak forms are usually nonlinear if physical and geometric nonlinearity exist. Physical nonlinearity occurs when the stress strain behavior by the constitutive relation is nonlinear (in the case of damage or inelasticity), whereas the latter occurs in the case of changes in the geometry having a significant effect on the load deformation behavior [1,26].

9.6 Linearization

In order to solve such system of nonlinear equations discussed in the previous section, incremental solution techniques, for example, the Newton-Raphson method, may be employed. Application of this method necessitates a consistent linearization of the system of equations. To obtain the consistent linearization, the residual equations have to be differentiated with respect to the unknown nodal degrees of freedom $\mathbf{d} = \{\mathbf{d}_u, \mathbf{d}_{\hat{\zeta}}\}^T$.

Subsequently, this method can be derived directly by the Taylor expansion of the residual vector function (9.39) in the neighborhood of a better approximated solution of unknown degrees of freedom $\mathbf{d}$ at $(i+1)^{th}$ iteration step within the time step t_{n+1} as follows:

$$\mathbf{R}(\mathbf{d}^{i+1}_{n+1}) = \mathbf{R}(\mathbf{d}^{i}_{n+1}) + \left.\frac{\partial \mathbf{R}(\mathbf{d}_{n+1})}{\partial \mathbf{d}}\right|_{\mathbf{d}^i} \Delta \mathbf{d}^{i+1}_{n+1} = \mathbf{0}, \tag{9.40}$$

where $\mathbf{d}^{i+1}_{n+1} = \mathbf{d}^i + \Delta\mathbf{d}^{i+1}_{n+1}$ is the approximated solution obtained at $(i+1)^{th}$ iteration step after convergence. Thereafter, the rearrangement and simplification of equation (9.40) leads to a linearized system of equations within the time step t_{n+1}

$$\mathbf{K}^i \, \Delta\mathbf{d}^{i+1} = -\mathbf{R}^i, \tag{9.41}$$

where $\mathbf{K}^i$ is the tangential stiffness matrix of the structural system, $\Delta\mathbf{d}^{i+1}$ is the iterative solution of the system of nonlinear equations upon convergence, and $\mathbf{R}^i$ refers to the vector of residuals. In addition, the inner terms in the lienarized equation (9.41) are given by

$$\mathbf{K}^{i} = \bigcup_{e=1}^{n_{\mathrm{e}}} \begin{bmatrix} \mathbf{k}_{uu}^{e,i} & \mathbf{k}_{u\hat{\zeta}}^{e,i} \\ \mathbf{k}_{\hat{\zeta}u}^{e,i} & \mathbf{k}_{\hat{\zeta}\hat{\zeta}}^{e,i} \end{bmatrix}, \qquad \Delta\mathbf{d}^{i+1} = \bigcup_{e=1}^{n_{\mathrm{e}}} \begin{bmatrix} \Delta\mathbf{d}_{u}^{e,i+1} \\ \Delta\mathbf{d}_{\hat{\zeta}}^{e,i+1} \end{bmatrix}, \qquad \mathbf{R}^{i} = \bigcup_{e=1}^{n_{\mathrm{e}}} \begin{bmatrix} \mathbf{r}_{u}^{e,i} \\ \mathbf{r}_{\hat{\zeta}}^{e,i} \end{bmatrix}, \tag{9.42a}$$

$$\mathbf{k}_{uu}^{e,i} = \left.\frac{\partial \mathbf{r}_{u}^{\mathrm{e}}(\mathbf{d}_{n+1})}{\partial \mathbf{d}_{u}^{\mathrm{e}}}\right|_{\mathbf{d}^{i}} = \int_{V_{\mathrm{e}}} \boldsymbol{B}_{u}^{T}\, \mathbb{H}_{uu}\, \boldsymbol{B}_{u}\, dV_{\mathrm{e}}, \tag{9.42b}$$

$$\mathbf{k}_{u\hat{\zeta}}^{e,i} = \left.\frac{\partial \mathbf{r}_{u}^{\mathrm{e}}(\mathbf{d}_{n+1})}{\partial \mathbf{d}_{\hat{\zeta}}^{\mathrm{e}}}\right|_{\mathbf{d}^{i}} = \int_{V_{\mathrm{e}}} \boldsymbol{B}_{u}^{T}\, \mathbb{H}_{u\hat{\zeta}}\, \boldsymbol{N}_{\hat{\zeta}}\, dV_{\mathrm{e}}, \tag{9.42c}$$

$$\mathbf{k}_{\hat{\zeta}u}^{e,i} = \left.\frac{\partial \mathbf{r}_{\hat{\zeta}}^{\mathrm{e}}(\mathbf{d}_{n+1})}{\partial \mathbf{d}_{u}^{\mathrm{e}}}\right|_{\mathbf{d}^{i}} = -\int_{V_{\mathrm{e}}} \boldsymbol{N}_{\hat{\zeta}}^{T}\, \mathbb{H}_{\hat{\zeta}u}\, \boldsymbol{B}_{u}\, dV_{\mathrm{e}}, \tag{9.42d}$$

$$\mathbf{k}_{\hat{\zeta}\hat{\zeta}}^{e,i} = \left.\frac{\partial \mathbf{r}_{\hat{\zeta}}^{\mathrm{e}}(\mathbf{d}_{n+1})}{\partial \mathbf{d}_{\hat{\zeta}}^{\mathrm{e}}}\right|_{\mathbf{d}^{i}} = \int_{V_{\mathrm{e}}} \boldsymbol{N}_{\hat{\zeta}}^{T}\, (1 - H_{\hat{\zeta}\hat{\zeta}})\, \boldsymbol{N}_{\hat{\zeta}}\, dV_{\mathrm{e}} + \int_{V_{\mathrm{e}}} \boldsymbol{B}_{\hat{\zeta}}^{T}\, l_{\mathrm{c}}^{2}\, \boldsymbol{B}_{\hat{\zeta}}\, dV_{\mathrm{e}}, \tag{9.42e}$$

where the terms appearing in the element matrices (9.42b, 9.42c, 9.42d, 9.42e) such as $\mathbb{H}_{uu}$, $\mathbb{H}_{u\hat{\zeta}}$, $\mathbb{H}_{\hat{\zeta}u}$ and $H_{\hat{\zeta}\hat{\zeta}}$, which refer to the consistent material tangents evaluated at every Guass-point considered in the element, are

$$\mathbb{H}_{uu} = \frac{\partial \boldsymbol{\sigma}}{\partial \boldsymbol{\varepsilon}}, \tag{9.43a}$$

$$\mathbb{H}_{\hat{\zeta}u} = \frac{\partial \zeta}{\partial \boldsymbol{\varepsilon}}, \tag{9.43b}$$

$$\mathbb{H}_{u\hat{\zeta}} = \frac{\partial \boldsymbol{\sigma}}{\partial \hat{\zeta}}, \tag{9.43c}$$

$$H_{\hat{\zeta}\hat{\zeta}} = \frac{\partial \zeta}{\partial \hat{\zeta}}. \tag{9.43d}$$

Thus, the coupling of the nonlocal variable with the equilibrium equation eventually results in non-symmetric element matrices $\mathbf{k}^{e}$. As a consequence, the structural matrix $\mathbf{K}$ resulting from the assembly of element matrices $\mathbf{k}^{e}$ also becomes non-symmetric.

In the case of local elastic-damage and coupled inelastic-damage models, the structural matrix of the global system (9.42a) reduces to

$$\mathbf{K}^{i} = \bigcup_{e=1}^{n_{\mathrm{e}}} \begin{bmatrix} \mathbf{k}_{uu}^{e,i} \end{bmatrix}, \tag{9.44}$$

and accordingly the consistent material tangent $\mathbb{H}_{uu}$ is determined using the relations (7.24) and (8.24) as discussed in Sections 7.1.6 and 8.3.

9.6.1 Material tangents

In order to compute the main and coupled element matrices (9.42b, 9.42c, 9.42d, 9.42e) in the case of gradient-enhanced damage models, the consistent material tangents are required to be evaluated at every Gauss point. For the gradient-enhanced elastic-damage model, these tangents can be explicitly computed from the algorithmic update functions of $\boldsymbol{\sigma}_{n+1}$ and ϵ_{n+1}.

On the other hand, for the gradient-enhanced version of coupled inelastic-damage model, it is necessary to find out the total differentiation of material residual equations including the residual $\mathbf{r}_{\hat{\epsilon}} := f = 0$, which is due to the damage consistency function. Thus, all the residual equations are grouped as

$$\mathbf{r}_{\mathrm{M}} = \begin{bmatrix} \mathbf{r}_{\mathrm{m}} \\ \mathbf{r}_{\hat{\epsilon}} \end{bmatrix} = \begin{bmatrix} \mathbf{r}_{\boldsymbol{\sigma}}(\boldsymbol{\sigma}, \hat{\epsilon}, \lambda) \\ \mathbf{r}_{\lambda}(\boldsymbol{\sigma}, \hat{\epsilon}) \\ \mathbf{r}_{\hat{\epsilon}}(\hat{\epsilon}) \end{bmatrix}. \tag{9.45}$$

where the global state variables are $\mathbf{g} = \{\boldsymbol{\varepsilon}, \hat{\epsilon}\}$ and the local state variables are $\mathbf{z} = \{\boldsymbol{\sigma}, \lambda\}$. The total differentiation of the residuals $\mathbf{r}_{\mathrm{M}}$ can be expressed as

$$d\mathbf{r}_{\mathrm{M}} = \frac{\partial \mathbf{r}_{\mathrm{M}}}{\partial \mathbf{z}} d\mathbf{z} + \frac{\partial \mathbf{r}_{\mathrm{M}}}{\partial \mathbf{g}} d\mathbf{g} = \mathbf{0}. \tag{9.46}$$

Subsequent total differentiation of the local variables $\mathbf{z}$ with respect to the global variables $\mathbf{g}$ and simplification leads to the linearized equations as follows:

$$d\mathbf{r}_{\mathrm{M}} = \left\{ \frac{\partial \mathbf{r}_{\mathrm{M}}}{\partial \mathbf{z}} \frac{\partial \mathbf{z}}{\partial \mathbf{g}} + \frac{\partial \mathbf{r}_{\mathrm{M}}}{\partial \mathbf{g}} \right\} d\mathbf{g} = \mathbf{0}. \tag{9.47}$$

Consequently, the linearized system of equations reads as

$$\begin{bmatrix} \frac{\partial \mathbf{r}_{\boldsymbol{\sigma}}}{\partial \boldsymbol{\sigma}} & \frac{\partial \mathbf{r}_{\boldsymbol{\sigma}}}{\partial \lambda} \\ \frac{\partial \mathbf{r}_{\lambda}}{\partial \boldsymbol{\sigma}} & \frac{\partial \mathbf{r}_{\lambda}}{\partial \lambda} \\ \frac{\partial \mathbf{r}_{\hat{\epsilon}}}{\partial \boldsymbol{\sigma}} & \frac{\partial \mathbf{r}_{\hat{\epsilon}}}{\partial \lambda} \end{bmatrix} \begin{bmatrix} \frac{\partial \boldsymbol{\sigma}}{\partial \boldsymbol{\varepsilon}} & \frac{\partial \boldsymbol{\sigma}}{\partial \hat{\epsilon}} \\ \frac{\partial \lambda}{\partial \boldsymbol{\varepsilon}} & \frac{\partial \lambda}{\partial \hat{\epsilon}} \end{bmatrix} = - \begin{bmatrix} \frac{\partial \mathbf{r}_{\boldsymbol{\sigma}}}{\partial \boldsymbol{\varepsilon}} & \frac{\partial \mathbf{r}_{\boldsymbol{\sigma}}}{\partial \hat{\epsilon}} \\ \frac{\partial \mathbf{r}_{\lambda}}{\partial \boldsymbol{\varepsilon}} & \frac{\partial \mathbf{r}_{\lambda}}{\partial \hat{\epsilon}} \\ \frac{\partial \mathbf{r}_{\hat{\epsilon}}}{\partial \boldsymbol{\varepsilon}} & \frac{\partial \mathbf{r}_{\hat{\epsilon}}}{\partial \hat{\epsilon}} \end{bmatrix}. \tag{9.48}$$

As the residual $\mathbf{r}_{\hat{\epsilon}}$ due to the damage consistency function is independent of the local variables $\mathbf{z}$, neglecting the respective zero terms in the above system (9.48) and further simplification yields

$$\begin{bmatrix} \frac{\partial \mathbf{r}_{\boldsymbol{\sigma}}}{\partial \boldsymbol{\sigma}} & \frac{\partial \mathbf{r}_{\boldsymbol{\sigma}}}{\partial \lambda} \\ \frac{\partial \mathbf{r}_{\lambda}}{\partial \boldsymbol{\sigma}} & \frac{\partial \mathbf{r}_{\lambda}}{\partial \lambda} \end{bmatrix} \begin{bmatrix} \frac{\partial \boldsymbol{\sigma}}{\partial \boldsymbol{\varepsilon}} & \frac{\partial \boldsymbol{\sigma}}{\partial \hat{\epsilon}} \\ \frac{\partial \lambda}{\partial \boldsymbol{\varepsilon}} & \frac{\partial \lambda}{\partial \hat{\epsilon}} \end{bmatrix} = - \begin{bmatrix} \mathbb{I} & \frac{\partial \mathbf{r}_{\boldsymbol{\sigma}}}{\partial \hat{\epsilon}} \\ \mathbf{0} & \frac{\partial \mathbf{r}_{\lambda}}{\partial \hat{\epsilon}} \end{bmatrix}. \tag{9.49}$$

By solving the system of equations (9.49), the required tangents that are in terms of implicit functions can be computed. Apart from these, the additional coupled tangents that are not part of the implicit return-mapping algorithm can be explicitly determined as described in the elastic-damage model.

9.7 Solving procedure

In this section, the numerical procedure of solving the nonlinear system of equations is discussed. The total solution of the problem is the unknown field variables or degrees of freedom $\mathbf{d}_{n+1}$ by satisfying the boundary conditions and equilibrium conditions. The entire computational process consists two levels of numerical computations, one at global level and the other at local level. A scheme of solving algorithm for the nonlinear problem is summarized in Algorithm 4.

Algorithm 4 (Scheme of solving algorithm)

Input: Number of steps n, time $t_{n+1} = t_n + \Delta t$, and material tangents $\mathbb{H}_{uu}$, $\mathbb{H}_{u\hat{\zeta}}$, $\mathbb{H}_{\hat{\zeta}u}$, $H_{\hat{\zeta}\hat{\zeta}}$

Output: Nodal values $\mathbf{d}_{n+1}$ at current time step t_{n+1}

```
Loop over time steps
Global level computations
Initialize $\mathbf{d}_0$ at $t_{n=0}$
    Loop over elements
    NR-iterative process
        Local level computations
            Loop over Guass points
            If elastic-damage model, Go to Algorithm 1
            If coupled inelastic-damage model, Go to Algorithm 2
                    Update stress $\boldsymbol{\sigma}_{n+1}$
                    Obtain tangents $\mathbb{H}_{uu}$, $\mathbb{H}_{u\hat{\zeta}}$, $\mathbb{H}_{\hat{\zeta}u}$, $H_{\hat{\zeta}\hat{\zeta}}$
    Consistent stiffness matrix $\mathbf{K}^i$ at $i^{th}$ iteration step
    Residual vector $\mathbf{R}^i$ at $i^{th}$ iteration step
    Solve the system of equations $\mathbf{K}^i\,\Delta\mathbf{d}^{i+1} = -\mathbf{R}^i$
    Update nodal values $\mathbf{d}^{i+1}_{n+1} = \mathbf{d}^i + \Delta\mathbf{d}^{i+1}_{n+1}$
    Check for convergence
    if $\Delta\mathbf{d}^{i+1}_{n+1} \geq \epsilon_{\mathrm{g}}$
    then
        Continue the above steps for the next iteration $i+1$
    else
        $\mathbf{d}_{n+1} = \mathbf{d}^{i+1}_{n+1}$
        $\mathbf{K}_{n+1} = \mathbf{K}^i$
        $\mathbf{R}_{n+1} = \mathbf{R}^i$
    exit
```

The computations at the global level means solving the equilibrium equation and the gradient equation using spatial and time discretizations. The linearized system of equations (9.41) are solved for improved approximations $\mathbf{d}_{n+1}^{i+1} = \mathbf{d}^i + \Delta\mathbf{d}_{n+1}^{i+1}$ using the NR-iterative process within each time step t_{n+1} with the help of known values from the previous time step t_n. If the norm of the residuals becomes less than a predefined tolerance ϵ_{g}, then the solving procedure is stopped otherwise the procedure is repeated until this convergence criterion has achieved. The estimated solution of nodal degrees of freedom is $\mathbf{d}_{n+1} = \mathbf{d}(t_{n+1})$ upon convergence. If the NR-iteration process does not converge, the program is restarted with a smaller time step size (halved from the previous time step size).

The computations at the local level means stress updating at each Gauss point using the solutions $\mathbf{d}_{n+1}$ from the global level. In this step, stresses, strains, and other internal variables such as equivalent strain, history parameters, and damage variable are evaluated from the constitutive equations and evolution equations within the current step.

10 Validation of Models

In order to check the ability of the damage models in predicting the material behavior, the numerical algorithm of the developed models has been implemented into a finite element program (an in-house code, which is also used for solving a coupled problem like Soil-Structure-Interaction analysis [133]). The model is investigated under several loadings such as monotonic uniaxial tensile, compression loadings, and various test series of biaxial loadings. In addition, the performance of the model is analyzed under direct cyclic tension, compression as well as cyclic tension-compression loadings.

A single 8-noded brick element of size $200\,[\mathrm{mm}] \times 200\,[\mathrm{mm}] \times 50\,[\mathrm{mm}]$ equivalent to the size of concrete plate tested by Kupfer and co-workers [91] is used for the above tests using 8 Gauss integration points. The material and model parameters used in this work are provided in Table 10.1. The material parameters are taken from the work [94]. The model parameters β_1 and β_2 have been chosen accordingly so as to reproduce the material behavior from the uniaxial tensile and compressive tests. The material length scale l_c is considered as $200\,[\mathrm{mm}]$. Linear shape functions have been used for nonlocal equivalent strains. The nonlinear system of resulting equations has been solved with the Newton-Raphson method. Displacements are imposed as applied loading. The validation of the elastic-damage model is presented in Sections 10.1-10.2. Section 10.3 discusses the performance of the coupled-inelastic model under various loadings and shows the ability of capturing inelastic evolution favorably.

10.1 Monotonic loading tests

10.1.1 Uniaxial tension and compression

The single element is first subjected to uniaxial tensile loading. Figure 10.1 shows the simulated stress-strain curve, which agrees well with the experimental curve of Karsan and Jirsa [84]. It

Table 10.1: Relevant parameters for isotropic damage model

	Adopted parameters	Data 1 [72]	Data 2 [84]	Data 3 [91]	Data 4 [102]	
Material parameters	f_c [MPa]	27.6	27.6	31.0	34.4	
	f_t [MPa]	3.48	3.48	3.1	1/3 f_c	
	E [GPa]	31.0	31.7	31.87	–	
	ν [-]	0.18	0.2	0.2	–	
Model parameters	$\beta_{1\mathrm{t}}$	$\beta_{2\mathrm{t}}$	$\beta_{1\mathrm{c}}$	$\beta_{2\mathrm{c}}$	$\kappa_{0\mathrm{t}}$	$\kappa_{0\mathrm{c}}$
	0.85	0.18	0.0	0.095	f_c/E	$10 f_\mathrm{t}/3E$
Internal length	l_c [mm]	200				

is noted that the model exhibits a gradual decrease of stress and ensuring the residual stresses to a large extent.

Secondly, the element is subjected to uniaxial compressive loading. The numerically predicted compressive stress-strain response is compared with the experimental curve [84] in Figure 10.2 and depicts very good agreement with experimental data. Moreover, the proposed model can predict the damage hardening as well as post-peak softening behavior well.

In addition, Figures 10.3 and 10.4 illustrate the evolution of history parameter and corresponding damage during the tensile and compressive loading respectively. As seen in Figure 10.3, the history parameter in both the load cases grows monotonically and thereby respects the thermodynamic inequality. It is also obvious from Figure 10.4 that the damage initiation in the case of compressive loading is later than that in the case of tension, which is physically reasonable.

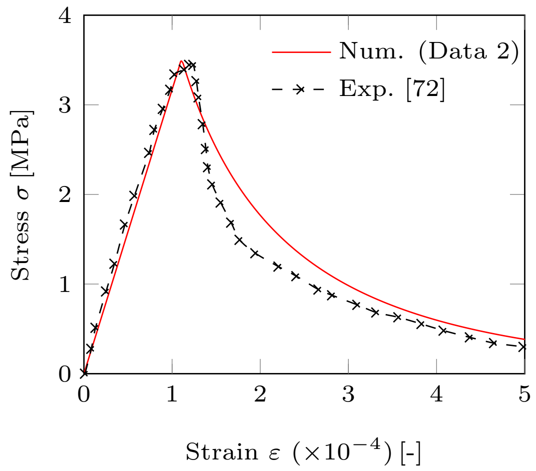

Figure 10.1: Uniaxial tension [72]

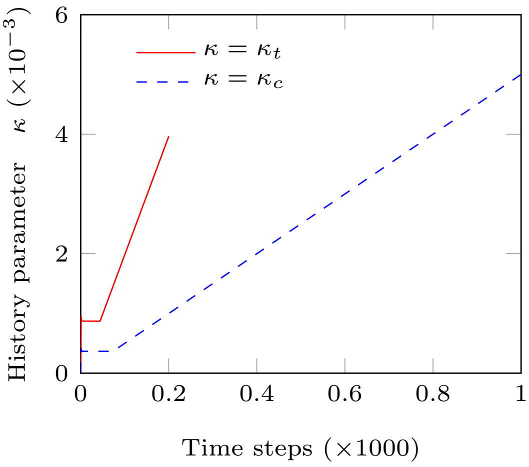

Figure 10.3: History parameter evolution

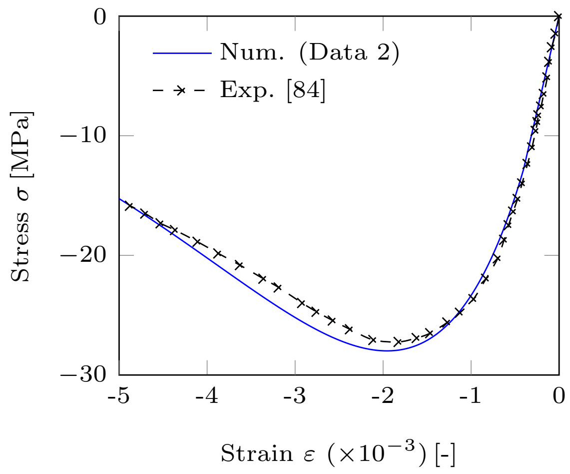

Figure 10.2: Uniaxial compression [84]

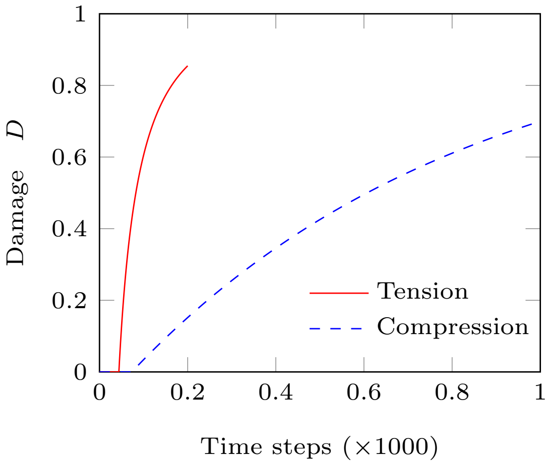

Figure 10.4: Damage evolution

10.1.2 Proportional biaxial loading

The same element is then investigated under several two-dimensional/biaxial loading along various prescribed load paths. The obtained numerical results are plotted against the experimental data of biaxial failure surface of Kupfer and Zelger [91]. As can be seen in Figure 10.5, the present model predicts the envelope of ultimate stresses, i.e., failure surface well in bi-tension, bi-compression, and compression-tension regions. Moreover, the envelope of damage surface ($D = 0$), which limits the elasticity domain, is also shown. Thus, the model provides very good results in all the regions.

10.1.3 Non-proportional biaxial loading (Tension-Compression)

Biaxial experiments with non-proportional loading were conducted by Maekawa and Okamura [102], which were stress-controlled tests. But the numerical simulations are performed under displacement control. Therefore, the compression loading is first applied monotonically up to a certain level and then the tensile loading is superimposed in the other principal direction. Both the experimental results [102] and the numerical predictions using material parameters (Data 2) are illustrated in Figure 10.6. In order to compare the numerical results with experimental results, the calculated principal stresses are normalized by the uniaxial compressive strength f_c and the tensile strength f_t from Data 2 and the calculated principal strains are also normalized by the compressive strain ε_c ($= -1.955 \cdot 10^{-3}$) corresponding to f_c. As observed from Figure 10.6, the numerically predicted tensile stresses and corresponding strains behave nearly linear for compressive strains, say $\varepsilon_2/\varepsilon_c < 0.25$. The nonlinear behavior appears with increasing compressive strains. Subsequently, the increase in the tensile stress accelerates the deformation of concrete leading to softening. Thus, the numerical predictions describe favorably the biaxial deformation behavior observed in the experimental investigations.

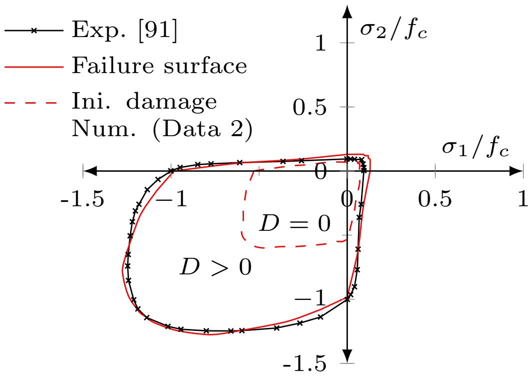

Figure 10.5: Biaxial proportional loading [91]

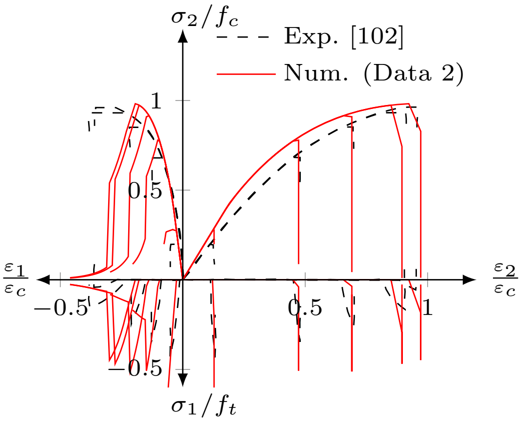

Figure 10.6: Biaxial non-proportional loading [102]

10.2 Cyclic loading tests

10.2.1 Uniaxial cyclic tension and compression

The ability of the present model is checked under uniaxial cyclic tensile as well as compressive loading. Figure 10.7 and 10.8 depict the simulated tensile and compressive behavior of stress-strain curves respectively. The numerical curves are compared with the experimental curves according to Gopalaratnam and Shah [72] and Karsan and Jirsa [84]. The model predictions agree fairly with the experimental data:

(a) the softening behaviors using material parameters (Data 1 and Data 2) under tension predicted by the model are almost close and comparable with the experimental one, as shown in Figure 10.7;

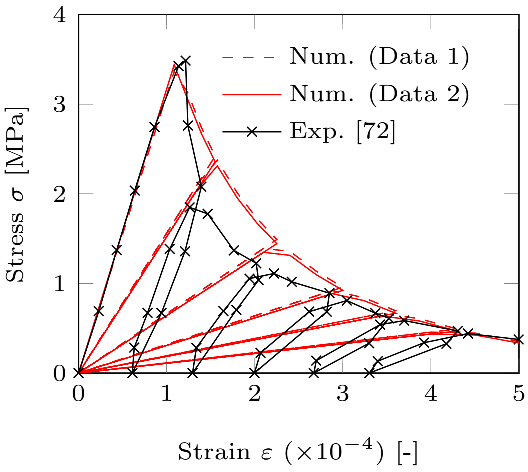

Figure 10.7: Uniaxial cyclic tension [72]

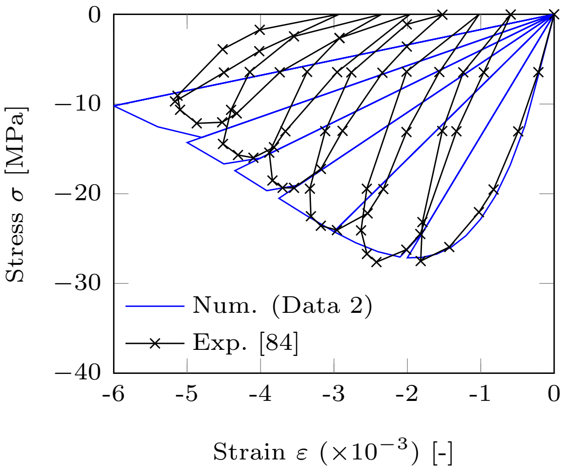

Figure 10.8: Uniaxial cyclic compression [84]

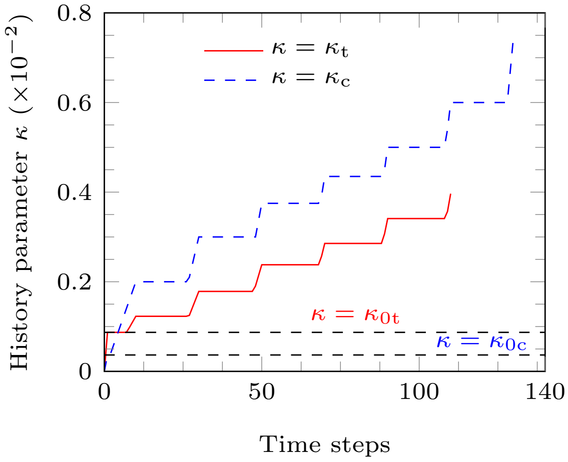

Figure 10.9: Evolution of history parameter (cyclic)

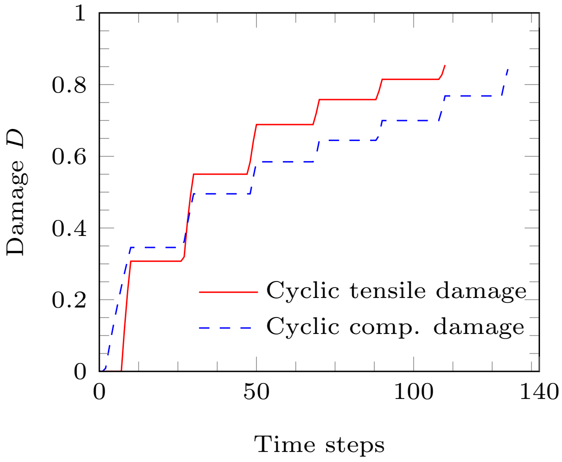

Figure 10.10: Evolution of damage (cyclic)

(b) the nonlinear behavior under compression, either in hardening or in softening, is rather close enough to the test, as shown in Figure 10.8;
(c) the history deformation parameter κ_t or κ_c grows monotonically, as shown in Figure 10.9, as every reloading follows the path of the previous unloading and thus thermodynamic consistency is verified;
(d) the tensile damage or compressive damage is monotonically increasing, as depicted in Figure 10.10, in other words, the increase in the slopes of the unloading curves in Figures 10.7 and 10.8 replicates monotonic increasing damage under tension or compression;
(e) the history deformation parameter and damage remain constant during unloading regions, as seen in Figures 10.9 and 10.10 respectively;
(f) the only discrepancy observed is that residual permanent strains are not described during the unloading cycles, since the model has not taken the inelastic evolution of strains into account.

10.2.2 Tension-compression loading

In order to investigate the effect of damage under uniaxial cyclic tension-compression loading, the displacement history is used to be cyclic with an increasing magnitude alternatively tension and compression as an imposed loading. As observed in Figure 10.11 κ_t or κ_c, is monotonically increasing during the tension-compression loading/unloading processes respectively. Consequently, a monotonic increase of the effective damage D is depicted in Figure 10.12. It is also observed that D becomes zero after the initial tensile loading (cycle 1) and thus the effective damage due to initial tensile loading does not affect the damage evolution in the first phase of compression (cycle 2). But D due to the first tensile loading is recovered, once the material experiences tension in reloading (cycle 3). During the unloading paths (B-O) and (D-O), the accumulated damage remains constant, i.e., $\dot{D} = 0$ as $\dot{\kappa} = 0$.

As a consequence, the actual tension-compression behavior exhibits a complete recovery of the initial stiffness of the material for the first compression loading, as shown in Figure 10.13. The magnified plot shows the model behavior during the tensile loading and unloading. The arrows denote the load path. In addition, the tensile-compressive stresses are normalized by the tensile strength f_t and the uniaxial compressive strength f_c from Data 2 respectively. The experimental response [104] is as well normalized by respective material data from their work in order to compare with numerical results. Hence, both the normalized numerical and experimental behavior (up to $3\frac{1}{4}$ cycles) are illustrated in Figure 10.14.

The degradation of stiffness is shown by softening, as the damage develops due to the opening of micro-cracks during the tensile loading path (O-A-B). Afterwards, the tensile unloading that occurs follows the path (B-O) and thus the damaged stiffness remains same. When the sign of loading changes meaning that the first compressive loading occurs (O-C), the initial stiffness is recovered due to the closure of opened micro-cracks. At this level, there is no damage development, as observed in Figure 10.12, since the damage criterion is not fulfilled. Further compressive unloading-tensile reloading (C-O-B-D') causes opening of closed cracks, and subsequent degradation of stiffness occurs during the cycle. The tensile unloading (D'-O) and compressive reloading (O-E) again close the opened cracks and hence recovers the initial stiffness. If the loading continues in this direction, the damage grows further.

Thus, the model describes the unilateral behavior quite well, and the numerical response agrees well with the experiments showing a full recovery of initial stiffness. This is typically observed in concrete when the sign of the load changes, according to the experimental investigations [104]. But there are certain discrepancies due to the fact that the permanent inelastic strains are not taken into account in the model so far. This discrepancy is overcome by the coupled-inelastic damage model. The performance and validation of the model is presented in the following section.

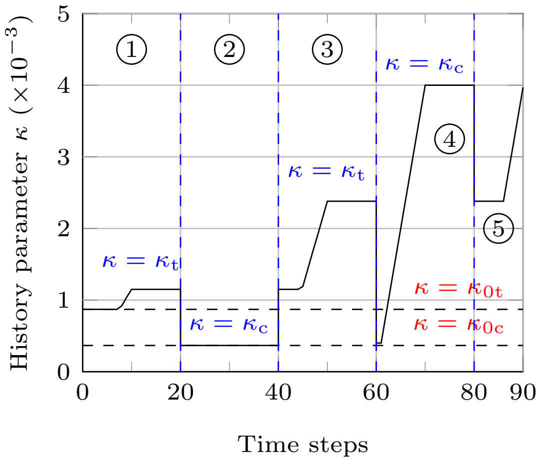

Figure 10.11: Evolution of parameter κ (unilateral)

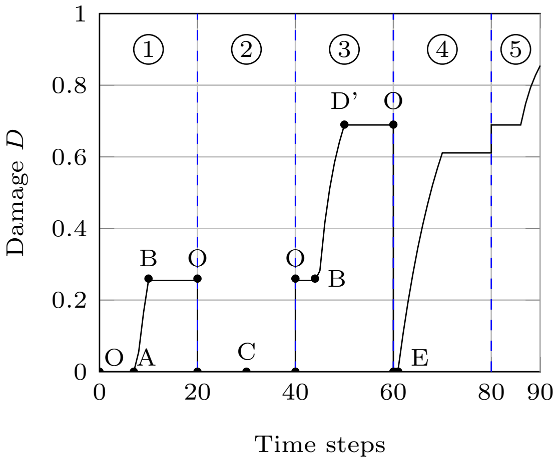

Figure 10.12: Evolution of damage (unilateral)

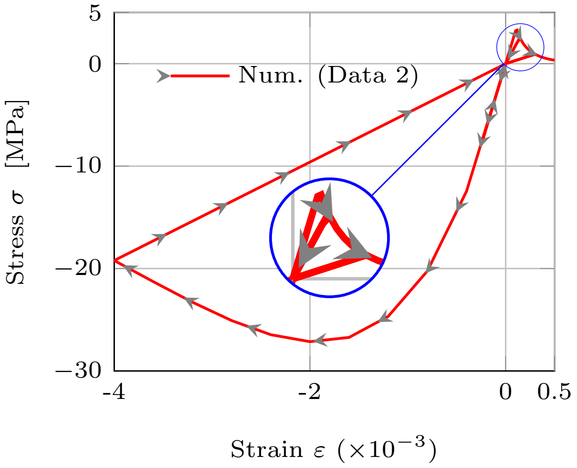

Figure 10.13: Unilateral behavior (actual)

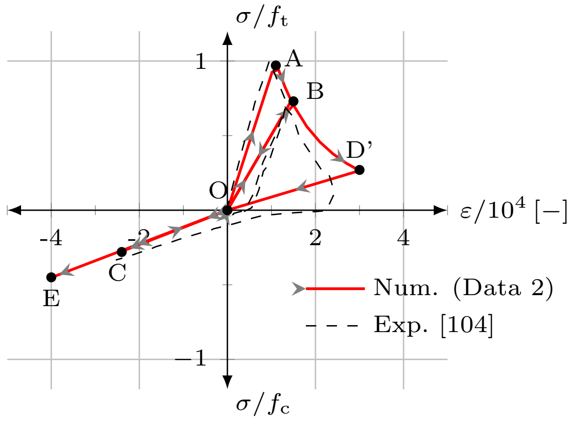

Figure 10.14: Unilateral behavior (normalized) [104]

10.3 Validations of inelastic model

This section presents the performance of the coupled-inelastic damage model under several loading conditions, which were performed earlier. The model and hardening parameters adopted in the following simulations are provided in Table 10.2, in addition to the material parameters (Data 2) of Table 10.1.

The numerical response under uniaxial tensile loading is compared with the experimental tensile curve [84] in Figure 10.15. On the other hand, Figure 10.16 compares the numerical response of the model under uniaxial compression with the respective experimental curve [84]. As seen in both the comparisons, the model predicts the hardening behavior under compression well in addition to the softening behavior in the post-peak region in tension as well as compression and thereby proves its ability by exemplifying fair agreement with experiments.

Likewise, biaxial tests with proportional and non-proportional loading are performed, as explained in Sections 10.1.2 and 10.1.3. Figure 10.17 shows both the envelopes of failure surface (maximum stresses) and damage loading surface ($D = 0$). The Kupfer's failure surface [91],

Table 10.2: Relevant parameters for coupled-inelastic damage model

Hardening parameters	H_{t} [MPa]	25.0						
	H_{c} [GPa]	42.0						
	f_{t0} [MPa]	f_{t}						
	f_{c0} [MPa]	$0.6\, f_{\mathrm{c}}$						
Model parameters	β_{1t}	β_{2t}	β_{3t}	β_{1c}	β_{2c}	β_{3c}	κ_{0t}	κ_{0c}
	0.25	0.25	1.0	0.00	0.105	1.20	f_{c}/E	f_{c0}/E
Internal length	l_{c} [mm]	200						

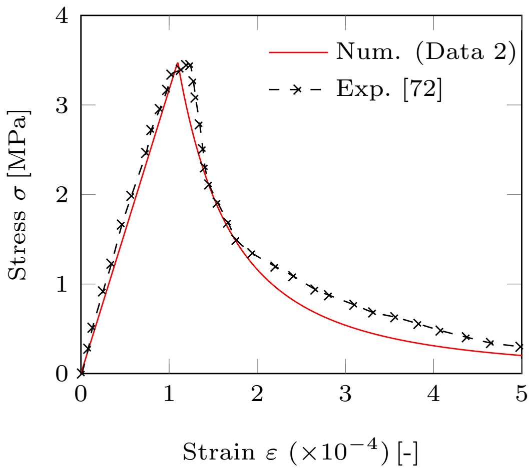

Figure 10.15: Uniaxial tension [72]

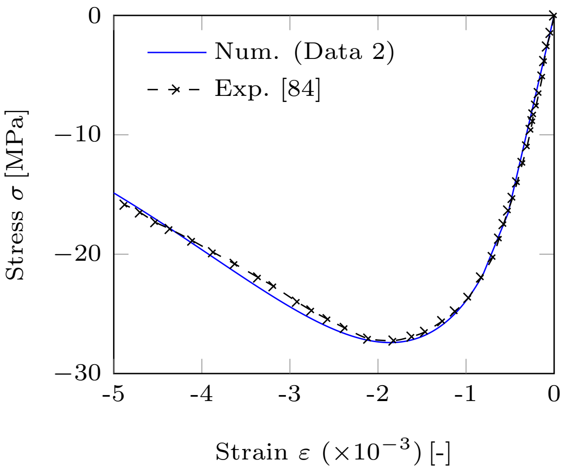

Figure 10.16: Uniaxial compression [84]

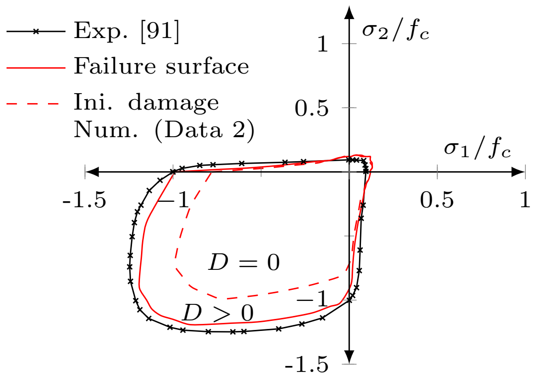

Figure 10.17: Biaxial proportional loading [91]

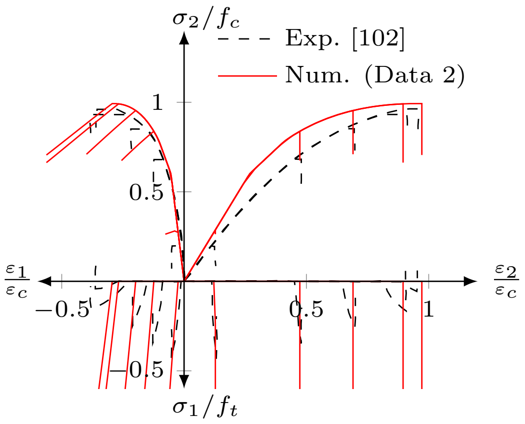

Figure 10.18: Biaxial non-proportional loading [102]

which is the experimental curve from several biaxial tests along proportional load paths, is also plotted. The model yields acceptable results with few differences in the compression region. These differences can be avoided by adjusting the model parameters for biaxial test cases specifically. Compared to the biaxial surface envelopes of elastic-damage model shown in Figure 10.5, the damage initiates later in the compression region, as the damage growth is only possible after the inelastic evolution. Thus, the different behavior of concrete material in compression and tension is described well. This is enabled by allowing compression active only in the pure compression and compression dominant areas (that is, the first stress invariant approximately greater than 64% of the uniaxial compressive strength f_c) of complex region, otherwise tension is made active (based on the Heaviside function (8.9)).

Both the normalized results of numerical tests of biaxial non-proportional loading and the experiment [102] are illustrated in Figure 10.18. As can be observed, the numerically predicted tensile stresses and corresponding strains behave linear for compressive strains, say $\varepsilon_2/\varepsilon_\mathrm{c} < 0.25$. As similar to the elastic-damage model, the nonlinear behavior appears with increasing compressive strains here as well. Subsequent increase in the tensile stress further accelerates the deformation of concrete leading to the softening behavior. Therefore, the model is able to describe fairly the biaxial deformation behavior observed in the experimental investigations.

On the other hand, the numerical responses obtained from the cyclic tensile and compressive loading are compared with the relevant experimental results in Figures 10.19 and 10.20. The results are reasonably good in agreement during the loading/unloading and reloading cycles. As can be observed, the permanent strains (inelastic strains) monotonically increase during the entire load history either in tension or in compression. Similarly, the stiffness decreases with the increase of damage, which can be observed from the unloading curves.

The effect of cyclic tension-compression loading on concrete is finally investigated using an increasing magnitude alternatively tension and compression as an imposed loading. The actual tension-compression behavior exhibits a complete recovery of the initial stiffness of the mate-

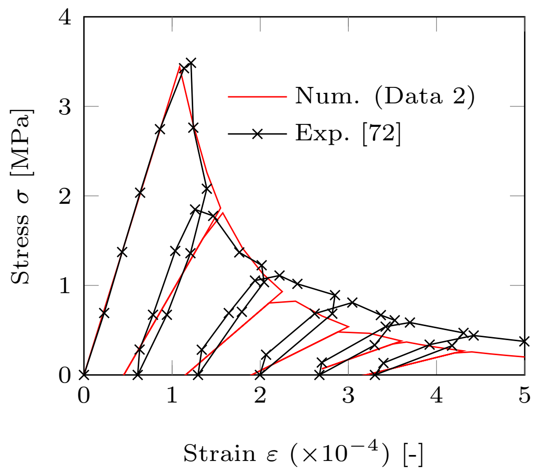

Figure 10.19: Uniaxial cyclic tension [72]

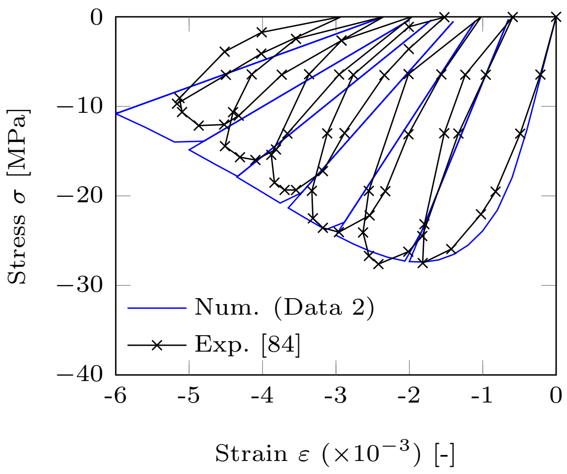

Figure 10.20: Uniaxial cyclic compression [84]

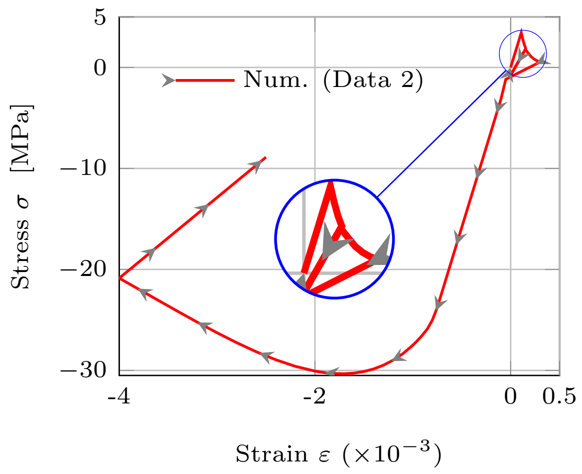

Figure 10.21: Unilateral behavior (actual)

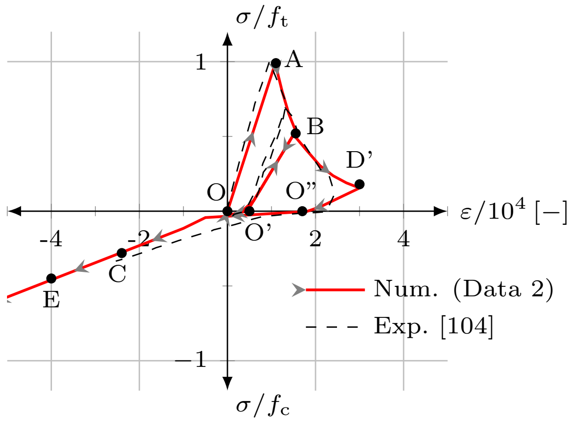

Figure 10.22: Unilateral behavior (normalized) [104]

rial for the first compression loading, as shown in Figure 10.21, that is after the second cycle of tension unloading. The magnified plot shows the model behavior during the tensile loading and unloading. The arrows denote the load path. It is also noticed that the permanent strains can be traced during the unloading after the first compression loading. In order to compare the numerical results with experimental results, the numerical response and the experimental response [104] are normalized as done earlier. Thus, both the normalized numerical and experimental behaviors are illustrated in Figure 10.22. The degradation of stiffness is shown by the softening, as the damage develops due to the opening of micro-cracks during the tensile loading path (O-A-B). Afterwards, the tensile unloading that occurs follows the path (B-O') and thus the damaged stiffness remains same. Herein, (O-O') refers to the inelastic strains that developed during the first tensile unloading (B-O'). Subsequently, tensile reloading (O'-B-D') occurs and in turn causes further opening of closed cracks and continuous softening (B-D'). Following that, tensile unloading (D'-O") leaves the total inelastic strains (O-O"). When the sign of loading changes meaning that the first loading in compression occurs (O"-C), the initial stiffness is recovered due to the closure of opened micro-cracks as well as vanishing of the inelastic strains developed due to the entire tensile loading. The tensile unloading (D'-O") and the compression reloading (O-C-E) again close the opened cracks and hence recovers the initial stiffness. If the loading continues in this direction, the damage grows further due to compression.

The model response of unilateral behavior also agree with the recent experimental investigations [113]. According to them, the inelastic strains progressively vanish and the material recovers its initial stiffness during the first compression loading phase. During the crack closure, the evolution of inelastic strains are partially explained by the friction developed by the discontinuity lips. Thus, the inelastic model is enabled to predict such behaviors of stiffness recovery and vanishing inelastic strains by means of allowing a stress-shift and defining the inelastic multiplier through two separate inelastic multipliers for tension and compression.

10.4 Illustration of localization phenomena

In order to visualize the localization phenomena of the gradient-enhanced damage model, a simple one-dimensional problem is analyzed using a bar subjected to a pure tensile loading. Displacement is applied at the free end of the bar, and the left end of the bar is fixed. Model parameters and material parameters (Data 2) used are from the Table 10.1, while the initial damage threshold is set as $\kappa_0 = 1 \cdot 10^{-3}$. Linear shape functions have been used for the nonlocal variables $\hat{\zeta}$ (nonlocal damage $\hat{D}$ or nonlocal equivalent strain $\hat{\epsilon}$). Section 10.4.1 demonstrates the effect of varying triggering zone and selection of solid elements on the localization phenomena with a constant length scale l_c, whereas Section 10.4.2 illustrates the influence of varying length scale l_c on the localization phenomena with a constant triggering zone.

10.4.1 Varying triggering zone

In this section, the numerical problem discussed in Section 11.1.1 is considered again. The bar is discretized along the loading direction with $N = \{16, 32, 64, 128\}$ - Hex8 elements and $n = \{16, 32, 64, 128\}$ - Hex27 elements of constant size respectively. In this example, nonlocal variable $\hat{\zeta}$ is the nonlocal equivalent strain $\hat{\epsilon}$. The numerical simulations are performed using the length scale $l_\mathrm{c} = 4.3\,[\mathrm{mm}]$. In order to trigger the damage localization, the initial damage threshold κ_0 is reduced by approximately 13% in the element, which is located near to the center of the bar when compared to rest of the portion.

Figures 10.23 and 10.24 show the converged results obtained using both Hex8 and Hex27-elements. It can be observed from Figure 10.23 that the stress-softening curves converged upon mesh-refinement and also the meshes of both Hex8 and Hex27 resulted in almost similar

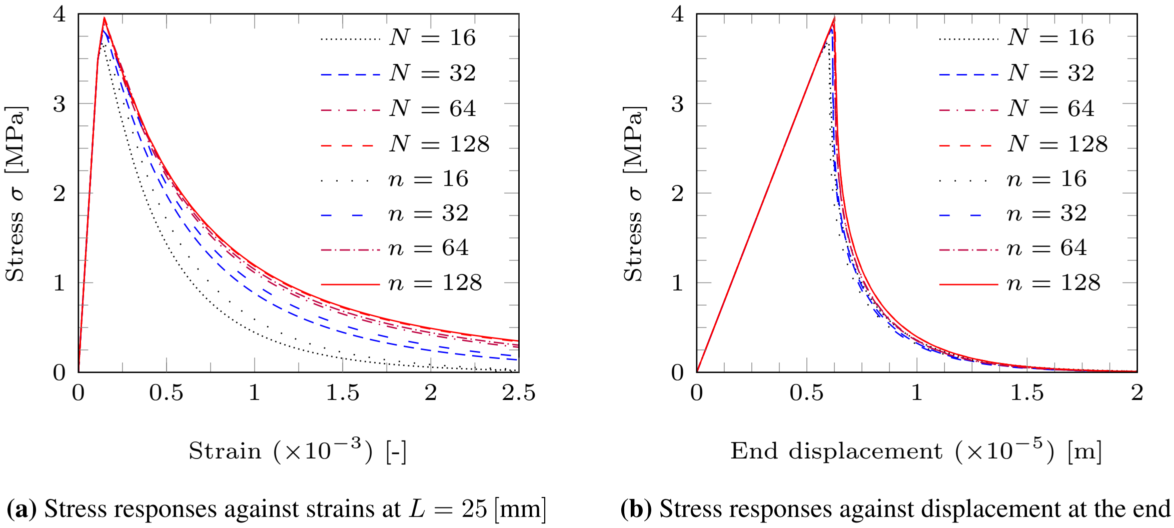

(a) Stress responses against strains at $L = 25$ [mm] **(b)** Stress responses against displacement at the end

Figure 10.23: Convergence of stress obtained using elements (Hex8 and Hex27) for $l_\mathrm{c} = 4.3$ [mm]

responses. Moreover, Figure 10.23a shows the stress responses plotted against strains at a distance of 25 [mm] from the left end. On the other hand, Figure 10.23b depicts the stress responses against the displacement at the end. As the discretization of equal size elements generates varying zone of triggering the damage initiation, i.e., decrease in triggering zone as mesh refines, there is a slight increase in peak stress values upon the mesh-refinement, as noticed in Figure 10.23. This interpretation is also practically acceptable. Nonetheless, finer meshes produce almost similar peak values.

In addition, Figure 10.24 displays the converged local, nonlocal equivalent strains, and damage along the length of bar for the meshes $N = n = 16$ and $N = n = 128$. The depicted results of each mesh correspond to the selected four different loading steps (t_1, t_2, t_3 and t_4) in the post-peak regime. The gray-shaded area inside the figures represents the size of internal length $l_\mathrm{c} = 4.3$ [mm], while the densely gray-shaded area outside the figure represents the triggering zone in the bar. At each time step, there are two distributions shown in every figure. The strain or damage distributions of slightly higher peak values correspond to the mesh of Hex8-elements and the other correspond to the mesh of Hex27-elements. The distributions of local equivalent strains (dashed lines) are compared with that of nonlocal equivalent strains (thick lines) over the localization zone in Figures 10.24a and 10.24c respectively. Similarly, Figures 10.24b and 10.24d display the corresponding damage distribution over the localization zone for the meshes respectively. Selection of meshes of different elements results in only a few differences in the damage distributions as well as nonlocal strains at the triggered zone but showing reasonable differences in the local strains. On the other hand, the comparison of course mesh ($N = n = 16$) and finest mesh ($N = n = 128$) exhibits noticeable observations that that mesh-refinement produces a smooth distribution of damage and strains as well as a better localization of either local or nonlocal equivalent strains irrespective of chosen elements.

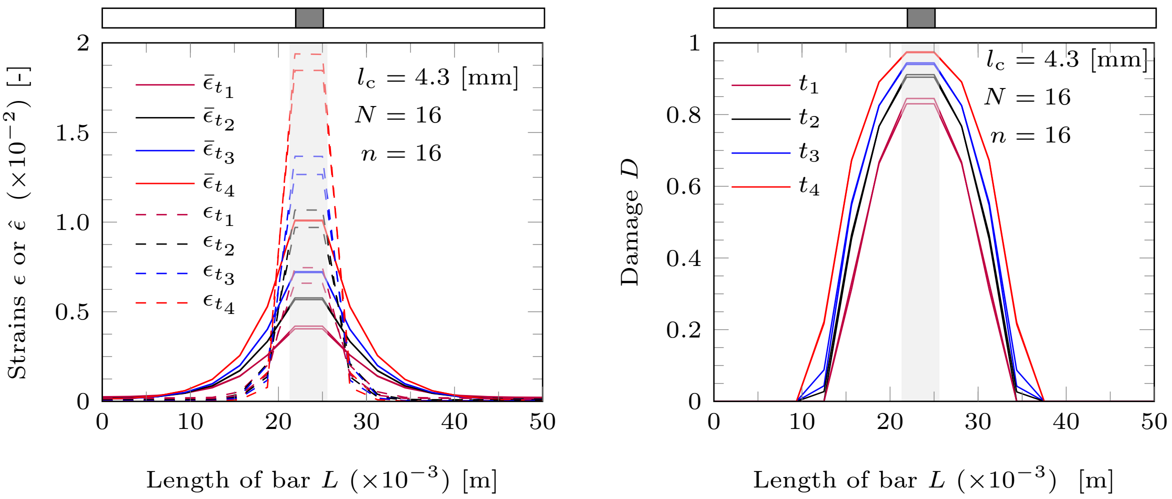

(a) Evolution of local and nonlocal strains

(b) Evolution of damage

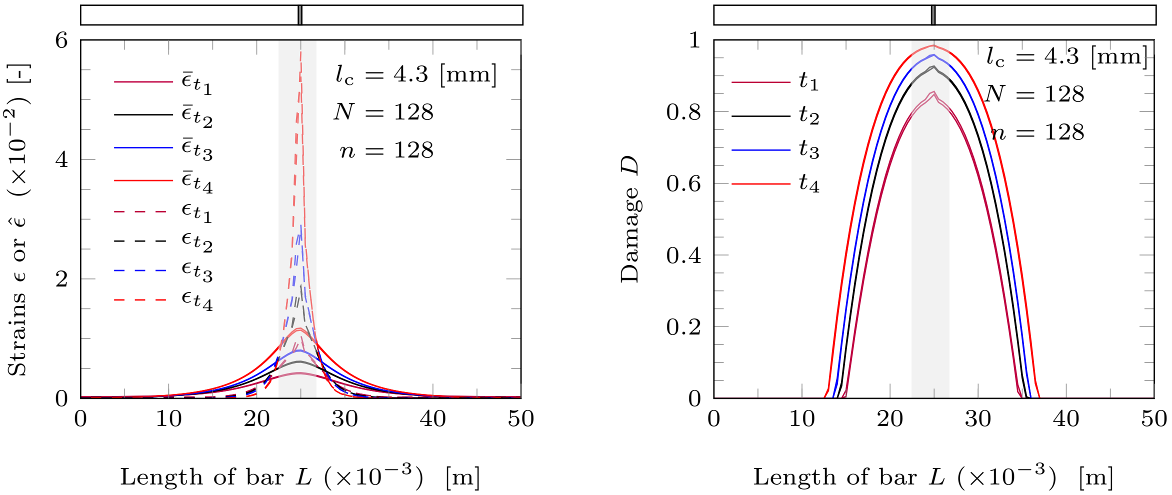

(c) Evolution of local and nonlocal strains

(d) Evolution of damage

Figure 10.24: Converged results using elements (Hex8 and Hex27) for $l_c = 4.3$ [mm]

The use of interpolation functions of same order may cause stress oscillations as it has already been found from the investigations on problems of one-dimension [119] and two-dimensions [22]. Nonetheless, it can not be taken straight a way to problems in three-dimensions. Therefore, the displacement and stress distributions along the bar have also been analyzed and depicted in Figure 10.25 for the respective meshes. In the case of linear-linear interpolations (Hex8), the displacements (dashed lines) are linear within each element, as seen in Figure 10.25a as similar to the local strains and as a consequence, the stress oscillations (dashed lines) due to stress gradients within the element are observed in the triggering zone where the damage and strains become high, as shown in Figure 10.25b. On the contrary, in the case of quadratic-linear interpolations (Hex27), the displacements (solid lines) are linear within each element of same

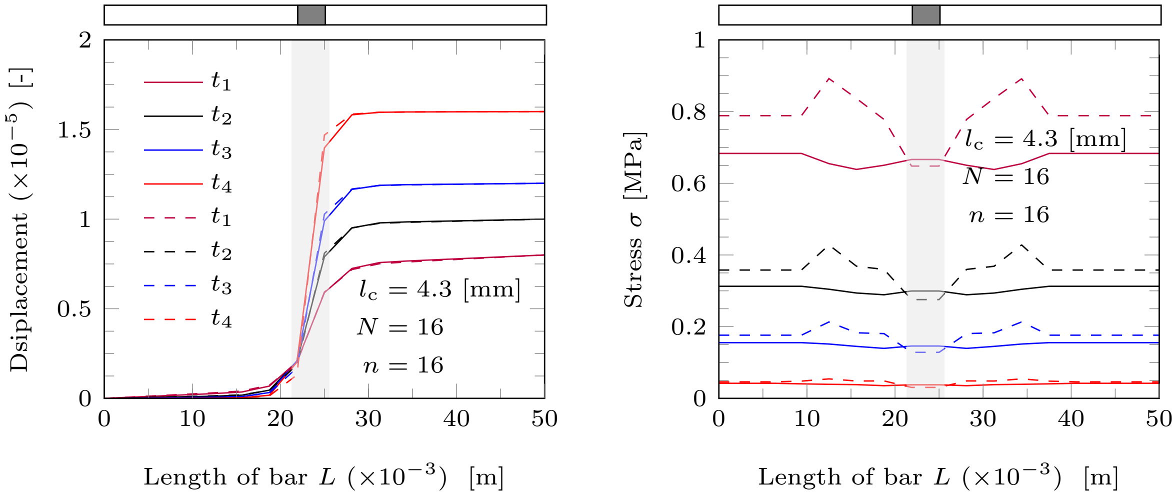

(a) Displacement profiles **(b)** Evolution of stress profiles

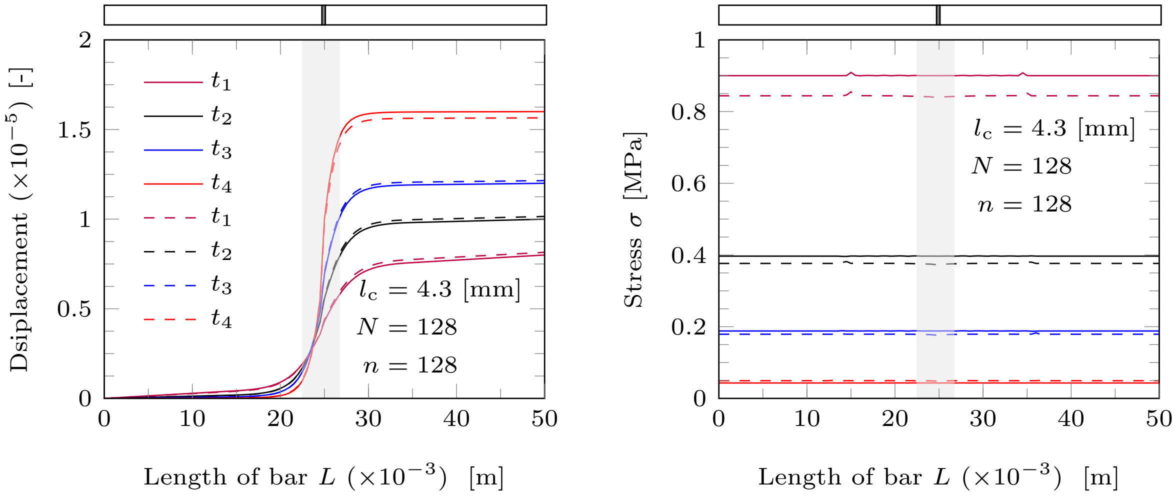

(c) Displacement profiles **(d)** Evolution of stress profiles

Figure 10.25: Converged displacement and stress profiles with Hex8 (dashed) and Hex27 (solid) for $l_c = 4.3$ [mm]

mesh size, as seen in Figure 10.25a, but the stress oscillations (solid lines) are very slightly pronounced in the triggering zone, as shown in Figure 10.25b. On the other hand, the finer meshes with the irrespective of the order of interpolation functions (Hex8 or Hex27) lead to almost no stress oscillations due to the decrease of the stress gradients, which is clearly understood from the Figures 10.25c and 10.25d. This contradicts with the conclusions of Peerlings [119] that the mesh-refinement of the linear-linear interpolation functions does not lead to decrease in stress oscillations.

Nevertheless, the present results of nonlocal equivalent strains and damage distributions are meaningful and acceptable. Thus, further loading increases the subsequent development of damage in broader area, whereas narrowing of localization zone occurs. Thereby, the strong localization/concentration of local equivalent strains replicates the formation of a macro crack, while the smooth distribution of nonlocal equivalent strains replicates the occurrence of microstructural interactions in the neighborhood.

10.4.2 Constant triggering zone

This section illustrates the influence of varying length scale l_{c} on the localization phenomena with a constant size of triggering zone. A bar of size $100\,[\mathrm{mm}] \times 10\,[\mathrm{mm}] \times 10\,[\mathrm{mm}]$ is used to analyze the one-dimensional problem. Triggering of the damage localization is achieved by reducing the initial damage threshold κ_0 by approximately 13% in a 10 [mm] wide zone in the middle of the bar when compared to rest of the portion. The size of the wide zone is constant irrespective of mesh-refinement throughout the analyzes. The bar is discretized into 40, 80, 160-equal sized solid (Hex27) elements along the loading direction (x-axis) respectively. The nonlocal enhancement of local quantities namely ϵ and D based on the implicit-gradient method has been analyzed. Thus, nonlocal variables are the nonlocal equivalent strain $\hat{\epsilon}$ or the nonlocal damage $\hat{D}$. The numerical simulations are performed using different length scales namely $l_{\mathrm{c}} = \{5, 7.5, 10\}$ [mm]. A pure tensile loading is applied under displacement control by means of an imposed displacement at the right end of the bar, which is monotonously increasing, as shown in Figure 10.26a. Figures 10.26b-10.26f show the nonlocal results of nonlocking formulation, whereas Figures 10.27b-10.27f depict the nonlocal results of locking formulation.

10.4.2.1 Nonlocking formulation

The stress-displacement curves generated for the three meshes and for varying internal length scales are depicted in Figure 10.26b. It is clearly observed that the softening curves of every mesh are almost identical and converging faster. It is obvious that a finite energy dissipation has been obtained due to mesh-independent solutions. In addition, the influence of characteristic internal length scale l_{c} on the softening behavior is illustrated in Figure 10.26b. It is also apparent that the brittleness of softening responses is influenced by the internal length. The model responses become brittle; the model loses its stiffness and the peak stress value reduces for decreasing internal lengths, and vice versa. It is due to the fact that the larger internal length makes the localization zone wider. Moreover, the softening responses are also physically meaningful and are free from any locking effects. In order to visualize how the strains and damage distributed over the localization zone, Figure 10.26c and Figure 10.26d display the distributions of nonlocal equivalent strains and resulting damage along the bar obtained for the fine mesh ($n = 160$) at the loading step t_3 using the different length scales respectively.

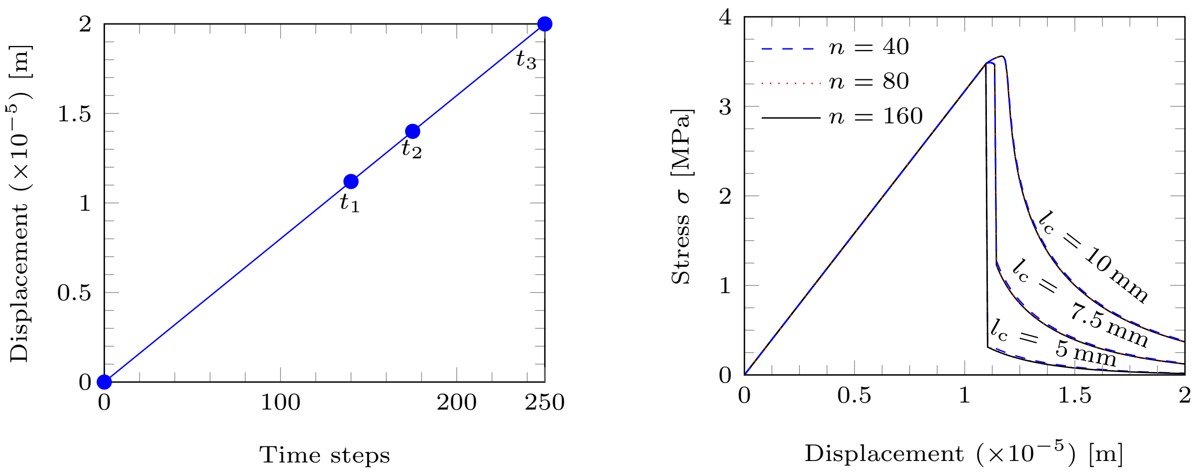

(a) Displacement over time steps

(b) Stress responses for $\hat{\zeta} = \hat{\epsilon}$

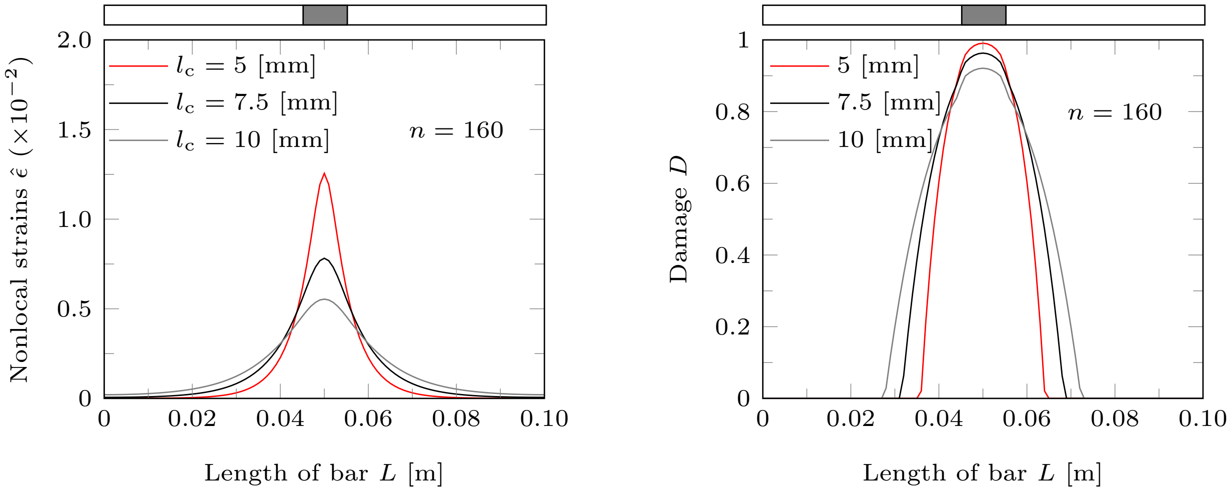

(c) Evolution of nonlocal equivalent strain

(d) Evolution of damage

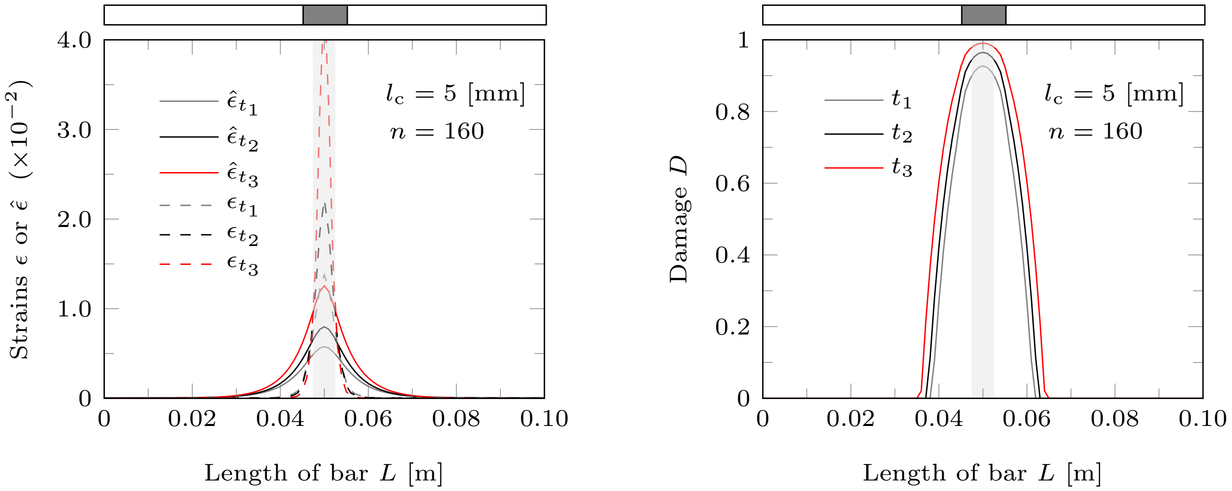

(e) Evolution of local and nonlocal equivalent strain

(f) Evolution of damage

Figure 10.26: Nonlocal solutions of bar for nonlocking formulations $\hat{\zeta} = \hat{\epsilon}$

Indeed, a larger value of l_c allows wider spreading of the nonlocal strains and accordingly the damage becomes wider. In other words, a smaller value of l_c yields strong (narrowing down) localization of nonlocal strains as well as damage at the center of triggered zone.

Furthermore, Figure 10.26e compares the evolution of local and nonlocal equivalent strains corresponding to the three different loading steps (t_1,t_2,t_3) in the post-peak regime, which are obtained for the fine mesh ($n = 160$) with $l_c = 5$ [mm]. As can be observed, the local equivalent strains (dashed lines) are concentrated near the vicinity of the triggered region and further loading increases the narrowing of zone leading to propagation of macro-crack. On the other hand, the nonlocal equivalent strains (thick lines) are spread over the localization zone, physically meaning the occurrence of micro-structural interaction in the neighborhood.

The respective evolution of damage is plotted over the length of the bar in Figure 10.26f. The continued loading leads to the subsequent development of damage. The damage formed in a broader area. Nonetheless, the narrow region of strains is obtained. Thus, the gradient-enhancement of present model describes the physical meaning of crack initiation, growth of micro-cracks, and coalescence of these into a macro-crack, as observed by Peerlings *et.al* [121].

10.4.2.2 Locking formulation

The inspiration of the previous investigations in the case of nonlocal integral models [18, 79] lead to the numerical analyzes of the one- dimensional problem using the present damage model incorporated with the gradient-enhanced damage variable, where the gradient-enhanced damage variable enters into the constitutive law that describes the characteristic behavior of the materials. The interesting results that have been observed are discussed here.

The stress-displacement curves generated for the three meshes and for varying internal length scales are depicted in Figure 10.27b. It is observed that the softening curves are almost identical and thus show convergence upon the mesh-refinement. Likewise, the influence of characteristic internal length scale l_c on the softening behavior can also be understood from Figure 10.27b. It is also apparent that the brittleness of softening responses is influenced by the internal length. The model responses show brittleness due to the loss of its stiffness and the peak stress value reduces for decreasing internal lengths, and vice versa. It is due to the fact that the larger internal length makes the localization zone wider. But the present formulation, on the whole, does not yield a reasonable behavior at later stages of softening, as observed in Figure 10.27b, as the applied displacement is increased. Consequently, this leads to locking effects and therefore fails to predict the realistic behavior of the material.

On the other hand, Figure 10.27c and Figure 10.27d display the distributions of local equivalent strains and nonlocal damage along the bar obtained for the fine mesh ($n = 160$) at the loading step t_3 using the different length scales respectively. A larger value of l_c allows wider spreading of the equivalent strain, as the gradient-enhanced damage (nonlcoal damage) expands wider.

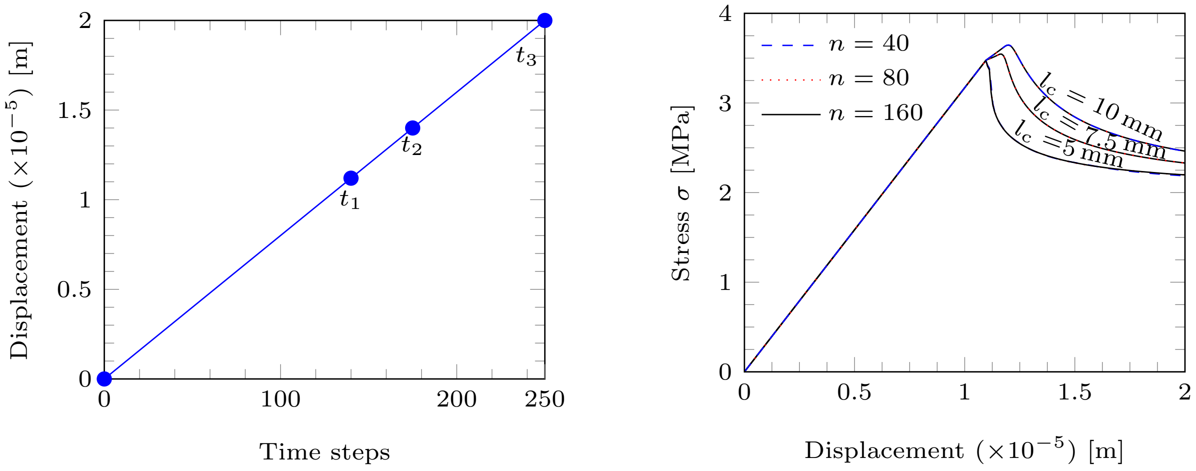

(a) Displacement over time steps

(b) Stress responses for $\hat{\zeta} = \hat{D}$

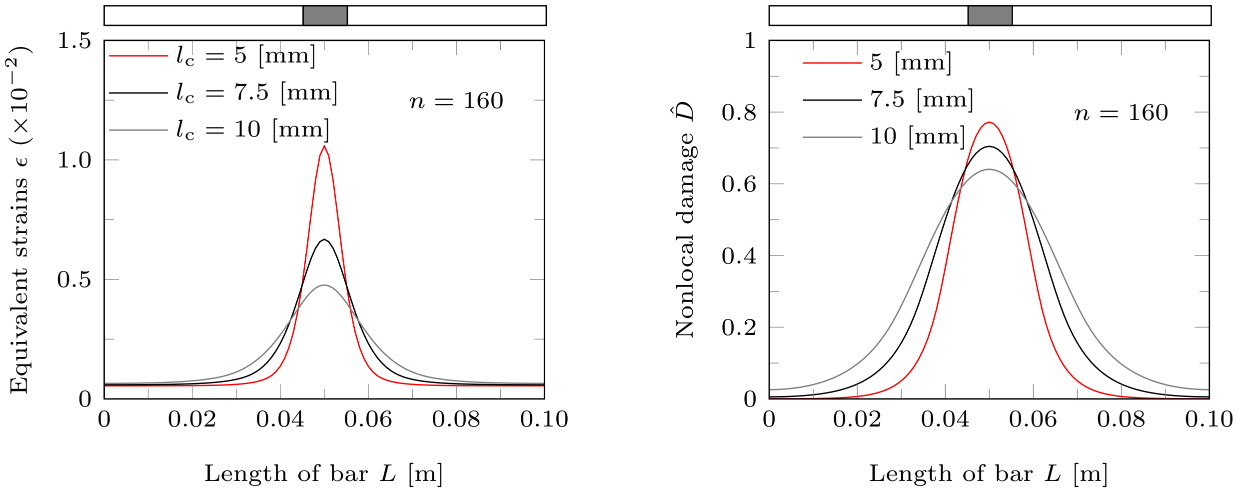

(c) Evolution of equivalent strain

(d) Evolution of nonlocal damage

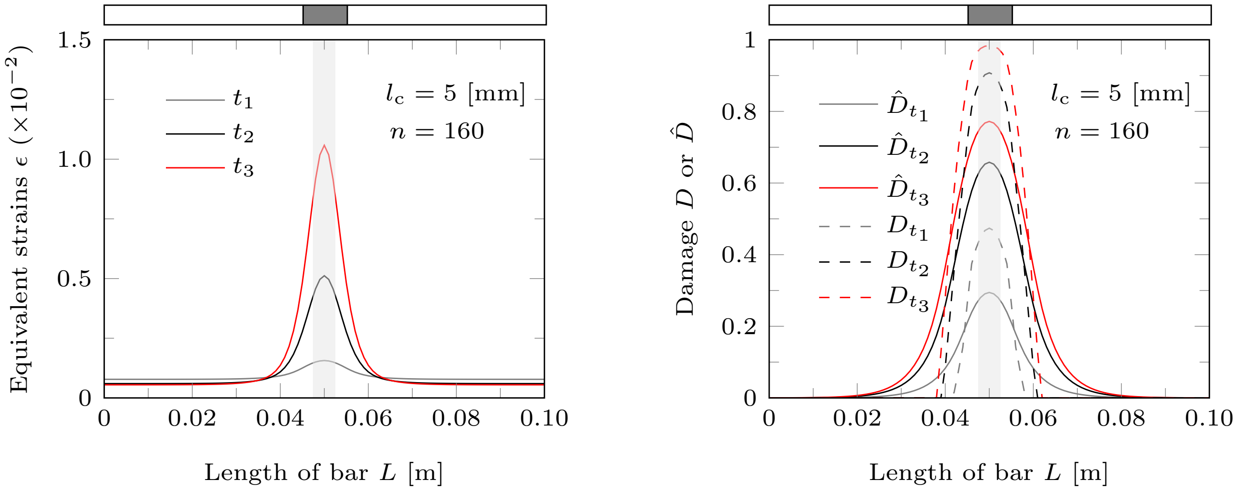

(e) Evolution of local equivalent strain

(f) Evolution of local and nonlocal damage

Figure 10.27: Nonlocal solutions of bar for locking formulations $\hat{\zeta} = \hat{D}$

In other words, a smaller value of l_c yields a strong (narrowed) localization of damage at the center of the triggered zone. At the same time, the widening of damage zone or softening zone occurs across the entire bar, as seen in Figure 10.27d.

Figure 10.27e shows the evolution of local equivalent strains corresponding to the three different loading steps (t_1, t_2, t_3) in the post-peak regime, which are obtained for the fine mesh $(n = 160)$ with $l_c = 5$ [mm]. As can be observed in Figure 10.27f, the local damage (dashed lines) are concentrated near the vicinity of the triggered region, whereas the nonlocal damage (thick lines) are spread over the localization zone.

It can be concluded that post-damage responses are converging upon the mesh-refinement, and the distribution of nonlocal equivalent strains and damage evolution along the bar are controlled by the characteristic internal length l_c. Nevertheless, the gradient enhancement of D leads to locking effects in the softening behavior, meaning that the model fails to produce a realistic behavior of brittle materials like concrete, instead shows a ductile nature beyond certain level of damage even though strains increase. This kind of locking effects in stress have already been observed in use of nonlocal integral models [18, 79] where it is identified that the averaging of damage variable leads to spurious residual stresses and expansion of the softening zone across the entire bar. On the contrary, the implicit gradient enhancement of damage variable D has also been considered as a promising approach to model ductile materials like steel [86, 144, 152] under various loading environments.

11 Applications

Although the mesh-sensitivity and the localization of deformation are illustrated using the developed elastic-isotropic damage model in the previous chapter, the capabilities of the damage model in describing the fracture processes must be verified. Hence, this chapter demonstrates the fracture processes of concrete by simulating the selected fracture problems available in the literature. The FE simulations have been carried out using the model described in Chapter 7.

11.1 Kupfer's plate tests

This section presents the numerical investigations on Kupfer's concrete plate specimen [90] under biaxial tests. The model and material parameters (Data 2) adopted are provided in Table 10.1. Considering homogeneous and non-homogeneous material, there are several loading scenarios such as uniaxial loading $\frac{\sigma_1}{\sigma_2} = 1/0$, biaxial tests $\frac{\sigma_1}{\sigma_2} = 1/1$, and $\frac{\sigma_1}{\sigma_2} = 1/0.54$ discussed in this section. Before performing various numerical tests, mesh-sensitivity is first analyzed to ensure that mesh-independent solutions are obtained, which is presented in the following Section 11.1.1.

11.1.1 Mesh-sensitivity analysis

The size of Kupfer's concrete plate is $200\,[\text{mm}] \times 200\,[\text{mm}] \times 50\,[\text{mm}]$. The geometry of the test specimen and the applied boundary conditions adopted in the numerical simulations are illustrated in Figure 11.1a. The specimen is supported in y-direction (xz-plane), and both the left

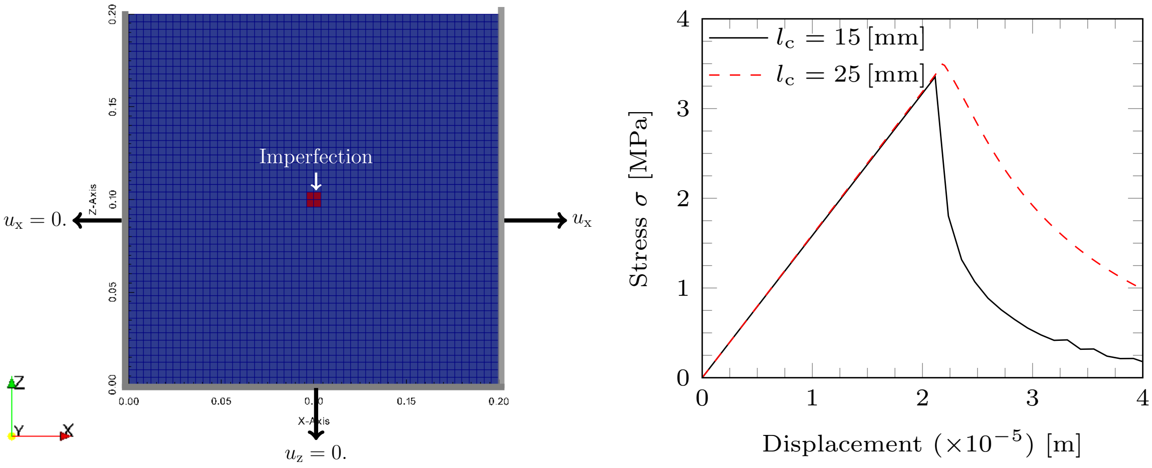

(a) Geometry and boundary conditions I (50 × 50)

(b) Stress responses

Figure 11.1: Kupfer's plate subjected to (a) uniaxial tension $\frac{\sigma_1}{\sigma_2} = 1/0$ - All dimensions are in [m] (b) Comparison of stress responses for different length scales. The model and material parameters (Data 2) are as provided in Table 10.1.

and bottom edge surfaces are prevented from moving horizontally, i.e., the displacements along x- and z-directions are constrained respectively). The tensile loading is applied incrementally, by means of prescribing the horizontal displacement increments on the right surface of the plate (displacement control). The horizontal displacement degrees of freedom on the right surface, i.e., the displacements along the x-axis direction are constrained to be equal in order to simulate the rigid platen at the loaded surface. The plate is discretized by 40×40 and 50×50 (Hex27) elements. An imperfection is additionally introduced into the specimens to trigger the localization of deformation, as shown in Figure 11.1a. In order to simulate the imperfection, the initial damage threshold κ_0 of four elements in the middle of both the meshes is reduced to $0.1\,\kappa_0$ in the mesh sensitivity analyses.

According to the recommendation [21], the internal length l_c must be approximately greater than 3 times the maximum size d_a of aggregate. The internal length scales $l_c = \{15, 25\}$ [mm] are used initially. Figure 11.1b displays the stress-deformation curves obtained using two different internal lengths. The lesser value of internal length leads to faster growth of damage and thus causes the narrow width of localization band. Therefore, the softening behavior that corresponds to $l_c = 15$ [mm] exhibits sudden decrease rather showing gradual decrease that observed in the case of $l_c = 25$ [mm]. Thus, the internal length $l_c = 25$ [mm]$(\approx 3\,d_a)$ is considered as an appropriate value for a reliable softening behavior.

Subsequently, the numerical results illustrated in Figures 11.2-11.4 are obtained from the two different finite element meshes for $l_c = 25$ [mm]. The stress-deformation curves are shown in Figure 11.2. It is observed that the responses of the coarse mesh are close to those of the fine mesh and thereby leading to mesh-insensitive results. The brittle failure, damage initiation, and propagation can be observed by means of the softening behavior after the peak stress, as the deformation starts localizing. Likewise, the nonlocal strain distributions along the middle x-axis of both the meshes are shown in Figure 11.3. It can also be seen that the results are converged

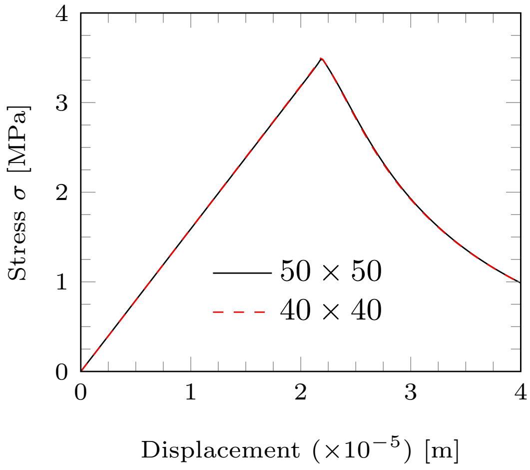

Figure 11.2: Softening curves

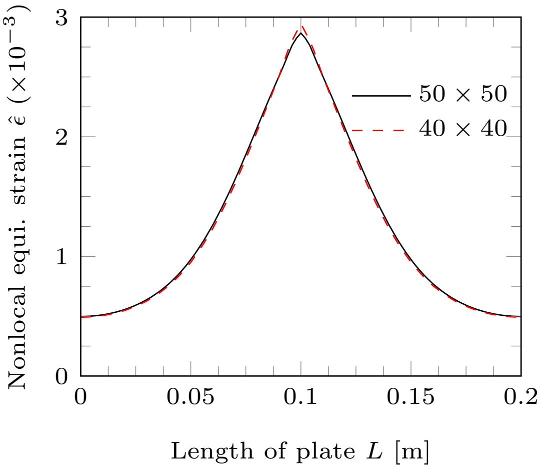

Figure 11.3: Convergence of strains

upon the mesh-refinement and exhibiting localization of strains at the triggered region.

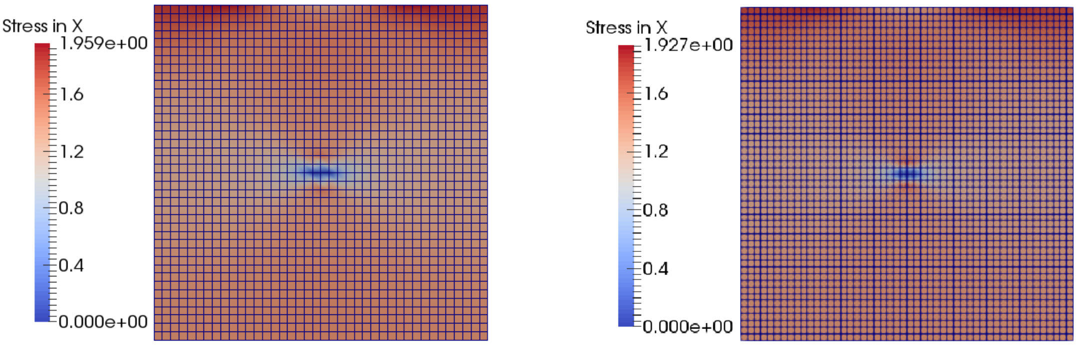

(a) Stress distribution 40×40 **(b)** Stress distribution 50×50

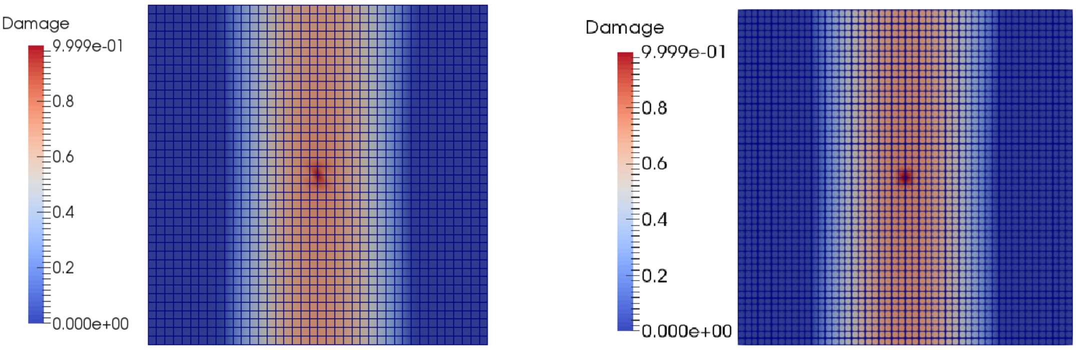

(c) Damage distribution 40×40 **(d)** Damage distribution 50×50

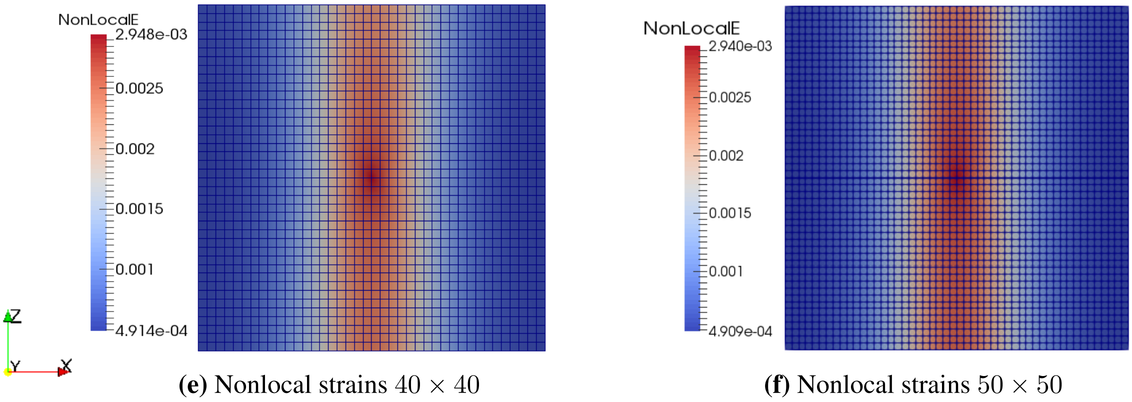

(e) Nonlocal strains 40×40 **(f)** Nonlocal strains 50×50

Figure 11.4: Kupfer's plate under uniaxial tension using the meshes 40×40 (left) and 50×50 (right) at displacement $u_x = 0.03\,[\mathrm{mm}]$

Furthermore, the distributions of stresses, damage, and nonlocal equivalent strains in xz-plane are depicted in Figure 11.4 for two different meshes. These results are corresponding to a selected load step in the post-peak region. As observed, the damage initiation begins in the middle of the plate specimen where the triggering point is located and propagates towards the sides. It can also be seen that damage propagation is normal to the direction of applied tensile loading, as displayed in Figures 11.4c and 11.4d. As a consequence, the stress decreases at the triggered region with respect to other regions, as shown in Figures 11.4a and 11.4b. The distributions of nonlocal strains of both the meshes are shown in Figures 11.4e and 11.4f, which evidence the localization of deformation at the triggered region. Thus, the gradient enhancement of local damage models is unavoidable to obtain mesh-insensitive and physically meaningful solutions.

11.1.2 Without any imperfection

This section provides the uniaxial ($\frac{\sigma_1}{\sigma_2} = 1/0$) and biaxial tests ($\frac{\sigma_1}{\sigma_2} = 1/1$ and $\frac{\sigma_1}{\sigma_2} = 1/0.54$) by considering the material as homogeneous. It means that no imperfection is introduced in the model. The mesh 40×40 is adopted using the internal length l_c as $25\,[\mathrm{mm}]$. The geometry

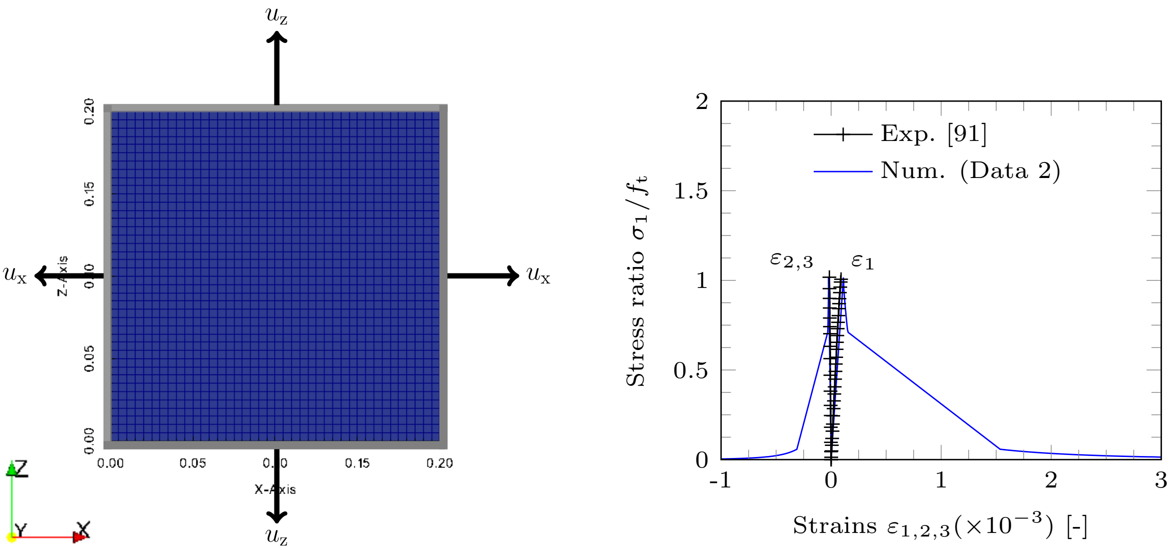

(a) Geometry and boundary conditions (40×40)

(b) Uniaxial tension $\sigma_1/\sigma_2 = 1/0$

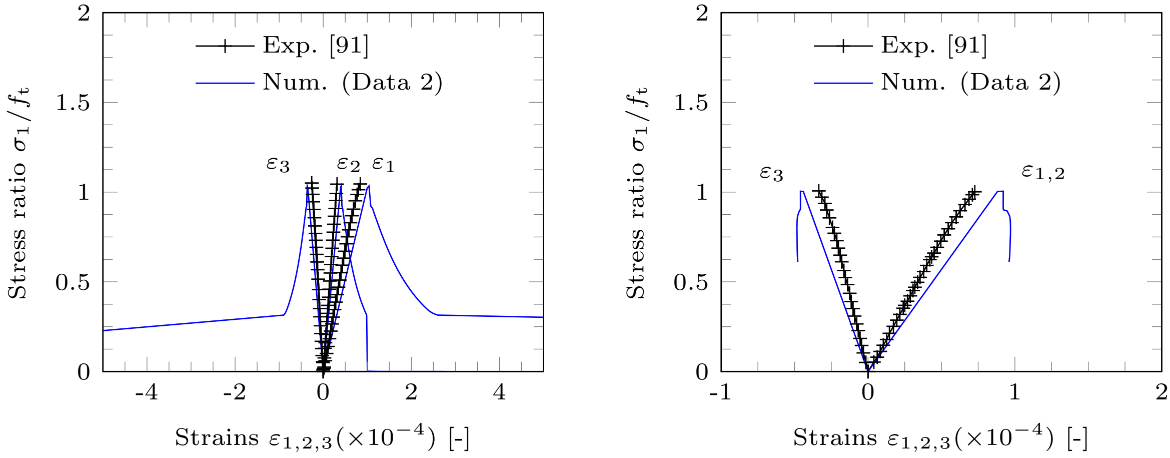

(c) Biaxial tension $\sigma_1/\sigma_2 = 1/0.54$

(d) Biaxial tension $\sigma_1/\sigma_2 = 1/1$

Figure 11.5: Without any imperfection. (a) Geometry and boundary conditions and (b-d) Stress-strain behavior

and boundary conditions are shown in Figure 11.5a. In the case of uniaxial test, incremental displacements are applied at the left and right end surfaces of the specimen (along x-axis) and the direction along z-axis is free to move. In the case of biaxial tests, the displacements are applied at all the end surfaces (along x-, and z-axes). But the movement along y-axis is restricted in both the test cases.

Figure 11.5 depicts the stress-strain behavior obtained at the top-right corner. The nonlocal

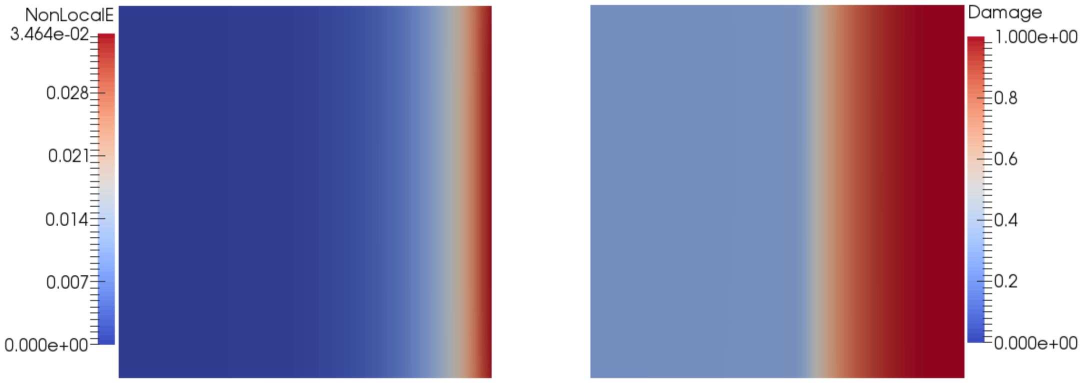

(a) Nonlocal strains $\sigma_1/\sigma_2 = 1/0$ **(b)** Damage $\sigma_1/\sigma_2 = 1/0$

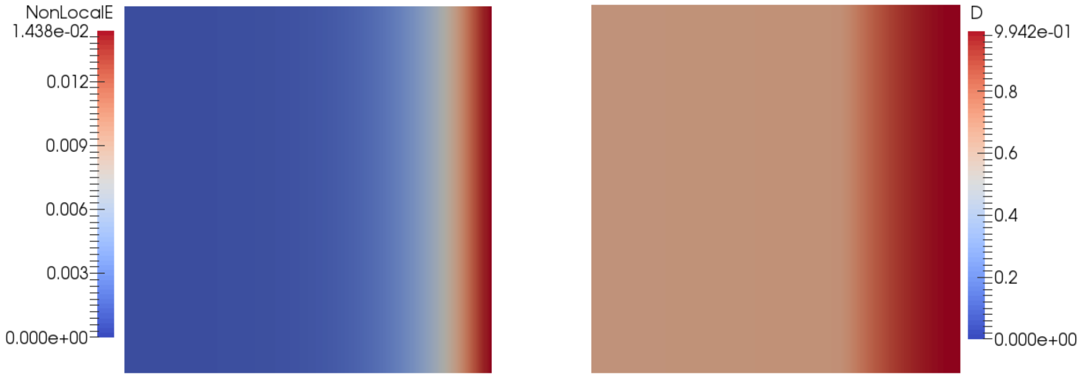

(c) Nonlocal strains $\sigma_1/\sigma_2 = 1/0.54$ **(d)** Damage $\sigma_1/\sigma_2 = 1/0.54$

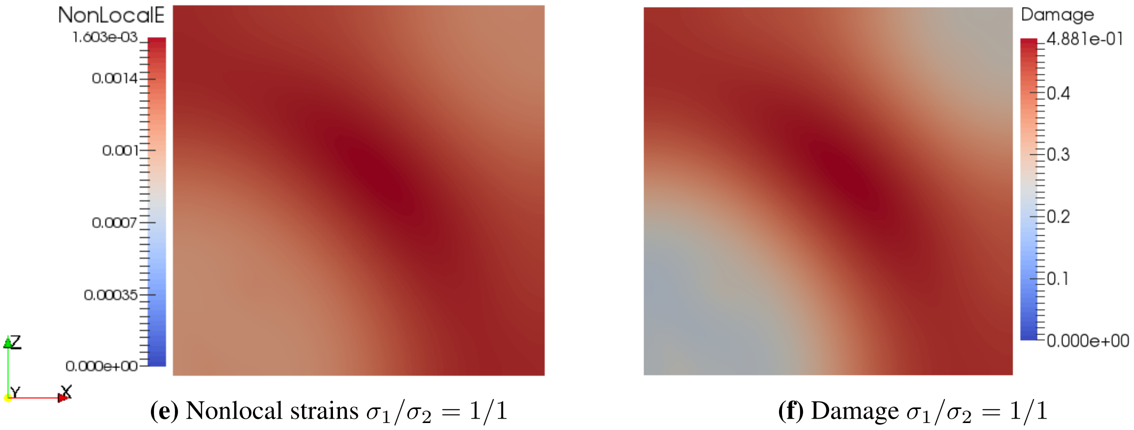

(e) Nonlocal strains $\sigma_1/\sigma_2 = 1/1$ **(f)** Damage $\sigma_1/\sigma_2 = 1/1$

Figure 11.6: Without any imperfection. Nonlocal strains and damage at displacements (a,b) $u_{\mathrm{x}} = 0.0583$ [mm], (c,d) $u_{\mathrm{x/z}} = 0.025/0.01$ [mm], and (e,f) $u_{\mathrm{x/z}} = 0.0125$ [mm]

equivalent strains and damage distribution at the final load step are shown in Figure 11.6. As long as a gradual decrease is observed in stress, as shown in Figures 11.5b and 11.5c, the model exhibits homogeneous deformation throughout the specimen, meaning that the nonlocal strain and the consequent damage are equally distributed throughout the specimen. As soon as a sudden drop in stress to a minimum or zero occurs, the nonlocal strain and the damage get maximum at the right end, as shown in Figures 11.6a-11.6d. By contrast, the nonlocal strains and damage under biaxial test $\sigma_1/\sigma_2 = 1/1$ are localized along the diagonal, as shown in Figures 11.6e and 11.6f respectively.

Thus, the localization bands of deformation shown in Figures 11.6a and 11.6c by considering homogeneous material do not agree with the actual crack formations observed in the uniaxial ($\sigma_1/\sigma_2 = 1/0$) and biaxial ($\sigma_1/\sigma_2 = 1/1$) experiments shown in Figure 11.19 and Figure 11.21 respectively. Nevertheless, the localized band of deformation observed in Figure 11.6e can only be comparable with the experimental crack shown in Figure 11.20.

11.1.3 With completely random imperfections

In this section, the numerical tests ($\sigma_1/\sigma_2 = 1/0$ and $\sigma_1/\sigma_2 = 1/1$) are performed by introducing the imperfections throughout the specimen. The imperfections are simulated by introducing randomness in the model in two ways. The randomness is introduced either in the elasticity modulus of the material E or in the initial damage threshold value κ_0. The geometry and boundary/loading conditions are as same as explained in the previous section 11.1.2.

11.1.3.1 Randomness in E

At first, the elasticity modulus of the material E is considered as a random variable. The randomness of the variable is based on the continuous uniform distribution defined by the boundary parameters as $\pm 10\%$ of the given value E.

Figure 11.7 shows the results of specimen introduced with random imperfections (in E) completely under uniaxial and equibiaxial test cases. The corresponding stress-strain behaviors obtained are shown in Figures 11.7a and 11.7b. As can be seen, the initial stress decrease corresponds to the initial damage that occurs shown in Figures 11.7c and 11.7d. After a certain level of damage, the damage does not propagate and localize, as softening does not occur. The reason behind is that the computations are stopped due to non-convergence of equation system, irrespective of increment size either smaller or larger.

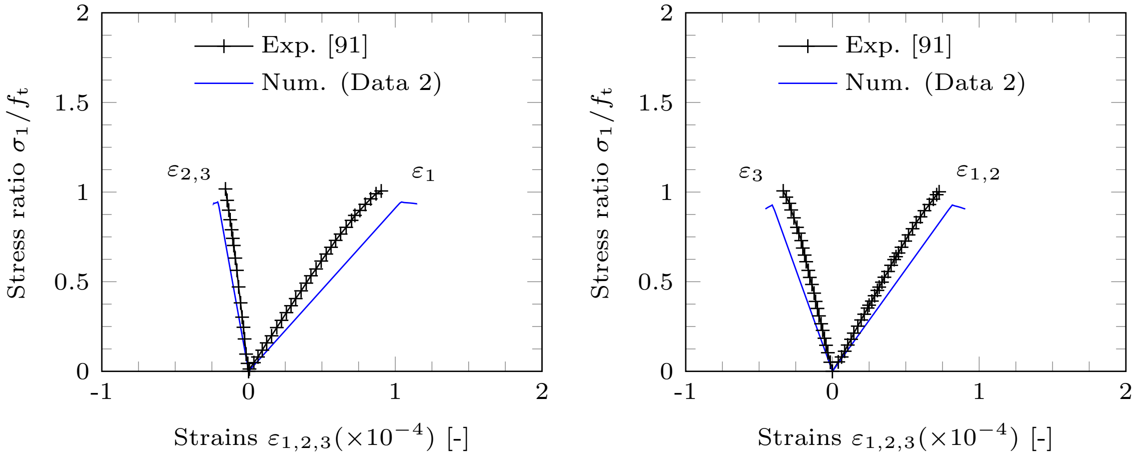

(a) Uniaxial tension $\sigma_1/\sigma_2 = 1/0$ **(b)** Biaxial tension $\sigma_1/\sigma_2 = 1/1$

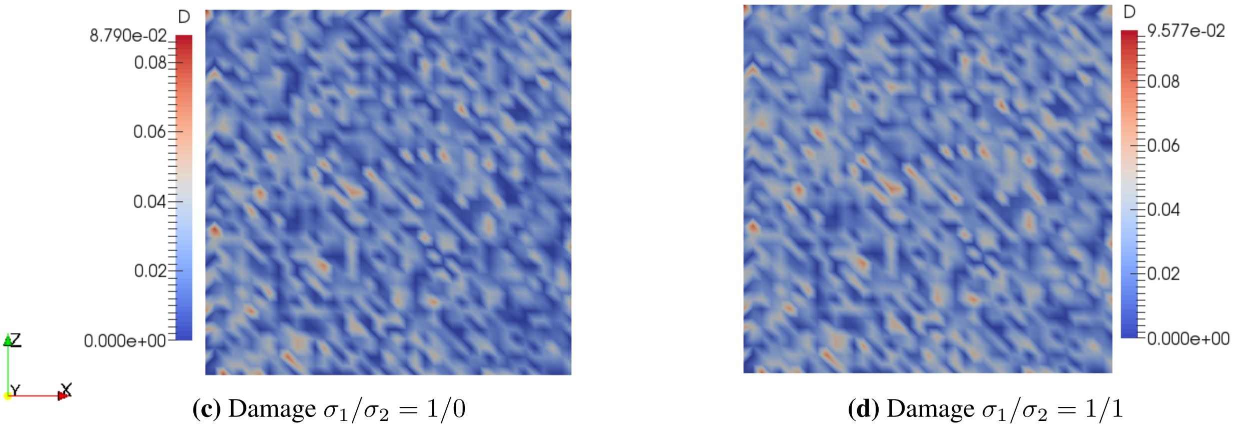

(c) Damage $\sigma_1/\sigma_2 = 1/0$ **(d)** Damage $\sigma_1/\sigma_2 = 1/1$

Figure 11.7: With completely randomness in E. (a,b) Stress-strain behavior and (c,d) damage distribution at displacement $u_{\mathrm{x}} = 0.0108$ [mm] and $u_{\mathrm{x/z}} = 0.0085$ [mm] respectively

11.1.3.2 Randomness in κ_0

Secondly, the initial threshold value κ_0 is considered as a random variable. Similarly, the randomness of the variable is based on the continuous uniform distribution defined by the boundary parameters as $\pm 10\%$ of the given value κ_0.

Figure 11.8 shows the results of specimen introduced with random imperfections (in κ_0) completely under uniaxial and equibiaxial test cases. The corresponding stress-strain behaviors obtained are shown in Figures 11.7a and 11.8b. As observed, Figure 11.7a shows that the softening does not occur even though there is some level of damage that occurs under uniaxial test, as shown in Figure 11.8c. The damage seems to be higher at the left end. Thereafter, the computations are stopped due to non-convergence of equation system as happened earlier. On the other hand, the softening behavior is observed under biaxial test, as seen in Figure 11.8b.

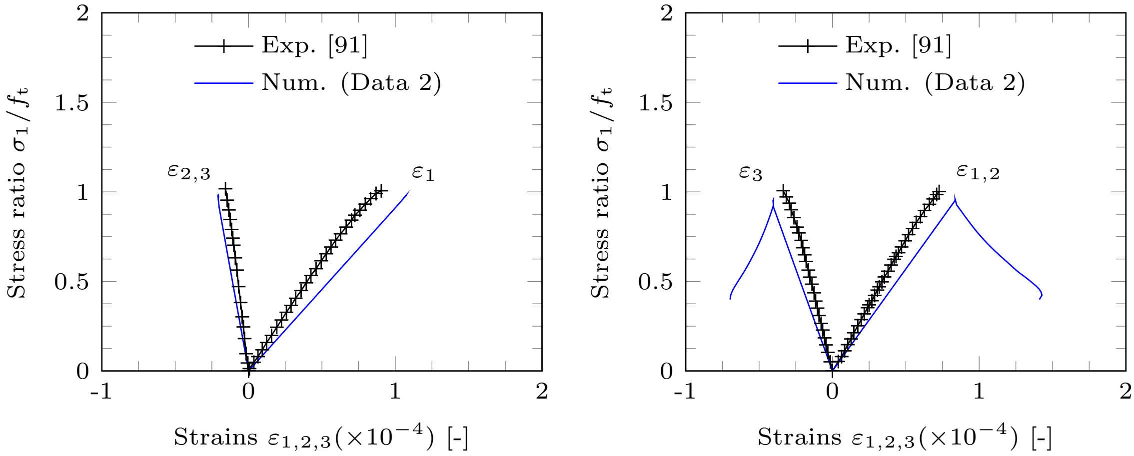

(a) Uniaxial tension $\sigma_1/\sigma_2 = 1/0$ **(b)** Biaxial tension $\sigma_1/\sigma_2 = 1/1$

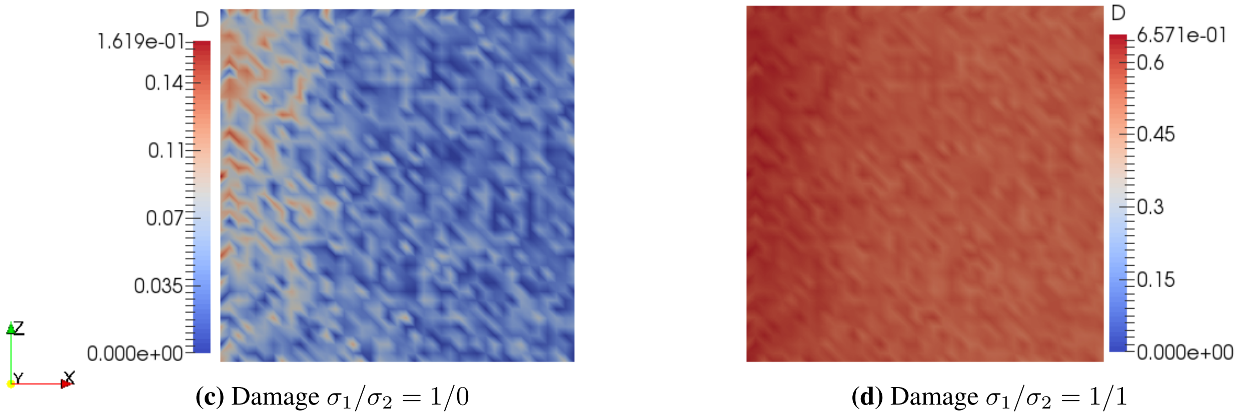

(c) Damage $\sigma_1/\sigma_2 = 1/0$ **(d)** Damage $\sigma_1/\sigma_2 = 1/1$

Figure 11.8: With completely randomness in κ_0. (a,b) Stress-strain behavior and (c,d) damage distribution at displacement $u_x = 0.0112$ [mm] and $u_{x/z} = 0.0175$ [mm] respectively

The corresponding damage distribution is shown in Figure 11.8d and the damage seems to be localized at the left end.

Thus, the introduction of complete randomness in the material parameters like E or κ_0 using the present model does not provide any meaningful information on the localization behavior during the fracture process. Therefore, it will also be interesting to analyze the models if the randomness in the material parameters is only introduced in the randomly selected elements of the mesh, which will be discussed in the following section.

11.1.4 With selectively random imperfections

In this section, the numerical tests such as uniaxial test ($\sigma_1/\sigma_2 = 1/0$) and biaxial tests ($\sigma_1/\sigma_2 = 1/1, \sigma_1/\sigma_2 = 1/1$) are performed by introducing the imperfections only in the selected elements of the mesh randomly. The imperfections are simulated by reducing the initial damage threshold value κ_0 by $3 - 15\%$.

11.1.4.1 Uniaxial tension $\frac{\sigma_1}{\sigma_2} = 1/0$

Moreover, an another numerical example using the mesh (40×40) is additionally considered by setting both the top and bottom surfaces free to displace and the tensile loading is applied at both the right and left edge surfaces horizontally by prescribing displacement increments along x-axis, as shown in Figure 11.9a. In this example, the imperfection is simulated by reducing the initial damage threshold κ_0 of four elements in the middle of the plate by 10%. The material

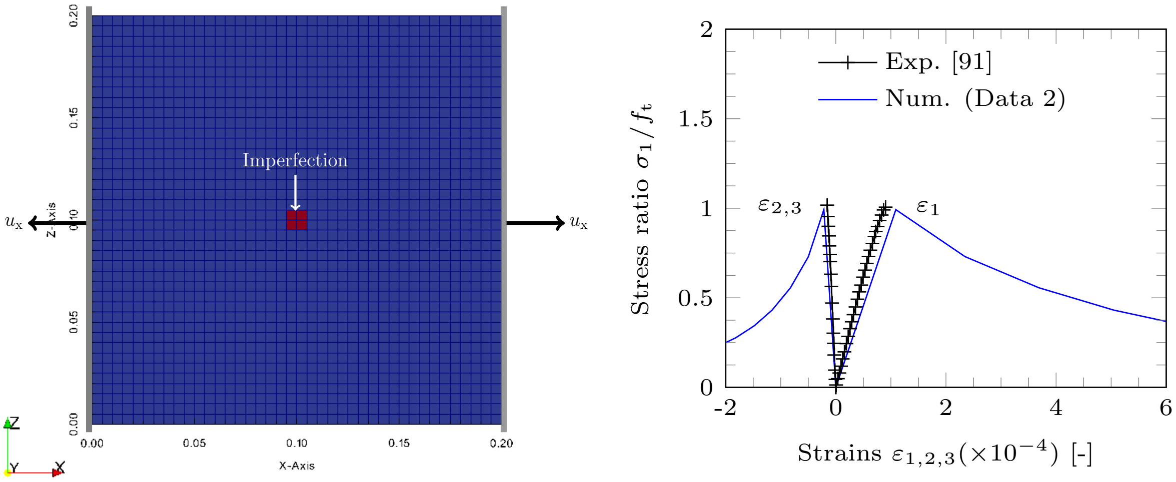

(a) Geometry and boundary conditions II (40×40)

(b) Normalized stress-strain curves

Figure 11.9: Kupfer's plate subjected to (a) uniaxial tension $\frac{\sigma_1}{\sigma_2} = 1/0$ - All dimensions are in [m] (b) Comparison of normalized stress responses with experiments [91]. The model and material parameters (Data 2) are as provided in Table 10.1.

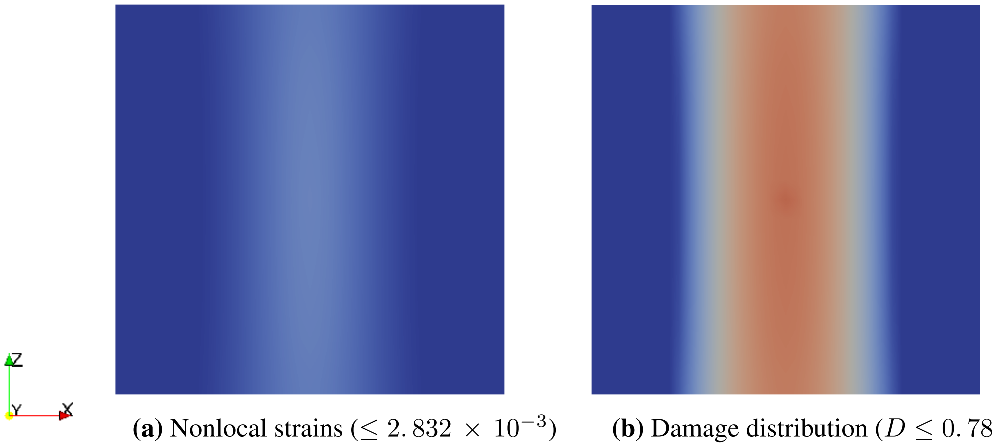

(a) Nonlocal strains $(\leq 2.832 \times 10^{-3})$

(b) Damage distribution $(D \leq 0.7897)$

Figure 11.10: Kupfer's plate under unaxial tension $\sigma_1/\sigma_2 = 1/0$ at displacements (a, b) $u_x = 0.01642$ [mm], (c, d) $u_x = 0.01936$ [mm], (e, f) $u_x = 0.2817$ [mm], and (g, h) $u_x = 0.04$ [mm]

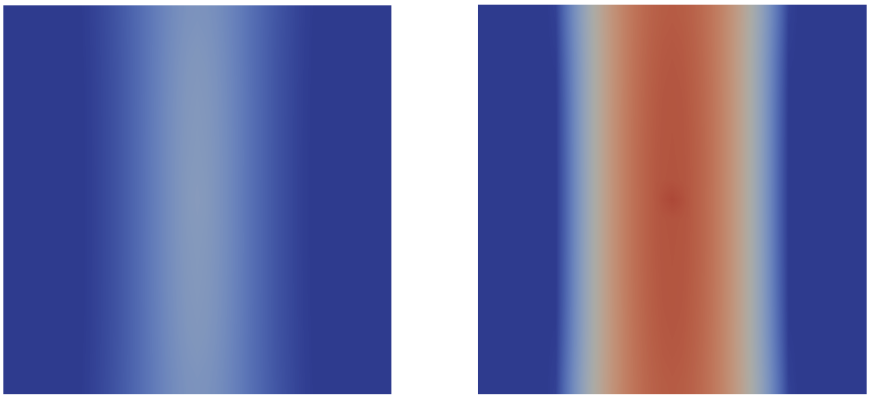

(c) Nonlocal strains ($\leq 3.733\ \times\ 10^{-3}$) **(d)** Damage distribution ($D \leq 0.8645$)

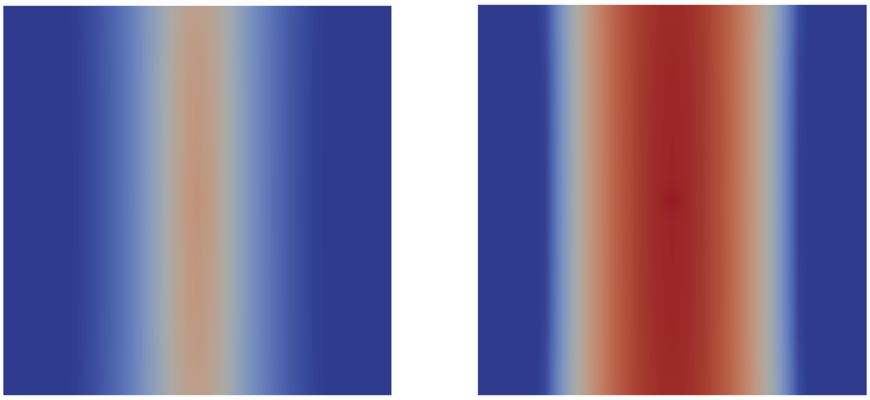

(e) Nonlocal strains ($\leq 6.360\ \times\ 10^{-3}$) **(f)** Damage distribution ($D \leq 0.9526$)

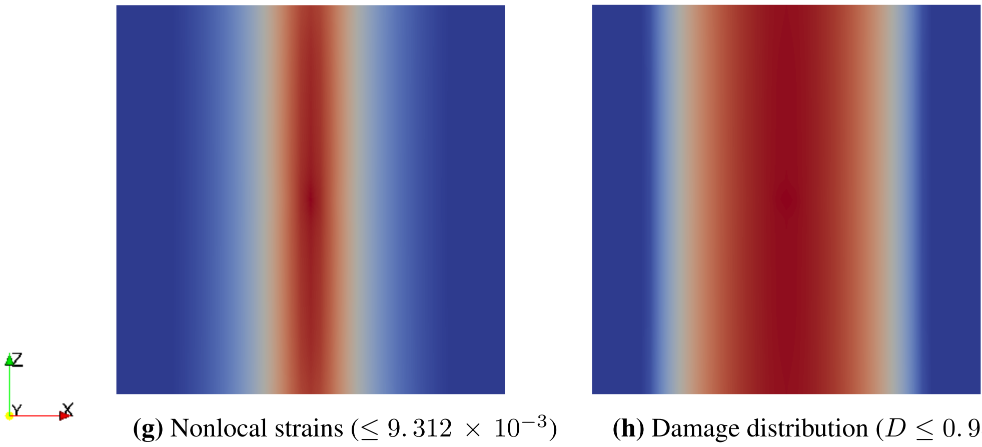

(g) Nonlocal strains ($\leq 9.312\ \times\ 10^{-3}$) **(h)** Damage distribution ($D \leq 0.9825$)

Figure 11.10: Kupfer's plate under uniaxial tension $\sigma_1/\sigma_2 = 1/0$ at displacements (a, b) $u_\mathrm{x} = 0.01642\,[\mathrm{mm}]$, (c, d) $u_\mathrm{x} = 0.01936\,[\mathrm{mm}]$, (e, f) $u_\mathrm{x} = 0.2817\,[\mathrm{mm}]$, and (g, h) $u_\mathrm{x} = 0.04\,[\mathrm{mm}]$

and model parameters and internal length are as same as in the previous example.

The stress values obtained at the triggered point are normalized by the uniaxial tensile strength f_t of concrete. The normalized stresses are plotted against strains and compared with experimental curves [91] in Figure 11.9b. The model predicts the softening behavior after the peak stress. But the experimental curves are only available upto peak stress values, as the experiments were performed under stress controlled loading. Nonetheless, the simulation results are well in agreement with experimental data. Figure 11.10 illustrates the evolution of nonlocal equivalent strains and corresponding damage evolutions along the length of the plate upon increase in the applied displacements. It is witnessed that both the nonlocal strains and damage originate at the triggered point and propagates normal to the direction of applied loading. Further increase in loading causes the propagation of damage or nonlocal strains along the loading direction, meaning that the width of localization increases. As displayed in Figure 11.10g, the localized strains can be comparable with the macro crack shown in Figure 11.19, which formed normal to the direction of applied loading in Kupfer's experimental investigations [91]. The damage broadened area shows the region of reduced stiffness of the material.

11.1.4.2 Biaxial tension $\frac{\sigma_1}{\sigma_2} = 1/1$

In this example, Kupfer's equi-biaxial test is simulated using two different internal lengths $l_\mathrm{c} = \{20, 25\}$ [mm]. The geometry and boundary conditions of the test problem are shown in Figure 11.11a. The right and bottom edge surfaces are restricted from movements along x- and z-directions. The prescribed displacements are applied on the left and top edge surfaces. Herein, few elements are randomly chosen as imperfections by reducing the initial damage threshold by $3-15\%$ in order to simulate in-homogeneity of concrete material in the model. These variations in the threshold values are highlighted by different colors in the mesh.

Figure 11.11b depicts the normalized stress-strain curves obtained that are compared against the experimental data [91] in which the softening data is not available. The results are still good in

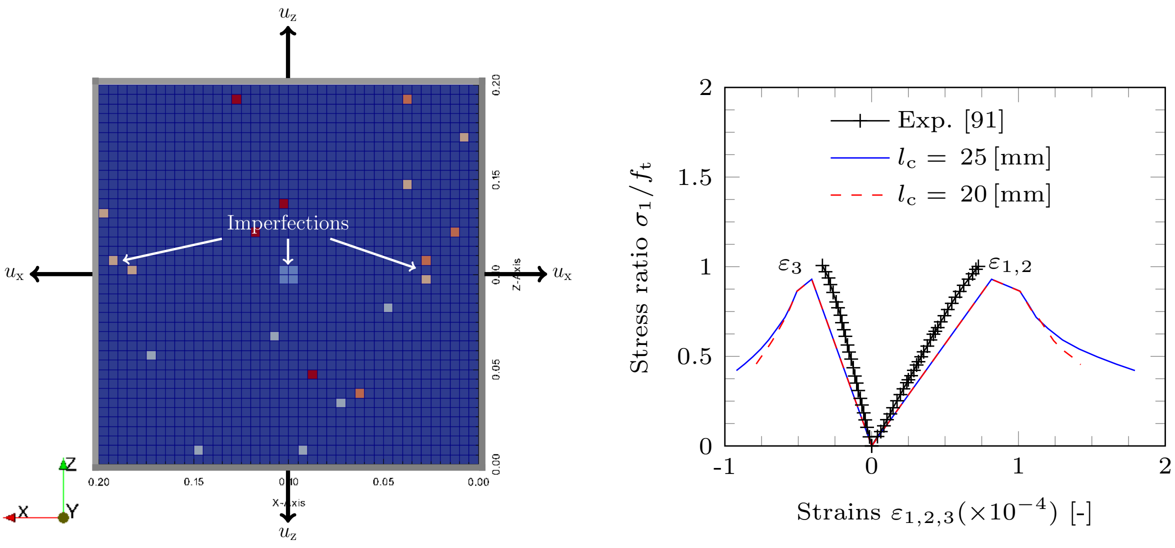

(a) Geometry and boundary conditions III (40 × 40)

(b) Normalized stress-strain curves

Figure 11.11: Kupfer's plate subjected to (a) biaxial tension $\frac{\sigma_1}{\sigma_2} = 1/1$ - All dimensions are in [m] (b) Comparison of normalized stress responses with experiments [91]. The model and material parameters (Data 2) are as provided in Table 10.1.

agreement. It can also be noticed that lower values of the internal length scale cause faster damage growth and in turn softening occurs faster than the use of higher length scale. Figure 11.12 shows the nonlocal strains and corresponding damage progression at various loading stages for $l_\mathrm{c} = 25\,[\mathrm{mm}]$. As soon as the damage criterion is fulfilled, the damage starts and further develops with the increase in the nonlocal strains. Figure 11.12a depicts the nonlocal strains during

(a) Nonlocal strains ($\leq 0.9088\ \times\ 10^{-3}$) **(b)** Damage distribution ($D \leq 0.1326$)

(c) Nonlocal strains ($\leq 1.052\ \times\ 10^{-3}$) **(d)** Damage distribution ($D \leq 0.2560$)

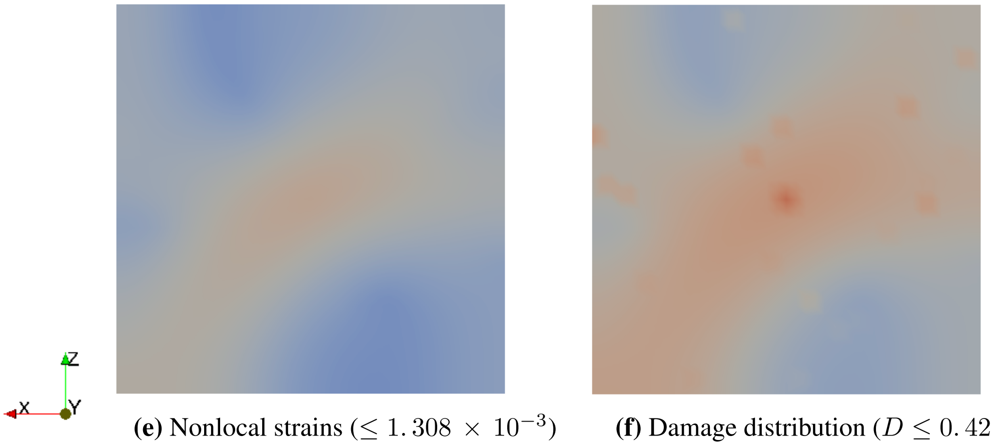

(e) Nonlocal strains ($\leq 1.308\ \times\ 10^{-3}$) **(f)** Damage distribution ($D \leq 0.4263$)

Figure 11.12: Kupfer's plate under biaxial tension $\sigma_1/\sigma_2 = 1/1$ for $l_\mathrm{c} = 25\,[\mathrm{mm}]$ at displacements (a, b) $u_{\mathrm{x/z}} = 0.01745\,[\mathrm{mm}]$, (c, d) $u_{\mathrm{x/z}} = 0.01968\,[\mathrm{mm}]$, (e, f) $u_{\mathrm{x/z}} = 0.02302\,[\mathrm{mm}]$, and (g, h) $u_{\mathrm{x/z}} = 0.02636\,[\mathrm{mm}]$

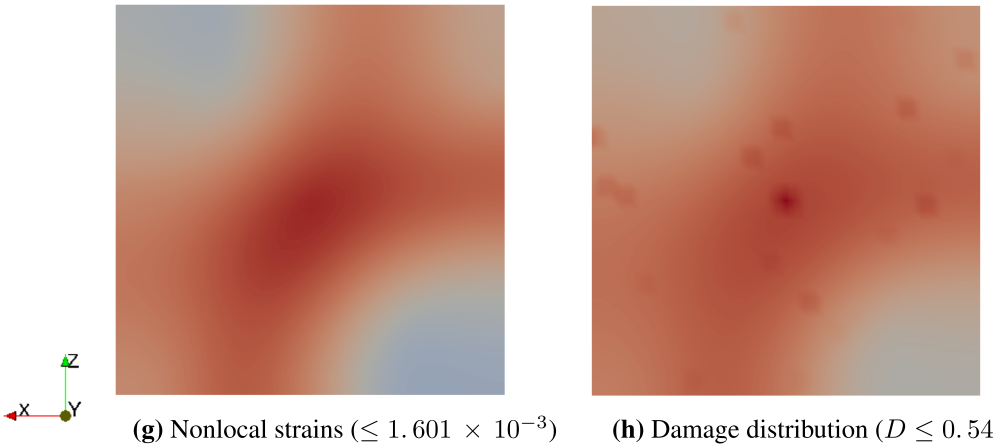

(g) Nonlocal strains ($\leq 1.601 \times 10^{-3}$) **(h)** Damage distribution ($D \leq 0.5476$)

Figure 11.12: Kupfer's plate under biaxial tension $\sigma_1/\sigma_2 = 1/1$ for $l_c = 25$ [mm] at displacements (a, b) $u_{x/z} = 0.01745$ [mm], (c, d) $u_{x/z} = 0.01968$ [mm], (e, f) $u_{x/z} = 0.02302$ [mm], and (g, h) $u_{x/z} = 0.02636$ [mm]

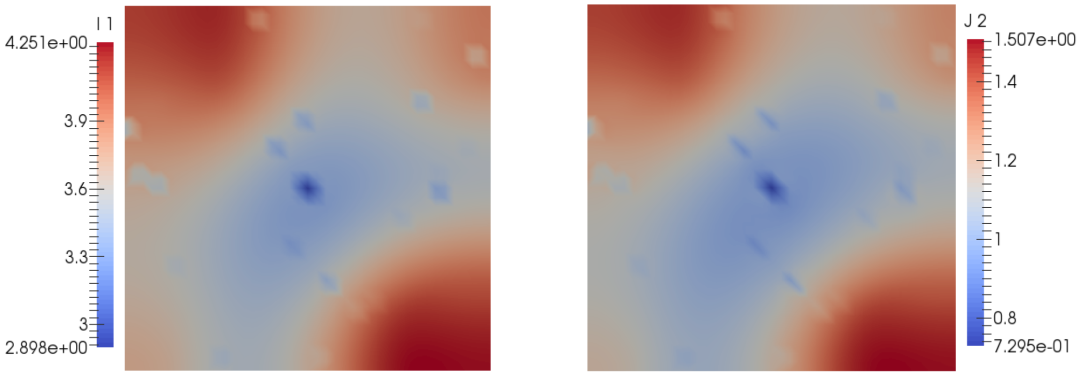

(a) $I_1 \geq 2.898$ [MPa] **(b)** $J_2 \geq 0.7295$ [MPa]

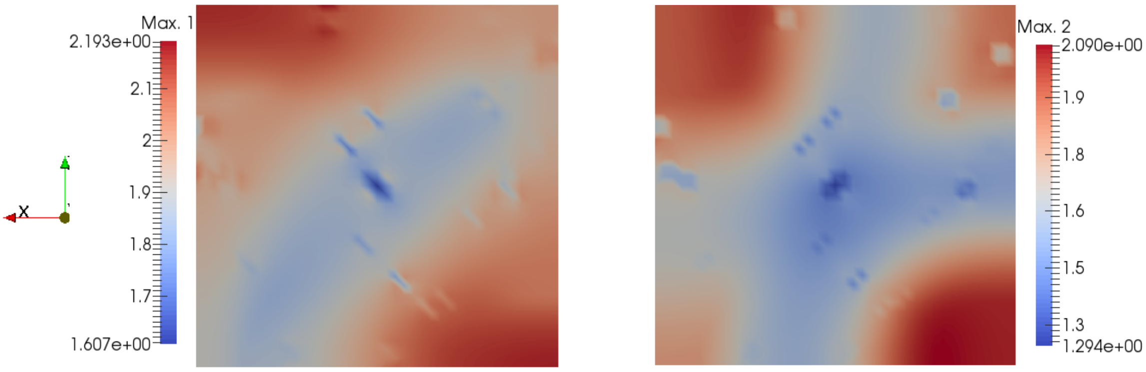

(c) Principal stress ($\sigma_1 \geq 1.607$ [MPa] **(d)** Principal stress ($\sigma_2 \geq 1.294$ [MPa]

Figure 11.13: Kupfer's plate under biaxial tension $\sigma_1/\sigma_2 = 1/1$ for $l_c = 25$ [mm] at displacement $u_{x/z} = 0.02636$ [mm] (a, b) Stress invariants and (c, d) Principal stresses

the initial stage of damage development. As can be seen, the nonlocal strains (over the damage threshold) and damage originate at the randomly chosen triggered locations and influence neighboring locations upon further increase in the loading. Thereby, the interactions between the triggered elements lead to the branching of deformation, which can be understood from the progressive nonlocal strains as well as the damage distributions. It seems like a macro-crack that opens from the central point of the specimen. Moreover, the stress invariants (I_1 and J_2) and principal stresses (σ_1 and σ_2) corresponding to the displacement of $0.02636\,[\mathrm{mm}]$ are illustrated in Figure 11.13. As observed, both the stress invariants and principle stress σ_2 have

(a) Nonlocal strains ($\leq 0.9068 \times 10^{-3}$) **(b)** Damage distribution ($D \leq 0.1345$)

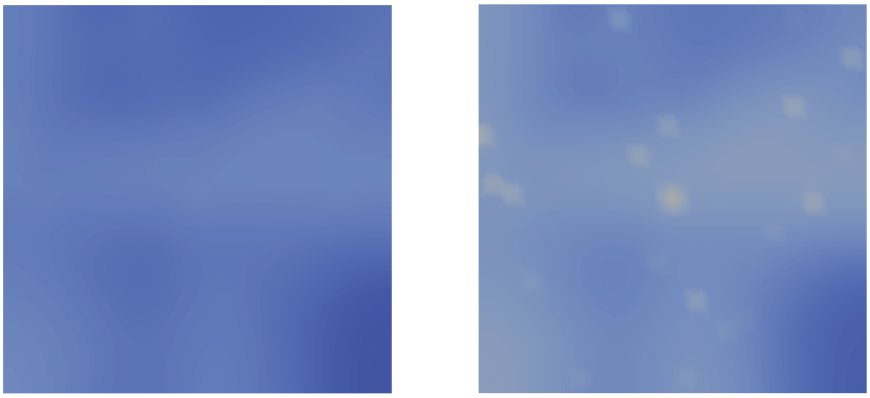

(c) Nonlocal strains ($\leq 1.060 \times 10^{-3}$) **(d)** Damage distribution ($D \leq 0.2654$)

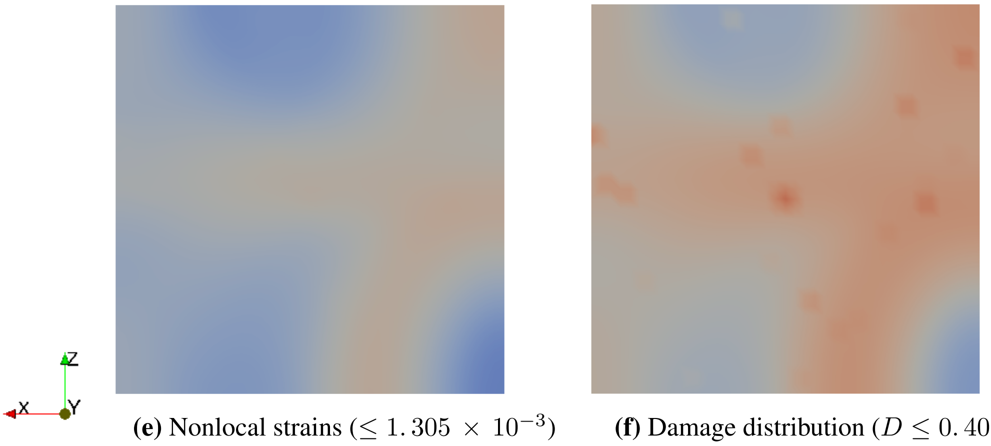

(e) Nonlocal strains ($\leq 1.305 \times 10^{-3}$) **(f)** Damage distribution ($D \leq 0.4060$)

Figure 11.14: Kupfer's plate under biaxial tension $\sigma_1/\sigma_2 = 1/1$ for $l_\mathrm{c} = 20\,[\mathrm{mm}]$ at displacements (a, b) $u_{\mathrm{x/z}} = 0.01745\,[\mathrm{mm}]$, (c, d) $u_{\mathrm{x/z}} = 0.01968\,[\mathrm{mm}]$, (e, f) $u_{\mathrm{x/z}} = 0.02302\,[\mathrm{mm}]$, and (g, h) $u_{\mathrm{x/z}} = 0.02525\,[\mathrm{mm}]$

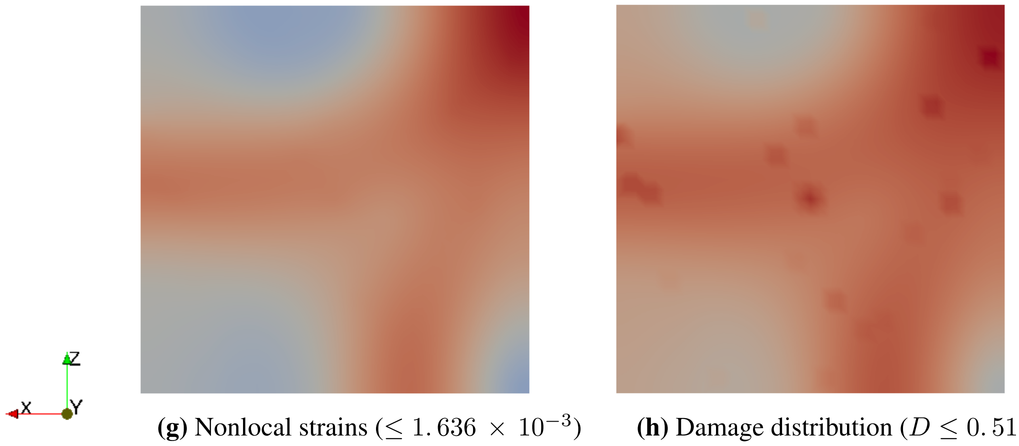

(g) Nonlocal strains ($\leq 1.636 \times 10^{-3}$) **(h)** Damage distribution ($D \leq 0.5152$)

Figure 11.14: Kupfer's plate under biaxial tension $\sigma_1/\sigma_2 = 1/1$ for $l_c = 20\,[\mathrm{mm}]$ at displacements (a, b) $u_{\mathrm{x/z}} = 0.01745\,[\mathrm{mm}]$, (c, d) $u_{\mathrm{x/z}} = 0.01968\,[\mathrm{mm}]$, (e, f) $u_{\mathrm{x/z}} = 0.02302\,[\mathrm{mm}]$, and (g, h) $u_{\mathrm{x/z}} = 0.02525\,[\mathrm{mm}]$

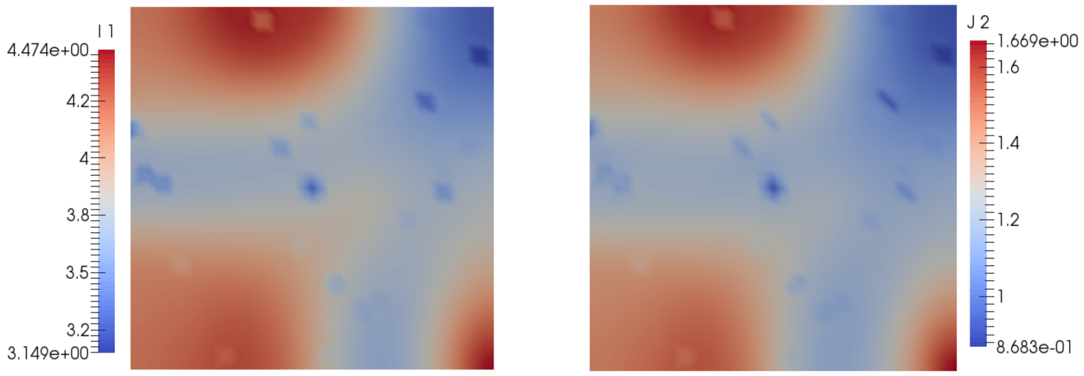

(a) $I_1 \geq 3.149$ [MPa] **(b)** $J_2 \geq 0.8683$ [MPa]

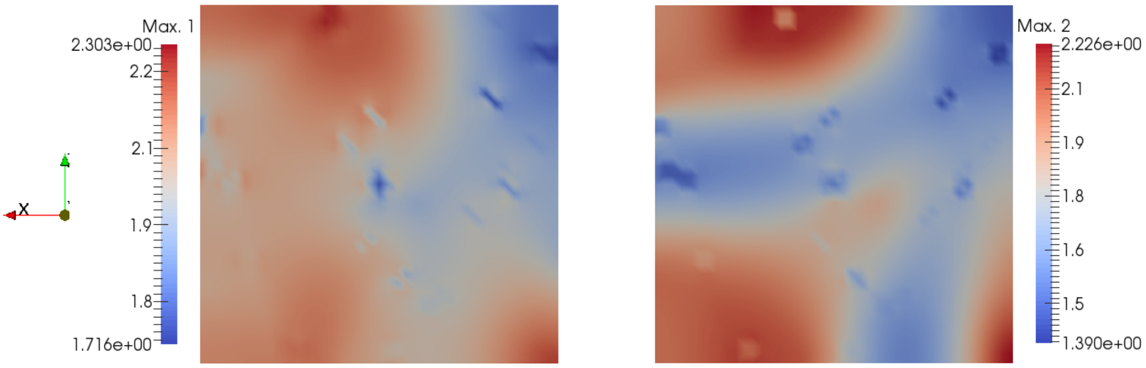

(c) Principal stress ($\sigma_1 \geq 1.716$ [MPa] **(d)** Principal stress ($\sigma_2 \geq 1.390$ [MPa]

Figure 11.15: Kupfer's plate under biaxial tension $\sigma_1/\sigma_2 = 1/1$ for $l_c = 20\,[\mathrm{mm}]$ at displacement $u_{\mathrm{x/z}} = 0.02525\,[\mathrm{mm}]$ (a, b) Stress invariants and (c, d) Principal stresses

lower values wherever the higher values of damage distribution occur, as seen in Figure 11.12h. By contrast, the principle stress σ_1 gets lower values only along the diagonal, as observed in Figure 11.13c.

On the other hand, the nonlocal strains and corresponding damage progression at various loading stages for $l_c = 20\,[\mathrm{mm}]$ are shown in Figure 11.14. The damage and nonlocal strain distributions for the first two steps shown are almost identical with the relevant steps of the previous case ($l_c = 25\,[\mathrm{mm}]$). Nevertheless, further loading steps leave considerable changes in branching of the nonlocal strains and damage, as can be seen in Figures 11.14e-11.14h. The reason behind this is that faster the growth of nonlocal strains/damage occurs, the width of localization narrows down due to lower value of the internal length. Furthermore, the stress invariants (I_1 and J_2) and principal stresses (σ_1 and σ_2) corresponding to the displacement of $0.02525\,[\mathrm{mm}]$ are illustrated in Figure 11.15. Both the stress invariants and principle stress σ_2 have lower values wherever the higher values of damage distribution occur, as seen in Figure 11.14h. But the principal stress σ_1 distribution is concentrated on the top right corner where the damage is more. It seems like a macro-crack that opens from that corner.

Therefore, the width of localization and interactions between the nonlocal strains merely depend on the size of internal length. The localized band of nonlocal strains obtained for $l_c = 25\,[\mathrm{mm}]$ pictured in Figure 11.12h nearly clones the diagonal crack formation in experiments [90], as shown in Figure 11.20.

11.1.4.3 Biaxial tension $\sigma_1/\sigma_2 = 1/0.54$

In this example, Kupfer's biaxial test ($\sigma_1/\sigma_2 = 1/0.54$) is simulated using the internal length $l_c = \{25\}\,[\mathrm{mm}]$. The geometry and boundary conditions of the test problem are shown in

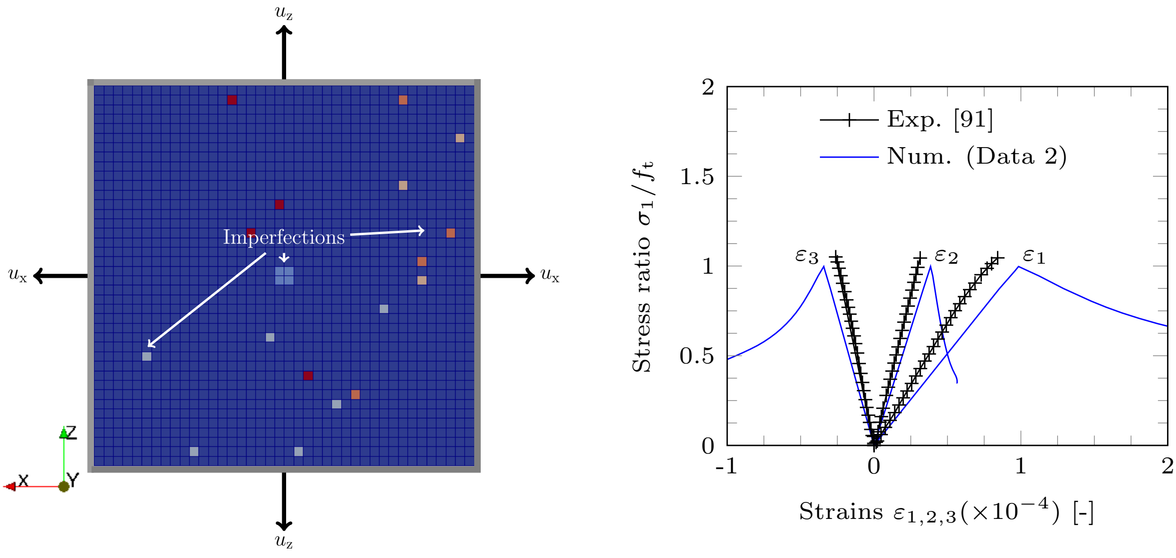

(a) Geometry and boundary conditions IV (40×40)

(b) Normalized stress-strain curves

Figure 11.16: Kupfer's plate subjected to (a) biaxial tension $\sigma_1/\sigma_2 = 1/0.54$ (b) Comparison of normalized stress responses with experiments [91]. The model and material parameters (Data 2) are as provided in Table 10.1.

Figure 11.16a. The boundary conditions are as similar to the previous example of equibiaxial tension. But the prescribed displacements are applied on the left and top edge surfaces such that $\sigma_1/\sigma_2 = 1/0.54$. Here as well, few elements are randomly chosen as imperfections by reducing the initial damage threshold by $3-15\%$ in order to model in-homogeneity of concrete material. These variations in the threshold values are highlighted by different colors in the mesh.

(a) Nonlocal strains ($\leq 0.9874 \times 10^{-3}$) **(b)** Damage distribution ($D \leq 0.2155$)

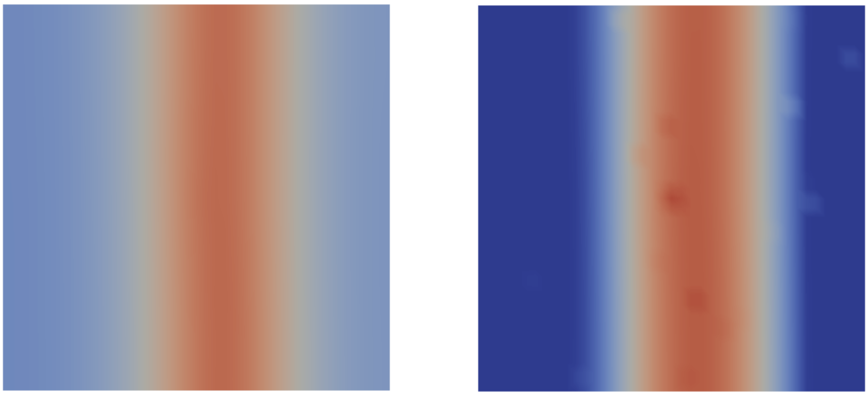

(c) Nonlocal strains ($\leq 1.842 \times 10^{-3}$) **(d)** Damage distribution ($D \leq 0.5966$)

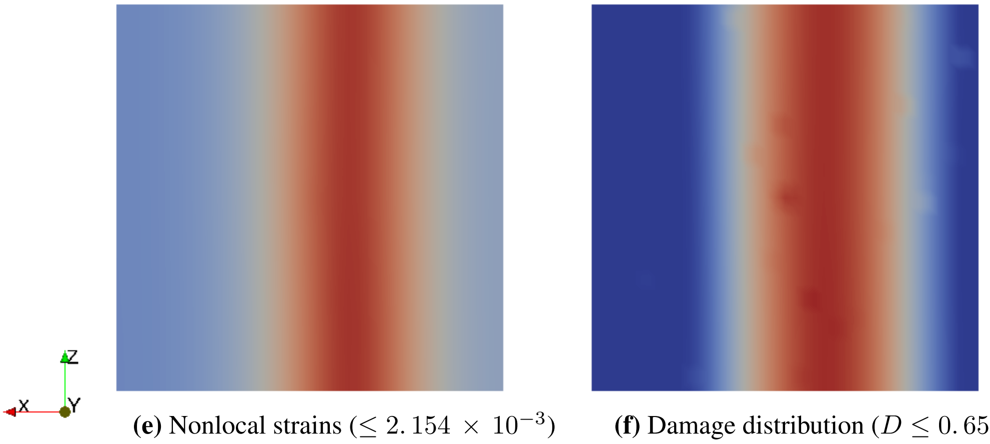

(e) Nonlocal strains ($\leq 2.154 \times 10^{-3}$) **(f)** Damage distribution ($D \leq 0.6541$)

Figure 11.17: Kupfer's plate under biaxial tension $\sigma_1/\sigma_2 = 1/0.54$ for $l_c = 25\,[\mathrm{mm}]$ at displacements (a, b) $u_{extx/z} = 0.0203/0.0080\,[\mathrm{mm/mm}]$, (c, d) $u_{extx/z} = 0.0248/0.0098\,[\mathrm{mm/mm}]$, (e, f) $u_{extx/z} = 0.0270/0.0106\,[\mathrm{mm/mm}]$, and (g, h) $u_{extx/z} = 0.0292/0.0115\,[\mathrm{mm/mm}]$

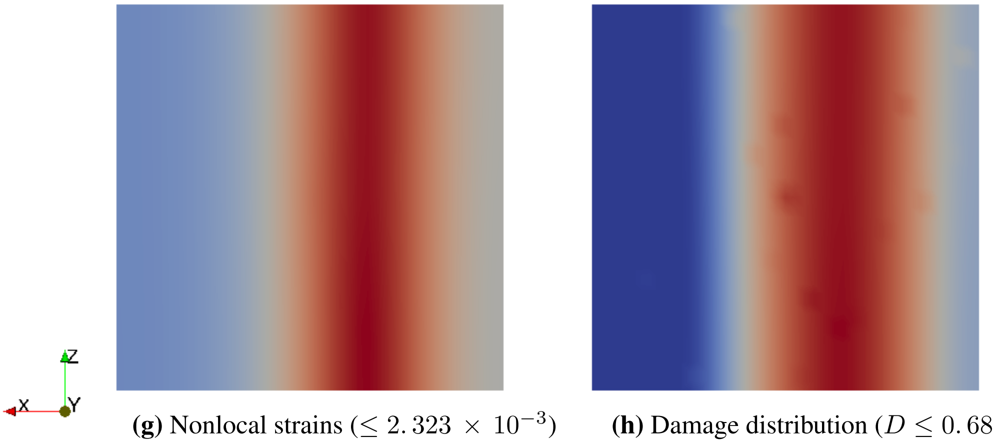

(g) Nonlocal strains ($\leq 2.323 \times 10^{-3}$) **(h)** Damage distribution ($D \leq 0.6834$)

Figure 11.17: Kupfer's plate under biaxial tension $\sigma_1/\sigma_2 = 1/0.54$ for $l_c = 25\,[\mathrm{mm}]$ at displacements (a, b) $u_{extx/z} = 0.0203/0.0080\,[\mathrm{mm/mm}]$, (c, d) $u_{extx/z} = 0.0248/0.0098\,[\mathrm{mm/mm}]$, (e, f) $u_{extx/z} = 0.0270/0.0106\,[\mathrm{mm/mm}]$, and (g, h) $u_{extx/z} = 0.0292/0.0115\,[\mathrm{mm/mm}]$

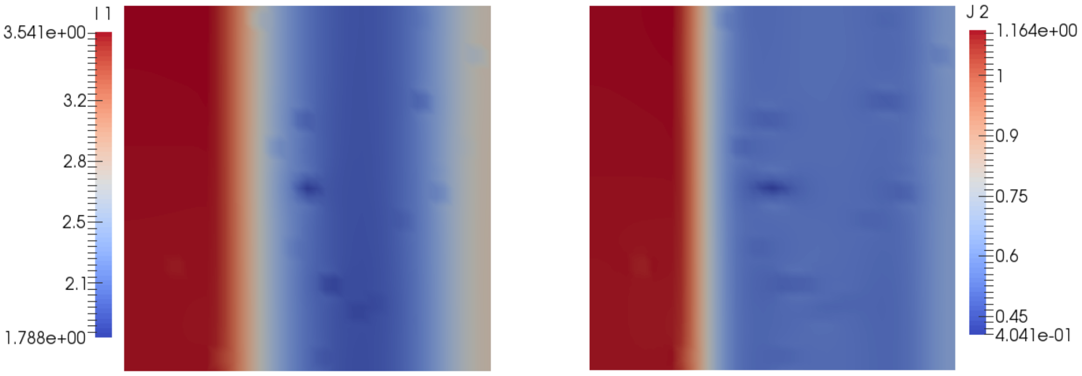

(a) $I_1 \geq 1.788$ [MPa] **(b)** $J_2 \geq 0.4041$ [MPa^2]

(c) Principal stress ($\sigma_1 \geq 1.263$ [MPa] **(d)** Principal stress ($\sigma_2 \geq 0.4523$ [MPa]

Figure 11.18: Kupfer's plate under biaxial tension $\sigma_1/\sigma_2 = 1/0.54$ for $l_c = 25\,[\mathrm{mm}]$ at displacement $u_{extx/z} = 0.0292/0.0115\,[\mathrm{mm/mm}]$ (a, b) Stress invariants and (c, d) Principal stresses

The normalized stress-strain curves obtained are compared against the experimental data [91] in Figure 11.16b. The results are reasonably good in agreement with data, but the predicted strain-softening is also shown. Figure 11.17 shows the nonlocal strains and corresponding damage

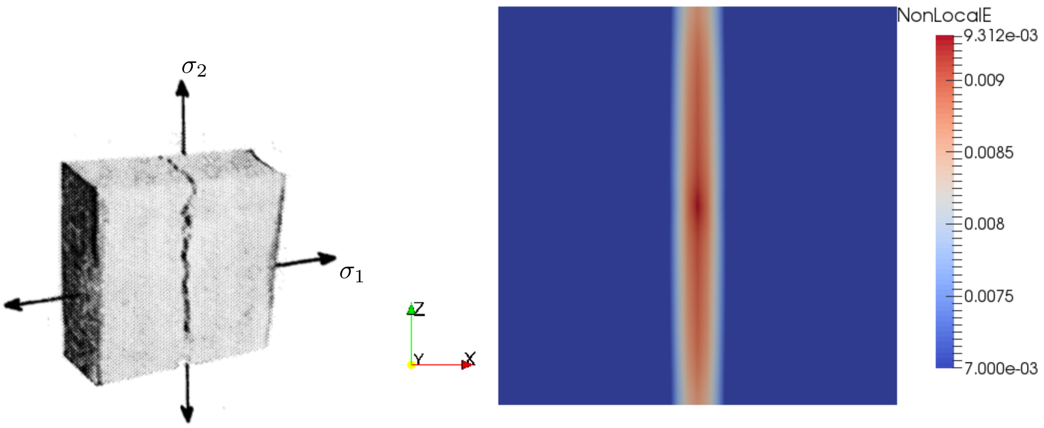

Figure 11.19: Kupfer specimen $\frac{\sigma_1}{\sigma_2} = 1/0$

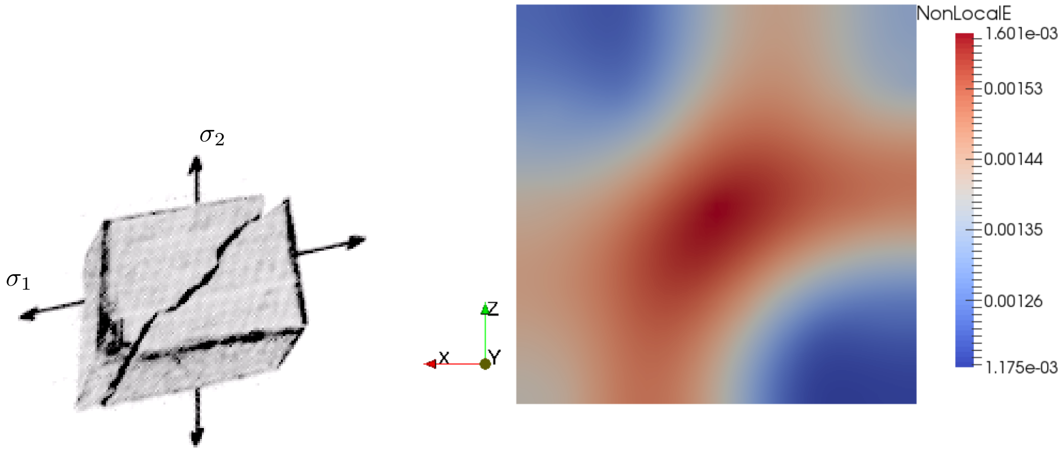

Figure 11.20: Kupfer specimen $\frac{\sigma_1}{\sigma_2} = 1/1$

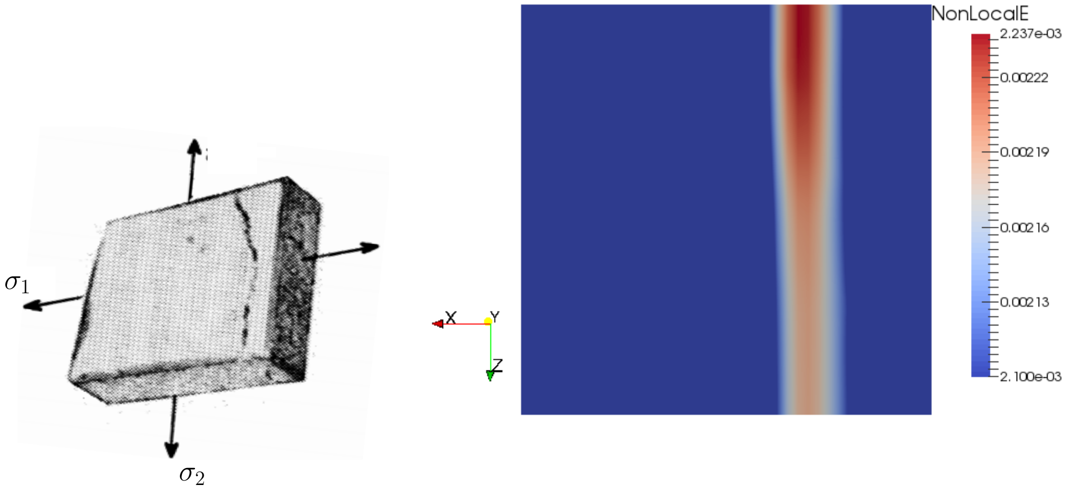

Figure 11.21: Kupfer specimen $\frac{\sigma_1}{\sigma_2} = 1/0.54$

progression at various loading stages. As soon as the damage criterion is fulfilled, the damage starts and further develops with the increase in the nonlocal strains. The growth of nonlcoal strains shown in Figure 11.17a corresponds to the initial stage of damage development. The nonlocal strains (over the damage threshold) and damage originate at the randomly chosen triggered locations and influence neighboring locations upon further increase in loading. Thereby, the interactions between the triggered elements lead to the formation of band in nonlocal strains as well as in damage distributions in between the middle of the specimen and the fully restrained right edge. Upon further increase in loading, the band concentrates near the right edge of the specimen until both the nonlocal strains and the damage get maximum. After that, the damage propagates towards the right edge, as the nonlocal strains do propagate towards the same edge.

As similar to the previous examples, the stress invariants (I_1 and J_2) and principal stresses (σ_1 and σ_2) corresponding to the displacement of 0.02636 $[\mathrm{mm}]$ are illustrated in Figure 11.18. The stress invariants and principle stresses have the lowest values of a band wherever the higher values of damage band occur, as noticed in Figure 11.17h. The principle stress σ_2 gets lower values along the band as shown in Figure 11.18d.

Figures 11.19-11.21 compares the experimental crack formations with those of equivalent crack formations from the present numerical investigations. Only the highest range of nonlocal strains are illustrated for comparison. It can be noticed that the performance and the ability of the damage model in describing the fracture phenomena in concrete is very convincing.

11.2 Single-edge notched specimen tests

In this section, a single-edge notched specimen, which is a well studied fracture problem in the scientific community of phase-field modeling [5, 6, 109], is investigated using the proposed model under tension and shear. It has a straight vertical notch running until the mid-height, located at a half distance of the left or right edge. Prior to loading, the mesh is refined in the regions where crack propagation is expected to occur. Both the simulations are performed under displacement control using two different internal length scales $l_c = \{0.2, 0.1\}$ $[\mathrm{mm}]$ such that l_c equals at least the size of two finest elements.

11.2.1 Tensile test

The geometry and boundary conditions of the tensile test problem are depicted in Figure 11.22a. As depicted, horizontal displacements are prescribed at the complete right edge. The specimen is discretized with 3933-Hex27 elements. The stress-displacement curves obtained at the point A on the right edge of the specimen are shown in Figure 11.22b. Similarly, the stress responses at the point B at the notch tip corresponding to the values of $l_c = \{0.2, 0.1\}$ $[\mathrm{mm}]$ are also obtained and plotted against the applied displacements in Figures 11.22c and 11.22d respectively. As shown in Figure 11.22b, a drop of stress values at A after the peak value occurs, as the stresses at B cease to minimum, as depicted in Figure 11.22c due to the growth of

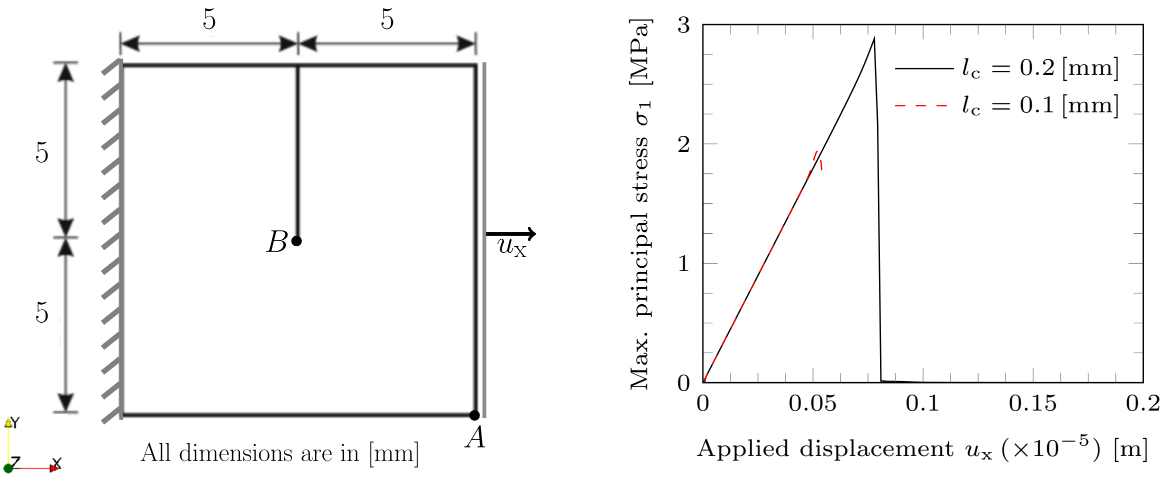

(a) Geometry and boundary conditions

(b) Stress response at A

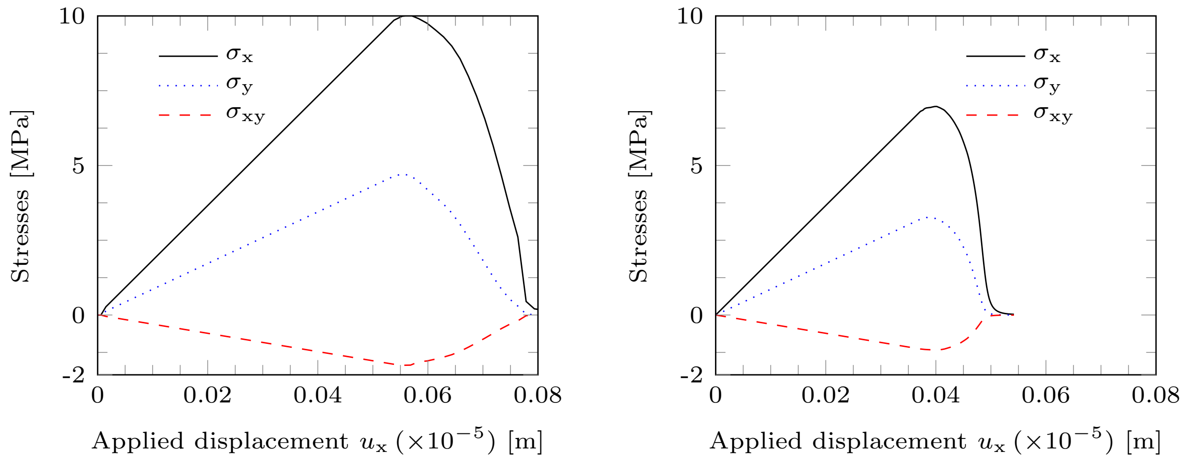

(c) Stress response at B for $l_c = 0.2$ [mm]

(d) Stress response at B for $l_c = 0.1$ [mm]

Figure 11.22: Single-edge notched specimen subjected to tension

damage. Thereafter, the growth of damage occurs along the crack path normal to the loading direction and in turn the decrease of the stresses occurs in the post-peak regions, as shown in Figure 11.22b. Nevertheless, the model exhibits very brittle response without allowing gradual decrease in stress when $l_c = 0.1$ [mm]. Hence, it is apparently clear that the lower value of the internal length causes reduction in the peak stresses and in turn the damage/softening grows faster. In other words, the higher value of the internal length causes increase in the peak stresses and consecutively damage/softening grows slower, and thus leads to reasonable damage propagation. These phenomena can be markedly observed by analyzing the growth of nonlocal strains and damage in specimen.

Figure 11.23 and 11.24 compare the growth of nonlocal strains and corresponding damage propagation at several stages of loading in the post-peak region for the meshes using $l_c = 0.2$ [mm] and $l_c = 0.1$ [mm] respectively.

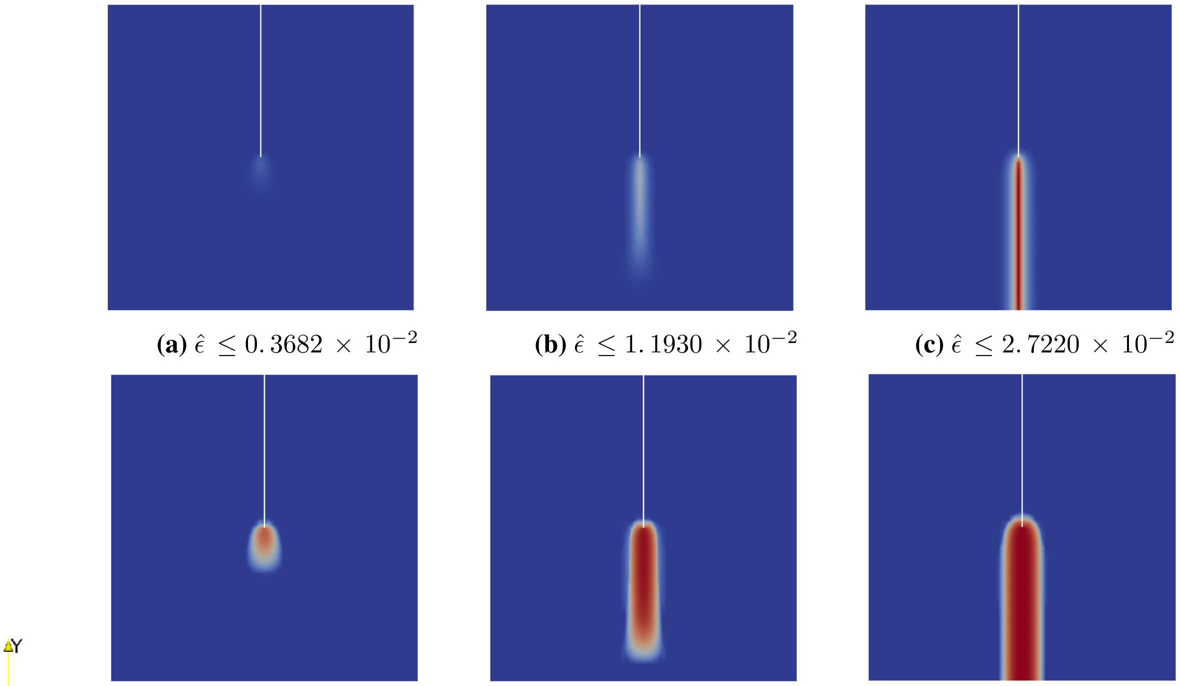

(a) $\hat{\epsilon} \leq 0.3682 \times 10^{-2}$ **(b)** $\hat{\epsilon} \leq 1.1930 \times 10^{-2}$ **(c)** $\hat{\epsilon} \leq 2.7220 \times 10^{-2}$

(d) $D \leq 0.8325$ **(e)** $D \leq 0.9890$ **(f)** $D \leq 0.9998$

Figure 11.23: Single-edge notched specimen under tension using $l_c = 0.2$ [mm]. Nonlocal strains (top) and damage (bottom) at displacements (a, d) $u_x = 0.7635 \times 10^{-3}$ [mm], (b, e) $u_x = 0.7935 \times 10^{-3}$ [mm], and (c, f) $u_x = 1.5135 \times 10^{-3}$ [mm]

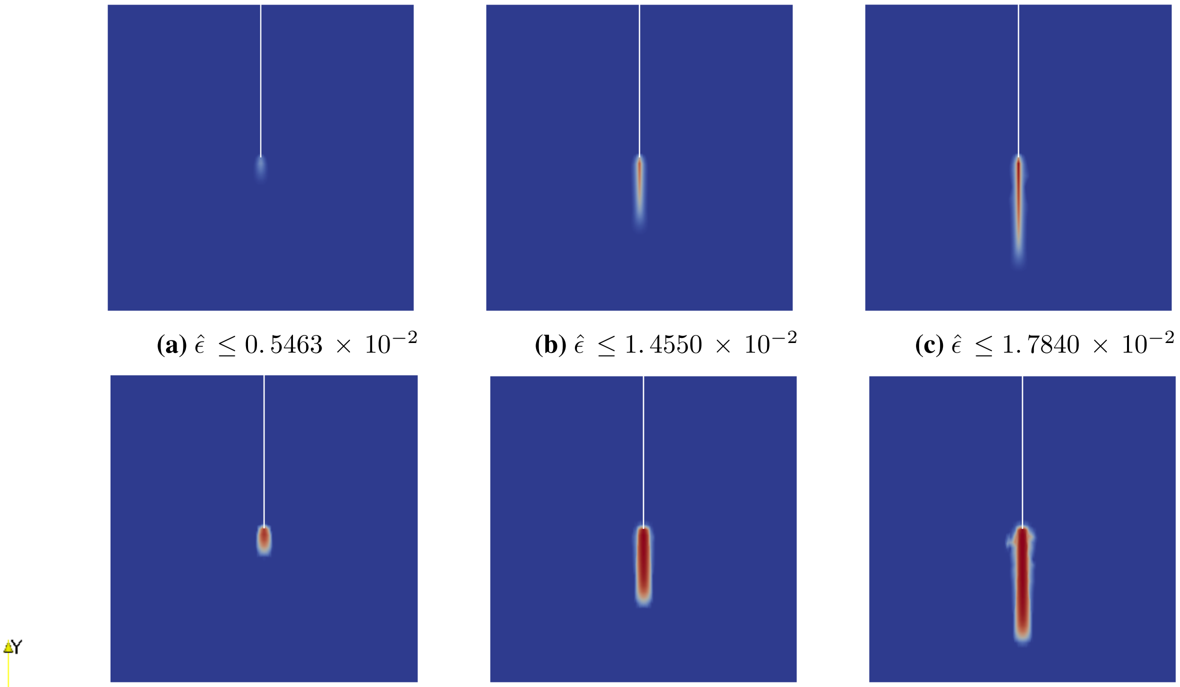

(a) $\hat{\epsilon} \leq 0.5463 \times 10^{-2}$ **(b)** $\hat{\epsilon} \leq 1.4550 \times 10^{-2}$ **(c)** $\hat{\epsilon} \leq 1.7840 \times 10^{-2}$

(d) $D \leq 0.9150$ **(e)** $D \leq 0.9941$ **(f)** $D \leq 0.9974$

Figure 11.24: Single-edge notched specimen under tension using $l_c = 0.1$ [mm]. Nonlocal strains (top) and damage (bottom) at displacements (a, d) $u_x = 0.4938 \times 10^{-3}$ [mm], (b, e) $u_x = 0.5239 \times 10^{-3}$ [mm], and (c, f) $u_x = 0.5419 \times 10^{-3}$ [mm]

As depicted in Figure 11.24, the values of nonlocal strains and damage at various loading stages have attained faster than those seen in Figure 11.23. Therefore, neither the propagation of nonlocal strains nor the propagation of damage runs through the complete specimen due to the lower value of l_c. Moreover, the width of deformation band (nonlocal strains or damage) is narrowed down due to the lower value of l_c. On the other hand, the growth of nonlocal strains and damage for the higher l_c run until the complete failure as shown in Figure 11.23, as the size of localization band is little broader than the previous case of lower l_c.

11.2.2 Shear test

The geometry and boundary conditions of the shear test problem are depicted in Figure 11.25a.

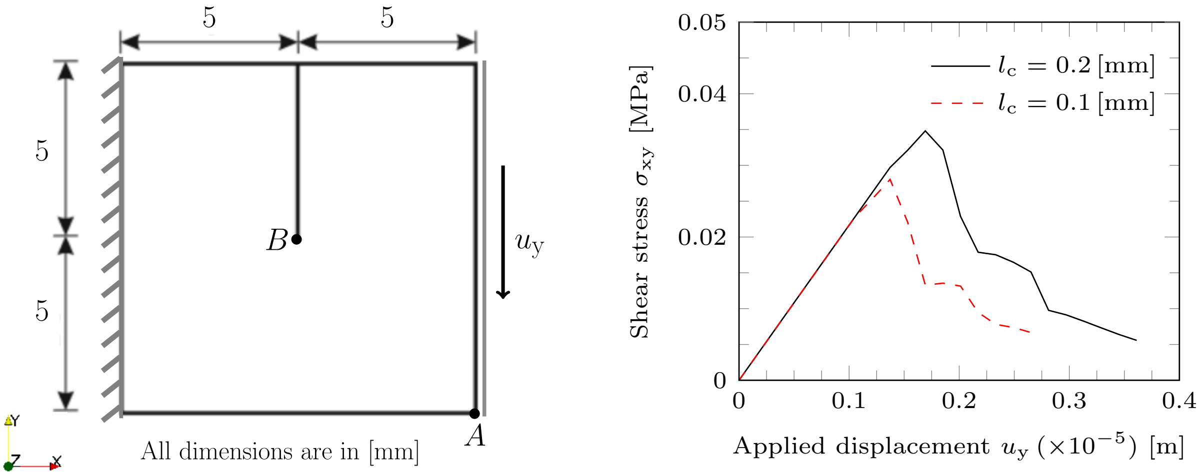

(a) Geometry and boundary conditions

(b) Stress response at A

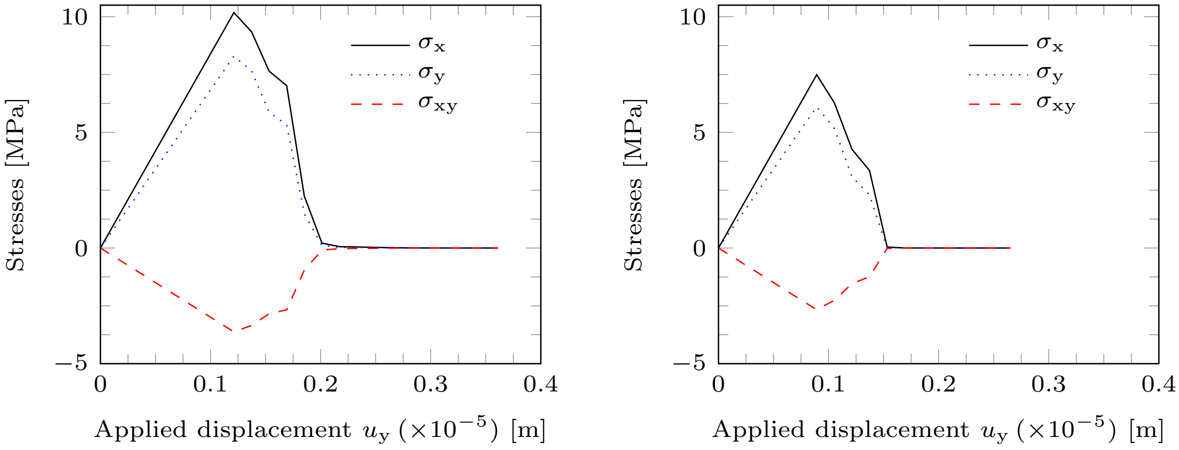

(c) Stress response at B for $l_c = 0.2$ [mm]

(d) Stress response at B for $l_c = 0.1$ [mm]

Figure 11.25: Single-edge notched specimen subjected to shear

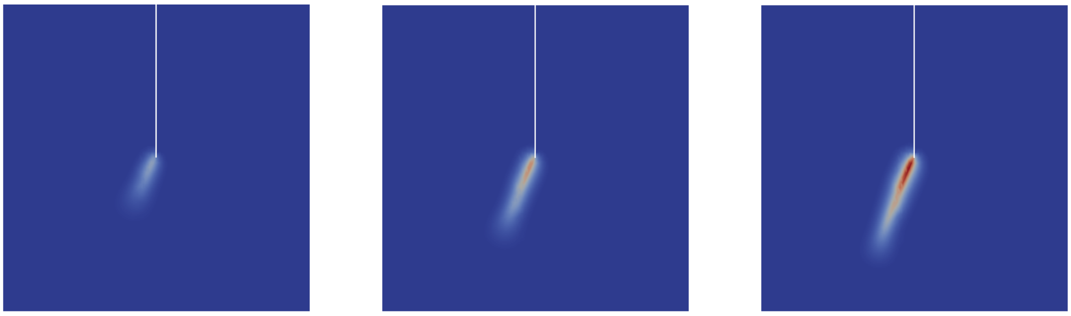

(a) $\hat{\epsilon} \leq 1.366 \times 10^{-2}$ **(b)** $\hat{\epsilon} \leq 2.421 \times 10^{-2}$ **(c)** $\hat{\epsilon} \leq 3.583 \times 10^{-2}$

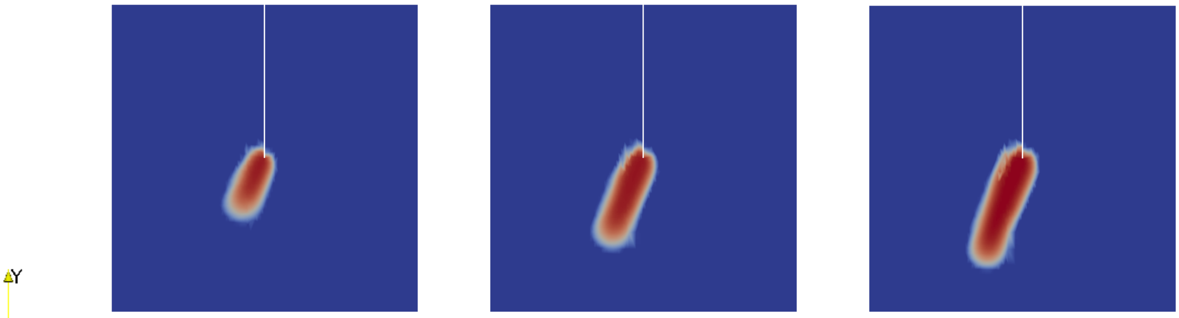

(d) $D \leq 0.9922$ **(e)** $D \leq 0.9994$ **(f)** $D \leq 1.0$

Figure 11.26: Single-edge notched specimen under shear using $l_c = 0.2$ [mm]. Nonlocal strains (top) and damage (bottom) at displacements (a, d) $u_y = 0.0022$ [mm], (b, e) $u_y = 0.0028$ [mm], and (c, f) $u_y = 0.0036$ [mm]

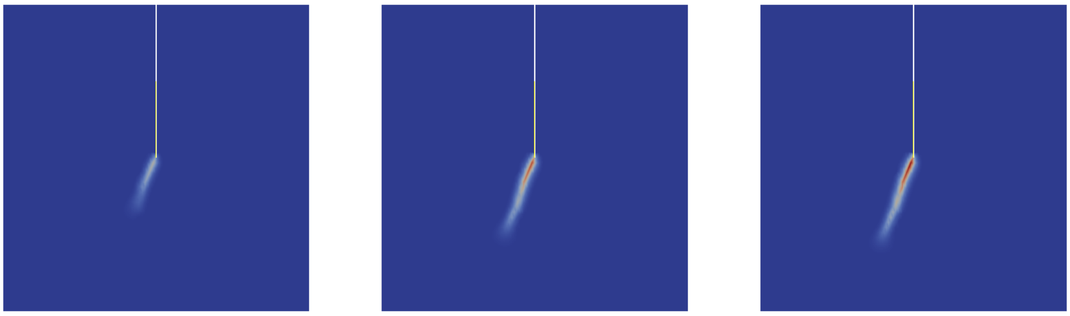

(a) $\hat{\epsilon} \leq 2.647 \times 10^{-2}$ **(b)** $\hat{\epsilon} \leq 4.567 \times 10^{-2}$ **(c)** $\hat{\epsilon} \leq 5.205 \times 10^{-2}$

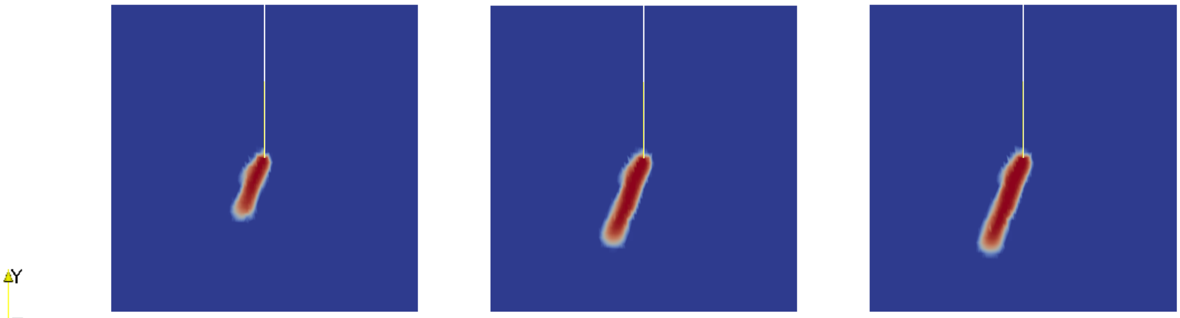

(d) $D \leq 0.9995$ **(e)** $D \leq 1.0$ **(f)** $D \leq 1.0$

Figure 11.27: Single-edge notched specimen under shear using $l_c = 0.1$ [mm]. Nonlocal strains (top) and damage (bottom) at displacements (a, d) $u_y = 0.0017$ [mm], (b, e) $u_y = 0.0023$ [mm], and (c, f) $u_y = 0.0027$ [mm]

As shown, the test is simulated by keeping the right edge subjected to downward vertical displacements. The specimen is discretized with 4046-Hex27 elements. The stress response curves obtained at the points A and B, which are plotted against the applied displacements u_{y} for the meshes using $l_{\mathrm{c}} = \{0.2, 0.1\}\,[\mathrm{mm}]$, are shown in the corresponding Figures 11.25b-11.25d. As can be seen in Figure 11.25b, the initial decrease of stresses at A occurs due to the strain-softening at B during the growth of damage, as shown in Figure 11.25d. Thereafter, further decrease of stresses at B upon subsequent load steps causes consecutive stress drops at A. However, the bumps that appear in the responses seen in Figure 11.25b are due to the fact that the model also allows the damage development in the compressed region near the vicinity of notch tip. It is seemingly noticed that the lower value of the internal length yields reduction in the peak stresses and thus causes faster growth in damage/softening, and *vice versa*. The strain-softening behavior is clearly observed for both the length scales.

Figures 11.26 and 11.27 illustrate the results of nonlocal strains and damage propagation at several stages of loading in the post-peak regime for the meshes with $l_{\mathrm{c}} = 0.2\,[\mathrm{mm}]$ and $l_{\mathrm{c}} = 0.1\,[\mathrm{mm}]$ respectively. It is also noticed that the lower l_{c} causes the faster growth of nonlocal strains and in turn causes the faster growth of damage when comparing to the results of the higher l_{c}. As similar to the tension test, the width of deformation band (nonlocal strains or damage) is narrowed down here as well, because of the adoption of the lower l_{c}. On the other hand, as displayed in Figure 11.26, the size of localization band is broader due to the use of the higher l_{c}.

The growth of nonlocal strains that clones the crack propagation and the stress-displacement behaviors are physically meaningful, although any relevant test data is not available. Therefore, it is noteworthy to mention that the selection of a proper value for the internal length scale l_{c} plays an essential role in the fracture phenomena to achieve physically meaningful results.

12 Conclusions and Outlook

The primary goal of the research work accomplished in this thesis was to develop a consistent nonlocal damage formulation, which can realistically describe the fracture process of concrete under various loading conditions. Thus, this thesis addressed the important features of modeling the different deformation behavior of concrete within the context of Continuum Damage Mechanics (CDM) as it is a promising approach to carry out failure predictions in many design and damage assessment situations within the framework of standard displacement finite element formulation. An implicit-gradient method is incorporated in the modeling to regularize mesh-dependencies and to avoid localization of deformation into a vanishing volume. The numerical implementation of the damage models into FEM codes is also discussed.

12.1 Summary and conclusions

The influence of various history deformation parameters and selection of model parameters on the softening behavior of concrete have been investigated. A suitable damage evolution law similar to Weibull's failure distribution is proposed for describing softening behavior.

A simplified constitutive model for concrete has been developed within a 3D-framework to take its distinct deformation behavior under monotonic and cyclic loading conditions into account. A unified equivalent strain is considered as a local deformation measure, which drives the evolution of effective isotropic damage. The damage evolution law proposed in this work is used in tension as well as in compression. The crack-opening and closure of micro-cracks under cyclic and reverse loading are described by the evolution of two independent history deformation parameters. The local equivalent strain and damage is enriched by the incorporation of an implicit gradient method. The investigations on the one-dimensional bar problem showed that mesh-dependency and ill-posedness of the boundary value problem are avoided due to gradient enhancement. Moreover, the influence of internal length scale on softening behavior and distribution of damage in the damage process zone are discussed. Nevertheless, the gradient enrichment of equivalent strains using the proposed model produced more reliable softening behavior than that of the damage variable in the case of concrete. Furthermore, the efficiency of the gradient-enhanced model is shown by validating the numerical responses obtained under monotonic (uniaxial, biaxial) loading as well as cyclic and reverse loading. Thus, the numerical predictions agree well with experimental results. In addition, it is demonstrated that the model can also simulate the unilateral behavior of concrete well by exhibiting a recovery of full initial stiffness for the first compression phase under the absence of inelastic strains.

The elastic-damage model has been extended to capture the irreversible deformations by considering the extended version of Lubliner-Lee failure surface. The failure surface has been slightly modified to allow the damage evolution due to the growth of the equivalent strains that has been measured from the total strains. Linear functions are adopted for isotropic tensile and compressive hardening. Therefore, the nonlinear behavior under compression is correctly modeled by an additional model parameter introduced in the damage evolution law. The crack-opening or closure effects have been included by two history damage parameters. In addition, the inelastic multiplier through two other multipliers in tension and compression is introduced in order to ensure that crack-closure and stiffness recovery occur appropriately but only after crossing crack-closure stress (shift-stress) in compression. The coupled inelastic-damage model is also validated under monotonic (uniaxial, biaxial) loading as well as cyclic and reverse loading conditions. Thus, the coupled inelastic-damage model is able to produce residual inelastic strains during unloading conditions, which was not captured by the elastic-damage model, and also to recover the original stiffness during the transition from tension to compression phase. Thence, the discrepancy of the elastic-damage model is overcome by the coupled model.

Finally, the performance and capabilities of the damage model in describing the fracture processes are demonstrated by means of simulating selected concrete fracture problems on Kupfer's plate specimen under several test cases. The homogeneous and non-homogeneous material properties are also simulated by introducing zero-, completely random, and selectively random distributions of imperfections. Without imperfections, the model produces incorrect localization of deformation behavior in case of uniaxial or biaxial test cases, except under equibiaxial tests in which the formation of diagonal crack is reasonably convincing. Whereas the model produces incorrect localization behavior and is strongly localized at one of the boundaries when completely random imperfections are simulated. But the simulations of selectively random imperfections provide very convincing results and identify the possible situations that form equivalent cracks as observed in experiments. Thus, it is demonstrated that the model is able to describe the crack initiation, propagation and branching phenomena occurring during the fracture processes equivalently. The detailed comparison of numerical results of all tests with the relevant experimental investigations proves the ability of the model and correctness of damage formulations. Additionally, a standard single-edge notched specimen is also investigated under tensile and shear tests. In the absence of experimental data, the notched specimen tests also provide physically fruitful information on crack initiation and propagation. It is observed that the lower value of the characteristic internal length scale causes faster growth of nonlocal strains and in turn causes faster growth of damage when comparing results at higher values. Thereby, the width of the deformation band (nonlocal strains or damage) is controlled by the internal length scale. Thus, the proposed model can provide a beneficial engineering tool for predicting different damage behavior in concrete structures under various loading circumstances.

12.2 Future scope of the work

As mentioned, Continuum Damage Mechanics hast still proven to be an efficient approach to develop powerful modeling tools. Although the gradient-damage models developed in this work satisfactorily describe the damage behavior of concrete, it is believed that there is still room for improvement in the developed models. Hence, the following plans and developments or possible extensions are lined up for the future research.

- **Additional verification** Both the proposed models have to be verified by modeling the fracture process involved in several other standard benchmark problems in absence and presence of inelastic strain evolution.
- **Anisotropic description** Due to micro-cracking pattern exhibited by concrete, the internal degradation of the material that depends on the direction of applied loading is inherently anisotropic. Therefore, damage induced anisotropy must be incorporated in the present damage model for a more reliable representation of damage in concrete to describe the direction of damage propagation. This can be achieved by introducing a fourth-order damage effect tensor $\mathbb{M}$ [34, 111] that enters into the constitutive law of the material model. The model should also be able to describe cyclic/unilateral behavior of concrete.
- **Local-nonlocal interactions** Nonlocal enhancement of certain softening models by either integral formulation or gradient formulation may not completely regularize the problem of localization and in turn yields different localization behavior [101]. Therefore, in order to achieve full regularization, the models must embody the concept of over-nonlocal, which uses a weighted sum of the local and nonlocal values [127, 128].
- **Modeling of reinforced concrete** The modeling of the reinforcement could be achieved by steel bars considering uniaxial visco-plastic constitutive relation [32]. The modeling of contact between concrete and steel necessitates an extension of the existing bond model [40, 142] that has been developed at the institute to account for cyclic loading conditions. The coupling of steel, concrete and bond model will be done to perform the numerical investigations of structural components under a realistic earthquake history and the model will be further validated.

References

[1] Ahrens, H; Dinkler, D: *Finite-Element-Methoden Teil II*. Institut für Statik, TU Braunschweig, 1996.

[2] Ahrens, H; Dinkler, D: *Finite-Element-Methoden Teil I*. Institut für Statik, TU Braunschweig, 2006.

[3] Al-Rub, RKA; Voyiadjis, GZ: On the coupling of anisotropic damage and plasticity models for ductile materials. *International Journal of Solids and Structures*, 40(11), 2611–2643, 2003.

[4] Altenbach, H; Skrzypek, JJ: *Creep and damage in materials and structures*. Springer, 1999.

[5] Ambati, M: *Phase-field modeling and computations of brittle and ductile fracture for solids and shells*. Diss., Techn. Univ. Braunschweig, 2017.

[6] Ambati, M; Gerasimov, T; De Lorenzis, L: A review on phase-field models of brittle fracture and a new fast hybrid formulation. *Computational Mechanics*, 1–23, 2014.

[7] Anderson, TL: *Fracture mechanics: fundamentals and applications*. CRC press, 2005.

[8] Babu, RR; Benipal, Gurmail S; Singh, AK: Constitutive modelling of concrete: an overview. *Asian Journal of Civil Engineering (building and housing)*, 6(4), 211–246, 2005.

[9] Bachmann, H: *Safety of structures against earthquakes(in German)*. Birkhäuser Verlag, 2002.

[10] Barenblatt, GI: The formation of equilibrium cracks during brittle fracture. General ideas and hypotheses. Axially-symmetric cracks. *Journal of Applied Mathematics and Mechanics*, 23(3), 622–636, 1959.

[11] Barenblatt, GI: The mathematical theory of equilibrium cracks in brittle fracture. *Advances in applied mechanics*, 7(1), 55–129, 1962.

[12] Bažant, ZP: Instability, ductility, and size effect in strain-softening concrete. *Journal of the Engineering Mechanics Division*, 102(2), 331–344, 1976.

[13] Bažant, ZP: Mechanics of distributed cracking. *Applied Mechanics Reviews*, 39(5), 675–705, 1986.

[14] Bažant, ZP; Belytschko, TB: Wave propagation in a strain-softening bar: exact solution. *Journal of Engineering Mechanics*, 111(3), 381–389, 1985a.

[15] Bažant, ZP; Belytschko, TB; Chang, TP: Continuum theory for strain-softening. *Journal of Engineering Mechanics*, 110(12), 1666–1692, 1984.

[16] Bažant, ZP; Caner, FC; Carol, I; Adley, MD; Akers, SA: Microplane model M4 for concrete. I: Formulation with work-conjugate deviatoric stress. *Journal of Engineering Mechanics*, 126(9), 944–953, 2000.

[17] Bažant, ZP; Chang, TP: Nonlocal finite element analysis of strain-softening solids. *Journal of engineering mechanics*, 113(1), 89–105, 1987.

[18] Bazant, ZP; Jirásek, M: Nonlocal integral formulations of plasticity and damage: survey of progress. *Journal of Engineering Mechanics*, 128(11), 1119–1149, 2002.

[19] Bažant, ZP; Oh, BH: Crack band theory for fracture of concrete. *Matériaux et construction*, 16(3), 155–177, 1983.

[20] Bažant, ZP; Pijaudier-Cabot, G: Nonlocal continuum damage, localization instability and convergence. *Journal of Applied Mechanics*, 55(2), 287–293, 1988.

[21] Bažant, ZP; Pijaudier-Cabot, G: Measurement of characteristic length of nonlocal continuum. *Journal of Engineering Mechanics*, 115(4), 755–767, 1989.

[22] Beckmann, MB: *Ein Gradientenabhängiges Modell für Anisotrope Schädigung von Beton unter Berücksichtigung von Porendruck.* Diss., Techn. Univ. Braunschweig, 2009.

[23] Benipal, GS; Singh, AK; others: Plasticity-based constitutive model for concrete in stress space. *Latin American Journal of Solids and Structures*, 3(4), 417–441, 2006.

[24] Besson, J; Cailletaud, G; Chaboche, JL; Forest, S: *Non-linear mechanics of materials*, Vol. 167. Springer Science & Business Media, 2009.

[25] Bilby, BA; Howard, IC; Li, ZH: Mesh independent cell models for continuum damage theory. *Fatigue & Fracture of Engineering Materials & Structures*, 17(10), 1221–1233, 1994.

[26] Bonet, J; Wood, RD: *Nonlinear continuum mechanics for finite element analysis*. Cambridge university press, 2015.

[27] Bourdin, B; Francfort, GA; Marigo, JJ: Numerical experiments in revisited brittle fracture. *Journal of the Mechanics and Physics of Solids*, 48(4), 797 – 826, 2000.

[28] Brekelmans, WAM; Schreurs, PJG; De Vree, JHP: Continuum damage mechanics for softening of brittle materials. *Acta mechanica*, 93(1-4), 133–143, 1992.

[29] Carmeliet, J; De Borst, R: Gradient damage and reliability instability as limit state function. In *In F. H. Wittmann, editor, Fracture Mechanics of Concrete Structures: Proceedings Second International Conference(FRAMCOS-2)*. Aedificatio Publishers, Freiburg, Germany., 1011–1020, 1995b.

[30] Cervera, M; Oliver, J; Manzoli, O: A Rate-Dependent Isotropic Damage Model for the Seismic Aanalysis of Concrete Dams. *Earthquake engineering & structural dynamics*, 25(9), 987–1010, 1996.

[31] Chaboche, JL; Lesne, PM; Maire, JF: Continuum Damage Mechanics, Anisotropy and Damage Deactivation for Brittle Materials Like Concrete and Ceramic Composites. *International Journal of Damage Mechanics*, 4(1), 5–22, 1995.

[32] Chaboche, JL; Rousselier, G: On the Plastic and Viscoplastic Constitutive Equations—Part I: Rules Developed With Internal Variable Concept. *Journal of Pressure Vessel Technology*, 105(2), 153–158, 1983.

[33] Chow, CL; Lu, TJ: On evolution laws of anisotropic damage. *Engineering Fracture Mechanics*, 34, 679–701, 1989.

[34] Chow, CL; Wang, J: An anisotropic theory of elasticity for continuum damage mechanics. *International Journal of Fracture*, 33(1), 3–16, 1987.

[35] Cicekli, U; Voyiadjis, GZ; Al-Rub, RKA: A plasticity and anisotropic damage model for plain concrete. *International Journal of plasticity*, 23(10), 1874–1900, 2007.

[36] Comi, C: Computational modelling of gradient-enhanced damage in quasi-brittle materials. *Mechanics of Cohesive-frictional Materials*, 4(1), 17–36, 1999.

[37] Comité Européen De Normalisation, : Eurocode 8–Design of Structures for earthquake resistance–Part 1: General rules, seismic actions and rules for buildings. *European Standard NF EN*, 1, 1998.

[38] Cook, RD; Malkus, DS; Plesha, ME; Witt, RJ: *Concepts and applications of finite element analysis*, Vol. 4. Wiley India, 2009.

[39] Cordebois, JP; Sidoroff, F: Damage induced elastic anisotropy. In *Mechanical Behavior of Anisotropic Solids/Comportment Méchanique des Solides Anisotropes*, Springer, 761–774, 1982.

[40] Cox, JV; Herrmann, LR: Validation of a plasticity bond model for steel reinforcement. *Mechanics of Cohesive-frictional Materials*, 4(4), 361–389, 1999.

[41] Cramer, F: *Mehrfeld-Modelle für chemisch-physicalische Alterungsprozesse von Beton*. Diss., Techn. Univ. Braunschweig, Diss., 2016.

[42] Cramer, F; Kowalsky, U; Dinkler, D: Coupled chemical and mechanical processes in concrete structures with respect to aging. *Coupled systems mechanics*, 3, 53–71, March 2014.

[43] Cramer, F; Ostermann, L; Kowalsky, U; Dinkler, D: Coupled analysis of Thermo-Chemical and mechanical degradation of concrete at high temperatures. In *H. Barros, C. Pina and C. Ferreira(Eds), Proceedings of 2nd International Conference on Recent Advances in Nonlinear Models Structural Concrete Applications(CoRAN2011)*, 1–10, 2011.

[44] De Borst, R; Benallal, A; Heeres, OM: A gradient-enhanced damage approach to fracture. *Le Journal de Physique IV*, 6(C6), C6–491, 1996.

[45] De Borst, R; Mühlhaus, HB: Gradient-dependent plasticity: Formulation and algorithmic aspects. *International Journal for Numerical Methods in Engineering*, 35(3), 521–539, 1992.

[46] De Borst, R; Pamin, J; Peerlings, RHJ; Sluys, LJ: On gradient-enhanced damage and plasticity models for failure in quasi-brittle and frictional materials. *Computational Mechanics*, 17(1-2), 130–141, 1995.

[47] De Borst, R; Remmers, JJC; Needleman, A; Abellan, MA: Discrete vs smeared crack models for concrete fracture: bridging the gap. *International Journal for Numerical and Analytical Methods in Geomechanics*, 28(7-8), 583–607, 2004.

[48] De Borst, R; Remmers, JJC; Needleman, A; others: Computational aspects of cohesive-zone models. *Advanced Fracture Mechanics for Life and Safety Assesments-Stockholm (Sweden)*, 2004.

[49] De Borst, R; Sluys, LJ; Mühlhaus, HB; Pamin, J: Fundamental issues in finite element analyses of localization of deformation. *Engineering computations*, 10(2), 99–121, 1993.

[50] De Borst, R; Verhoosel, CV: Gradient damage vs phase-field approaches for fracture: Similarities and differences. *Computer Methods in Applied Mechanics and Engineering*, 312(Supplement C), 78 – 94, 2016. Phase Field Approaches to Fracture.

[51] De Souza Neto, EA; Peric, D; Owen, DRJ: *Computational methods for plasticity: theory and applications*. John Wiley & Sons, 2011.

[52] De Vree, JHP; Brekelmans, WAM; Van Gils, MAJ: Comparison of nonlocal approaches in continuum damage mechanics. *Computers & Structures*, 55(4), 581–588, 1995.

[53] Desmorat, R; Gatuingt, F; Ragueneau, F: Nonlocal anisotropic damage model and related computational aspects for quasi-brittle materials. *Engineering Fracture Mechanics*, 74(10), 1539–1560, 2007.

[54] Desmorat, R; Gatuingt, F; Ragueneau, F: Nonstandard Thermodynamics Framework for Robust Computations with Induced Anisotropic Damage. *International Journal of Damage Mechanics*, 19(1), 53–73, 2010.

[55] Dimitrijevic, BJ; Hackl, K: A method for gradient enhancement of continuum damage models. *Tech. Mech*, 28(1), 43–52, 2008.

[56] Dimitrijevic, BJ; Hackl, K: A regularization framework for damage–plasticity models via gradient enhancement of the free energy. *International Journal for Numerical Methods in Biomedical Engineering*, 27(8), 1199–1210, 2011.

[57] Dugdale, DS: Yielding of steel sheets containing slits. *Journal of the Mechanics and Physics of Solids*, 8(2), 100–104, 1960.

[58] Ehlers, W: A single-surface yield function for geomaterials. *Archive of Applied Mechanics*, 65(4), 246–259, 1995.

[59] Emmrich, E; Lehoucq, RB; Puhst, D: Peridynamics: A Nonlocal Continuum Theory. In *Meshfree Methods for Partial Differential Equations VI*, Vol. 89, Springer Berlin Heidelberg, 45–65, 2013.

[60] Engelen, RAB; Geers, MGD; Baaijens, FPT: Nonlocal implicit gradient-enhanced elasto-plasticity for the modelling of softening behaviour. *International journal of Plasticity*, 19(4), 403–433, 2003.

[61] Evans, RH; Marathe, MS: Microcracking and stress-strain curves for concrete in tension. *Materials and Structures*, 1(1), 61–64, 1968.

[62] Faria, R; Oliver, J; Cervera, M: A strain-based plastic viscous-damage model for massive concrete structures. *International Journal of Solids and Structures*, 35(14), 1533–1558, 1998.

[63] Faria, R; Oliver, J; Cervera, M: Modeling material failure in concrete structures under cyclic actions. *Journal of Structural Engineering*, 130(12), 1997–2005, 2004.

[64] Francfort, GA; Marigo, JJ: Revisiting brittle fracture as an energy minimization problem. *Journal of the Mechanics and Physics of Solids*, 46(8), 1319 – 1342, 1998.

[65] Frost, NE; Dugdale, DS: The propagation of fatigue cracks in sheet specimens. *Journal of the Mechanics and Physics of Solids*, 6(2), 92–110, 1958.

[66] Geers, MGD: *Experimental analysis and computational modelling of damage and fracture*. Diss., Technische Universiteit Eindhoven, 1997.

[67] Geers, MGD; De Borst, R; Brekelmans, WAM; Peerlings, RHJ: Strain-based transient-gradient damage model for failure analyses. *Computer Methods in Applied Mechanics and Engineering*, 160(1), 133–153, 1998.

[68] Geers, MGD; De Borst, R; Brekelmans, WAM; Peerlings, RHJ: Validation and internal length scale determination for a gradient damage model: application to short glass-fibre-reinforced polypropylene. *International Journal of Solids and Structures*, 36(17), 2557 – 2583, 1999.

[69] Geers, MGD; Peerlings, RHJ; Brekelmans, WAM; De Borst, R: Phenomenological non-local approaches based on implicit gradient-enhanced damage. *Acta Mechanica*, 144(1-2), 1–15, 2000.

[70] Gerstle, W; Sau, N; Silling, SA: Peridynamic modeling of plain and reinforced concrete structures. In *SMiRT18, Int. Conf. Structural Mech. Reactor Technol*, 2005.

[71] Gerstle, W; Sau, N; Silling, SA: Peridynamic modeling of concrete structures. *Nuclear engineering and design*, 237(12), 1250–1258, 2007.

[72] Gopalaratnam, VS; Shah, SP: Softening response of plain concrete in direct tension. *Journal Proceedings*, 82(3), 310–323, 1985.

[73] Hill, R: A general theory of uniqueness and stability in elastic-plastic solids. *Journal of the Mechanics and Physics of Solids*, 6(3), 236–249, 1958.

[74] Hillerborg, A: A model for fracture analysis. *Report TVBM*, 1978.

[75] Hillerborg, A: Application of fracture mechanics to concrete: summary of a series of lectures 1988. *Report TVBM-3030, Div. of Building Materials, Lund Inst. of Technology, Sweden*, 1988.

[76] Hillerborg, A: Application of the fictitious crack model to different types of materials. *International Journal of Fracture*, 51(2), 95–102, 1991.

[77] Hillerborg, A; Modéer, M; Petersson, PE: Analysis of crack formation and crack growth in concrete by means of fracture mechanics and finite elements. *Cement and concrete research*, 6(6), 773–781, 1976.

[78] Häussler-Combe, U; Hartig, J: Formulation and numerical implementation of a constitutive law for concrete with strain-based damage and plasticity. *International Journal of Non-Linear Mechanics*, 43(5), 399 – 415, 2008.

[79] Jirásek, M: Nonlocal models for damage and fracture: comparison of approaches. *International Journal of Solids and Structures*, 35(31), 4133–4145, 1998.

[80] Ju, JWW; Chaboche, JL; Voyiadjis, GZ: *Damage mechanics in engineering materials*. Elsevier, 1998.

[81] Kachanov, LM: Time of the rupture process under creep conditions. *Isv. Akad. Nauk. SSR. Otd Tekh. Nauk*, 8, 26–31, 1958.

[82] Kachanov, LM: *Introduction to continuum damage mechanics*, Vol. 10. Springer Science & Business Media, 1986.

[83] Kachanov, LM: Rupture time under creep conditions. *International Journal of Fracture*, 97(1-4), 11–18, 1999.

[84] Karsan, ID; Jirsa, JO: Behavior of concrete under compressive loadings. *Journal of the Structural Division*, 95(12), 2543–2564, 1969.

[85] Kesler, CE; Naus, DJ; Lott, JL: Fracture mechancis - Its Applicability to concrete. In *Proceedings of the Society of Materials Science Conference on the Mechanical Behavior of Materials.* Transport and Road Research Laboratory, Old Wokingham Road Crowthorne RG11 6AU, Berkshire England, 113–124, 1972.

[86] Kowalsky, U; Meyer, J; Heinrich, S; Dinkler, D: A nonlocal damage model for mild steel under inelastic cyclic straining. *Computational Materials Science*, 63, 28 – 34, 2012.

[87] Krajcinovic, D: *Damage mechanics*, Vol. 41. Elsevier, 1996.

[88] Kuhl, E; Ramm, E: Simulation of strain localization with gradient enhanced damage models. *Computational Materials Science*, 16(1), 176–185, 1999.

[89] Kuhl, E; Ramm, E; De Borst, R: An anisotropic gradient damage model for quasi-brittle materials. *Computer Methods in Applied Mechanics and Engineering*, 183(1), 87–103, 2000.

[90] Kupfer, HB; Gerstle, KH: Behavior of concrete under biaxial stresses. *Journal of the Engineering Mechanics Division*, 99(4), 853–866, 1973.

[91] Kupfer, HB; Zelger, C: *Das Verhalten des Betons unter mehrachsiger Kurzzeitbelastung unter besonderer Berücksichtigung der zweiachsigen Beanspruchung: Bau und Erprobung einer Versuchseinrichtung für Zweiachsige Belastung*. Ernst, 1973.

[92] Lasry, D; Belytschko, T: Localization limiters in transient problems. *International Journal of Solids and Structures*, 24(6), 581 – 597, 1988.

[93] Lee, J; Fenves, GL: A plastic-damage concrete model for earthquake analysis of dams. *Earthquake engineering & structural dynamics*, 27(9), 937–956, 1998.

[94] Lee, J; Fenves, GL: Plastic-Damage Model for Cyclic Loading of Concrete Structures. *Journal of Engineering Mechanics*, 124, 08 1998.

[95] Lemaitre, J: *A course on damage mechanics*. Springer Science & Business Media, 2012.

[96] Lemaitre, J; Chaboche, JL: *Mechanics of solid materials*. Cambridge University Press, Cambridge, 1990.

[97] Lemaitre, J; Desmorat, R: *Engineering damage mechanics: ductile, creep, fatigue and brittle failures*. Springer Science & Business Media, 2005.

[98] Lubliner, J; Oliver, J; Oller, Sand; Onate, E: A plastic-damage model for concrete. *International Journal of solids and structures*, 25(3), 299–326, 1989.

[99] Luccioni, B; Oller, S; Danesi, R: Coupled plastic-damaged model. *Computer methods in applied mechanics and engineering*, 129(1), 81–89, 1996.

[100] Luo, Albert CJ: *Nonlinear Deformable-body Dynamics*. Springer Science & Business Media, 2011.

[101] Luzio, GD; Bažant, ZP: Spectral analysis of localization in nonlocal and over-nonlocal materials with softening plasticity or damage. *International Journal of Solids and Structures*, 42(23), 6071 – 6100, 2005.

[102] Maekawa, K; Okamura, H: The Deformational Behavior and Constitutive Equation of Concrete Using the Elasto-Plastic and Fracture Model. *Journal of the Faculty of Engineering, The Univ. of Tokyo (B)*, XXXVII(2), 252–328, 1983.

[103] Mazars, J: A description of micro-and macroscale damage of concrete structures. *Engineering Fracture Mechanics*, 25(5), 729–737, 1986.

[104] Mazars, J; Berthaud, Y; Ramtani, S: The unilateral behaviour of damaged concrete. *Engineering Fracture Mechanics*, 35(4), 629–635, 1990.

[105] Mazars, J; Grange, S: Modeling of reinforced concrete structural members for engineering purposes. *Computers and Concrete*, 16(5), 683–701, 2015.

[106] Mazars, J; Hamon, F; Grange, S: A new 3D damage model for concrete under monotonic, cyclic and dynamic loadings. *Materials and Structures*, 48(11), 3779–3793, 2015.

[107] Mazars, J; Pijaudier-Cabot, G: Continuum damage theory-application to concrete. *Journal of Engineering Mechanics*, 115(2), 345–365, 1989.

[108] Miehe, C; Hofacker, M; Welschinger, F: A phase field model for rate-independent crack propagation: Robust algorithmic implementation based on operator splits. *Computer Methods in Applied Mechanics and Engineering*, 199(45), 2765–2778, 2010.

[109] Miehe, C; Welschinger, F; Hofacker, M: Thermodynamically consistent phase-field models of fracture: Variational principles and multi-field FE implementations. *International Journal for Numerical Methods in Engineering*, 83(10), 1273–1311, 2010.

[110] Mühlhaus, HB; Alfantis, EC: A variational principle for gradient plasticity. *International Journal of Solids and Structures*, 28(7), 845 – 857, 1991.

[111] Murakami, S: *Continuum damage mechanics: a continuum mechanics approach to the analysis of damage and fracture*, Vol. 185. Springer Science & Business Media, 2012.

[112] Murakami, S; Kamiya, K: Constitutive and damage evolution equations of elastic-brittle materials based on irreversible thermodynamics. *International Journal of Mechanical Sciences*, 39(4), 473–486, 1997.

[113] Nouailletas, O; La Borderie, C; Perlot, C; Rivard, P; Ballivy, G: Experimental Study of Crack Closure on Heterogeneous Quasi-Brittle Material. 141, 04015041, 05 2015.

[114] Öchsner, A: *Continuum damage and fracture mechanics*. Springer, 2016.

[115] Ostermann, L: *Hochtemperaturverhalten von Beton – Gekoppelte Mehrfeld-Modellierung und numerische Analyse*. Diss., Techn. Univ. Braunschweig, Diss., 2011.

[116] Ostermann, L; Dinkler, D: Modelling and numerical simulation of concrete structures subject to high temperatures. *Coupled systems mechanics*, 3(1), 73–88, 2014.

[117] Ottosen, NS: Constitutive model for short-time loading of concrete. *Journal of the Engineering Mechanics Division ASCE*, 105, 127–141, 1979.

[118] Paas, MHJW; Schreurs, PJG; Brekelmans, WAM: A continuum approach to brittle and fatigue damage: theory and numerical procedures. *International journal of solids and structures*, 30(4), 579–599, 1993.

[119] Peerlings, RHJ: *Enhanced Damage Modelling for Fracture and Fatigue: Proefschrift*. Technische Universiteit Eindhoven, 1999.

[120] Peerlings, RHJ; De Borst, R; Brekelmans, WAM; De Vree, JHP: Computational modelling of gradient-enhanced damage for fracture and fatigue problems. In *Computational Plasticity, Fundamentals and Applications: Proceedings of the 4th International Conference*. Pineridge Press: Swansea, 975–986, 1995.

[121] Peerlings, RHJ; De Borst, R; Brekelmans, WAM; De Vree, JHP: Gradient enhanced damage for quasi-brittle materials. *International Journal for numerical methods in engineering*, 39, 3391–3403, 1996.

[122] Peerlings, RHJ; De Borst, R; Brekelmans, WAM; De Vree, JHP; Spee, I: Some observations on localisation in non-local and gradient damage models. *European Journal of Mechanics Series a Solids*, 15, 937–954, 1996.

[123] Peerlings, RHJ; De Borst, R; Brekelmans, WAM; Geers, MGD: Gradient-enhanced damage modelling of concrete fracture. *Mechanics of Cohesive-Frictional Materials*, 3(4), 323–342, 1998.

[124] Peerlings, RHJ; De Borst, R; Brekelmans, WAM; Geers, MGD: Wave propagation and localisation in nonlocal and gradient-enhanced damage models. *Le Journal de Physique IV*, 8(PR8), Pr8–293, 1998.

[125] Peerlings, RHJ; Geers, MGD; De Borst, R; Brekelmans, WAM: A critical comparison of nonlocal and gradient-enhanced softening continua. *International Journal of solids and Structures*, 38(44), 7723–7746, 2001.

[126] Pijaudier-Cabot, G; Bazant, ZP: Nonlocal damage theory. *Journal of Engineering Mechanics*, 113(10), 1512–1533, 1987.

[127] Poh, LH; Swaddiwudhipong, S: Gradient-enhanced softening material models. *International Journal of Plasticity*, 25(11), 2094 – 2121, 2009.

[128] Poh, LH; Swaddiwudhipong, S: Over-nonlocal gradient enhanced plastic-damage model for concrete. *International Journal of Solids and Structures*, 46(25), 4369 – 4378, 2009a.

[129] Reddy, JN: *An introduction to the finite element method*, Vol. 2. McGraw-Hill New York, 1993.

[130] Reddy, JN: *An introduction to nonlinear finite element analysis*. OXFORD University Press, 2008.

[131] Remmers, JJC; De Borst, R; Needleman, A: A cohesive segments method for the simulation of crack growth. *Computational mechanics*, 31(1-2), 69–77, 2003.

[132] Rodríguez-Ferran, A; Morata, I; Huerta, A: A new damage model based on non-local displacements. *International Journal for Numerical and Analytical Methods in Geomechanics*, 29(5), 473–493, 2005.

[133] Schauer, M; Roman, JE; Quintana-Ortí, ES; Langer, S: Parallel computation of 3-D soil-structure interaction in time domain with a coupled FEM/SBFEM approach. *Journal of Scientific Computing*, 52(2), 446–467, 2012.

[134] Schreyer, HL: Analytical Solutions for Nonlinear Strain-Gradient Softening and Localization. *Journal of Applied Mechanics*, 57(3), 522–528, 1990.

[135] Schreyer, HL; Chen, Z: One-Dimensional Softening With Localization. *Journal of Applied Mechanics*, 53(4), 791–797, 1986.

[136] Silling, SA: Reformulation of elasticity theory for discontinuities and long-range forces. *Journal of the Mechanics and Physics of Solids*, 48(1), 175–209, 2000.

[137] Simo, JC; Hughes, TJR: *Computational inelasticity*, Vol. 7. Springer Science & Business Media, 2006.

[138] Simo, JC; Ju, JW: Strain-and stress-based continuum damage models-I. Formulation. *International journal of solids and structures*, 23(7), 821–840, 1987a.

[139] Simo, JC; Ju, JW: Strain- and stress-based continuum damage models-II. Computational aspects. *International Journal of Solids and Structures*, 23(7), 841 – 869, 1987b.

[140] Singh, AK: *Mechanics of solids*. PHI Learning Pvt. Ltd., 2007.

[141] Skrzypek, JJ; Ganczarski, A: *Modeling of material damage and failure of structures: theory and applications*. Springer Science & Business Media, 1999.

[142] Stein, T; Kowalsky, U; Dinkler, D: Numerical analysis of reinforced concrete structures with particular focus on bond behaviour. *PAMM*, 16(1), 241–242, 2016.

[143] Triantafyllidis, N; Aifantis, EC: A gradient approach to localization of deformation. I. Hyperelastic materials. *Journal of Elasticity*, 16(3), 225–237, 1986.

[144] Velde, J: *3D Nonlocal Damage Modeling for Steel Structures under Earthquake Loading*. Diss., Techn. Univ. Braunschweig, Diss., 2010.

[145] Velde, J; Kowalsky, U; Zümendorf, T; Dinkler, D: 3D-FE-Analysis of CT-specimens including viscoplastic material behavior and nonlocal damage. *Computational Materials Science*, 46(2), 352–357, 2009.

[146] Vignjevic, R; Djordjevic, N; Gemkow, S; De Vuyst, T; Campbell, J: SPH as a nonlocal regularisation method: Solution for instabilities due to strain-softening. *Computer Methods in Applied Mechanics and Engineering*, 277, 281–304, 2014.

[147] Voyiadjis, GZ; Taqieddin, ZN; Kattan, PI: Anisotropic damage–plasticity model for concrete. *International Journal of Plasticity*, 24(10), 1946–1965, 2008.

[148] Willam, KJ; Warnke, EP: Constitutive models for the triaxial behavior of concrete. *International Assoc. for Bridge and Structural Engineering Proceedings*, 19, 1 – 30, 1975.

[149] Zhang, J; Li, J: Elastoplastic damage model for concrete based on consistent free energy potential. *Science China Technological Sciences*, 1–9, 2014.

[150] Zhang, W; Cai, Y: *Continuum damage mechanics and numerical applications*. Springer Science & Business Media, 2010.

[151] Zhu, JZ; Taylor, ZRL; Zienkiewicz, OC: *The finite element method: its basis and fundamentals*. Elsevier, 2013.

[152] Zümendorf, T: *Ein gradientenabhängiges Modell für Schädigung bei viskoplastischem Materialverhalten*. Diss., Techn. Univ. Braunschweig, Diss., 2006.

Berichte aus dem Institut für Statik ab 2007

Nr. 2007-105	C. LEPPERT: Mehrphasenmodell für granulare Medien zur numerischen Untersuchung des Phasenübergangs bei der Entleerung von Silos
Nr. 2007-106	V. KRASE: Stability of Municipal Solid Waste Landfills
Nr. 2007-107	J. PONTOW: Imperfektionsempfindlichkeit und Grenzlasten von Schalentragwerken
Nr. 2009-108	M. BECKMANN: Ein gradientenabhängiges Modell für anisotrope Schädigung von Beton unter Berücksichtigung von Porendruck
Nr. 2010-109	P. SUN: Fluid-Struktur-Wechselwirkung mit aktiver Schwingungskontrolle durch piezoelektrische Materialien
Nr. 2010-110	J. VELDE: 3D Nonlocal Damage Modeling for Steel Structures under Earthquake Loading
Nr. 2010-111	K. SCHUSTER: Systemidentifikation und Bauwerksüberwachung mit piezokeramischen Aktuatoren
Nr. 2011-112	S. BENTE: Interaction of Degradation, Deformation and Transport Processes in Municipal Solid Waste Landfills
Nr. 2011-113	L. OSTERMANN: Hochtemperaturverhalten von Beton – Gekoppelte Mehrfeld-Modellierung und numerische Analyse
Nr. 2012-114	B. BRODERSEN: Modellierung des thermo-mechanischen Verbundverhaltens von Asphalt in Straßenaufbauten
Nr. 2012-115	J. KINDLEIN: Gekoppelte Analyse von Reaktions- und Transportprozessen in Deponiestrukturen
Nr. 2015-116	F. PASENOW: Modellierung oberflächengekoppelter Mehrfeldsysteme und numerische Analyse rutschender Bodenmaterialien
Nr. 2015-117	M. SCHAUER: Ein effizienter gekoppelter FEM-SBFEM Ansatz zur Analyse von Boden-Bauwerk-Interaktionen im Zeitbereich
Nr. 2016-118	A. ALFARRA: Numerische Analyse von Bauwerk-Wind-Wechselwirkungen mit RANS-Turbulenzmodellen
Nr. 2016-119	S. REINSTÄDLER: Modellierung und numerische Analyse der Entleerung von dünnwandigen Silos
Nr. 2016-120	F. CRAMER: Mehrfeld-Modell für chemisch-physikalische Alterungsprozesse von Beton
Nr. 2018-121	T. BLUME: Mikromechanisch begründete Modellbildung des thermomechanischen Werkstoffverhaltens von Asphalt
Nr. 2018-122	F. OCKELMANN: Modellierung und numerische Analyse von Beton und faserverstärktem Ultrahochleistungsbeton mit der Diskrete Elemente Methode

Sonderdrucke

Phänomenologische Modelle für Werkstoffe des Bauwesens.
Hermann Ahrens zum 60. Geburtstag (1998).
Herausgeber: D. Dinkler, U. Kowalsky.

Baustatik-Baupraxis 8.
Berichte der Fachtagung am 21. und 22. März 2002 in Braunschweig.
Herausgeber: D. Dinkler.

Institut für Statik, Technische Universität Braunschweig
Beethovenstraße 51, 38106 Braunschweig, Deutschland
Telefon +49 (0)531 / 391-3667, Telefax +49 (0)531 / 391-8116
E-Mail statik@tu-bs.de, Homepage https://www.tu-braunschweig.de/statik